UNIVERSIDAD COMPLUTENSE DE MADRID
FACULTAD DE CIENCIAS FÍSICAS

TESIS DOCTORAL

Integration of half-metallic ferromagnetic thin films on silicon by means of a tunnel contact

Integración de láminas delgadas de materiales feromagnéticos medio-metálicos en silicio por medio de un contacto túnel

MEMORIA PARA OPTAR AL GRADO DE DOCTOR

PRESENTADA POR

Iciar Arnay Ortigosa

Director

Juan Rubio Zuazo

Madrid

© Iciar Arnay Ortigosa, 2019

Universidad Complutense de Madrid-Facultad CC Físicas

Departamento de Física de materiales

Tesis doctoral

Integration of half-metallic ferromagnetic thin films on silicon by means of a tunnel contact

Integración de láminas delgadas de materiales ferromagnéticos semimetálicos en silicio por medio de un contacto túnel

Iciar Arnay Ortigosa

Director

Dr. Juan Rubio Zuazo

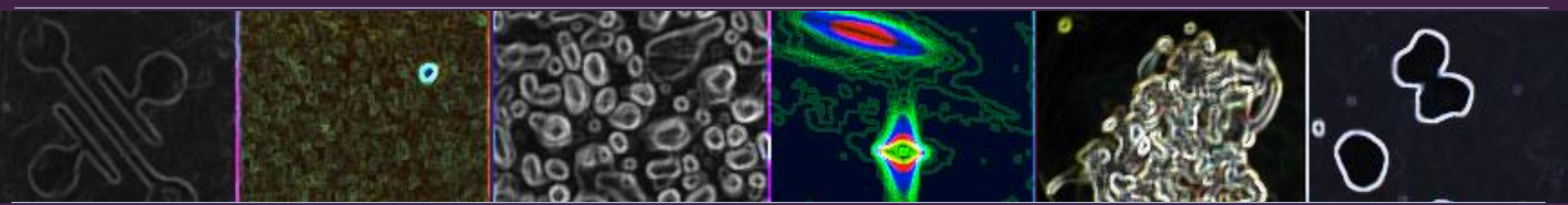

Spanish CRG BM25-SpLine at The ESRF

Madrid, 2019

UNIVERSIDAD COMPLUTENSE MADRID

DECLARACIÓN DE AUTORÍA Y ORIGINALIDAD DE LA TESIS PRESENTADA PARA OBTENER EL TÍTULO DE DOCTOR

D./Dña. Iciar Arnay Ortigosa,
estudiante en el Programa de Doctorado en F'isica,
de la Facultad de Ciencias Físicas de la Universidad Complutense de Madrid, como autor/a de la tesis presentada para la obtención del título de Doctor y titulada:

Integración de láminas delgadas de materiales ferromagnéticos medio-metálicos en silicio por medio de un contacto túnel

y dirigida por: Juan Rubio Zuazo

DECLARO QUE:

La tesis es una obra original que no infringe los derechos de propiedad intelectual ni los derechos de propiedad industrial u otros, de acuerdo con el ordenamiento jurídico vigente, en particular, la Ley de Propiedad Intelectual (R.D. legislativo 1/1996, de 12 de abril, por el que se aprueba el texto refundido de la Ley de Propiedad Intelectual, modificado por la Ley 2/2019, de 1 de marzo, regularizando, aclarando y armonizando las disposiciones legales vigentes sobre la materia), en particular, las disposiciones referidas al derecho de cita.

Del mismo modo, asumo frente a la Universidad cualquier responsabilidad que pudiera derivarse de la autoría o falta de originalidad del contenido de la tesis presentada de conformidad con el ordenamiento jurídico vigente.

En Madrid, a 6 de mayo de 2019

Fdo.: Iciar Arnay

Digitally signed by Iciar Arnay
Date: 2019.05.06 10:27:06 +02'00'

Esta DECLARACIÓN DE AUTORÍA Y ORIGINALIDAD debe ser insertada en la primera página de la tesis presentada para la obtención del título de Doctor.

Universidad Complutense de Madrid
Facultad de Ciencias Físicas
Departamento de Física de Materiales

Tesis Doctoral

Integration of half-metallic ferromagnetic thin films on silicon by means of a tunnel contact

---

Integración de láminas delgadas de materiales ferromagnéticos medio-metálicos en silicio por medio de un contacto túnel

Iciar Arnay Ortigosa

Tesis dirigida por:

Dr. Juan Rubio Zuazo

CRG española BM25-SpLine en el ESRF

Instituto de Ciencia de Materiales de Madrid (ICMM-CSIC)

Madrid, 2019

Contents

Contents i

List of Figures viii

List of Tables ix

Resumen I

Summary V

1 Introduction 1
- 1.1 Semiconductor spintronics . . . 1
- 1.2 Spin injection into a semiconductor . . . 4
  - 1.2.1 The impedance mismatch problem . . . 4
  - 1.2.2 Quantum tunneling through a potential barrier . . . 7
  - 1.2.3 Spin-dependent tunneling in MTJ . . . 9
  - 1.2.4 Role of the tunnel barrier on spin dependent tunneling . . . 10
  - 1.2.5 Formation of the Schottky barrier . . . 11
  - 1.2.6 Extrinsic contributions to spin relaxation . . . 13
- 1.3 Half metal electrodes . . . 14
- 1.4 Electrical spin injection in semiconductors nowadays . . . 16
- 1.5 Aim of the thesis . . . 19
- 1.6 Organization of the manuscript . . . 20

2 Experimental techniques 21
- 2.1 Introduction . . . 21
- 2.2 Physical vapor deposition (PVD) . . . 21
  - 2.2.1 Pulsed Laser Deposition (PLD) . . . 21
  - 2.2.2 Molecular beam epitaxy (MBE) . . . 23
- 2.3 X-Ray Photoelectron Spectroscopy (XPS) . . . 24
  - 2.3.1 Experimental set-up . . . 24
  - 2.3.2 XPS intensity . . . 26

2.3.3 Determination of the thickness of an over layer A on a substrate surface B . . . 26
2.4 Low Energy Electron Diffraction (LEED) . . . 27
2.5 Reflection High Energy Electron Diffraction (RHEED) . . . 28
2.6 Synchrotron-based techniques . . . 29
2.6.1 Introduction . . . 29
2.6.2 Specular X-Ray Reflectivity (XRR) . . . 34
2.6.3 X-Ray Diffraction (XRD) . . . 35
2.6.4 Hard X-Ray Photoelectron Spectroscopy (HAXPES) . . . 42
2.6.5 X-Ray Absorption Spectroscopy (XAS) . . . 42
2.7 Scanning Electron Microscopy (SEM) . . . 44
2.8 Transmission Electron Microscopy (TEM) . . . 45
2.9 Atomic Force Microscopy (AFM) . . . 46
2.10 Raman spectroscopy . . . 47
2.11 Surface Magneto-Optical Kerr Effect (MOKE) . . . 48
2.12 Transport measurements . . . 49

3 Materials used during this thesis **51**
3.1 Introduction . . . 51
3.2 Silicon . . . 51
3.2.1 General overview . . . 51
3.2.2 Elimination of silicon native oxide on Si(100) by thermal procedures . . . 53
3.2.3 Elimination of silicon native oxide on Si(100) by SrO-deoxidation 55
3.3 Magnetite (Fe_3O_4) . . . 55
3.3.1 General overview . . . 55
3.3.2 Identification of iron oxide phases . . . 58
3.4 Strontium titanate ($SrTiO_3$) . . . 60
3.4.1 General overview . . . 60
3.4.2 Oxygen defects in $SrTiO_3$ . . . 61
3.5 Iron Silicide (Fe_3Si) . . . 63
3.5.1 General overview . . . 63
3.5.2 Identification of iron silicides phases . . . 63

4 Fe_3O_4 based heterostructures **67**
4.1 Introduction . . . 67
4.2 $Fe_3O_4/SiO_2/Si$ heterostructures . . . 69
4.2.1 Introduction . . . 69
4.2.2 *In situ* study of the first stages of evaporation . . . 70
4.2.3 Preparation of $Fe_3O_4/SiO_2/Si$ heterostructures by PLD . . . 77
4.2.4 Characterization of the magnetite films . . . 83
4.2.5 Conclusions . . . 91

4.3 $Fe_3O_4/SrTiO_3/Si$ heterostructures 92
4.3.1 Introduction 92
4.3.2 Preparation of epitaxial $SrTiO_3$ films on Si(001) 94
4.3.3 Preparation of the $Fe_3O_4/SrTiO_3/Si$ heterostructures 102
4.3.4 Characterization of the Fe_3O_4/ $SrTiO_3/Si$ heterostructures . 104
4.3.5 Conclusions 121
4.4 General conclusions from the study of Fe_3O_4 based heterostructures 123

5 Fe_3Si epitaxial thin films **125**
5.1 Introduction 125
5.2 Evaporation of epitaxial Fe_3Si films on $SrTiO_3$ by PLD 126
5.2.1 Influence of the substrate temperature 127
5.2.2 Influence of the layer thickness 135
5.3 Conclusions 140

6 General conclusions **143**

Bibliography **147**

List of Figures

1.1 Operation of a spin valve 2
1.2 Scheme of a spin-FET 3
1.3 Charge transport between a ferromagnetic metal and a non-magnetic semiconductor 5
1.4 Tunneling in metal-insulator-metal structures 7
1.5 Different strategies for contact engineering in order to improve injection through the Schottky barrier 12
1.6 Formation of local magnetostatic fields produce by the finite roughness of a tunnel contact interface 13
1.7 Band structure at the Fermi level for paramagnets, ferromagnets and half-metals 15
1.8 Detection geometries used to measure spin accumulation in semiconductors by electrical means 17

2.1 Experimental set-up used for the deposition of samples by PLD and a schematic inside-view of the chamber 22
2.2 XPS experimental set-up 25
2.3 LEED experimental set-up 28
2.4 Configuration for RHEED acquisition and a typical diffraction pattern for a single oriented film 29
2.5 XAS experimental set-up installed in the Spanish CRG BM25-SpLine beamline 31
2.6 Multipurpose x-ray diffractometer installed at the first focal point of the Branch B of the Spanish CRG BM25-SpLine beamline 32
2.7 Surface X-Ray diffraction and HAXPES station installed in the Branch B of the Spanish CRG BM25-SpLine beamline 33
2.8 Schematic view of specular X-ray reflectivity measurement configuration and XRR profiles recorded on $SrTiO_3$/Si films 34
2.9 Illustration of the Laue condition 36
2.10 2D-representation of the Edwald construction 38

2.11 Powder diffraction configuration geometry and powder pattern recorded on a Fe_3O_4 powder reference 41
2.12 Photoelectron absorption, fluorescence emission and Auger electron emission processes derived from x-ray matter interaction 43
2.13 Processes derived from electron-matter interactions 45
2.14 Light scattering processes involved in Raman spectroscopy 47
2.15 Different configurations for S-MOKE measurements depending on the orientation of the applied magnetic field respect to the dispersion plane. 48
2.16 Home-designed experimental set-up used for S-MOKE characterization installed in the Spanish CRG BM25-SpLine beamline support laboratory 49
2.17 Experimental set-up used for electrical transport measurements situated at the Spanish CRG BM25-SpLine beamline support laboratory in the ESRF 49

3.1 Silicon crystallographic structure 52
3.2 Evolution of the C1s and Si 2p core level spectra with annealing temperature on Si(100) substrates 53
3.3 Evolution of LEED patterns recorded on a Si(100) surface after UHV annealing 54
3.4 Crystalographic structure of magnetite and band diagram 56
3.5 Modification of the Verwey transition by changes on the Fe^{+3}/Fe^{+2} ratio (a) and by variation of the film thickness (b) 57
3.6 Fe1s and Fe2p core level HAXPES spectra on iron oxide references . 59
3.7 XAS spectra measured on the Fe K-edge for different iron oxide standards and calibration line 60
3.8 Strontium titanate crystallographic structure 61
3.9 Characterization of oxygen defects on $SrTiO_3$ substrates by XPS . . 62
3.10 Crystallographic structure of Fe_3Si 63
3.11 Fe-Si phase diagram 64
3.12 XAS spectra of the Fe K-edge for $FeSi_3$, ϵ-FeSi and $\beta FeSi_2$ single crystal references 65

4.1 Fit of the XPS intensity during evaporation 72
4.2 Characterization of silicon native oxide for the evaluation of R_0 value 73
4.3 Evolution of the Fe2p and Si2s core level XPS spectra during Fe_3O_4 evaporation on SiO_2-Si substrates 75
4.4 Evolution of the integrated HAXPES for the Si1s and Fe1s spectra for $Fe_3O_4/SiO_2/Si$ heterostructures as a function of number of PLD cycles for Fe_3O_4 evaporation 78
4.5 HAXPES (a) and XRR (b) characterization of the prepared $Fe_3O_4/Si_2/Si$ heterostructures for different Fe_3O_4 thickness 80

4.6 Evolution of the SiO_2 thickness as a function of magnetite thickness on $Fe_3/SiO_2/Si$ heterostructures 81
4.7 Cross section TEM measurements performed on a $Fe_3O_4(37.5nm)/SiO_2/Si$ sample 82
4.8 Characterization of the iron oxide phase by HAXPES and XPS of $Fe_3O_4/SiO_2/Si$ heterostructures with differente Fe_3O_4 thickness. . . 84
4.9 XRD characterization of $Fe_3O_4/SiO_2/Si$ heterostructures with different Fe_3O_4 thickness 85
4.10 Raman spectra recorded on $Fe_3O_4/SiO_2/Si$ heterostructures with increasing magnetite thickness 87
4.11 SEM and AFM images for the magnetite films with different thickness. 88
4.12 Characterization of the in plane electronic transport properties on magnetite films integrated on $Fe_3O_4/SiO_2/Si$ systems with different Fe_3O_3 thickness 90
4.13 Hysteresis loops recorded in transversal configuration by MOKE for different magnetite thickness on $Fe_3O_4/SiO_2/Si$ heterostructures . . 91
4.14 XRR measurements at low and high angle on $SrTiO_3$ films evaporated on Si by MBE 95
4.15 Evolution of the $SrTiO_3$ lattice parameter values with film thickness on $SrTiO_3/Si$ samples 96
4.16 Cross section TEM characterization of the $SrTiO_3/Si$ films 98
4.17 XRR measurements on $SrTiO_3$ films before and after annealing at 650°C under oxygen atmosphere 99
4.18 Ti2p core level XPS spectra measured on the as inserted films and after subsequently annealed them up to 650°C under O_2 atmosphere 100
4.19 Evolution of the Si2p core level XPS spectra for $SrTiO_3$ films upon annealing 101
4.20 XAS spectra recorded on the Fe K-edge for the Fe_3O_4 heterostructures for different $SrTiO_3$ thickness and evaporation temperatures 103
4.21 RSM images before and after the evaporation of magnetite for $SrTiO_3$ thickness of 1.8, 4.8 and 10.9 nm 105
4.22 Rocking curves measured on (311) Fe_3O_4 reflection and (111) $SrTiO_3$ reflection on $Fe_3O_4/SrTiO_3/Si$ heterostructures 106
4.23 RHEED patterns (left) and XRR measurements (right) on $Fe_3O_4/SrTiO_3/Si$ systems with different $SrTiO_3$ thickness before and after evaporation of magnetite 108
4.24 SEM images of the Fe_3O_4 surface for films evaporated using different $SrTiO_3$ thickness acquired at 70000X 108
4.25 HAXPES measurements on the Si1s core level spectra on $Fe_3O_4/SrTiO_3/Si$ heterostructures with different $SrTiO_3$ thickness 110
4.26 HRTEM measurements on sample with 5 nm $SrTiO_3$ thickness and prepared at 350°C 111

4.27 MOKE hysteresis loops recorded on $Fe_3O_4/SrTiO_3/Si$ heterostructures prepared under identical conditions with a variable $SrTiO_3$ thickness . . . 112
4.28 MOKE hysteresis loops recorded on $Fe_3O_4/SrTiO_3$(1.8 nm)/Si applying the magnetic field with a different angle respect to the crystallographic axis . . . 113
4.29 Rocking curves measured on Fe_3O_4 311 reflection and $SrTiO_3$ 111 reflection on $Fe_3O_4/SrTiO_3$(10.9 nm)/Si heterostructures prepared at different temperature . . . 114
4.30 Reciprocal space maps of H_{Si} versus K_{Si} on the L_{Si} position corresponding to $L_{Fe_3O_4}$=4 on the reference system of the magnetite film 115
4.31 XRR measurement at low angle and SEM images for $Fe_3O_4/SrTiO_3$(10.9 nm)/Si heterostructures prepared at 350 and 550°C. . . . 116
4.32 HAXPES measurements at 10 keV on the Si 1s core level spectra on $Fe_3O_4/SrTiO_3$(10.9 nm)/Si heterostructures prepared at 350 and 550°C 117
4.33 TEM image of the $Fe_3O_4/SrTiO_3$(10.9 nm)/Si heterostructure prepared at 350°C . . . 118
4.34 TEM image of the $Fe_3O_4/SrTiO_3$(10.9 nm)/Si heterostructure prepared at 550°C. . . . 119
4.35 HRTEM close-up images of the $Fe_3O_4/SrTiO_3$ interface . . . 120
4.36 Comparative graphic of the hysteresis loops recorded by MOKE at RT and ambient pressure on $Fe_3O_4/SrTiO_3$(10.9 nm)/Si heterostructures prepared at 350 and 550°C . . . 121

5.1 XRR measurements on the $Fe_3Si/SrTiO_3$ films evaporated at different substrate temperatures . . . 128
5.2 H versus L reciprocal space maps recorded at K=0 for $Fe_3Si/SrTiO_3$ samples evaporated at 200, 300, 400, 600 and 800°C respectively . . 130
5.3 Rocking curves on the Fe_3Si 202 reflection . . . 131
5.4 XANES measurements on the Fe K-edge for Fe_3Si films evaporated on $SrTiO_3$ substrates at different temperature . . . 133
5.5 Hysteresis loops measured by MOKE at RT in Fe_3Si films evaporated on $SrTiO_3$ substrates deposited at different temperature . . . 134
5.6 XRR measurements for $Fe_3Si/SrTiO_3$ films with different layer thickness 136
5.7 Reciprocal space maps on $Fe_3Si/SrTiO_3$ films with different thickness 137
5.8 Rocking curves on the Fe_3Si(202) reflection on $Fe_3Si/SrTiO_3$ films with different thickness . . . 138
5.9 Fe K-edge XANES spectra for samples evaporated at 400° with different thickness . . . 139

List of Tables

1.1 Bulk Curie temperature for some half metal materials 15
1.2 Electrically induced spin accumulation in semiconductors 18

3.1 Structural parameters and properties of the different iron oxides . . 58
3.2 XPS peaks and satellite positions for FeO, Fe_3O_4 and γ-Fe_2O_3 bulk references 59
3.3 Structural parameters of different iron silicides 64

4.1 Fitting parameters and results corresponding to the fitting curves showed in Figure 4.1 72
4.2 R_0 values calculated from the XPS measurements on silicon native oxide and theoretical calculations for porous and compact silicon . . 74
4.3 Evolution of the system during the deposition of Fe_yO_x films on SiO_2-Si(100) substrates 76
4.4 Fitting parameters for the evolution of the HAXPES intensity measured on $Fe_3O_4/SiO_2/Si$ heterostructures 78
4.5 Relation of magnetite thickness for the $Fe_3O_4/SiO_2/Si$ samples prepared by PLD 79
4.6 Magnetite crystalline grain sizes 86
4.7 Roughness values obtained from the analysis of the AFM images . . 89
4.8 Crystal domain size for $SrTiO_3$ films evaporated on Si 96
4.9 Annealed conditions used to study the stability of $SrTiO_3$/Si films . 97
4.10 Composition of the magnetite films evaporated on $SrTiO_3$/Si systems under different conditions 103
4.11 Lattice parameter calculated for the Fe_3O_4 films evaporated on top of different $SrTiO_3$ thick films 106

5.1 Composition in percentage of the samples evaporated on $SrTiO_3$ obtained from XANES measurements 134
5.2 Composition in percentage of the samples evaporated on $SrTiO_3$ obtained from XANES measurements 139

Resumen

Se ha demostrado que el uso de contactos túnel magnéticos es uno de los métodos más eficientes para la inyección y detección de corrientes polarizadas en espín en semiconductores no magnéticos. En este tipo de sistemas, los portadores de carga polarizados en espín del electrodo ferromagnético se transfieren al semiconductor por efecto túnel a través de una barrera aislante. La inyección de espín por transporte difusivo de forma directa a través de la intercara ferromagnético/aislante es muy poco eficiente en términos de polarización debido a la gran diferencia de impedancia eléctrica entre los dos materiales. La introducción de una barrera túnel permite mejorar la eficiencia del sistema y aumentar la acumulación de espín en el semiconductor. Sin embargo, para poder obtener una inyección eficiente el sistema debe además cumplir ciertos requisitos. Una de las condiciones principales es que las heteroestructuras presenten intercaras abruptas tanto morfológicamente como desde el punto de vista químico. Esto se debe a que una rugosidad alta puede generar campos magnetoestáticos en la intercara que induzcan la precesión de los espines y reduzcan la polarización en el semiconductor. Además, los defectos presentes en la intercara pueden funcionar como centros de dispersión y reducir a su vez la polarización en espín de los portadores.

Es importante tener en cuenta además la formación de la barrera de Schoktty en la intercara del semiconductor con el aislante, la cual produce una deformación de las bandas de conducción y valencia generando una barrera adicional de potencial. Es imprescindible controlar este fenómeno ya que el transporte a través de la barrera de Schoktty se produce mayoritariamente por emisión termo-iónica en lugar de por efecto túnel. Esto genera que los electrones que llegan al semiconductor procedan de los niveles de energía superiores, donde la polarización de espín del ferromagnético es mucho menos significativa. Además, la alta resistencia del contacto impide la operación del sistema a alta frecuencia. Una manera efectiva de reducir la altura de la barrera de Schoktty es, entre otras, el uso de semiconductores dopados.

El trabajo desarrollado durante esta tesis se ha centrado en el desarrollo de estrategias para la fabricación de contactos túnel magnéticos en semiconductores basados en materiales medio-metálicos (half-metals). Los materiales medio-metálicos han despertado gran interés, especialmente en espintrónica, ya que se predice que presentan una polarización 100 % en espín en el nivel de Fermi. La implementación

de estos materiales en el diseño de dispositivos de inyección de espín puede añadir nuevas prestaciones al sistema y aumentar significativamente su eficiencia. Sin embargo, su uso con este fin ha sido raramente explorado. En algunos casos se ha estudiado el crecimiento de materiales medio-metálicos en silicio pero en ningún caso incluyendo una barrera túnel. Además, estos trabajos no prestan especial atención a las propiedades de la intercara con el semiconductor, lo cual es fundamental para la aplicación de estos materiales al diseño de dispositivos de inyección de espín.

En una primera parte del trabajo se estudiaron diferentes estrategias para la fabricación de contactos túnel magnéticos en silicio utilizando electrodos de magnetita. Numerosos trabajos han apuntado al carácter medio-metálico de este material, que además presenta una temperatura de Curie muy elevada (858 K). Uno de los grandes desafíos para el crecimiento de este tipo de sistemas multi-capa es conseguir la estabilización del silicio durante la evaporación del óxido. Durante esta tesis se utilizaron se utilizaron dos métodos diferentes. En un primer lugar se evaporó Fe_3O_4 por deposición de láser pulsado (PLD) en Si(100) manteniendo el óxido nativo amorfo como barrera túnel. El óxido nativo ha sido ampliamente estudiado y se sabe que presenta una alta estabilidad, un espesor entre 1-2 nm y una intercara abrupta con el Si. Además presenta altas prestaciones como aislante, siendo ideal para su uso como barrera túnel. En el segundo estudio, el óxido nativo fue eliminado para evaporar láminas epitaxiales ultra-delgadas de $SrTiO_3$ y posteriormente depositar las láminas de magnetita. Este método de preparación es mucho más complejo pero permite el control del espesor de la barrera túnel, pudiendo modificar este parámetro a voluntad en el diseño de los sistemas.

Las muestras Fe_3O_4/ aislante/ Si obtenidas por ambos métodos fueron caracterizadas para evaluar su calidad, tomando como referencia los requisitos especificados para conseguir un sistema eficiente de inyección de espín. Con este propósito se utilizaron un gran número de técnicas como LEED, XPS, RAMAN o SEM para caracterizar las propiedades estructurales, morfológicas y químicas de las hetero-estructuras preparadas. En ambos casos se demostró la ausencia de fases no estequiométricas en las láminas. En el caso en el que se usó el óxido nativo del silicio como barrera túnel, el carácter amorfo de este favoreció la formación de láminas poli-cristalinas. Sin embargo, para barreras túnel de $SrTiO_3$ se observó el crecimiento epitaxial de la magnetita. Las láminas depositadas presentaban parámetros estructurales similares a aquellos establecidos para el material en su forma masiva. La respuesta magnética de las muestras se caracterizó por MOKE, demostrando una respuesta ferrimagnética de las láminas de Fe_3O_4 a temperatura ambiente. Las láminas poli-cristalinas mostraron campos coercitivos más pequeños y una respuesta más rápida al invertir el signo del campo magnético.

Una parte importante del trabajo fue el uso de técnicas de radiación sincrotrón, entre ellas XRD, XAS y HAXPES, especialmente enfocadas a la caracterización exhaustiva de las intercaras enterradas. Este punto es especialmente importante debido a la gran importancia que estas tienen en las propiedades de transporte del

sistema. Junto con TEM, estas técnicas permitieron determinar en los dos sistemas estudiados una relación directa entre la evolución de la intercara de la barrera túnel aislante con el silicio y la obtención de láminas estequiométricas de magnetita. En el caso del $Fe_3O_4/SiO_2/Si$ el espesor de óxido de silicio aumentió progresivamente en las primeras etapas de la evaporación hasta estabilizarse con un espesor final de aproximadamente 5 nm. Por debajo de este valor, el crecimiento del oxido impedía el crecimiento de magnetita, resultando en la formación de fases reducidas. En el caso de $Fe_3O_4/SrTiO_3/Si$, se observó la formación de una pequeña capa de un silicato de composición indeterminada en la intercara $SrTiO_3/Si$. Se pudo observar como el espesor de esta capa aumentaba progresivamente durante la evaporación de la magnetita, pasando de unas décimas de nm a un espesor final de casi 2 nm. También se demostró que este crecimiento era más acentuado al aumentar la temperatura de evaporación. La presencia de esta capa se relaciona con la formación de siliciuros de hierro durante la evaporación si el espesor de $SrTiO_3$ es demasiado bajo o la temperatura de deposición demasiado elevada.

En la segunda parte del trabajo se estudió el crecimiento de láminas delgadas de Fe_3Si en $SrTiO_3$. Numerosos estudios apuntan a las propiedades medio-metálicas de este material que además presenta una temperatura de Curie de 840 K. Los trabajos que reportan el crecimiento de láminas epitaxiales de Fe_3Si son reducidos y en su mayoría se centran en el GaAs debido a la similitud entre sus estructuras. En ningún caso se ha reportado el crecimiento epitaxial de este material en $SrTiO_3$. El crecimiento exitoso de láminas delgadas de Fe_3Si en $SrTiO_3$ podría ser un primer paso para la integración de este material en silicio con un método equivalente al presentado para la magnetita. En esta tesis se analizaron diferentes condiciones para la obtención de láminas epitaxiales de Fe_3Si en $SrTiO_3(001)$ por deposición de láser pulsado (PLD). Para estudiar las propiedades cristalográficas de las láminas en función de las condiciones de evaporación se caracterizaron los sistemas por XRD utilizando radiación sincrotrón. También se utilizó XRR para evaluar la calidad de las intercaras y XAS para descartar la posible presencia de otras fases independientemente de si tenían un carácter cristalino o amorfo. Además se caracterizaron las propiedades magnéticas del Fe_3Si por MOKE. Los resultados demostraron el crecimiento de láminas epitaxiales monofase de Fe_3Si en $SrTiO_3(001)$ por PLD a temperaturas de 200 y 300^oC. Aunque se observó que las láminas no presentaban orden a largo alcance, la caracterización magnética demostró un comportamiento ferromagnético a temperatura ambiente con bajos campos coercitivos y una respuesta magnética rápida ($M_R/M_S \approx 1$). El crecimiento a temperaturas superiores resultó en la aparición de Fe en una cantidad no despreciable, lo cual tuvo una respuesta muy negativa en las propiedades magnéticas de las láminas, aumentando la coercitividad y resultando en respuestas más lentas bajo la inversión del campo.

Summary

The use of magnetic tunnel contacts have been proved as one of the most efficient methods for the efficient injection and detection of spin polarized currents on non-magnetic semiconductors. In this kind of systems, the spin polarized carriers of the ferromagnetic electrode are transferred by tunneling through an insulator barrier into the semiconductor. The diffusive transport directly through the ferromagnet/semiconductor interface is limited by the large impedance mismatch between the two materials. The introduction of a tunnel barrier allows to improve the efficiency of the system and increase spin accumulation in the semiconductor. However, in order to achieve high spin rates the system needs to fulfill certain requirements. One of the fundamental conditions is the formation of flat and abrupt interfaces. High interface roughness can induce the presence of magnetostatic fields that might induce spin precession and reduce spin polarization. Moreover, the presence of defects on the interface can act as scattering centers and reduce even more spin accumulation in the semiconductor.

Besides, the formation of the Schoktty barrier in the insulator/ semiconductor interface needs to be taken into account, which induce a bending of the conduction and valence band creating an additional potential barrier in the contact. One of the consequence of this is that transport through the Schoktty barrier is mainly produced by thermoionic transport instead of tunneling, so that arriving electrons come from energy levels well above the Fermi level, where the spin polarization in the ferromagnet is much less significant. Moreover, the high resistance of the contact impedes the operation of the system at high frequencies. Therefore, it is essential to control this effect. An effective method to reduce the height of the Schoktty barrier is the use of doped semiconductors.

The work developed during this thesis has been focused in the study of strategies for the fabrication of magnetic tunnel contacts on silicon based on the use of half metal materials. This kind of materials have attracted great interest, especially for spintronics, because of the prediction of a 100 % spin polarization at the Fermi level. The implementation of this sort of materials on the design of spin injection devices could add new capabilities to the system and increase significantly its efficiency. Nevertheless, the use of half metals for this purpose has been rarely explored. Some works studied the integration of half metallic thin films on silicon but in none of these

works a tunnel barrier was included. Besides, the studies reported until now do not pay attention to interface properties, which have a key role for the achievement of an efficient spin injection.

In the first part of the work, the fabrication of magnetic tunnel contacts on silicon based on the use of magnetite electrodes was pursued. Numerous works have pointed to the half metallic properties of this material, which also presents a high Curie temperature up to 858 K. One of the biggest challenges for the growth of this multi-layer systems is to achieve the passivation of the silicon surface during the evaporation of the oxide. During this thesis two different strategies were explored. In a first attempt, Fe_3O_4 was evaporated by pulse laser deposition (PLD) on Si(100) substrates keeping the silicon native oxide as tunnel barrier. Silicon native oxide has been widely study and it is known to present high thermal stability, a thickness between 1-2 nm and a flat interface with Si. Besides, it presents excellent insulator properties, being an optimal candidate for its use as a tunnel barrier. In a second attempt, silicon native oxide was eliminated and epitaxial ultra-thin $SrTiO_3$ films were deposited. Subsequently, Fe_3O_4 was evaporated by PLD. This second method of preparation is significantly more complex but allows to control the thickness of the tunnel barrier.

Fe_3O_4/ insulator/Si heterostructures prepared by both methods were characterized in order to evaluate its properties in terms of the specific requirements for an efficient spin injection. With this objective, a large number of techniques as LEED, XPS, RAMAN or SEM were used to characterize the morphological, structural and chemical properties of the systems. In both cases, the obtention of single phase stoichiometric magnetite films was proved. In the case of SiO_2 tunnel barriers, the amorphous character of the insulator favored the formation of polycrystalline magnetite films. On the contrary, when using $SrTiO_3$ tunnel barriers magnetite grew epitaxially. Deposited films presented strucutural parameters similars to that stablished for the bulk material. Magnetic properties were characterized by MOKE, proving a ferrimagnetic response of the magnetite films at room temperature in both systems. Polycrystalline films presented lower coercitive films and faster reversal mechanisms.

An important part of the work performed was the use of synchrotron techniques as XRD, XAS or HAXPES, which were especially focused to the exhaustive characterization of the buried interfaces. This is a fundamental aspect of the work as the transport properties of the system are directly related with interface properties. Together with TEM, the use of synchrotron radiation allowed to determine a direct relation between the evolution of the insulator/Si interface and the stabilization of stoichiometric Fe_3O_4 films. In the case of $Fe_3O_4/SiO_2/Si$ systems, the SiO_2 thickness increased progressively in the first stages of evaporation until it stabilized with a final thickness of around 5 nm. Below this value, magnetite films presented reduced phases and iron clusters were observed. In the case of $Fe_3O_4/SrTiO_3/Si$ heterestructures the formation of an uncertain silicate layer on the $SrTiO_3$/Si interface was observed. The thickness of this interlayer increased progressively during magnetite

evaporation going from a tenths of nms to a final thickness of almos 2 nm. It was proved that this increased was more noticeable when evaporation temperature was increased. The presence of this layer was related with the formation of iron silicides during magnetite evaporation when the $SrTiO_3$ barrier was too thin or the deposition temperature too high.

In the second part of the work, the growth of Fe_3Si thin films on $SrTiO_3$. Several works point to the half metallicity of Fe_3Si and it also presents a high Curie temperature of 840 K. The works reporting on the growth of epitaxial Fe_3Si films are reduced and are mostly centered on GaAs given the similarity between their structures. However, in none of these works the epitaxial growth of Fe_3Si has ben reported on $SrTiO_3$. The sucessful growth of Fe_3Si films on $SrTiO_3$ could be a first step for the integration of this material on Si using a similar method to that reported for magnetite. During this thesis different conditions were studied for the epitaxial growth of Fe_3Si on $SrTiO_3(001)$ by PLD. The films were characterized by XRD, XRR and XAS in order to determine the crystallographic propertie, the single phase character of the films and the interface properteies as a function of the deposition conditions. The films were also characterized by MOKE to determine the magnetic properties. The results proved the epitaxial growth of single phase Fe_3Si films on $SrTiO_3(001)$ by PLD at temperatures of 200 and 300 ^oC. Although it was observed that the films did not present long range structural order, the films presented a ferromagnetic response at room temperature with low coercive fields of only a few mT and an almost inmediat reversal mechanism ($M_R/M_S \approx 1$). The growth at higher temperatures resulted in the formation of Fe phases in a non negligible proportion, which had a detrimental effect in the magnetic behavior of the films increasing the coercitivity and reducing the velocity of the reversal mechanisms.

Chapter 1

Introduction

1.1 Semiconductor spintronics

Spintronic is one of the most active fields in nowadays scientific context. This term involves the study of active control and manipulation of spin information in solid-state systems [1–3]. In the decade of 1930s, Mott already provided the basis to understand spin polarized transport [4]. He observed at low temperature how antiparallel and parallel oriented magnetic moments did not mix during the scattering process. Consequently, the conductivity can be expressed as the sum of two independent unequal parts for each spin projection. This two current model was later extended by Campbell and Fert in 1968 [5] and it is still the main mechanism used to explain magnetoresistance phenomena. First experimental approach to spintronic was the discovery of giant magnetoresistance (GMR) in 1988 at Orsay and Julich simultaneously [6,7]. The phenomenon was observed in Fe-Cr multilayer systems when an enhanced electrical conductivity was measured under the effect of a magnetic field, evidencing for the first time the influence of spin momentum in electrical conductivity. GMR was the base for the development of spin valves being this the main device used for the fabrication of read heads in current magnetic hard disks. The simplest structure for a spin valve device is constituted of an antiferromagnetic layer, a bottom ferromagnetic layer, a non-magnetic metal spacer and a top ferromagnetic layer (Figure 1.1). The magnetization of the bottom layer (pinned layer) is fixed by coupling with the antiferromagnetic layer meanwhile the top layer (free layer) can switch its magnetization to align with the particular magnetization of the magnetic medium to read, acting as a sensor. Electrons can be transferred through the spacer layer due to its metallic character. The resistance of the junction is modified by the change in the relative magnetization of the top electrode respect to the fixed bottom layer. The difference in resistance between parallel and anti parallel states gives rise to the GMR effect. Such behavior is a consequence of the spin dependent elastic scattering of arriving electrons on the ferromagnetic electrode and especially on the

non-magnetic/magnetic interface region [8, 9]. As shown schematically in figure 1.1, strong elastic scattering effects occur for antiparallel alignment of the magnetization of the FM layers, i.e., high resistance state, while low elastic scattering effects occur for parallel alignment, i.e., low resistance state. Schad *et al.* reported GMR ratios up to 220 % in Fe/Cr superlattices with ultra thin Fe layers [10].

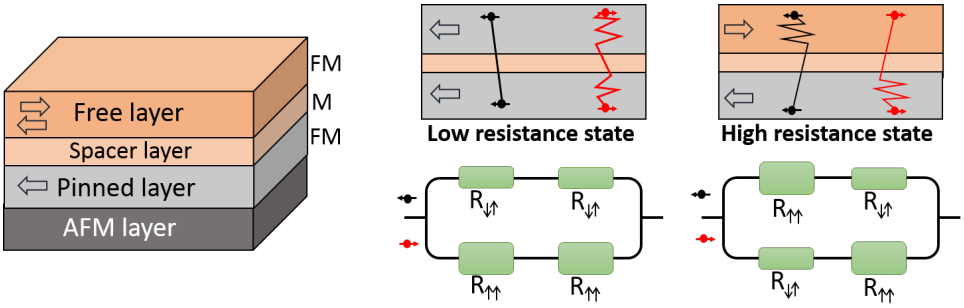

Figure 1.1: Schematic view of a spin valve GMR-based read head and its operation. The spin dependent scattering of electrons produce a low and a high resistance states depending on the relative magnetization of the electrodes.

The discovery of tunneling magnetoresistance (TMR) on magnetic tunnel junctions (MTJ) in 1975 [11] opened new possibilities for the development of much more sensitive devices. MTJs are constitued of two ferromagnetic electrodes separated by a highly resistive layer. The electrical current flows vertically through these layers while the electrons pass from the first electrode through the insulator by quantum-mechanical tunnel effect and are injected in the second ferromagnet. The electric resistance to the current significantly changes depending on the relative angular difference between the magnetization of the two magnetic layers. If the magnetization of the layers is parallel a low resistance state occurs meanwhile if they present antiparallel magnetization a high resistance state is produced. There exist two main differences between GMR and TMR sensors i) in GMR the spacer layer is a non-magnetic metal (low R) contrary to TMR sensors where it is an insulator (high R), ii) In GMR the current flows parallel to the electrodes while in TMR the transport is perpendicular to the electrodes. Moreover, TMR sensors provide an output several times larger, a larger magnetoresistance ratio and present higher stability with temperature than GMR sensors [12]. Nevertheless, due to the limitations imposed by fabrication techniques experimental results were well below the predictions and the application of the these sensors had to wait almost 30 years. In 1995, Moodera *et al.* developed a reproducible method to produce smooth and pinhole-free Al_2O_3 tunnel barriers reporting MR values of 24 % at 4.2 K in $CoFe/Al_2O_3/Co$ junctions, in agreement with the 27 % predicted by Julliere's model [13]. Since then great advances have been made on the fabrication procedures of MTJs and TMR ratios as high as 600 % have been achieved at RT [14]. Nowadays, MTJs heterostructures

used are mainly based on 3d-metal ferromagnets and Al_2O_3 tunnel barriers that can be routinely fabricated with reproducible characteristics, which is an essential requirement for industrial application. These heterostrucutures play a key role in current technology and are the base of information-storage devices [15, 16].

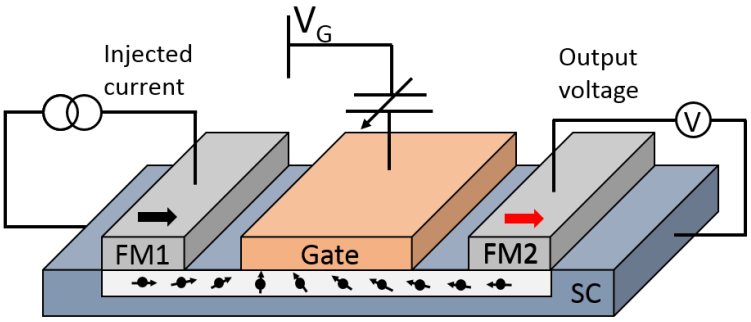

Figure 1.2: Structure of the spin-FET proposed by Datt and Dash in 1990. Spin polarized electrons are injected from the ferromagnetic source into the semiconductor. The spin-orbit interaction of the electrons in the channel is controlled by the applied electric field and the detection is produced in the drain terminal. The output voltage will get a high or low resistance state depending on the magnetization of the drain terminal respect to arrival electrons.

A step forward in spintronic research is its combination with semiconductor technology, which will open new possibilities for the buildout of hybrid devices able to perform logic, communication and storage operations all in one. Semiconductor spintronic promises to significantly reduce consumption energy and processing times in comparison with nowadays devices [17–19]. One of the first proposals for a spin-based logic device was the spin field effect transistor (Spin-FET) proposed by Datt and Dash in 1990 [20]. A schematic diagram of the device is shown in Figure 1.2. Analogously to conventional field effect transistors, the device designed by Datt and Dash counts with three terminals: a source, a drain and a gate, with the difference that in this case the source and the drain terminals are constituted of ferromagnetic materials. What Datt and Dash suggested was a transistor where the output voltage is dependent on the drain magnetization respect to the spin orientation of the arriving electrons, which will be determined by the magnetization of the source, the semiconductor material, the channel length and the gate voltage.

However, the beginning of spintronic research on non-magnetic semiconductors can be dated much earlier. On the late 60s the detection of nuclear spin polarization on silicon was reported by Lampel and coworkers [21].This first work already pointed two fundamental aspects for spin transport on semiconductors: the spin orbit interaction and the hyperfine interaction between electrons and nuclear spins. Since then numerous studies have been carried out on the creation, detection and

manipulation of spin on different semiconductor materials [22]. On this regard, silicon have shown especially attractive properties as significant long spin lifetimes and diffusion lengths. In 2007, Appelbaum *et al.* reported remarkably large distances of 350 μm for coherent spin precession on undoped silicon at room temperature [23]. Two years later, Dash *et al.* demonstrated electrical spin creation, and manipulation on highly doped Si at room temperature. They reported diffusion lengths greater than 310 nm and spin lifetimes higher than 270 ps for p-type silicon [24]. Although coherent diffusion of electron spins in semiconductors have been experimentally observed [25–27] the production of a functional spin-FET device is still to be achieved. This is mainly related with some fundamental problems as the impedance mismatch problem, spin relaxation and the spread of spin precession angles which critically reduced the efficiency of the system [28].

1.2 Spin injection into a semiconductor

1.2.1 The impedance mismatch problem

One of the fundamental requirements for the development of semiconductor based spintronic devices is the efficient creation of spin polarized currents on non-magnetic semiconductors. In order to do so, one of the options is to use a ferromagnetic material (FM) as spin source to polarize the electric current and then transfer it into the semiconductor (SC) by means of diffusive transport by placing both materials in contact. The spin polarization α at any point can be defined as:

$$\alpha(x) = \frac{j_{\uparrow}(x) - j_{\downarrow}(x)}{j_{\uparrow}(x) + j_{\downarrow}(x)} \tag{1.1}$$

Where $j_{\uparrow}$ and $j_{\downarrow}$ denotes the current of electrons with up and down spin polarization, respectively. Under the assumption that spin-scattering occurs on a much slower timescale than other electron scattering effects as it is supported by some experimental works [29], the two electrochemical potentials $\mu_{\downarrow}$ and $\mu_{\uparrow}$ are not necessary equal and can be considered independently. The relation between the chemical potential and the current flow is given by Ohm's law

$$J_{\uparrow,\downarrow} = \frac{\sigma_{\uparrow,\downarrow}}{q} \frac{d\mu_{\uparrow,\downarrow}}{dx} \tag{1.2}$$

where σ is the conductivity of the material for each spin orientation. As long as the conductivity of electrons in the non-magnetic semiconductor is equal for both spin orientations, in order to keep the spin imbalance, i.e in order to have more flux for one spin orientation, the chemical potential gradient must be different. Therefore, in order to produce spin injection it is mandatory that in the FM/SC interface $\Delta\mu = \mu_{\uparrow} - \mu_{\downarrow} \neq 0$. The evolution of the potential gradient $(\mu_{\uparrow} - \mu_{\downarrow})$ will obey diffusion equation

$$\frac{\mu_\uparrow - \mu_\downarrow}{\tau_{sf}} = \frac{D\partial^2(\mu_\uparrow - \mu_\downarrow)}{\partial x^2} \tag{1.3}$$

where D is a weighted average constant of the diffusion constants for both spin directions [30] and τ_{sf} is the spin-flip time constant. Figure 1.3 shows the spin dependent band diagram of the chemical potential near to the FM/SC interface showing the chemical potential gap at the interface and the restauration of the equilibrium ($\mu_\uparrow = \mu_\downarrow$) far from the interface. The length scale for spin flip inside each material can be defined as $\lambda = \sqrt{D\tau_{sf}}$. Ferromagnetic materials generally presents high conductivity but short spin length scales while non-magnetic semiconductors present low conductiviy but long spin lengthscale.

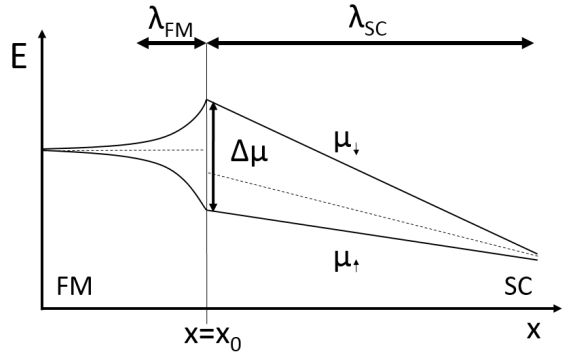

Figure 1.3: Spin dependent charge transport through an Ohmnic contact between a ferromagnetic metal and a non-magnetic semiconductor. Diagram adapted from reference [31]

The splitting $\Delta\mu_{FM}$ on the ferromagnetic material at the interface can be written as:

$$\Delta\mu_{FM} j = q\lambda_{FM}\left(\frac{J_\uparrow}{\sigma_\uparrow} - \frac{J_\downarrow}{\sigma_\downarrow}\right) = 2qJ\frac{\lambda_{FM}}{\sigma_{FM}}\frac{(\alpha-\beta)}{(1-\beta^2)} \tag{1.4}$$

where β is the spin polarization in the ferromagnetic source far from the interface:

$$\beta = \frac{\sigma_\uparrow - \sigma_\downarrow}{\sigma_\uparrow + \sigma_\downarrow} \tag{1.5}$$

On the other hand, the splitting $\Delta\mu_{SC}$ on the semiconductor can be expressed as:

$$\Delta\mu_{SC} = q\lambda_{SC}\left(\frac{J_\downarrow - J_\uparrow}{\sigma_{SC}}\right) = -2qJ\alpha\frac{\lambda_{SC}}{\sigma_{SC}} \tag{1.6}$$

Considering an ideal interface between the ferromagnetic electrode and the semiconductor where spin relaxation is not produced, the splitting of the chemical potential $\Delta\mu$ must preserve the continuity at the interface so that $\Delta\mu_{FM} = \Delta\mu_{SC}$ and spin polarization α on the interface can be written as:

$$\alpha = \frac{\beta\varepsilon}{\varepsilon + 1 - \beta^2} \tag{1.7}$$

where ε is defined as:

$$\varepsilon = \frac{\sigma_{SC}}{\sigma_{FM}} \frac{\lambda_{FM}}{\lambda_{SC}} \tag{1.8}$$

As in general $\sigma_{SC} \ll \sigma_{FM}$ and $\lambda_{FM} \ll \lambda_{SC}$ the value of ε will be very small by definition and consequently the spin polarization on the semiconductor will be also very small .This limitation is known as the impedance mismatch problem and was first demonstrated by Schmidt *et al.* in 2000. As a consequence of this problem, for a real-life system spin polarization will be limited to the 0.1% [32]. Several approaches have been proposed to overcome this problem and improve the efficiency of the spin injection into the semiconductor. The simplest solution would be using a source with a 100 % spin polarization ($\beta = 1$) which lead straightforward to α=1. Half metal materials have been theoretically predicted to present a full spin polarization at the Fermi level but experimental values are remarkably below the calculations [33, 34]. Recently, some groups explored on the use of ferromagnetic semiconductors as EuS or EuO which present impedance values closer to that of the non-magnetic semiconductor [35, 36]. However, the main limitation for these materials is their extremely low Curie temperature, (EuO (T_C=77 K), EuS (T_C=16.5 K)), which limit its application to cryogenic temperatures. Great efforts have been made in order to find ferromagnetic semiconductors with higher Curie temperatures, encouraged by the theoretical work by Dietl in 2000 who predicted Curie temperatures above RT for Mn doped semiconductors [37]. Some reassuring advances have been made since then as the observation of an enhanced Curie temperature of 200 K in (Ga,Mn)As by nanostructure engineering [38]. Nevertheless, further work is still needed to reach room temperature application using these materials. In 2000, Rashba showed that the insertion of a spin-dependent resistive tunnel contact between the ferromagnetic electrode and the semiconductor could circumvent the impedance mismatch problem [39]. Later that year, Fert & Jaffrès extended the model by Smidth including a spin dependent interface resistance which under certain requirements could recover the spin polarization on the interface [40]. Since then several groups have reported on the successful electrical injection and detection of spin polarized currents on Si by using an insulator tunnel barrier to circumvent the impedance mismatch problem. In 2007 Jonker *et al.* reported electrical spin injection into Si from a ferromagnetic Fe contact across an Al_2O_3 tunnel barrier at 5 and 125 K [41] and later that year vanť Erve *et al.*, reported electrical injection, transport and detection at 10 K on the same system [42]. First measurements at room temperature had to wait until 2009 when Dash *et al.* demonstrated the electrical creation, detection and manipulation of spin polarization at 300 K by using $Ni_{80}Fe_20/Al_2O_3$ tunnel contacts on n-type and p-type heavily doped silicon [24]. More recently Suzuky *et al.* reported the first non-local detection of spin accumulation on Si at room temperature by using a

crystalline MgO tunnel barrier [43]. These results have legitimized tunnel transport through a highly resistive barrier as an efficient method to achieve spin injection into non-magnetic semiconductors and nowadays is one of the preferred methods for this purpose.

1.2.2 Quantum tunneling through a potential barrier

Quantum tunneling is a pure quantum effect with no classical analog that plays a key role in explaining several physical phenomena pertaining to diverse fields such as nuclear physics, astrophysics, semiconductors, superconductors and quantum technology [44, 45]. The basic theory describing the quantum tunneling effect has been first developed in the 1920s [46, 47]. From a classical mechanics perspective, if a particle with energy E finds a potential barrier of height U_0, the particle will only be able to go through this region if $E>U_0$, otherwise all the intensity will be reflected by the barrier. Nevertheless, from the quantum mechanical point of view, there exists a finite probability for the particle to tunnel through the potential barrier even if $E<U_0$ keeping the same energy E, as it is schematized in Figure 1.4(a). In order to study this phenomenon with more detail one of the simplest systems is a metal(M1) -insulator(I) -metal(M2) structure, commonly called a tunnel junction, where the insulator layer is generally provided by a metal oxide as Al_2O_3. Although most of the intensity will be reflected on the M/I interface as predicted by classical mechanics, if the insulator layer is thin enough (typically a few nm) a tunnel current will be produced between the two electrodes.

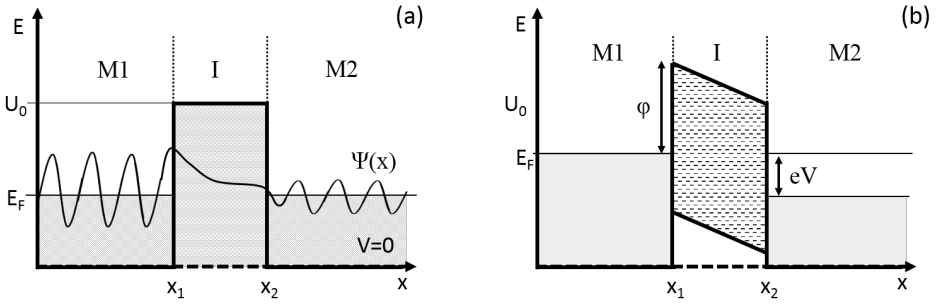

Figure 1.4: (a) Tunneling in a metal-insulator-metal structure. The electron wave function decays exponentially within the potential barrier. If the barrier is thin enough some intensity will remain in the second electrode. (b) Potential diagram of the metal-insulator-metal structure after applying a bias voltage V. Colored areas represent filled states meanwhile open areas represent unoccupied states. The dashed area represents the forbidden gap on the insulator.

If we consider two metallic electrodes fabricated of the same material, after applying a bias voltage V, the Fermi level of the left electrode (M1) will be shifted by

eV respect to the right electrode (M2). The potential diagram for a metal-insulator-metal structure under a bias voltage V is shown in Figure 1.4(b). The tunnel current from M1 to M2 through the insulator is generally studied as a function of the bias voltage applied across the tunnel junction and will be given by:

$$I_{M1\to M2}(V) = \int_{-\infty}^{\infty} \underbrace{\boxed{\rho_{M1}(E)f(E)}}_{\substack{\text{Occupied}\\ \text{states in M1}}} \cdot T \cdot \underbrace{\boxed{\rho_{M2}(E+eV)[1-f(E+eV)]}}_{\substack{\text{Unoccupied}\\ \text{states in M2}}} dE \quad (1.9)$$

Where T is the tunneling probability for an incident particle in M1 to cross the potential barrier and arrive to M2. In order to calculate the tunneling probability it is necessary to consider the evolution of the wave function of the particle $\Psi(x)$ under the action of the potential V(x) describing the barrier, which will be described by the time-independent Schrödinger equation [48]:

$$-\frac{\hbar}{2m}\frac{d^2\Psi(x)}{dx^2} + V(x)\Psi(x) = E\Psi(x) \quad (1.10)$$

The solution of this equation can be calculated using the Wentzel-Kramers-Brillouin (WKB) approximation so the wave function is defined as

$$\Psi(x) \approx \frac{1}{\sqrt{k(x)}} \exp\left(\pm i \int^x k(x')dx'\right) \quad (1.11)$$

and

$$\begin{aligned} k(x) &= \frac{\sqrt{2m(E-V(x))}}{\hbar} \quad \text{if} \quad E > V \\ k(x) &= i\frac{\sqrt{2m(V(x)-E)}}{\hbar} = i\kappa(x) \quad \text{if} \quad E < V \end{aligned} \quad (1.12)$$

The validity of this approximation is limited to the cases where $|dk(x)/dx| \ll |k^2(x)|$. The physical meaning of this condition is that the change on the local momentum $p(x) = \hbar k(x)$ of the wave function over the wavelength must be much smaller than the local momentum itself in order to approximate the solution to equation 1.10 by solution 1.11. In the particular case of a potential barrier defined between x_1 and x_2 three different regions can be defined:

$$\Psi(x) = \begin{cases} \frac{A}{\sqrt{k(x)}} \exp\left(i\int_{x_1}^x k(x)dx\right) + \frac{B}{\sqrt{k(x)}} \exp\left(-i\int_{x_1}^x k(x)dx\right) & x < x_1 \\ \frac{C}{\sqrt{\kappa(x)}} \exp\left(-i\int_{x_1}^x \kappa(x)dx\right) + \frac{D}{\sqrt{\kappa(x)}} \exp\left(i\int_{x_1}^x \kappa(x)dx\right) & x_1 < x < x_2 \\ \frac{F}{\sqrt{k(x)}} \exp\left(i\int_{x_2}^x k(x)dx\right) + \frac{G}{\sqrt{k(x)}} \exp\left(-i\int_{x_2}^x k(x)dx\right) & x_2 < x \end{cases} \quad (1.13)$$

From the boundary conditions of continuity and smoothness (continuity of the first derivative) for the wave function on the turning points x_1 and x_2, it is possible to stablish a linear relation between the coefficients A, B and F, G, which is given bythe matrix M, so that:

$$\begin{pmatrix} A \\ B \end{pmatrix} = \frac{1}{2} \begin{pmatrix} 2\theta + \frac{1}{2\theta} & i\left(2\theta - \frac{1}{2\theta}\right) \\ -i\left(2\theta - \frac{1}{2\theta}\right) & 2\theta + \frac{1}{2\theta} \end{pmatrix} \begin{pmatrix} F \\ G \end{pmatrix} \tag{1.14}$$

where

$$\theta = \exp\left(\int_{x_1}^{x_2} \kappa(x)dx\right) \tag{1.15}$$

The tunneling probability is given by

$$T = \frac{|\Psi_{trans}\sqrt{k_{trans}}|^2}{|\Psi_{inc}\sqrt{k_{inc}}|^2} = \frac{|F|^2}{|A|^2} \tag{1.16}$$

Considering that there is no wave incident from the right side of the junction (G=0) it can be directly obtained from 1.14

$$T = \frac{1}{|M_{11}|^2} = \frac{4}{\left(2\theta + \frac{1}{2\theta}\right)^2} \tag{1.17}$$

For a high and a broad barrier, where $\theta \gg 1$

$$T \approx \frac{1}{\theta^2} = \exp\left(-2\int_{x_1}^{x_2} \kappa(x)dx\right) \tag{1.18}$$

Hence, the parameter θ will determine the transmission of the tunnel current through the potential barrier, being a quantification of its opacity. Simultaneously, this parameter will depend on the width and the height of the potential barrier and therefore the tunnel current can be strongly influenced by the insulator material choice and the thickness of the tunnel barrier.

1.2.3 Spin-dependent tunneling in MTJ

First insights about spin dependent tunneling were presented by Tedrow and Meservey in 1971 [49]. They performed an extended study of tunneling currents using ferromagnetic electrodes and analyzing the polarization of the injected current into superconductors [49, 50]. In 1975, Jullière studied for the first time the dependence of the tunnel current on the relative orientation of the ferromagnetic moments in MTJs [11] which opened the possibility of manipulating tunnel current by means of an applied magnetic field. Although the clear interest of the system from the point of view of application, and also from the point of view of fundamental physics, it took almost 30 years to have an active research on this effect. This was partly

due to the limitations related with the fabrication of high quality magnetic tunnel junctions and the critical dependence of the phenomena on the characterisitcs of the tunnel barrier. This first tunneling magnetoresistance (TMR) effect reported by Jullière was observed on Fe/Ge/Co junctions with an amorphous Ge tunnel barrier of 10 nm thickness. The change of the resistance was 14% at 4.2 K at zero bias voltage [11]. Jullière defined the changes observed on the resistance as a function of the polarization of the two electrodes as:

$$\Delta R/R = (R_{\downarrow\uparrow} - R_{\uparrow\uparrow})/R_{\downarrow\uparrow} = 2P_1P_2/(1 + P_1P_2) \tag{1.19}$$

According to this model P_1 and P_2 are the spin polarization at the two ferromagnetic electrodes and $R_{\downarrow\uparrow}$ and $R_{\uparrow\uparrow}$ are the resistance values measured at antiparallel and parallel magnetization respectively. Equation 1.19 has been adopted in later works to explain magnetoresistance phenomena. However, this model does not take into account important experimental limiting factors as domain walls, spin scattering at the interface or magnetic coupling between the electrodes, which can critically reduce or even suppress the expected magnetoresistance effect. A few years after the experimental studies of Tedrow and Meservey, Stearns proposed a theoretical model to explain their observations of positive spin polarization for all ferromagnetic 3d metals [51]. She was able to explain the experimental results by using a realistic band structure and assuming a majority contribution of itinerant 3d electrons to the tunnel current. Although the success of Stearns idea, the origin of this predominant d orbitals contribution was not completely cleared. Later, Slonczewski presented an alternative model analyzing the influence of the tunnel barrier height on spin tunneling through the interface, obtaining values in agreement with some low $\Delta R/R$ values observed experimentally which could not be explained using Jullières model [52]. More recent studies determined that the spin polarization of the tunnel current can be predicted from the symmetry of the Bloch states in the bulk ferromagnetic electrodes and the band structure of the insulator barrier [53, 54]. In the particular case of a crystal lattice, the electron wave function will be defined by Bloch states as a consequence of the periodic potential of the lattice. These states will present different symmetry depending on the hybridization of the electron orbitals which can affect to the spin polarization of the tunnel current. Nevertheless, this model is not appropriate to predict the polarization of MTJ with amorphous barriers as the information of the Bloch states on the electrode is lost during the tunneling process.

1.2.4 Role of the tunnel barrier on spin dependent tunneling

In Jullière's model the spin dependence of the conductivity of the junction is related uniquely on the spin polarization of the two electrodes, completely dismissing the influence of the tunnel barrier on the TMR which is completely incongruous with experimental observations. Generally, amorphous Al_2O_3 has been the preferred

material for the fabrication of MTJs. Consequently, significant efforts have been made in order to understand and improve the characteristics of the fabricated Al_2O_3 barriers [13,55–58]. Nevertheless, in the last years, different materials as $SrTiO_3$ have been successfully introduced, with a significant modification of the TMR response in some cases [59]. Experimental observations in magnetic tunnel junctions completely proved the critical influence of the electronic structure of the ferromagnetic/insulator interface on spin dependent tunneling [55–57]. However, the specific ways in which the TMR is conditioned by interface properties is still to be understood.

LeClair *et al.* observed how the introduction of a 1 $\AA$ Ru interlayer on Co /Ru /Al_2O_3 /Co structures produces a drop of the 50% on the TMR values. Moreover, increasing the Ru thickness over 2 $\AA$ could even inverse the sign of the spin polarization respect to that of the Co/Al_2O_3/Co reference system. They related this inversion of the spin polarization with exchange effects on the Ru/Co interface, which lead to the modification of the band diagram and the density of states of the Co electrode, modifying the TMR of the junction [57]. Other works related this effect with the formation of quantum well states on the metallic layer, inducing resonant tunneling for majority spin and inversing the sign of the TMR [58]. These different interpretations are an example of the aspects still to be clarified in order to understand spin dependent tunneling in MTJs. Belaschenko and coworkers showed by first principle calculations how the absence or presence of a single oxygen atom absorbed on the Co/Al_2O_3 interface could change the spin polarization of Co /Al_2O_3 /Co MTJ from negative to positive due to the formation of resonant states that assist tunneling on the majority spin channel by antibonding of Co-O states, illustrating the high sensitivity of the phenomena to interface quality [60]. Regarding the influence of the material chosen, Teresa *et al.* showed how the substitution of alumina by $SrTiO_3$ could inverse the sign of the TMR in Co/ insulator/ LSMO heterostructures remarking the need of more complex models including the characteristics of the tunnel barrier [61].

1.2.5 Formation of the Schottky barrier

Due to the different concentration of free carriers between the semiconductor and the ferromagnet, the formation of a Schottky barrier is induced on the tunnel contact, which generates a depletion region near to the interface and a bending of the conduction and valence band on the semiconductor. In fact, some works reported on electrical spin injection by direct tunneling through Schottky contacts on Si and Ge using FM alloys such as Fe_3Si [62, 63] or CoFe [64] so that the oxide tunnel barrier is dismissed and substituted by the Schottky barrier. The formation of the Schottky barrier has three consequences for spin injection. First, due to the high resistance of the contact, the time electrons spent in the semiconductor channel increases exceeding the spin-relaxation time and reducing spin accumulation in the semiconductor [40]. Second, the high resistance of the contact increases the switching

time and impede the operation of the device at high frequencies. Third, the transport through a wide Schottky barrier is mainly produced by thermionic emission and not through tunneling. As a consequence, electrons arriving to the conduction band of the semiconductor proceed from levels far from the Fermi level where the spin polarization in the ferromagnetic material is much less significant [65].

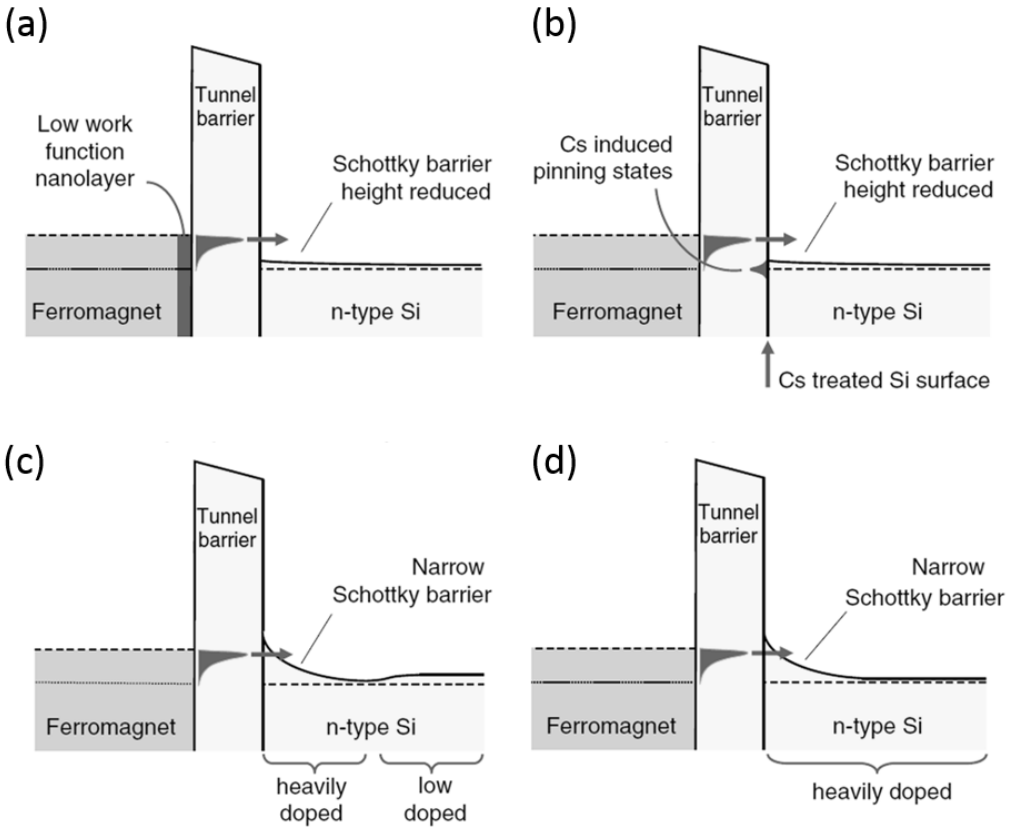

Figure 1.5: Different strategies for contact engineering. (a) The use of a low-work-function ferromagnetic layer and (b) treating Si surface by Cs reduce the height of the Schottky barrier. (c) Low doped semiconductor with a heavily doped interface by δ-doping or (d) heavily doped semiconductor provide a narrow barrier that allow tunneling transport through it. Figure adapted from reference [66]

The Schottky barrier is characterized by the potential barrier and its width. In order to optimize the efficiency of the system, the height of the potential barrier must be kept as low as possible and the depletion region the narrowest . Figure 1.5 shows different strategies to engineer contacts and improve the spin accumulation on Silicon using tunnel contacts. Increasing the number of carriers on the semiconductor

by heavily doping it can significantly reduce the width of the depletion region and favor tunneling transport through the Schottky barrier [43, 67, 68]. Nevertheless, it needs to be remembered that doping impurities act as spin scattering centers and reduce spin lifetimes on the semiconductor. The introduction of a Cs interlayer between the insulator and Si creates interface states and reduce the height and the width of the Schottky barrier [24, 69]. However, Cs-treated substrates showed much lower spin signals compared to untreated substrates, indicating a low efficiency of the method [24]. Min *et al.* proposed the use of ferromagnetic materials with a low work-function interlayers in order to reduce the height of the Schottky barrier [70].

1.2.6 Extrinsic contributions to spin relaxation

Spin lifetime on the semiconductor will determine how long the spin accumulation created is maintained without further injection. Spin relaxation mechanism will depend on the characteristics of the semiconductor, as for example its atomic number, its nuclear spin and the crystallographic structure. For the particular case of silicon the dominant mechanism is the Elliot-Yafet spin relaxation, which is related with the interaction of conduction electrons with phonons and impurities and the spin-orbit interaction. However, the magnetic tunnel contact can modify relaxation mechanism reducing spin lifetime and accelerating spin relaxation. For instance, the formation of a rough interface promotes the appearance of local magnetostatic fields that can induce spin precession and reduce spin accumulation on the semiconductor as illustrated in Figure 1.6

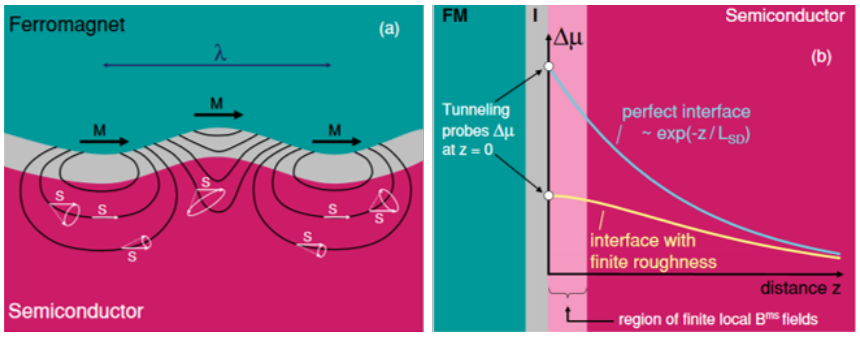

Figure 1.6: (a) Inhomogeneous magnetic field near to a ferromagnetic interface with a finite roughness sketched for a sinusoidal interface of period λ. The spins injected on the semiconductor initially aligned with the magnetization of the ferromagnet will precess in different trajectories by the effect of this local magnetic fields. (b) Decay of the spin accumulation with distance for a perfect interface and for a finite roughness interface. Figure reproduced from reference [71]

Moreover, the formation of interface states and barrier defects which act as scattering centers can increase the spin relaxation rate by means of the Elliot-Yafet

mechanism. Besides, the presence of interface defects can modify the structural properties of the semiconductor. For instance, in the case of silicon this can break the crystal-inversion symmetry of the lattice generating electric fields that can interact with conduction electrons and produce spin relaxation via the D'Yakanov Perel mechanism, which is not present in the bulk semiconductor [66]. Therefore, it is mandatory to be able to fabricate homogeneous and high quality ferromagnetic tunnel contacts presenting atomically abrupt interfaces.

1.3 Half metal electrodes

One of the possible solutions to overcome the impedance mismatch problem and improve spin polarization rate on non-magnetic semiconductors is the use of 100 % spin polarized sources, as can be deduced from equation 1.7. The concept of half metal ferromagnet was introduced by Groot *et al.* in 1983 after their studies on the band structure of Mn-based Heusler alloys [72]. A schematic image of the band structure for paramagnetic, ferromagnetic and half metal materials is presented in Figure 1.7. For a paramagnetic material the density of states is equal for both spin orientations and consequently there is no spin polarization (P=0) meanwhile a conventional ferromagnet presents spin polarization because of the higher density of states for majority spin orientation (P<1). In the particular case of half-metal ferromagnets it was observed how these magnetic compounds were metallic for majority-spin electrons whereas the minority-spin electrons presented an energy gap. In other words, there exists only one spin channel for conduction and the material shows a complete spin polarization (P=1). First experimental evidence of half metallicity had to wait until 1990, when Hanssen *et al.* reported spin dependent momentum distributions on NiMnSb [73]. Since then, half metallic behavior has been observed in several materials as CrO_2 [74], $La_{1-x}Sr_xMnO_3$ manganites [75], Fe_3O_4 [76] or $SrRuO_3$ [77]. Different applications have been considered for these particular materials on spinctronics as giant magnetoresistance (GMR) [78] or the injection of spin polarized currents on non-magnetic materials [79].

However, some factors can partially destroy the half metallic behavior of these materials reducing the effective spin polarization. Studies on Sr_2FeMoO_6 discussed the critical effect of disorder on magneto-transport properties for double perovskites [81]. They observed how for ordered samples the absolute value of the magnetoresistance (MR) critically increased at low field meanwhile disordered samples only presented a slight increase with the magnetic field. At the highest magnetic field (7 T) the magnetoresistance for ordered samples was four times larger than for disordered samples, going from a 10 to a 40 % at 4.2 K. Doping or strain can also modify the density of states at the Fermi level shifting its energy position or reducing the enegy gap for minority spin orientation [82]. Besides. a strong reactivity to air and humidity has been observed for these magnetic compounds, which creates difficulties

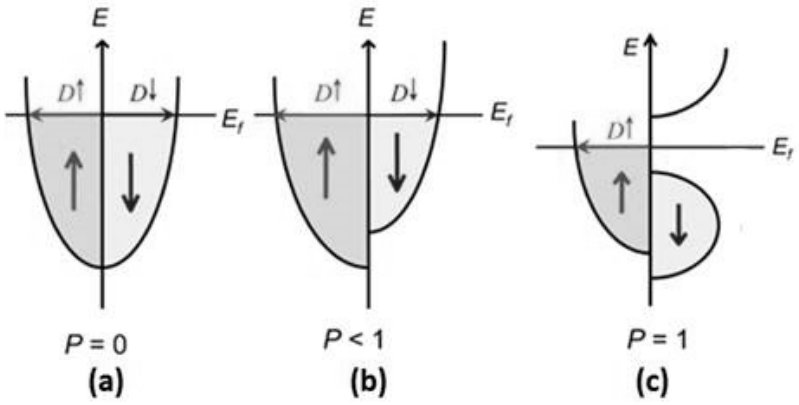

Figure 1.7: Band structure at the Fermi level for (a) paramagnets, (b) ferromagnets and (c) half-metals and the resulted spin polarization (P). Figure extracted from reference [80]

for the storage and processing of the devices [83].

An important parameter to consider when choosing the appropiate material is the Curie temperature (T_C). Permanent magnetic properties of ferromagnets are lost at a critical temperature T_C, becoming paramagnetic above such temperature. Some materials, as for example $SrRuO_3$, present Curie temperatures as low as 160 K which hamper any room temperature application [77]. Some values of T_C for half metal materials are resumed in table 1.1. Nevertheless, it has been observed how thermal excitations can destroy the half metallic character well below this temperature as the splitting between the two spin subbands for the minority and majority spin is reduced. Dowben *et al.* concluded after their theoretical studies on NiMnSb that finite-temperature spin disorder destroys the complete spin polarization characteristics of half metallic ferromagnets for temperatures lower than T_C [84]. In agreement with these results, Lezaic *et al.* predicted a fast drop of the spin polarization to 35% for $T = 0.67\ T_C$ also on NiMnSb [85].

$SrRuO_3$	$La_{1-x}Sr_xMnO_3$	CrO_2	Sr_2FeMoO_6	NiMnSb	Fe_3Si	Fe_3O_4	Co_2MnSi
160 K	370 K	395 K	410 K	730 K	820 K	840 K	985 K

Table 1.1: Bulk Curie temperature for some known half-metal materials

All the effects discussed above can be even more remarked when the half metal ferromagnets are prepared in the form of a thin film, which is mandatory for the integration of these materials on semiconductors. Although the preparation of half metallic thin films have been successfully achieved [86, 87] additional considerations must be hold. A critical decrease of the Curie temperature is typically observed in magnetic materials when they are prepared as a thin film respect to bulk values, em-

phasizing the need of choosing half metals with Curie temperature wide above room temperature. Other considerations are related with the fabrication process of the electrodes. Metallic alloys with half metallic properties present complex stoichiometry and in most of the cases require extreme conditions of temperature or pressure for its synthesis, which will have critical consequences on the properties of the system in terms of morphology and interface quality. On the other hand, a significant part of the materials presenting half metallic properties are oxides. The fabrication of oxide electrodes can generate complications due to the presence of oxygen during the deposition, especially in semiconductors like silicon with a promptly trend to oxidaze. The previous deposition of an oxide tunnel barrier can reduce the interaction of the half metal electrode with the silicon surface. Still, evaporation conditions need to be controlled in order to avoid oxygen diffusion and/or formation of mixed interfaces in the oxide/Si interface. Hence, the control of the structural, chemical and electronic properties of half metal films is mandatory in order to keep spin polarization and successfully integrated them in half metal - insulator - semiconductor heterostructures for spin injection.

1.4 Electrical spin injection in semiconductors nowadays

The most used technique to achieve spin injection in semiconductors by electrical means is the use of magnetic tunnel contacts. Magnetic tunnel contacts fabricated on semiconductors are generally composed of a soft ferromagnet electrode. as $Ni_{80}Fe_{20}$ [24, 68, 69] or CoFe [64, 67], and an oxide tunnel barrier, which is mostly a few nanometers thick amorphous Al_2O_3 layer [24,69]. Nonetheless, some works reported also on SiO_2 [68] and crystalline MgO [43,67]. Most of the works published until now are centered on Si, given its advategeous properties in terms of long spin lifetimes [88] but some authors also measured electrically induced spin accumulation into other semiconductors as Ge [89] or GaAs [90]. Table 1.2 resumed the most representative results reported of spin signal measurements on semiconductors at room temperature since the first report by Dash *et al.* in 2009. As it can be clearly seen, an active research on semiconductors spintronics dates only to 10 years. Hence, semiconductor spintronics is a modern research field, being nowadays still in its early stages of development.

Spin accumulation on the semiconductor can be electrically injected and detected using a local three-terminal (3T) geometry [24] or a non-local (NL) four-terminal geometry [91]. Both configurations are schematized in Figure 1.8. The three terminal configuration presents a single ferromagnetic contact that acts as injector and detector. This geometry is more sensitive to aditional effects such as Hall or anisotropy magnetoresistance (AMR) but this artifacs can be eliminate by a proper control of the experiment [24]. Non-local four terminal devices allow to separate charge cur-

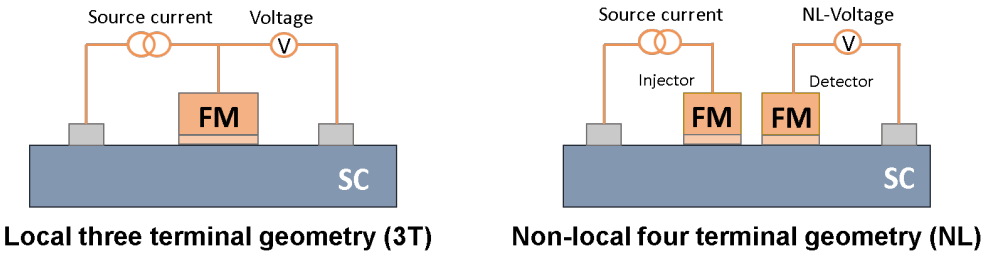

Figure 1.8: Detection geometries used to measure spin accumulation in semiconductors by electrical means.

rent path from the spin current path, eliminating this kind of effects if the device is properly designed [91].

Theory predicts a spin signal $(\Delta R)A = P^2\rho L_{SD}$ where ΔR is the resistance change in Hanle measurements, P the tunnel spin polarization of the magnetic contact, A the area of the contact, ρ the resistivity of the semiconductor and L_{SD} the spin diffusion length [88]. This yielded to values of 0.001 k$\Omega\mu$m^2 at RT for n-type Si using $Ni_{80}Fe_{20}/Al_2O_3$ magnetic tunnel contacts as predicted by Dash *et al.* [24]. Nevertheless, they measured spin signal values of 2-6 kΩ μm^2, two orders of magnitude above the theoretical predictions. These values have been later reproduced by other authors using similar 3T devices, with heavily doped Si and large contacts but using different tunnel barriers as crystalline MgO [43,67] or SiO_2 [68], obtaining values in the range of 1-5 kΩ μm^2 (Table 1.2). Unexpectedly large spin signals were also reported on Ge heterostructures, reaching values as high as 170 K$\Omega\mu$m^{-2} [89,92]. On the contrary, measurements on non-local devices showed spin signal several orders of magnitud below the theoretical predictions. Suzuki *et al.* concluded that the low non-local signal observed $\sim 10^{-5}$ was in agreement with theory [43]. However, in that case a tunnel spin polarization (P) of only 1-2 % needs to be assumed for the Fe/MgO contacts.

Different reasons have been discussed about the origin of these discrepancies between the theory and the different experimental results without reaching a clear conclusion. Tran *et al.* tried to explained the disagreement through a two-step tunneling model assisted by the formation of localized states near the oxide/semiconductor interface in 3T devices [90]. Jansen *et al.* extended this model a few years later including a parallel current by direct tunneling. Uemura and co-workers proposed a two step tunneling model via localized states near the oxide/FM interface [93]. However, there is no experimental evidence that these localized states at the interface would produce such a spin accumulation. Dash *et al.* pointed to the lateral inhomogeneity of the tunnel current density [24]. In a later work, he and his coworkers also discussed the understimation of spin lifetimes on the semiconductor as a consequence of magnetostatic fringes fields arising from interface roughness as the cause of these

Semicond.	$\mathbf{n_e(cm^{-3})}$	**Tunnel oxide**	**Electrode**	**P (%)**	**Method**	**Spin signal at RT ($\mathbf{K\Omega\mu m^{-2}}$)**	**Reference**
n-type Si	1.8×10^{19}	Al_2O_3	$Ni_{80}Fe_{20}$	∼30	3T	5.6	Dash *et al.* (2009) [24]
n-type Si	1.8×10^{19}	Al_2O_3	$Ni_{80}Fe_{20}$	∼30	3T	2.8	Dash *et al.* (2009) [24]
n-type Si	3×10^{19}	SOi_2	$Ni_{80}Fe_{20}$	∼25	3T	1.2	Li *et al.* (2011) [68]
n-type Si	2.5×10^{19}	MgO	CoFe	∼50	3T	4.8	Jeon *et al.* (2011) [67]
n-type Si-Cs	1.5×10^{18}	Al_2O_3	$Ni_{80}Fe_{20}$	∼30	3T	15	Jansen *et al.* (2010) [69]
n-type Si	3×10^{18}	SiO_2	$Ni_{80}Fe_{20}$	∼25	3T	129	Li *et al.* (2011) [68]
p-type Si	4.8×10^{18}	Al_2O_3	$Ni_{80}Fe_{20}$	∼30	3T	23	Dash *et al.* (2009) [24]
n-type Si	5×10^{19}	MgO	Fe	∼50	NL	$\sim10^{-5}$	Suzuki *et al.* (2011) [43]
n-type Ge	2.5×10^{18}	MgO	CoFe	∼50	NL	170	Jeon *et al.* (2011) [92]

Table 1.2: Electrically induced spin accumulation in semiconductors. Spin signal is expressed as the ΔV divided by the current density. P is the polarization in the ferromagnetic electrode far from the interface. Table adapted from reference [88]

incongruities. The lack of feasible explanations for the differences between the theoretical predictions and the experimental results seems to point, as some recent works defend [88, 94], to a more fundamental origin of these discrepancies. In other words, neither the theoretical models can describe the experimental observations nor the experimental results can prove the theory, which indicates either an incompleteness of the theoretical models or the presence of uncontrolled factors during the measurements. In any case, the only possible conclusion is the need for further research in this field.

1.5 Aim of the thesis

Although the first observations of spin-related phenomena in semiconductors can be dated earlier, active research in semiconductor spintronics is extremely recent, being this a field still on its early stages. The works reported until now have focused on the development of theoretical models to describe the phenomena involved and validated the experimental observations. From these works some key impediments to the design of efficient spin injection systems have been identified. The fabrication of high quality heterostructures has been proved mandatory, especially regarding interface properties, in order to achieve significant spin accumulation in non-magnetic semiconductors by means of tunnel contacts. Nevertheless, relevant studies about the morphological and structural properties of the ferromagnet- insulator- semiconductor heterostructures are almost nonexistent. Besides, the use of half metallic electrodes for the design of TMR devices is completely novel. The integration of half metallic thin films in silicon is more extended but still these works do not include the use of a tunnel barrier for this purpose. In some cases, a buffer layer has been used in order to avoid the interaction of the material to deposit with silicon, but in these cases neither the properties of this layer nor the characteristics of the interface with silicon are taken into account. The search of novel materials with high spin polarization is a key point for the development of more efficient systems.

Hence, the main aim of this thesis is the integration of half metallic ferromagnetic thin films on silicon by means of tunnel contacts. For that, two important objectives have been stablished. The first objective concerns with the successful growth of half-metal/ tunnel contacts/ Si heterostructures fulfilling the requirements established for the design of magnetic tunnel contacts in semiconductors in terms of an efficient spin injection. Those are:

i) A tunnel barrier thin enough so that the tunneling probability is large enough.

ii) A narrow and/or low Schottky barrier has to be achieved in order to have majority tunneling transport.

iii) The formation of flat and abrupt interfaces to avoid extrinsic contributions to spin relaxation.

Moreover, some aditional features are required as it is the obtention of single phase films for the half-metal electrode in order to keep its good intrinsic properties as it is a low resistance, a high magnetoresistance ratio and high spin polarization rates.The second objective concerns with a complete characterization of the heterostructures determining its morphological (surface and interface roughness), compositional (presence of mixed phases, chemical diffusion) and structural properties (crystallinity, epitaxy, oxygen defects, strain) of the half metal layer, tunnel contact and buried interfaces.

More concretely, the work developted during this thesis was structured in two differenciated blocks:

(a) The integration of **Fe_3O_4** on **Si(001)** using oxide tunnel contacts. The aim of the work was to obtain Fe_3O_4/oxide/Si heterostructures which present flat and abrupt interfaces without the formation of non-stoichiometric phases. The work is especially focused on analyzing and overcoming the difficulties found during the manufacture of high quality FM/oxide contacts on Si as can be the stabilization of Si during the evaporation of oxides, the formation of mixed interface or the lost of the magnetic properties of the ferromagnet. Fe_3O_4 is integrated with different crystalline behaviors. Textured Fe_3O_4 is integrated using epitaxial **$SrTiO_3$** as tunnel barrier meanwhile polycrystalline Fe_3O_4 is grown by using amorphous **SiO_2** native oxide tunnel barrier.

(b) The successful growth of epitaxial **Fe_3Si** films on **$SrTiO_3$(001)** for the first time as an alternative material to normally used ferromagnets. Fe_3Si is a promising material and its functionality has been proved in the design of Schottky tunnel devices. However, the reports on the growth of epitaxial films are limited to a few and none of them reported the growth on $SrTiO_3$. The aim of this part of the work was the stabilization of single phase epitaxial films on $SrTiO_3$ substrates as a first step to integrate this material for the fabrication of magnetic tunnel contacts.

1.6 Organization of the manuscript

This thesis is organized in six chapters. The current chapter presents the basis and current advances on semiconductor spintronic and the objectives of this work. Chapter 2 is dedicated to the description of the different experimental methods used during this thesis for sample preparation as well as for the characterization of the growth process and final heterostructures. On chapter 3, a brief description of the different materials used during this thesis is presented. Chapter 4 is focused on the fabrication and characterization of Fe_3O_4-based heterostructures on silicon by two different strategies for the fabrication of the tunnel contact, using silicon native oxide and crystalline $SrTiO_3$ films. In chapter 5, the preparation and characterization of Fe_3Si half metallic thin films as an alternative material for the fabrication of electrodes is discussed. Finally, Chapter 6 resumes the general conclusions an final remarks of the presented work.

Chapter 2

Experimental techniques

2.1 Introduction

During this chapter, the concepts related with the fabrication of the samples studied on the present thesis as well as the techniques used for their characterization are described. The methods utilized during this work are well known and established. All the information related with the theoretical basis and the technical aspects are described in different specialized books and articles, so the following pages will be focused on the relevant aspects for the study carried out. This thesis was carried out on the Spanish CRG BM25-SpLine at the The European Synchrotron (ESRF). Therefore, there is an important contribution of Synchrotron-based techniques and a more extended section is dedicatedhe work carried out, including some general aspects about synchrotron radiation.

2.2 Physical vapor deposition (PVD)

All the samples studied on this thesis were fabricated using physical vapor deposition (PVD) methods. PVD is characterized by the transition of the material source from a condensed to a vapor phase and then condensed again on a substrate forming a thin film or a coating. The suitability of each technique belonging to this group depends on the material to evaporate and the request on the deposited films in terms of control of the composition, morphology, crystallinity and amount of impurities [95]. Two different PVD methods were used on this work, pulsed laser deposition (PLD) and molecular beam epitaxy (MBE).

2.2.1 Pulsed Laser Deposition (PLD)

Pulsed laser deposition (PLD) consists on the deposition of a material by ablating a target of the aforesaid material under the action of an ultra-high power laser

light [96]. From the point of view of film formation the most important factor is that the time scale for ablation is short enough to suppress the dissipation of the excitation energy beyond the volume ablated during the pulse, so the damage of the remaining target and its segregation into different components is avoided. In this regime, the stoichiometry of the target within the plasma plume remains almost unchanged and nearly equal for successive pulses. For this reason this technique is especially suitable for the deposition of oriented films with complex stoichiometry. In addition, the high temperature raised on the plasma plume allows the synthesis of metastable materials that cannot be synthesized otherwise.

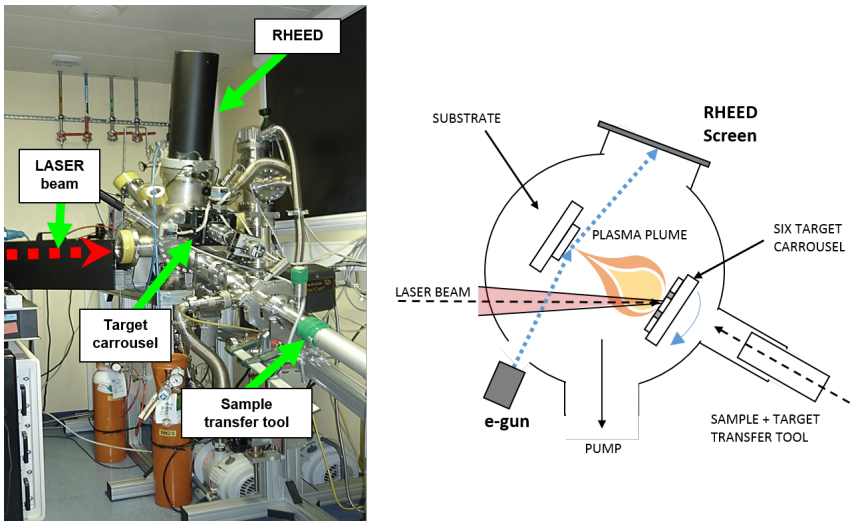

Figure 2.1: Experimental set-up used for the deposition of samples by PLD and a schematic inside-view of the chamber. The carrousel target can be rotated to select the material to ablate. The laser hit the target and the evaporated material condenses on the substrate.

The PLD experimental set-up used during this thesis for the deposition of half-metallic films is shown in Figure 2.1, together with a schematic drawing of the growth configuration inside the chamber. The equipment is localized at the BM25-SpLine support laboratory and is constituted by an ultra-high vacuum chamber with a laser source focused on a six target carrousel that allows the preparation of multilayer systems without exposition of the samples to air. The substrates and the targets are introduced on the chamber using a home-designed sample transfer tool that is compatible with the experimental set-ups for X-ray photoelectron spectroscopy and X-Ray diffraction + HAXPES set-ups from the Spanish CRG BM25-SpLine beamline at the ESRF, which allows the complete characterization of the samples keeping them in a free-contaminant environment during the whole process. The source is a Nd:YAG Quantel 981C high energy pulsed laser with a maximum repetition rate of 10 Hz, a wavelength of 1065 nm and a pulsed width of 8 ns. During this work an

interchangeable unit to work with the third harmonic was used so the incident light had a wavelength of 355 nm (between IR and UV), corresponding to a pulse energy of 280 mJ. The chamber includes a gas leakage source that allows working under different environments as oxygen, nitrogen or argon. The sample holder includes a heating system so the substrates can be heated up in a range from RT to 1273 K. The temperature is controlled by a thermocouple installed on the sample holder and a pyrometer placed out of the chamber.

It has to be taken into account that films deposited by PLD tends to be highly particulate due to different processes as, for instance, the formation of nodules on the target surface during the ablation that are susceptible to be ejected and deposited on the sample in subsequent laser pulses [97]. In order to reduce this effect the substrate was displaced slightly outside from the center of the plasma plume. The efficiency and deposition rate are hence decreased but the achievement of particulate-free surfaces is benefited. To ablate the target uniformly, a scan on the surface by horizontal and vertical translating the target is performed during the evaporation so different points of it are reached at each pulse. The crystalline growth of the films is monitored by in situ reflection high energy electron diffraction (RHEED).

2.2.2 Molecular beam epitaxy (MBE)

Molecular beam epitaxy is an especial variation of physical vapor deposition devoted to the deposition of epitaxial thin films on single crystals [98]. The physical mechanisms involved are very similar to those present in thermal or electron beam evaporation where the material source is heated so that its vapor pressure is raised and then condensed on the substrate surface forming a thin film. In order to favor a high degree of order in the growth structures the deposition is usually very slow, keeping evaporation rates under 3000 nm/hour. Such a low rate requires proportional good vacuum to achieve the same impurity level as with other faster deposition techniques. Meanwhile thermal evaporation can be realized in a vacuum pressure of only 10^{-6} mbar, MBE requires ultrahigh vacuum (10^{-8} mbar or better) to take place. As the process is fulfilled in an ultrahigh vacuum system the mean free path between collisions becomes large enough for the vapor beam to arrive to the substrate without interacting. Some variations of the method include a gas source that reacts with the beam of molecules before they are absorbed on the substrates in a similar way to chemical vapor deposition (CVD). There are three types of MBE, solid source MBE, plasma assisted (PA-MBE) and reactive MBE (R-MBE). Again, the suitability of one or another will depend on the characteristics of the material to be evaporated.

The material source can be introduced inside the evaporator in the form of a bar, a rod or pieces placed on a crucible and is heated by electron bombardment from a tungsten filament. The electrons produced by the filament are accelerated through a high potential and focused on the material, raising temperatures as high as 300^{o}C on the focused spot. The operational parameters will depend strongly on the material

to be evaporated and on the choice of a rod or a crucible. MBE is mostly oriented to metal and simple compounds as during the deposition of of complex materials the compositional control becomes an issue as a result of the different evaporation and vapor pressures for each constituent. This effect can lead to preferential evaporation of some of the elements and therefore to the alteration of the stoichiometry of the compound.

2.3 X-Ray Photoelectron Spectroscopy (XPS)

X-Ray photoelectron spectroscopy (XPS) is based on the photoelectric effect described by Einstein. A photon with energy hν impinges on the sample and electrons are liberated from their bound state with a kinetic energy E_{kin}. The binding energy of the electron is defined by the difference in the energies of the un-ionized N electrons initial system E_i and the N-1 ionized final state E_f. Energy conservation yields straightaway to:

$$E_i(N) + h\nu = E_f(N-1,k) + E_{kin} \rightarrow E_B^V(k) = E_i(N) - E_f(N-1,k) \qquad (2.1)$$

Where k labels the level from which the ejected photoelectron has been removed. The binding energy is explained due to the positive attraction of the electron to the nucleus and its repulsion to the other electrons present in the atom. Changes on the binding energy due to modifications on the initial state energy are denominated chemical shifts and provide the most significant information for element characterization. Nevertheless, considering final state effects as, for instance, the relaxation of the remaining electrons of the atom after the ejection of the photoelectron can modify its energy and provide insight information about the electronic structure of the sample.

2.3.1 Experimental set-up

XPS measurements were performed in a home-designed experimental set-up devoted to surface characterization which is localized on the BM25-SpLine support laboratory. A standard XPS spectrum is normally acquired using a fixed photon energy and recording the number of photoelectrons as a function of the kinetic energy. The UHV chamber is equipped with a standard non-monochromatic x-ray tube with two anodes, Mg and Al, which provide a photon energy of 1253.6 and 1486.6 eV respectively. The kinetic energy of the photoelectrons emitted is discriminated with a hemispherical deflection analyzer (HDA). Besides, the chamber counts with two evaporators for MBE growth, an ultraviolet lamp for UV-VIS spectroscopy, an electron gun and a fluorescent screen for LEED characterization and an ion sputtering gun. The design incorporates a sample manipulator that provides the possibility of

tuning exit angle during XPS measurements, changing the surface sensibility, and allowing the alignment of the samples respect to the evaporator, the electron gun or the sputtering gun. The sample transfer tool is compatible with the PLD and X-Ray diffraction + HAXPES stations from BM25-SpLine, so the samples can be transferred between the equipments in a free-contaminant environment.

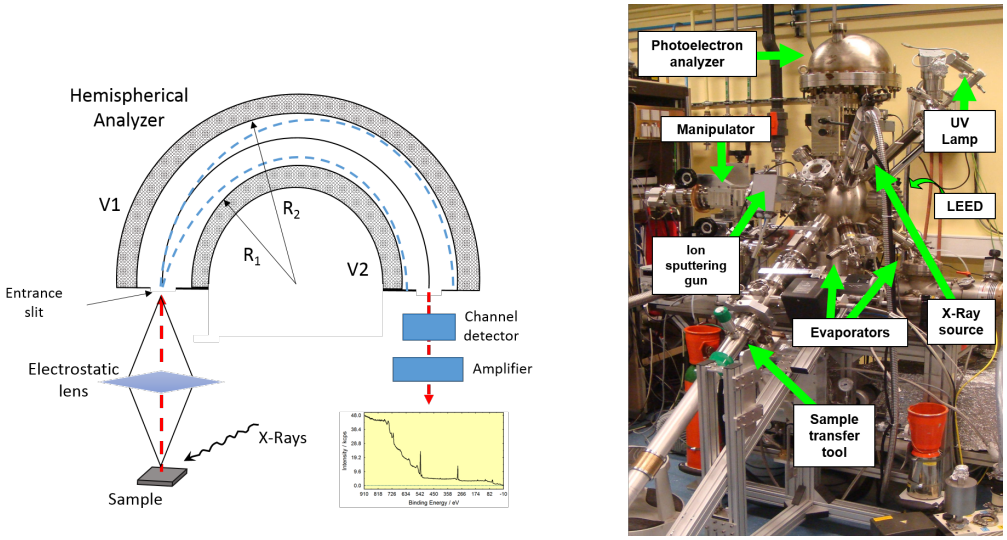

Figure 2.2: Experimental set-up used during this thesis to perform XPS measurements and a schematic view of the operation of a hemispherical analyzer.

Figure 2.2 shows a picture of the experimental set-up used during this thesis and a scheme of a standard hemispherical analyzer. The electron analyzer consists on two plates held at different potentials so that when the electrons are directed into the electric field created between them they are deflected with a different ratio as a function of their energy. The number of electrons are then counted using a parallel algorithm on a channel plate with 20 channels.A slit is centered at the entrance of the analyzer, as indicated in Figure 2.2, positioned on the mean of the radius of the two hemispheres R_0. A potential is applied between the two hemispheres so that the outer one is negative respect the inner one. The energy resolution of the analyzer, understood as the band of energies detected at the electron counter can be expressed as:

$$\Delta E = E_0[\frac{w}{2R_0} + \frac{\alpha^2}{4}] \tag{2.2}$$

Where E_0 is the pass energy of the analyzer, R_0 the mean radius of the two hemispheres, w the slit size and α the total acceptance angle in radians. The pass energy, which can be set on the acquisition software, represents the kinetic energy

of the electrons that fulfill the central trajectory inside the deflection part of the analyzer. A lower pass energy will provide a better resolution as can be seen in equation 2.2, but it will also reduce the number of counts the channel plate receives. The pass energy stablished will depende on the signal to noise ratio requirements. The analyzer also counts with a set of different slits that can be changed. A higher aperture will increase the probe area of the sample and increase the number of counts but also will reduce the energy resolution of the analyzer.

2.3.2 XPS intensity

The basis of the quantitative analysis of XPS intensity is that the ionization probability of a core level is practically independent on the valence state of the respective element so that the intensity is proportional to the number of atoms in the detected volume. The intensity I_A of a certain level of an element A in a matrix M can be written as:

$$I_A = \sigma_A D(E_A) \int_{\gamma=0}^{\pi} \int_{\varphi=0}^{2\pi} L_A(\gamma_1) \int_x \int_y J_0(x,y) T(x,y,\gamma,\varphi,E_A) \int_z N_A(x,y,z) \exp\left[-z/\lambda_M(E_A)\cos\theta\right] dx dy dz d\varphi d\gamma \tag{2.3}$$

Where σ_A is the photoionization cross section, D(E_A) the detection efficiency of the electron analyzer ,L_A the angular asymmetry of the emitted intensity with respect to the angle γ between the direction of incidence and detection, φ the azimuthal angle, J_0 is the flux of primary photons on the sample surface, T the transmission of the electron analyzer and N_A the density of atoms A. λ is the inelastic mean free path (IMFP) of the photoelectrons coming from the matrix with energy E_A and θ the angle between the surface normal and the direction of detection. If the spectrometer has a small entrance aperture and the sample is uniformly illuminated, which can be fulfilled in most of the cases, the equation can be simplified as follows:

$$I_A = \sigma_A D(E_A) L_A(\gamma_1) J_0(x,y) G_1(E_A) \int_z N_A(x,y,z) \exp\left[-z/\lambda_M(E_A)\cos\theta\right] dz \tag{2.4}$$

Where γ_1 and θ_1 are now fixed by the set-up geometry and G_1 is the spectrometer transmission

2.3.3 Determination of the thickness of an over layer A on a substrate surface B

Different information can be obtained evaluating equation 2.4 . One of the practical cases of interest for this thesis was the determination of the thickness d_A of a

thin layer of the material A on the surface of a substrate B. Considering a constant density of atoms on both layers and an abrupt interface the system can be described by the following distribution:

$$N_A = \begin{cases} N_A & \text{if } d_A \geq z \geq 0 \\ 0 & \text{elsewhere} \end{cases}$$
$$N_B = \begin{cases} N_B & \text{if } 0 > z > -\infty \\ 0 & \text{elsewhere} \end{cases} \tag{2.5}$$

If the values for N_A and N_B at each z value are now introduced in equation 2.4 the intensities I_A and I_B for each element can be written as:

$$I_A = \frac{I_A^0}{\lambda_A(E_A)\cos\theta}\left[1 - \exp\left(-\frac{d_A}{\lambda_A(E_A)\cos\theta}\right)\right] \tag{2.6}$$

$$I_B = \frac{I_B^0}{\lambda_A(E_B)\cos\theta}\left[\exp\left(-\frac{d_A}{\lambda_A(E_B)\cos\theta}\right)\right] \tag{2.7}$$

The constants I_A^0 and I_B^0 include all the constant factors related with the geometry and efficiency of the analyzer and are equivalent to the intensity that would be measured in the same conditions for a bulk reference sample of the material A or B respectively. By dividing equation 2.6 by equation 2.7 it is obtained:

$$\frac{I_A}{I_B} = \frac{I_A^0 \lambda_A(E_B)\left(1 - \exp\left[-\frac{d_A}{\lambda_A(E_A)}\cos\theta\right]\right)}{I_B^0 \lambda_A(E_A)\exp\left[-\frac{d_A}{\lambda_A(E_B)}\cos\theta\right]} \tag{2.8}$$

In particular cases, equation 2.8 can be used to calculate the over layer thickness d_A from the XPS intensity for each element. It has to be remembered that this model does not consider the effects of the surface and interface roughness on the XPS intensity. Still, in most of the cases it can provide a good estimation for the value d_A. The values for the inelastic mean free path used during this thesis were obtained using the Quases-Tougaard code based on the TPP2M formula [99]. All the mathematical development presented on this section can be found with full detail on reference [100].

2.4 Low Energy Electron Diffraction (LEED)

The first theoretical background of electron diffraction techniques appear with the discovery of the wave nature of matter by Louis de Broglie in 1924. By the principle of wave-particle duality, electrons can be considered as waves with wavelength λ=h/p, where h is the Planck constant and p the linear momentum of the electrons. Due

to the energy range of the incident electrons used for this technique (20-200eV), the associated wavelength will be on the order of atomic distances, expecting an interference with the crystal lattice just as x-rays of similar wavelengths. Low energy electron diffraction (LEED) measurements are performed by hitting a single crystal sample with a collimated electron beam of low energy (20-200eV) and recording the resultant diffraction pattern with a fluorescence screen and a CCD camera. The experimental set-up used during this thesis is installed in the home-designed UHV chamber devoted to surface characterization described in Section 2.3 and localized in the BM25-SpLine support laboratory. A simplified scheme of the LEED experimental set-up is shown in Figure 2.3.

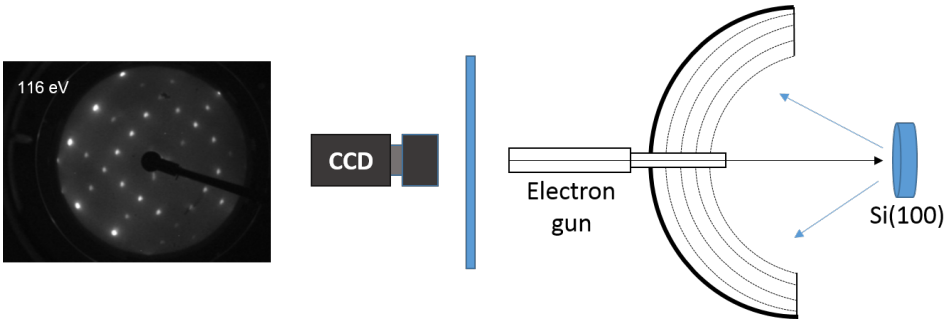

Figure 2.3: Scheme of LEED and an example of a LEED pattern obtained from a Si (100) substrate. Electrons are accelerated against the sample surface and diffracted electrons are collected on a fluorescent screen.

Qualitatively, the recorded diffraction pattern gives information about the symmetry of the surface structure or about the relation between structures in the case of adsorbate or reconstructed layers. The quantitative analysis of the spots intensities can give also accurate information on the atomic positions on the surface by comparison with theoretical data, but the accurate measure of the intensities requires a careful process that have not been faced during this work. X-ray diffraction measurements were carried out for this purpose instead.

2.5 Reflection High Energy Electron Diffraction (RHEED)

Reflection high energy electron diffraction (RHEED) is an electron diffraction technique similar to LEED. RHEED patterns are acquired by hitting the sample surface with grazing angle (1-5 degrees) with a high energy electron beam (1-30 keV). The interaction of the electron with the crystalline lattice of the sample produce a diffraction pattern that is collected in a phosphorescent screen and recorded with a CCD camera. The reflection geometry is adopted in order to obtain surface structural information. Under these conditions, the electron might travel substantial distances

in the solid with low penetration, ensuring surface sensitivity. The basic set-up for a RHEED experiment is shown in Figure 2.4 together with a characteristic diffraction pattern for a single oriented film.

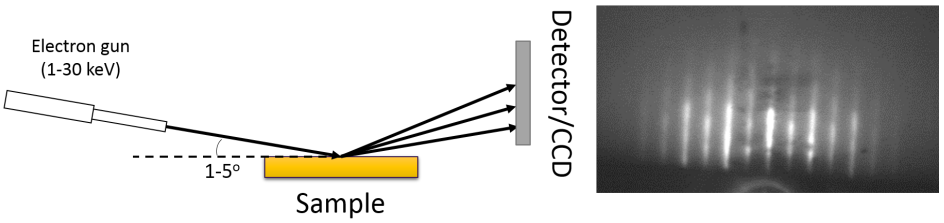

Figure 2.4: Configuration for RHEED acquisition and a typical diffraction pattern for a single oriented film. The presence of intensity strikes is related with the formation of a low particulate film.

As incidence angle for the acquisition of RHEED pattern is considerable small, the reciprocal lattice rods intersect the Edwald sphere at very low angles, producing a streak like pattern as the one shown in Figure 2.4. As the roughness of the deposited film increases, these streaks become non-uniform and adopt a spotty structure. In the case of a polycrystalline sample, the RHEED pattern appears in the shape of rings as there is always some grain fulfilling diffraction condition for a certain angle. Regarding the information that can be extracted from its analysis, the diffraction patterns obtained by LEED and RHEED are equivalent. The advantage offered by RHEED configuration is that the geometry of the experiment allows better access to the sample during observation of the RHEED pattern, being a suitable technique to monitor the crystalline growth during deposition.

2.6 Synchrotron-based techniques

2.6.1 Introduction

Synchrotron radiation is the electromagnetic radiation emitted by charged particles moving at relativistic speed under a radial acceleration. The emitted radiation is characterized by a high flux and by a wide energy range that goes from a few eV to several hundred of keV. The potential of synchrotron radiation as an intense and versatile x-ray source motivated a great interest on designing and developing better synchrotron sources, which has culminated in the so-called third generation of synchrotrons. In synchrotron sources the radiation is produced in what is called the storage ring. In practice, the storage ring is not a circle but a succession of linear sections separated by short curved sections where the trajectory of the electrons is modified and synchrotron radiation is produced. Third generation synchrotrons also include insertion devices on the linear sections which are a succession of magnets

that force the electron to define an oscillating trajectory in the linear stretches of the ring, emitting radiation at each turn. The most attractive feature of synchrotron radiation is with no doubt its high brilliance. The brilliance is defined as the number of photons per second, per unit of solid angle and per emission surface unit referred to a particular percentage of the spectral band. This concept allows to characterize the flux of photons at a particular energy, space and solid angle. Besides this, others attractive properties of synchrotron are the polarization and the time structure. Synchrotron light is an ideal tool in diverse fields of research as physics, chemistry, biology or material science, and can be applied to several techniques as diffraction, spectroscopy or imaging. In the following sections, the synchrotron based techniques used during this thesis will be discussed. Besides, some experimental details about the facility used are presented.

The Spanish CRG BM25-SpLine at the ESRF

Synchrotron experiments performed during this thesis were carried out at the Spanish CRG-BM25 SpLine at The European Synchrotron (ESRF) in Grenoble (France). The beamline is situated at the D25 bending magnet and it is divided in two branches that can cover an energy range from 5 to 45 keV. The synchrotron radiation emitted by a bending magnet has a large horizontal divergence and this was taken advantage of to select two different regions of the radiation cone and install two independent beamlines fully equipped that can operate simultaneously, the branch A and the branch B. Branch A is located on the soft edge of the bending magnet with a critical energy of 9.7 keV and presents two different experimental stations, one dedicated to x-ray absorption spectroscopy (XAS) and the other one devoted to high resolution powder diffraction (HRPD). Branch B is located in the hard edge with a critical energy of 20.6 keV and counts with two different experimental stations dedicated to single crystal and grazing incidence X-ray diffraction techniques and hard X-ray photoemission spectroscopy. Both branches count with a Si(111) double crystal monochromator (DCM) that provides an energy resolution of ΔE/E= 1.5×10^{-4}.

X-Ray Absorption Spectroscopy station (Branch A)

Figure 2.5 shows a picture of the XAS station installed on the Branch A of the Spanish CRG BM25-SpLine beamline, which is consisted of three ionization chambers, a sample stage and a nitrogen cooled 13 element Si(Li) fluorescence detector. X-ray absorption spectroscopy measurements can be carried out in three different modes, transmission, total (or partial) electron yield (TEY or PEY) and in fluorescence yield (FLY). An ionization chamber is situated before the sample in order to measure the input signal I_0. After the sample emplacement there are two identical

ionization chambers used for transmission mode measurements. This allows to measure a reference sample at the same time as the real sample is being measured. The signal collected by the first ionization chamber after the sample is used to measure the absorption of the sample as well as it acts as input signal for the reference situated after it. The second one records the signal transmitted after the reference. The absorption coefficient is calculated directly from the relation between the incident and the transmitted signal. However, in contrast to TEY and FLY which can be used for all conventional samples, transmission mode requires thin foils. TEY (PEY) and FLY measure the absorption coefficient indirectly through the excitations produced as a consequence of the interaction of the sample with the x-rays. In TEY the photoelectrons created by the absorbed x-rays are measured meanwhile in FLY mode the radiation produced by the relaxation of the atom after the photoelectron is expelled is the output signal. The platform for the sample emplacement is wide enough to allow the installation of different set-ups as for example baby chambers, reactors or cryostats, to perform experiments in different conditions.

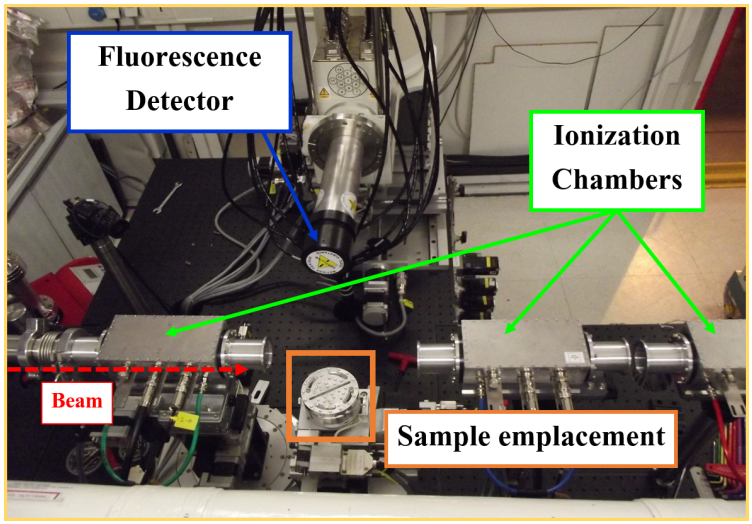

Figure 2.5: X-Ray Absorption Spectroscopy set-up installed on the Branch A of the Spanish CRG BM25-SpLine beamline.

Multipurpose X-Ray diffraction station (Branch B)

The multipurpose XRD station consists on a six-circle diffractometer in vertical geometry in which single crystal diffraction measurements including surfaces, interfaces, super lattices and thin films can be performed. A picture of this multifunctional station is shown in Figure 2.6. The sample stage allows the installation of different set-ups up to a load of 50 Kg for measurements in different conditions. UHV baby chambers, cryostats and reactor cells can be located according to the

requirements of each experiment. Besides the standard circles for diffraction additional motions are available to align the surface normal along predefined directions (vertical or horizontal) which is required for interface scattering experiments, as it is customary in surface diffraction. The experimental station incorporates a large CCD detector with an input active area of 250 mm x 125 mm. The CCD has 3 x 11 Megapixel, with a pixel size of 32.8 microns square and a final image resolution of 7651 x 3825 pixels. The sample-detector distance can be varied between few mm up to 1500 mm. For short sample-detector distances the detector area covers a solid angle of the reciprocal space wide enough to acquire reciprocal space maps from thin films and multilayers in few seconds. For large sample-detector distances, the resolution is increased, as the solid angle accepted by each pixel is extremely low.

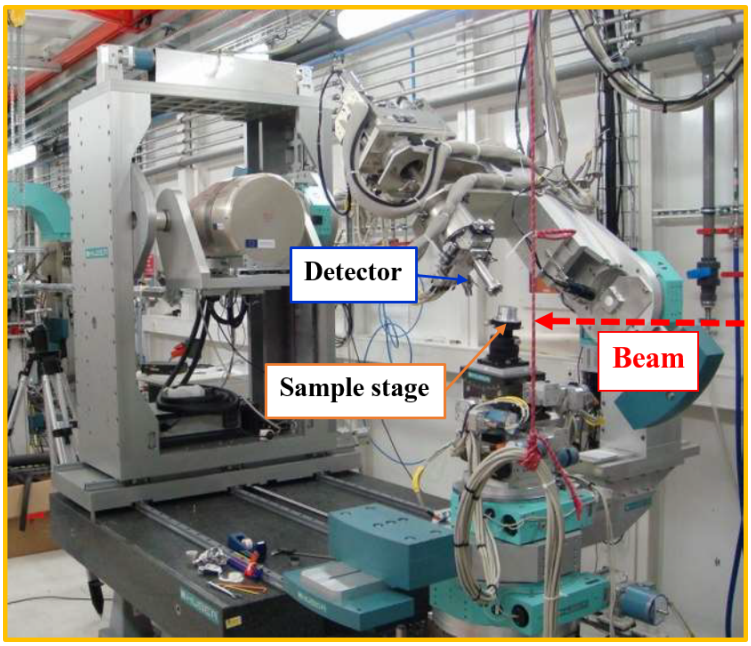

Figure 2.6: Multipurpose x-ray diffractometer installed at the first focal point of the Branch B of the Spanish CRG BM25-SpLine beamline.

Surface X-Ray diffraction and Hard X-Ray Photoelectron spectroscopy station (Branch B)

The second station of the Branch B is designed to combine surface x-ray diffraction (SXRD) and hard x-ray photoelectron spectroscopy (HAXPES). A picture of the station is shown in Figure 2.7. The experimental set-up includes a 2S+3D diffractometer in horizontal geometry, a UHV chamber and a high kinetic energy electrostatic analyzer [101]. The UHV chamber incorporates also MBE evaporation sources, an ion gun, an electron gun, a UV discharge lamp, a LEED optic, a sample heating

and cooling device, leak valves and a load-lock port. The sample surface is mounted vertically and the X-rays enter and leave the vacuum system through Be-windows welded onto the UHV chamber. A 200^o in-plane access and a 50^o out-of-plane access are allowed by the exit Be-window so that a wide portion of the reciprocal space is accessible. The electron analyzer is an electrostatic cylinder-sector (FOCUS HV CSA), with a compact geometry and a high transmission because of a second order focusing. The analyzer is based on a cylinder sector with 90^o deflection and 300 mm slit-to-slit distance and an entrance lens with 50 mm focal distance [102, 103]. This provides a very compact design of the analyzer so it can be easily integrated into a multipurpose experimental set-up like the present diffractometer. The analyzer is capable to handle kinetic energies both up to 15 keV and down to a few eV with the same analyzer set-up and power supply. Both, SXRD and HAXPES tools can be operated either simultaneously or independently, which offers the opportunity to obtain, on a sample and under identical experimental conditions, electronic, geometrical and chemical information. The UHV chamber includes a home-design sample transfer tool compatible with the experimental set-ups for PLD growth and XPS characterization, so the sample can be transferred between the three equipments in a contamination-free environment.

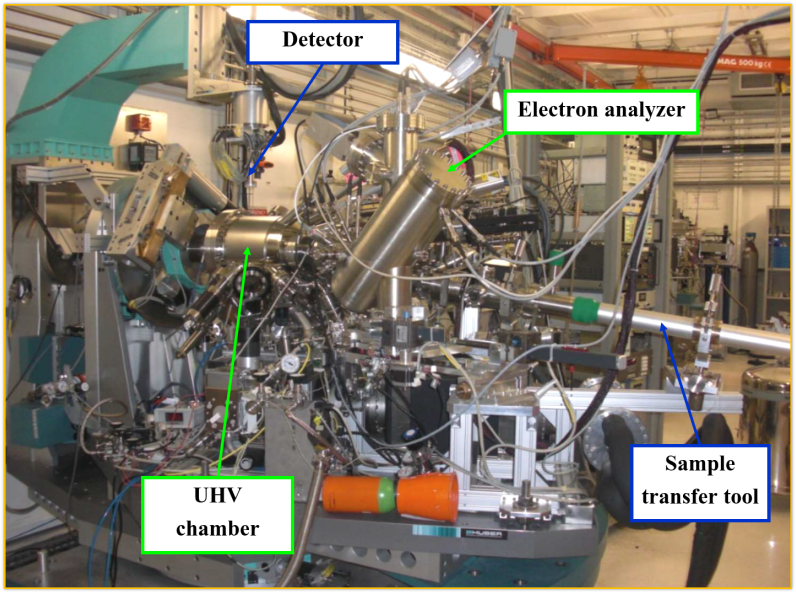

Figure 2.7: Experimental station dedicated to surface x-ray diffraction combined with hard x-ray photoelectron spectroscopy installed in the Spanish CRG BM25-SpLine beamline at the ESRF.

2.6.2 Specular X-Ray Reflectivity (XRR)

X-ray reflectivity (XRR) is used for the determination of different structural and morphological parameters on single films as well as on multilayer structures. The experiments are normally performed at low angle of incidence (θ_i) respect to the sample surface meanwhile the reflected beam is analyzed at the exit angle θ_r. During this thesis only specular XRR analysis was performed, which imply θ_i=θ_r [104]. Figure 2.8 shows a schematic representation of the used geometry, in which the X-rays incide with an angle θ and the reflected beam forms an angle 2θ respect to the transmitted beam.

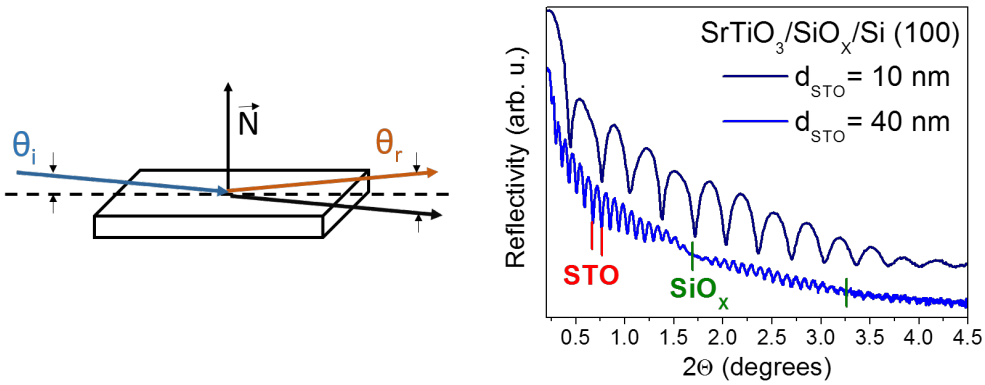

Figure 2.8: (Left) Schematic view of the configuration used for specular XRR measurements. (Right) Experimental XRR profiles recorded on $SrTiO_3$ films deposited on Si with different thicknesses. The appearance of a second group of oscillations indicates the presence of a residual oxide/silicate layer on the $SrTiO_3$/Si interface.

For X-rays the refraction index n of the materials is slightly lower than 1 and can be expressed as:

$$n = 1 - \delta - i\beta \tag{2.9}$$

Where δ is a dispersion coefficient and β an absorption one. The relation between the incidence angle and refraction angle is defined by the Snell-Descartes law:

$$\frac{\sin\theta_i}{\sin\theta_r} = \frac{n_f}{n_i} \tag{2.10}$$

Only when $n_i \sin(\theta_i)/n_f < 1$, x-ray will penetrate inside the material and reflection phenomena will be produced on the top and bottom layer of the film. The minimum incidence angle for which the previous condition is fulfilled is denominated critical angle and is determined by the density of the top layer of the film or heterostructure to be characterized. The constructive and destructive interference between the beam reflected on the surface and the beam reflected on the subsequent

buried interfaces will result on the oscillation of the measured intensity as a function of the incident angle θ_i. The thickness d of the film can be obtained from the reflectivity profile by linearly fitting the position of the minima (maxima) of intensity observed as a function of the minima (maxima) order m using the following expression:

$$\theta_m^2 = \theta_c^2 + \left(\frac{\lambda}{2d}\right) m^2 \tag{2.11}$$

Where θ_m denominates the angles θ_r for which a minima (maxima) of intensity is observed, θ_c is the critical angle, λ the wavelength of the incident radiation, d the film thickness and m the minima (maxima) order, which is defined by an integer number. When fitting the data with equation 2.11 the thickness of the layer can be directly solved from the calculated slope s as:

$$d = \frac{\lambda}{2\sqrt{s}} \tag{2.12}$$

Although the most direct application of this technique is the calculation of film thickness, the strong dependence of the interference phenomena on surface and interface roughness provide additional information. However, the quantification of these parameters requires more complex procedures that were not faced during this thesis. Figure 2.8 shows experimental reflectivities measured on $SrTiO_3$ films deposited on Si with different thickness. In both cases well defined oscillations appeared with different periodicity depending on the film thickness. The amplitude of the oscillations is releated with the density contrast between the substrate and the film. The oscillation amplitude decay with increasing angle is related with surface and interface roughness as well as XRR intensity decay has a strong dependence on surface roughness. High surface and interface roughness will lead to a fast decay of the oscillations or even to its complete extinction. In the presented case (Fig. 2.8), a modulation of the oscillation amplitude is also observed, which indicate the presence of a second periodicity related with the existence of a buried interlayer.

2.6.3 X-Ray Diffraction (XRD)

Diffraction is produced when light is scattered by a periodic arrangement with long range order producing constructive interference at specific angles. In order to produce this interaction, the wavelength of the scattered light must be of the same order of the periodicity of the array. Hence, for the study of the atomic structure x-ray radiation must be used. Due to the importance of this technique a more extended theoretical background is presented. Still, due to its complexity, the complete discussion of the theoretical aspects is left to classical references [105, 106]. Only three aspects are presented briefly due to its importance which are the Bragg law, the Laue formulation and the Edwald sphere. Besides this, the section is more

focused on the practical aspects relevant to understand the measurements and the data analysis presented on the following chapters of this thesis.

2.6.3.1 Theoretical concepts

Bragg law

In 1913, W.L. Bragg presented a simple but convincing model to explain the behavior of diffracted beams. An incident radiation of wavelength λ impinges on a crystal with angle θ and is reflected in a specular way from the crystallographic planes of the crystal separated by a distance d. The reflected beams from each plane will only interact in a constructive way when the path difference between them is an integral number of λ, which is formalized by:

$$2d \sin\theta = n\lambda \tag{2.13}$$

Bragg law is a direct consequence of the periodicity of the lattice and does not take into account any information related with the atomic composition at each point of the lattice, which will determine the relative intensity of the different orders n of diffraction. Bragg law gives a clear statement for constructive interference conditions. However a much deeper analysis is needed in order to analyze the intensity of the scattered waves considering the basis of atoms.

The Laue condition

Figure 2.9 presents a graphical representation of the scattered waves by two continuous points of a lattice separated by the vector $\vec{d}$ after being hitted by and incident radiation of wavelenght λ. The path difference d between waves (1) and (2), remarked in the Figure 2.9 with a red line, can be written by simple trigonometry as:

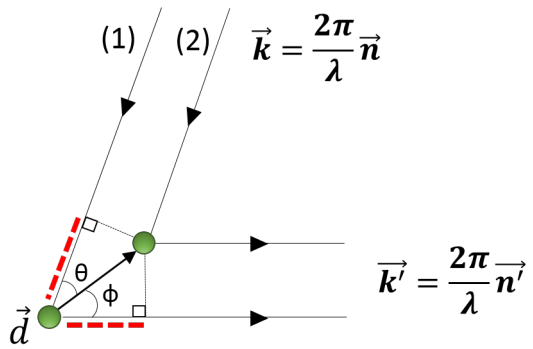

Figure 2.9: Illustration of the path difference (marked in red) between two waves (1) and (2) scattered by two points of the Bravais lattice separated by a vector d.

$$d\cos\theta + d\cos\phi = \vec{d}\left(\vec{n} - \vec{n'}\right) \tag{2.14}$$

Where $\vec{n}$ and $\vec{n'}$ are the unitary vectors defining the direction of the incident and scattered waves. The condition for the constructive interference between the two diffracted beams will be given by:

$$\vec{d}\left(\vec{n} - \vec{n'}\right) = m\lambda \tag{2.15}$$

Being m an integral number. Multiplying both sides of the equation by $2\pi/\lambda$ it is obtained:

$$\vec{d}\left(\vec{k} - \vec{k'}\right) = 2\pi m \tag{2.16}$$

Generalizing this expression to all the positions of a Bravais lattice, defined by the family of vectors $\vec{R} = n_1\vec{a_1} + n_2\vec{a_2} + n_3\vec{a_3}$, the diffraction condition can be expressed as:

$$\vec{R}\left(\vec{k} - \vec{k'}\right) = 2\pi m \tag{2.17}$$

Which can also be expressed as:

$$\exp\left(-i\vec{R}\left(\vec{k} - \vec{k'}\right)\right) = \exp\left(-i\vec{R}\vec{K}\right) = 1 \tag{2.18}$$

Equation 2.18 is the Laue condition, which imply that a constructive interference will occur provided that the change in the wave vector is a vector $\vec{K}$ of the reciprocal lattice of $\vec{R}$. The reciprocal lattice is defined as the Fourier transformation of the Bravais lattice being a fundamental tool for the analytic study of periodic structures. Equations 2.13 for Bragg law and 2.18 for Laue condition are equivalent. However Laue formulation is more practical due to its description of the crystal Bravais lattice instead of using a parametrization based on different families of parallel planes.

The Edwald sphere

The Edwald sphere is a geometrical construction that helps visualizing and understanding the relation between the incident and diffracted wave vector, the diffraction angle and the reciprocal lattice. Figure 2.10 shows a two dimensional representation of the Edwald construction. The sphere is centered in the diffraction origin and its ratio is determined by the wavelength of the incident x-ray beam. The angle formed between the incident vector $\vec{k}$ and the scattered vector fulfilling diffraction conditions is two times the diffraction angle of that given family of planes, in which the periodicity is defined by the modulus of the reciprocal vector $\vec{K}$. There will be diffraction only when the sphere surface intersects with some point of the reciprocal lattice.

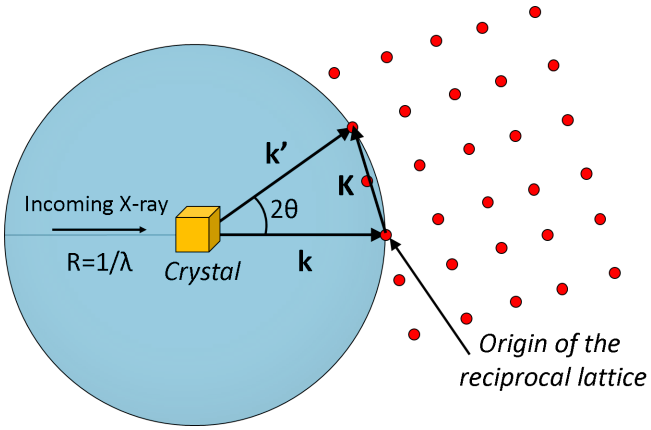

Figure 2.10: Two dimensional representation of the Edwald construction. Diffraction occurs when a point of the reciprocal space intersects with the Edwald sphere

2.6.3.2 Scattered amplitude in a bulk crystal

The intensity scattered by a block crystal with N_1, N_2 and N_3 unit cells along each crystal axis defined by the vectors $\vec{a_1}$, $\vec{a_2}$ and $\vec{a_3}$ can be written as [107, 108]:

$$I(\vec{Q}) = A \cdot \underbrace{\boxed{F^2(\vec{Q})}}_{\text{Structure factor}} \cdot \underbrace{\boxed{S^2_{N_1}(\vec{Q}\cdot\vec{a_1})S^2_{N_2}(\vec{Q}\cdot\vec{a_2})S^3_{N_3}(\vec{Q}\cdot\vec{a_3})}}_{\text{Lattice sum}} \tag{2.19}$$

The expression can be factorized in two terms which are multiplied by a constant. The first term on equation 2.19 is the structure factor F_{hkl}, which is determined by the atomic factor f_j and the positions x_j, y_j, z_j of the j^{th} atom inside the unit cell:

$$F_{hkl} = \sum_{j=1}^{N} f_j \exp\left[-2i\pi(hx_j + ky_j + lz_j)\right] \tag{2.20}$$

where h, k, l are integers and N is the number of atoms within the unit cell. The structure factor describes how the atomic arrangement of the atoms inside of the unit cell influence the intensity of the scattered beam. The Fourier analysis of the unit cell can provide some basic relations for the h,k,l values that define allowed and forbidden reflections. For example, for a body centered cubic lattice, the unit cell is defined by a two atoms basis where the atoms are situated on the (0, 0, 0) and (1/2, 1/2, 1/2) positions. If these two vectors are introduced in equation 2.20, the following expression is obtained

$$F_{hkl} = f(1 + \exp\left(i\pi(h + k + l)\right))$$

which results in non-zero intensity only when the sum of h, k and l is an even number. These restrictions to the diffraction condition are denominated selection

rules. Regarding the second factor, it corresponds with the lattice sum and can be rewritten as:

$$S_{N+j}(\vec{Q}\cdot\vec{a_j}) = \sum_{n=0}^{N_j-1} \exp\left(in\vec{Q}\cdot\vec{a_j}\right) = \frac{\sin^2\left(N_j\vec{Q}\cdot\vec{a_j}/2\right)}{\sin^2\left(\vec{Q}\cdot\vec{a_j}/2\right)} for j = 1,2,3 \qquad (2.21)$$

In the limit of an infinite crystal, equation 2.21 tends to a periodic array of Dirac delta functions in which the intensity is non-zero only when $\vec{Q}\cdot\vec{a_1} = 2\pi h$, $\vec{Q}\cdot\vec{a_2} = 2\pi k$ and $\vec{Q}\cdot\vec{a_3} = 2\pi l$ with h, k, l integers. This is equivalent to say that the intensity is only non-zero when the Laue condition is fulfilled.

2.6.3.3 Diffraction by an ideal surface

Considering an isolated two dimensional (2D) monolayer (N_3=1), the diffracted intensity is then independent of $\vec{q}\cdot\vec{a_3}$ so that in the three dimensional (3D) reciprocal space, the diffraction pattern is found to be a 2D lattice of diffuse scattering rods, in which each rod is discrete in the two directions parallel to the surface and diffuse in the out of plane direction.Taking into account that this monolayer is on top of a semi-infinite crystal, the diffraction pattern will be simply the superposition of the rod pattern of the 2D monolayer and the discrete pattern of the bulk. Nevertheless, the intensity profile of these rods is no longer constant due to the contribution of the other layers of the crystal. The intensity profile can be derived from equation 2.21 provide some considerations. The numerator of the $S_{N_3}(\vec{Q}\cdot\vec{a_3})$ can be approximated by its average value 1/2 for large N values, giving a simpler form for the intensity profile on the out of plane direction:

$$|S(\vec{Q}\cdot\vec{a_3}|^2 = \frac{1}{2\sin^2\left(\vec{Q}\cdot\vec{a_3}/2\right)} \qquad (2.22)$$

Although this approximation is not valid when the Laue condition is fulfilled ($\vec{q}\cdot\vec{a_3} = 2\pi l$), it is a simple demonstration of how the intensity between Bragg points is non zero along the surface normal. These intensity rods are denominated crystal truncation rods (CTR) and are a direct consequence of the presence of a sharp termination on the crystal lattice. The CTR profile shows a strong dependence on the properties of the last atomic layer, showing sensitivity to changes on the occupancy or the structural parameters on surface cells. If the last monolayer does not present the same structure than the bulk, intensity rods will appear but they will not overlap with bulk reciprocal lattice points. This is the case for reconstructed surface where the outer layer of the crystal rearranges and produces a new periodicity.

2.6.3.4 X-Ray diffraction measurements on thin films

A single oriented film can be seen as a single crystal where one of the dimensions is considerably smaller than the other two. The first consequence of this is a critical loss of intensity. Therefore, the use of more intense sources is required to perform an accurate characterization by XRD. The use of synchrotron radiation overcomes the problem of the intensity, providing valuable information as, for instance, phase identification, crystal structure, crystal domain size, orientation respect to the substrate or the presence of strain on the lattice. Due to the wide variety of measurements that can be performed to characterize crystalline thin films only the relevant aspects to the analysis performed during this thesis will be commented. XRD measurements presented on this thesis were all measured on the Branch B of the Spanish CRG BM25-SpLine at the ESRF, using both of the stations described in section 2.6.1.

Lineshape analysis

In the case of a finite size perfect crystal the Laue conditions are relaxed. Consequently, the diffraction spots are no longer Dirac delta functions as shown in section 2.6.3.2, but are extended over a volume on the reciprocal space that is inversely proportional to the size of the crystal. The analysis of the line shape of the experimental diffraction peaks can provide information about the crystallographic domain sizes (D). The value D represents the maximum distance between two atoms scattering in a coherent way. For example, in the $Q_1(= 2\pi h/a_1)$ direction the diffraction peaks will have a finite width Δh $1/N_1$. The domain size D on this plane can be approximated as D=$N_1 a_1$, where N_1 is the number of cells and a_1 the lattice parameter of the crystal in that direction. So D can be related with the peak full width half maximum (FWHM) $\Delta\omega$ by:

$$D = \frac{a_1}{\Delta h} \quad or \quad D = \frac{2\pi}{Q_{\parallel}\Delta\omega} \tag{2.23}$$

The angular width $\Delta\omega$ for a given reflection can be measured by rocking the sample around its surface normal.

Powder diffraction

In order to record powder diffraction patterns on polycrystalline films the incident angle α was fixed and the detector was moved over a wide 2θ range. The configuration geometry is schematized in Figure 2.11 together with an example of a powder pattern recorded in a magnetite powder reference supported by copper tape and measured at different incident angles. Due to the random orientation of the different micro or nanocrystals present in the sample there would always be a contribution for a given family of hkl planes defined by the diffraction angle 2θ. The

dependence of the intensity with the incident angle is a compromise between the increase of the signal because of the larger penetration and the consequent increase of the absorption.

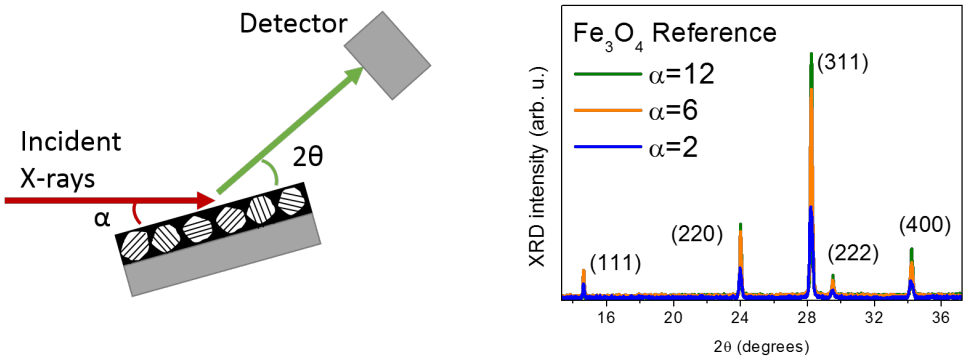

Figure 2.11: (Left) Geometry used for powder diffraction measurements during this thesis. Incident angle α was fixed and the diffraction angle 2θ was scanned by moving the detector. (Right) Example of a powder pattern recorded on a magnetite powder reference at different incident angles (α).

The average size of the different crystals or grains conforming the film or the powder can be calculated from the broadening of the diffraction peaks. The Scherrer equation relates the grain size (GS) with the peak broadening $\Delta(2\theta)$ of the measured peaks as follows:

$$GS = \frac{K\lambda}{\Delta(2\theta)\cos\theta} \tag{2.24}$$

Where K is a dimensionless shape factor that can vary from 0.62 to 2.08. A complete review on the different values of K can be found on [109]. For the calculations performed on this thesis it was considered K=1 as a round up for 0.94, which is the value estimated for spherical crystals with cubic symmetry.

Reciprocal space maps

Reciprocal space maps (RSM) consist on a representation of the diffracted intensity on the reciprocal space. These distributions are recorded by varying the diffraction angle as well as the rotation angle of the sample and recording the diffracted intensity as a function of the momentum transferred. RSMs can provide complete and reliable information about the degree of crystallinity, the epitaxial orientation of the growth film and the distortion or relaxation of the film. Due to the direct visualization of an extended area or volume of the reciprocal space it allows to see effects that might be

covered up on linear scans. On the contrary, the recording of wide RSM can take a considerable amount of time, so an area of interest must be defined before launching this kind of measurements.

2.6.4 Hard X-Ray Photoelectron Spectroscopy (HAXPES)

X-rays are generally classified in soft and hard x-rays depending on the photon energy. The limit between them is not strict but normally x-rays are considered hard when photon energy is above 5 keV. Consequently, in HAXPES emitted photoelectrons present high kinetic energy which is translated in large probing depths respect to conventional XPS described in section 2.3. Quantitatively, meanwhile probe depth are between 5-7 nm for an standard Al source in HAXPES distance from 20 to 30 nm can be reached at 10keV [110]. Photoemission techniques are a powerful technique for the non-destructive characterization of chemical composition and electronic structure. High energy sources provide the opportunity of using XPS for the characterization of bulk samples and buried interfaces. In addition, the possibility of tuning photon energy, which is provided by the use of a synchrotron source, allows to perform compositional or electronic depth profiles. On the contrary, increasing the excitation energy dramatically reduces the photoemission cross section, which is a quantification of the probability of exciting an atom and emitting an electron. Consequently the output signal will be critically reduce, normally by several orders of magnitude, increasing acquisition time and requiring high brilliance synchrotron sources. HAXPES measurements presented on this thesis were performed on the SXRD+HAXPES station on the Branch B of the Spanish CRG BM25-SpLine at the ESRF.

2.6.5 X-Ray Absorption Spectroscopy (XAS)

X-ray absorption spectroscopy (XAS) is a common technique for the characterization of the local geometry and/or the electronic structure of matter. This technique is suitable for a wide variety of scientific cases and can be applied with samples in gas-phase, solution as well as in a solid form.

When x-rays reach a material the intensity of the electromagnetic radiation is reduced due to the interaction of photons with matter through different mechanisms, such as scattering or absorption. When a monochromatic x-ray beam goes through a sample of thickness x, the intensity of the beam is reduced according to the Lamber-Beer law:

$$I(z) = I_0 \exp(-\mu x) \tag{2.25}$$

Where I_0 is the intensity of the incident beam, x is the thickness of the sample and μ is the linear absorption coefficient, which depends on the elemental composition and the density of the sample. In the energy range between the 100 eV and

500 keV, the main interaction process is photoelectron absorption. On this process, when the photon interacts with an electron of the inner shell of the atom, its energy is completely transferred to the electron and this is expelled. The kinetic energy of the emitted electron is equivalent to the incident photon energy minus the energy required to overcome the binding energy of the core level electron.After the photoelectron is expelled from an inner shell of the atom (usually from a K shell) the core hole created is instantly filled by a L- or M- shell electron and the excess energy is liberated as a photon in what is denominated fluorescence emission. Sometimes this released energy can be used to expel a second electron from an outer shell of the atom in what is known as Auger electron emission, which is more likely to occur as the atomic number Z decreases. The two processes are schematized in Figure 2.12

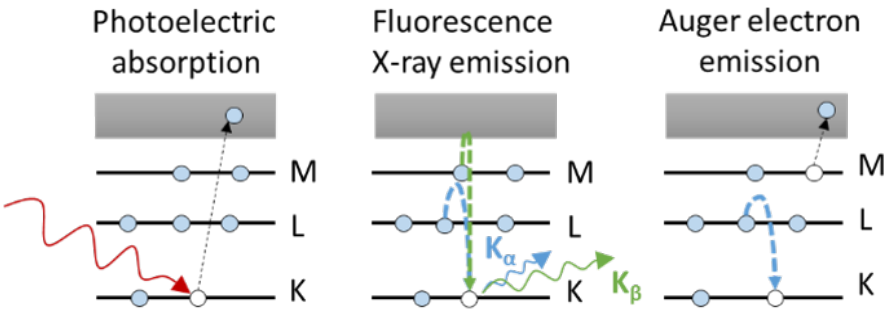

Figure 2.12: Photoelectron absorption, fluorescence emission and Auger electron emission processes derived from x-ray matter interaction. Figure adapted from reference [111].

At certain energies, due to the discrete character of electronic levels, the absorption increases critically giving rise to an absorption edge. Such edge corresponds with the binding energies of electrons in the K, L, M shells of the absorbing elements. The energy position of the edge is very sensible to the oxidation state of the materials and gives useful information about the electronic structure. There exists two main regions of interest in the XAS spectra which can provide complementary information:

- *X-ray absorption near edge structrure (XANES):* This region is normally defined from 10 eV before the edge to 50 eV above it. In this range, the energy of the incident photons is on the order of the binding energy of the absorbed atom, so the kinetic energy of the excited electrons is not large enough to expell them to a continuum state. Instead, excited electrons are promoted to unoccupied states on non-bound levels with energies close to the Fermi level. Because of the high probability of such transitions narrow and intense peaks are observed on this region. The study of the XANES region provide information about the electronic structure and it is highly sensitive to oxidation state and geometry.

- *Extended x-ray absorption fine structure (EXAFS):* This region goes from 50 eV up to 1000 eV above the edge. In this region, the kinetic energy of the electrons is high enough to be expelled out of the material in the form of photoelectrons, therefore all the electronic information is lost. This region shows soft oscillations of the absorption coefficient due to scattering processes of the photoelectrons with neighbor atoms. The study of those oscillations provides information about the radial distribution of the electron density around the absorbing atom. The analysis of EXAFS is used for the quantitative determination of bond length and coordination numbers.

During this thesis, XAS measurements were performed in two different facilities. Measurements on the Fe K-edge and on Ti K-edge were performed in the Branch A of the Spanish CRG-BM25 Spline, described in section 2.6.1. Complementary soft x-ray measurements were performed in collaboration with the Physikalisch -Technische Bundesanstalt (PTB) in Berlin (Germany), using the multipurpose ultra-high vacuum instrument developed by the PTB for x-ray reflectometry and spectroscopy-related techniques and installed at the PGM beamline in BESSY II [112]. The analysis of the data has been performed using the Demeter software package [113].

2.7 Scanning Electron Microscopy (SEM)

Scanning electron microscopy (SEM) uses a focused electron beam of high energy electrons to generate different signals at the sample surface derived from electron-matter interaction. Some of the main processes produced are resumed in Figure 2.13. The incident electrons are generated by a thermal emission source, generally a heated tungsten filament, and subsequently accelerated and focused by a series of electromagnetic lenses. The energy of the primary electrons can range from as low as 100 eV up to as high as 30 keV depending on the objectives of the measurement. SEM is commonly based on the analysis of secondary electrons (SE) and backscattered electrons (BSE) contributions. SE are most valuable to obtain morphological and topological information and BSE is most valuable for illustrating contrasts in composition in multiphase samples. SEM microscopes also include an x-ray detector in order to analyze characteristic x-ray emitted, which gives information about the atomic composition of the sample (EDX). The most common SEM imaging mode consists on collecting low energy (<50eV) secondary electrons generated as ionization products of the interaction of the atoms of the sample with the electron beam. The output signal is collected with a scintillator-photomultiplier system and the amplified electrical output is displayed as a two dimensional intensity distribution that can be converted and treated digitally. The brightness of the signal will depend on the number of secondary electrons reaching the detector. On this mode, lateral image resolution down to 0.5 nm can be achieved.

During this thesis, SEM measurements were performed in order to characterize

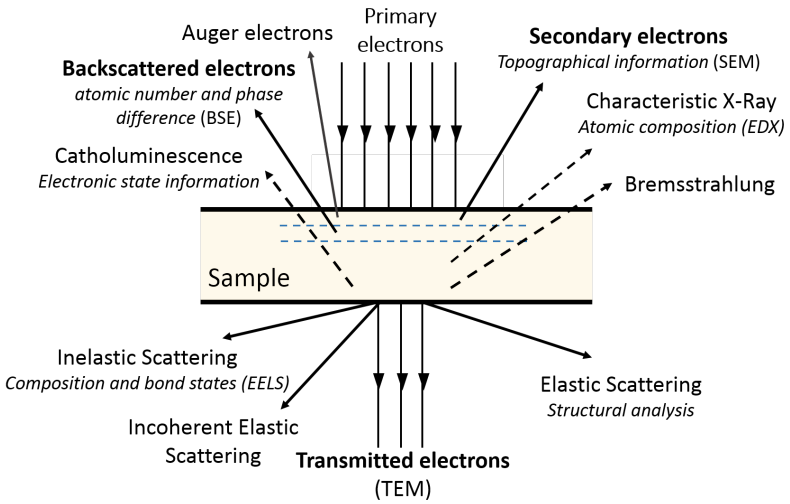

Figure 2.13: Processes derived from electron-matter interactions.

morphology surface of magnetite thin films. The characterization of $Fe_3O_4/SiO_2/Si$ heterostructures was performed in the Centro Nacional del Microscopía electrónica (CNME-ICTS) in Madrid (Spain) using a JSM-6400 scanning electron microscope. Contrary, the characterization of $Fe_3O_4/SrTiO_3/Si$ heterostructures was performed in collaboration with the Universitat de Barcelona, using a SEM microscope belonging to the facilities of the Centres Cientificis i Tecnologics of the UB (CCiTUB). No preparation of the samples was required for image acquisition due to their conductive character.

2.8 Transmission Electron Microscopy (TEM)

Transmission electron microscope (TEM) uses a high energy electron beam to illuminate the sample and to obtain an image from the signal transmitted through the sample. TEM is used to obtain morphological, compositional and crystallographic information and can be applied in diverse scientific cases. The generation of the primary beam is identical to that of SEM microscopes but in this case the transmitted beam is collected. This is done by means of a fluorescent screen which can be coupled to a CCD camera for recording. At lower magnifications, TEM image contrast is mainly due to the different absorption of electrons depending on the changes in the composition, density or thickness of the specimen. At higher magnifications more complex interactions modify the intensity of the output signal and a deeper analysis is requested to extract information. In order to obtain a TEM image, electrons need to be able to go through the specimen, which can limit the depth of information that can be obtained. Therefore, in some cases samples need to be prepared prior to the

measurement. For electron energies of 300 keV a penetration depth of ≈100 nm is reached.

During this thesis, cross section TEM images were obtained using two different facilities. Images were acquired in the Centro Nacional del Microscopía electrónica (CNME-ICTS) in Madrid (Spain) using a JEM 3000F TEM microscope. This microscope uses an accelerate voltage of 300 keV and has an image resolution of 0.17 nm in TEM mode. A XEDS detector is also coupled to the microscope for analytical characterization. High resolution measurements were also performed in collaboration with the Universitat de Barcelona (UB). In this case a JEOL-2010F microscope belonging to the Centres Cientifics i Tecnologics of the UB (CCiTUB) was used. All the TEM images included in the present thesis were recorded using cross sections of the samples. The cross sections were cut from the sample using a diamond saw and then polished using diamond powder paper with a decreasing grain size as the section was thinned. In order to reach electron transparency the sample was treated using a Precision Ion Polishing System (PIPS).

2.9 Atomic Force Microscopy (AFM)

Atomic force microscopy (AFM) is a powerful technique that allows to obtain information about surface morphology with a resolution of the order of fractions of nanometers. The information is gathered by scanning the sample with a tip and measuring the interaction between this tip and the sample. The tip is attached to the free end of a mobile cantilever. The forces resultant from the interaction between the sample and the tip will cause the bending of the cantilever and this movement is recorded using a laser beam and a photodiode detector. The laser beam is pointed to the end of the cantilever and reflected. The oscillation of the tip modify the reflected beam and this changes are recorded by the photodiode. AFM microscope can work in different modes: contact mode, noncontact mode or tapping mode.

Topography information is obtained from the changes in the height of the tip on contact mode. Additional useful information can be collected through phase measurements in non-contact or tapping mode. Changes in the phase signal of the oscillating cantilever are recorded on the photodiode simultaneously with topographic information. In heterogeneous samples, phase contrast allow to distinguish the different local compositions present. AFM images were obtained using the Nanotec Atomic Force Microscope installed in the Instituto de Cerámica y Vidrio (ICV-CSIC) in Madrid (Spain). The microscope was operated in air environment using a noncontact mode and the resulting images were analyzed using the WSXM software [114]

2.10 Raman spectroscopy

Raman spectroscopy is a non-destructive technique used to observe vibrational, rotational and other low frequency modes in a system. The technique was named so after the physicist C. V. Raman, who first observed the effect on liquids [115]. When a molecule interacts with photons, in most of the cases those photons are elastically scattered, keeping the same energy (Rayleigh scattering). Still, there is a part of the photons that interact with molecular vibrations, phonons or other excitations in the system, resulting in a shift of the energy of the photon respect to the source energy. If the material absorbs energy and the emitted photon has a lower energy than the absorbed photon it is named Stokes Raman scattering. If otherwise the material losses energy and the emitted photon has a higher energy it is called anti-Stokes Raman scattering. These three processes are schematized in Figure 2.14

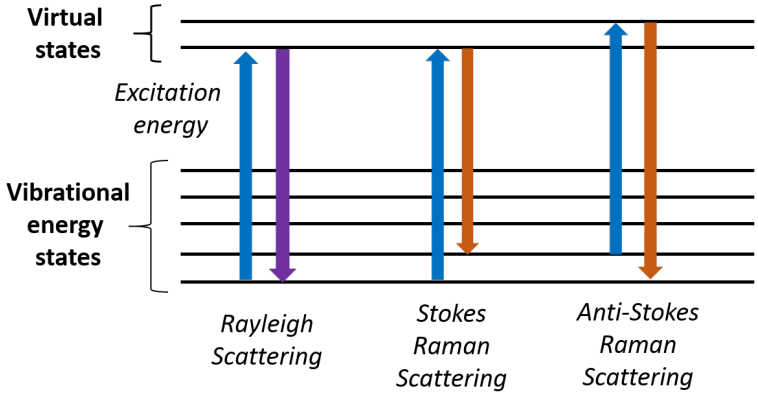

Figure 2.14: Light scattering processes involved in Raman spectroscopy.

There are three parameters that characterize the Raman spectra: band position, intensity and bandwidth [116]. The band position depends directly on the mass and position of the atoms, the interatomic forces and the bond length. Consequently, any modification of these parameters, as for example strain or stresses of the lattice, will influence the frequency of the bands. Band intensity is in general proportional to the amount of material. However, the presence of defects in the lattice lead to a loss of intensity due to the breaking of the atomic bonds and changes in the atomic force. The presence of structural disorder produces a decrease of the photon life-time increasing the bandwidth. Besides, it has been observed in nanocrystalline Si a relation between the average grain shape and the bandshape and position which was related to phonon confinement models [117] and density of defects [118]. Raman measurements presented in the current thesis were recorded in the Instituto de Cerámica y Vidrio (ICV-CSIC) in Madrid (Spain). The experimental set-up consists on a confocal Raman microscope Witec ALPHA 300RA with a Nd:YAG laser

light source (532 nm) in p-polarization. The optical resolution of the microscope is 200 and 500 nm approximately in the lateral and vertical directions respectively while the spectral resolution of the system is 0.02 cm^{-1} under optimal measurement conditions. The Raman measurements where performed with a numerical aperture (NA) of 0.95 and a laser output power of 0.5 mW.

2.11 Surface Magneto-Optical Kerr Effect (MOKE)

Surface magneto-optical Kerr effect is produced when light is reflected in a magnetic material and the magnetization of the material induces a rotation of the light polarization. The study of this effect allows to characterize different phenomena as magnetic ordering, magnetic anisotropies or exchange coupling in multilayer systems. Different configurations are possible depending on the relative orientation of the magnetic field respect to the sample surface and the dispersion plane. These configurations are shown in Figure 2.15.

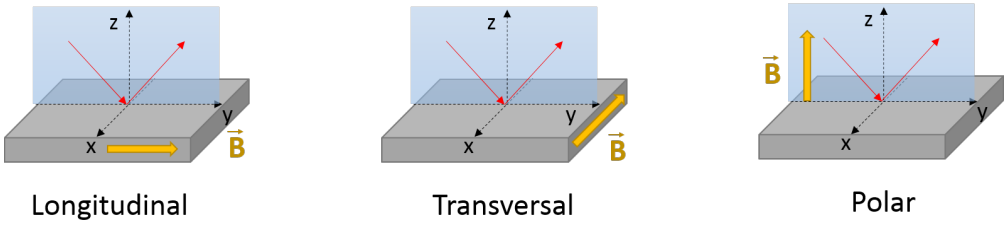

Figure 2.15: Different configurations for S-MOKE measurements depending on the orientation of the applied magnetic field respect to the dispersion plane.

MOKE measurements presented in this thesis were performed in a home-designed set-up localized at the Spanish CRG BM25-SpLine beamline support laboratory. Figure 2.16 shows a picture of the experimental set-up used. The light source is a red laser (670 nm) and magnetic fields up to 2500 Oe can be applied. The incident light is linearly polarized and modulated by a photoelastic modulator (PEM). The refraction index of the crystal in the PEM is changed by tuning the applied voltage modifying consequently the polarization of the incident signal. A small portion of the incident light is deviated to a photodiode situated after the PEM in order to quantify the intensity of the input signal and correct the effect of the laser drift on the output signal. After being reflected on the magnetized sample surface the signal is filtered by an analyzer, detected on a second photodiode and extracted in a lock-in amplifier. The output signal is composed by a continuous contribution and an alternate signal. The lock-in amplifier allows to separate and amplify each signal independently. The continuous background is eliminated to avoid the saturation of the detector. Hysteresis loops are recorded by changing the applied magnetic field

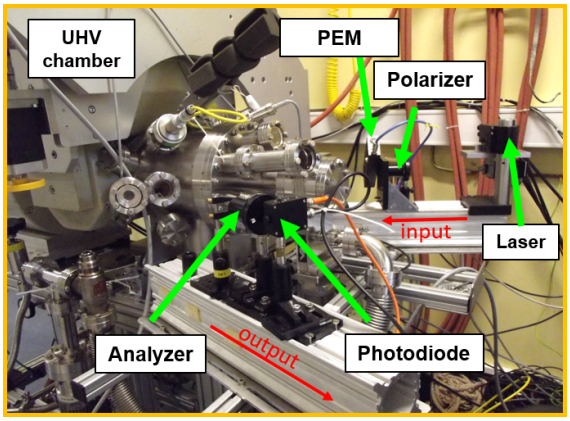

Figure 2.16: Home-designed experimental set-up used for S-MOKE characterization installed in the Spanish CRG BM25-SpLine beamline support laboratory.

and analyzing the phase and intensity of the reflected beam.

2.12 Transport measurements

Electrical transport measurements were performed using a CF-V cryostat from Oxford instruments that allow to measure in a range temperature from 3 to 500 K. Figure 2.17 shows a picture of the experimental set-up localized on the Spanish CRG BM25-SpLine beamline support laboratory at the ESRF. The set-up also counts with a voltage source and an amperimeter to measure the current on the sample at a given voltage so the resistance on the sample can be determined. During this thesis resistance versus temperature curves were measured using a two-points probe method.

Figure 2.17: Experimental set-up used for electrical transport measurements situated at the Spanish CRG BM25-SpLine beamline support laboratory in the ESRF.

Chapter 3

Materials used during this thesis

3.1 Introduction

In this chapter, the materials used for the preparation of half metallic thin films and silicon-based heterostructures during this thesis are presented. Other aspects important for the development of the main work of the thesis are also specified, as for instance the references used for the characterization of the samples studied or the technical aspects related with the preparation of the substrates before the evaporation.

3.2 Silicon

3.2.1 General overview

Silicon is a key material in nowadays technology and an out-standing candidate for the development of new spin-based technology. Spin transport and coherent spin precession has been observed for undoped Si at low temperatures over remarkably large distances of 350 μm [119], making it specially suitable for semiconductor spintronic applications [88, 120]. These very favorable results are based on the intrinsic properties of the semiconductor. On the first place, it presents a reduced spin-orbit interaction due to its low atomic number (Z=14). Second, the spatial inversion symmetry of the diamond lattice avoids the spin-splitting of the conduction band which leads to spin relaxation as described by DÝakanov-Perel [121]. Last, due to the absence of nuclear spin on its most abundant isotope (^{28}Si) the spin-nuclear (hyperfine) coupling is weak. This interaction might cause spin relaxation and dephasing if electrons are confined over a certain region with many nuclear spins (^{29}Si centers). Although the beneficial properties of silicon, spin injection measurements have been delayed due to the impossibility of studying spin propagation on silicon by standard optical methods because of its indirect gap. First demonstration of electrical

injection, transport and detection of spin polarized currents on silicon was reported by Appelbaum *et al.* in 2007. They injected spin polarized hot electrons into the conduction band of undoped Si at 85 K [23]. Later that year Jonker *et al.* reported diffusive injection using a Fe/Al_2O_3 contact at 10 K [42]. Spin measurements at room temperature were reported two years later in heavily doped silicon using $Ni_{80}Fe_{20}/Al_2O_3$ contacts, obtaining an electron spin polarization of 4.6% and spin lifetimes greater than 140 ps in n-type Si [24]. These results were later reproduced also increasing the temperature up to 500 K [68], confirming the suitability of silicon based heterostructures for the development of spintronic devices.

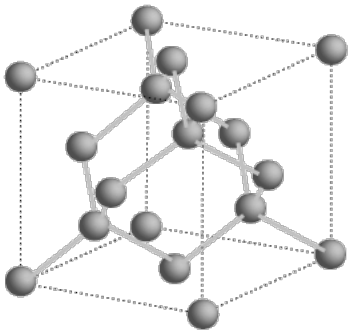

Figure 3.1: Silicon crystallographic structure. Extracted from reference [105]

Bulk silicon presents a diamond structure, which can be interpreted as a face centered cubic lattice with a basis containing two identical atoms in the (0,0,0) and (1/4,1/4,1/4) so that it can be represented as two interpenetrating fcc lattices [105]. The conventional cubic cell is shown in Figure 3.1 and for silicon it presents a 0.543 nm lattice parameter. Each atom is covalently bounded to the four nearest neighbors, drawing the vertices of a regular tetrahedron.

Due to the exposition to air a thin layer of oxide is naturally formed on silicon surface, which is known to present high stability. In normal conditions, this native oxide layer is amorphous, mainly composed of SiO_2 an presents a thickness between 1-2 nm [122]. The controlled growth of silicon native oxide has been an important tool for the fabrication of integrated devices and consequently it has been an important topic of research [123–126]. Its importance as gate oxide was motivated by its good insulating properties, its high stability and the presence of a flat SiO_2/Si interface. These same features make it an outstanding candidate for tunnel barrier on spin injection devices. Nevertheless, despite these advantageous properties, due to its amophous character silicon native oxide must be completely eliminated for the deposition of epitaxial films on silicon. Atomically clean Si(100) surfaces have been routinely obtained by flashing the substrates at 1250°C under UHV conditions [127]. However, in the fabrication of nanoscale device such a high temperature can modify the dopant profile and hence modify the semiconducting properties of Si. There-

fore, alternative low temperature methods as chemical etching have been preferred. Etching in a diluted HF solution has been reported to produce well-ordered and oxide-free Si(100) surfaces [128]. Nevertheless, further annealing need to be performed in order to eliminate carbon and oxygen contamination produced during the chemical treatment. Ion sputtering has also been reported as an alternative to high temperature annealing [129]. Still, studies about the effect of ion bombardment on the structural properties of silicon proved ion implantation and amorphization of the sample surface [130].

3.2.2 Elimination of silicon native oxide on Si(100) by thermal procedures

The aggressive character of cleaning procedures involving annealing at high temperature can result on a poor surface quality in terms of high roughness and inhomogeneity, limiting the quality of the epitaxial films subsequently evaporated. Besides, clean silicon surfaces are prompt to reoxidize quickly, so the clean substrates must be kept in a contamination free environment. The consequences of thermal cleaning procedures on silicon surface were experimentally evaluated during this thesis. In order to do so, Si(100) substrates were annealed under UHV conditions progressively increasing the temperature from 750ºC to 1150ºC, which was the maximum stated by the experimental set-up. The substrates were *in situ* characterized by XPS and LEED at different temperatures. XPS measurements were used to characterize the amount of silicon dioxide and carbon contaminants present at the surface by measuring the Si2p and C1s core levels meanwhile LEED patterns provided information about the surface quality regarding short range structural properties.

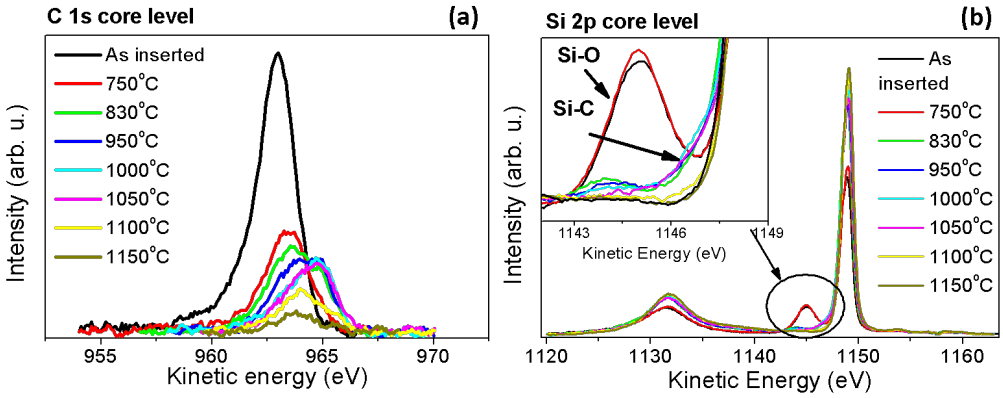

Figure 3.2: Evolution of the C1s (a) and Si 2p (b) core level spectra with annealing temperature. It can be seen how the oxide signal is reduced meanwhile the elemental Si signal becomes more intense

Figure 3.2 shows the evolution of the C1s (Left) and Si2p (Right) core level spectra with annealing temperature. The most intense contribution observed on the Si 2p core level spectra correspond to Si-Si bounds and is characterized by a small spin-orbit energy splitting of only 0.67 eV, which make both peaks look as a single contribution under the energy resolution used during this experiment. In the spectrum of the as inserted sample a second contribution was observed with a binding energy shift ΔE of +4.1 eV which is related to the presence of the SiO_2 native oxide layer. A third peak, considerably wider, is observed at higher binding energy corresponding to a plasmon loss. As the temperature is increased over 830°C the silicon oxide signal is drastically decreased. Nevertheless, a strong asymmetry occurs on the Si2p peak related with the appearance of silicon carbides [127]. The elimination of these species required increasing the temperature up to 1100°C, which significantly reduced the intensity of this contribution on the XPS spectra.

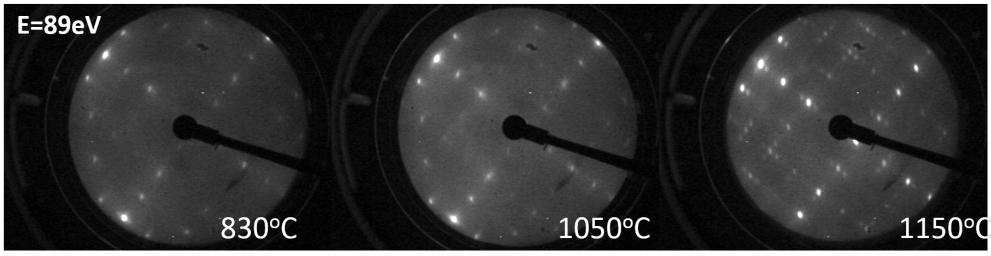

Figure 3.3: Evolution of the LEED pattern of the Si(100) surface at different temperatures during annealing under UHV conditions

LEED patterns recorded during the annealing at different temperature are shown in Figure 3.3. As inserted substrates did not show any LEED pattern due to the amorphous character of the silicon native oxide. Only after annealing at 830°C, when most of the oxide had been eliminated, the LEED pattern appeared showing a (1x1) structure. The achievement of a clean Si(001) surface is characterized by the event of a (2x1) reconstruction due to the formation of Si dimers [131,132]. However, after increasing the temperature up to 1150°C the pattern kept a (1x1) structure with a progressive increase of intensity. This can be related with the presence of remaining traces of silicon carbides. Moreover, after annealing at 1150°C the LEED pattern showed the multiplicity of the diffraction spots on the (1x1) structure which indicates the formation of multiple domains and probably a high mosaicism of the Si crystal, which can significantly limit the quality of the deposited films in terms of large crystal domain sizes. Such an effect could be caused by heating under not well enough UHV conditions. Heating at high temperatures under UHV conditions better than 1×10^{-9} mbar is mandatory, otherwise traces of SiC will remain at the Si surface preventing from perfect cleaning.

3.2.3 Elimination of silicon native oxide on Si(100) by SrO-deoxidation

As it was proved, cleaning procedures which required high temperature can result on the damage of the substrate surface. Therefore, alternative methods are desirable in order to prepare high quality epitaxial films. The elimination of silicon native oxide using Sr o SrO as catalyst is one of the most effective procedures for the passivation of silicon surface. Strontium is an alkaline earth metal with a strong reductant power on Si. This means that the formation of Sr-silicide, Sr-silicides or SrO is more favorable than the formation of SiO_x compounds [133]. Moreover, Sr or SrO deposited on the silicon surface is able to transform the SiO_2 native oxide on SiO, which can be evaporated at 650°C, avoiding annealing at temperatures over 1000°C as it was required to eliminate the highly stable SiO_2 native oxide. Wei *et al.* described the removal of native oxide by Sr containing species by the following catalytic reaction [134],

$$SiO_2 + Sr(orSrO) \longrightarrow SiO(g) + O + Sr(orSrO) \tag{3.1}$$

although there are small variations on the process depending on the authors. During this thesis metallic strontium was used to eliminate native oxide and passivate Si surface prior to evaporation. In order to do so, untreated Si(100) substrates were loaded in the UHV chamber and characterized by RHEED showing a weak (1x1) pattern. The substrate was heated up to 400°C and then exactly two monolayers (ML) of Sr were evaporated by MBE under UHV conditions. The substrate with the two Sr monolayers was heated up to 800°C keeping a heating rate of 60°C/min. At this point the deposited Sr layer uptook oxygen from silicon native oxide and crystallizes as SrO revealing a (2x1) reconstruction on the RHEED pattern. For the successful finalization of the procedure the (2x1) reconstruction must be kept when the sample cools down to room temperature (RT). Sometimes when cooling the (2x1) reconstruction is transformed in a (3x2) reconstruction which means that the temperature was not enough during the de-oxidation [135]. After the process a remaining SrO buffer layer is present avoiding further oxidation of the silicon surface. This buffer layer is particularly suitable for the deposition of epitaxial $SrTiO_3$ films due to the structural compatibility between both materials. Consequently, nowadays this method is almost systematically adopted for the evaporation of $SrTiO_3$ films on Si by MBE [136, 137] and more recently also by PLD [135, 138].

3.3 Magnetite (Fe_3O_4)

3.3.1 General overview

The prediction of half metallic behavior by early local density approximation (LDA) calculations made magnetite especially attractive for its integration on spintronics devices [139, 140]. At ambient conditions, Fe_3O_4 presents a cubic F3dm

inverse spinel AB_2O_4 structure with a lattice parameter of 0.8396 nm. The crystallographic structure is presented in Figure 3.4(a). Oxygen atoms form a slightly distorted fcc lattice where iron cations are inserted. Fe^{+3} cations occupy tetrahedral coordinated A sites meanwhile Fe^{+3} and Fe^{+2} cations in a 1:1 ratio occupied the 16 inequivalent octahedral B sites, with an alternate order in the (100) planes. Theoretical studies foresaw a band gap of around 0.4 eV for the spin-up band gap and a partially filled metallic spin-down conduction band [139]. Figure 3.4(b) shows an schematic diagram of the total electron density of states (DOS) for spin up and spin down in bulk magnetite with cubic Fd3m symmetry, showing that there exists only minority spin electrons at the Fermi level. Due to crystal field splitting, the d levels of the Fe ions on the octahedral positions are split into three degenerate t_{2g} levels and two degenerate e_g levels. For both Fe^{+2} and Fe^{+3} ions the majority spin band is located below the Fermi level and is occupied by five spin-up electrons. The extra electrons of the Fe^{+2} ions occupies the t_{2g} level of the minority spin band, which is the only subband located at the Fermi level, resulting in a 100% spin polarization [141]. In practice, although the real half metallic character of magnetite has been discussed by some authors [142, 143] and defended by others [144–146], high spin polarization values up to -80 % have been experimentally measured by spin resolved ARPES on Fe_3O_4 films at room temperature [144]. Since the appearance of a half-metallic behavior in magnetite is related with the crystal field it presents a strong dependence on the structural properties of the samples.

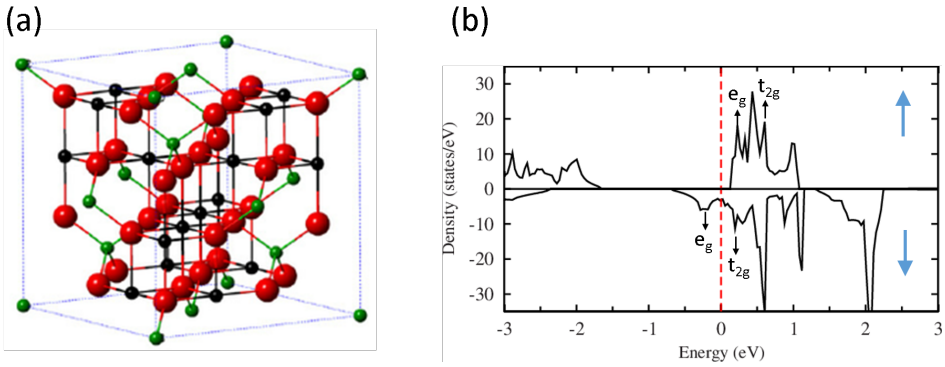

Figure 3.4: (a) Crystallographic structure of magnetite. Red spheres represent oxygen atoms meanwhile green and black spheres represent Fe^{+3} and Fe^{+2} cations respectively. Image extracted from reference [147]. (b) Spin resolved DOS calculated from DFT calculations for bulk magnetite with a Fd3m symmetry. Figure adapted from reference [148]

At room temperature, magnetite is a poor metal with an electronic conductivity of 4mΩcm and presents ferrimagnetic properties up to 858 K [149]. From its discovery, one of the most studied particularities of magnetite is the Verwey transition [150]. This is a first order transition where the system undergoes a structural

transformation from a cubic Fd3m symmetry to a monoclinic Cc unit cell for temperatures below 120 K, which is accompanied by a significant increase of the resistivity. The origin of this transition has been widely discussed over the years [139,151]. Verwey attributed the transition to the arrangement of Fe^{2+} cations on the B sub-lattice but different charge ordering models have been proposed since then. Nowadays, the accepted explanation is that the transition is triggered by electron-phonon coupling in the presence of strong electron correlations [152, 153].

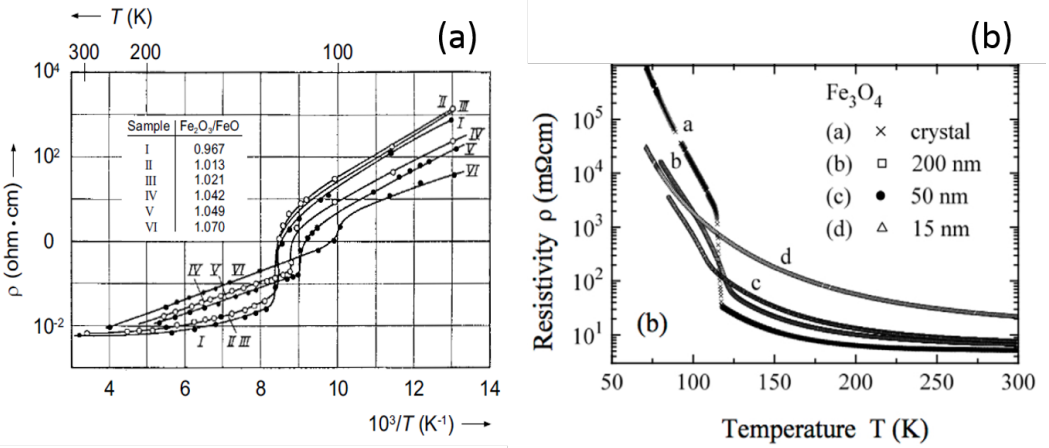

Figure 3.5: (a) Modification of the resistivity (ρ) *vs* temperature (T) curves on magnetite with increasing proportion of Fe^{+3} cations. The Verwey transition occurs at lower temperature when increasing Fe^{+3}/Fe^{+2} ratio (reproduced from reference [154]). (b) Evolution of the ρ *vs* T curves with magnetite thickness. Decreasing Fe_3O_4 thickness results on a smoother Verwey transition in contrast with the sharp transition proved in bulk crystals (extracted from reference [155]).

As an example of the influence of structural properties on this phenomenon, two studies on magnetite resistivity under different conditions are reproduced in Figure 3.5. Figure 3.5(a) shows measured resistivity as a function of the temperature on magnetite samples where the Fe^{+3}/Fe^{+2} ratio has been modified by inducing the presence of octahedral vacancies [154]. It can be seen how the excess of Fe^{+3} cations induced a displacement of the Verwey transition to lower temperatures. Figure 3.5(b) shows equivalent measurements in stoichiometric samples with different thickness. When reducing the film thickness the most remarkable effect is a broadening of the Verwey transition and also a displacement to lower temperatures. This effect has been related with a decrease of the electrical conductivity due to the formation of anti phase boundaries (APBs) and with an inhibition of long range order because of the formation of small domains [156].

3.3.2 Identification of iron oxide phases

The iron-oxygen system presents three stable phases, all based on a closed packed O^{-2} anion lattice where the Fe cations occupy the interstice sites in between. Those phases are FeO (Wustite), Fe_3O_4 (Magnetite) and α-Fe_2O_3 (Hematite). There exists a fourth phase, γ-Fe_2O_3 (Maghemite), which is a metastable phase respect to hematite (α-Fe_2O_3) but exists partly because the conversion between FeO, Fe_3O_4 and γ-Fe_2O_3 only requires a rearrangement of the iron ions within the common fcc oxygen lattice. Under the most reductive conditions Wustite is formed, meanwhile under oxidative conditions hematite is synthesized. The different iron oxides show different structural and magnetic properties, some of them resumed in Table 3.1. A fundamental aspect of the work presented in this thesis is the achievement of single phase Fe_3O_4 films in order to obtain highly spin polarized sources. Consequently, it is important to know which techniques and strategies will allow an accurate identification of the iron oxide phases present in Fe_yO_x samples.

Mineral	**Wustite**	**Magnetite**	**Maghemite**	**Hematite**
Formula	$Fe_{1-x}O$	Fe_3O_4	γ-Fe_2O_3	α-Fe_2O_3
Cation	Fe^{+2}	Fe^{+2}/Fe^{+3}	Fe^{+3}	Fe^{+3}
Crystallographic system	Cubic	Cubic	Cubic/ Tetragonal	Hexagonal
Space group	Fm3m	Fd3m	$P4_332$	R3c
Lattice parameter (nm)	a=0.4302-0.4275	a=0.8396	a=0.83474	a=0.50436/ c=1.37489
Magnetism	Antiferro-	Ferri-	Ferri-	Weak ferro/ anti-
T_C (°C)	203-211	850	820-986	956

Table 3.1: Structural parameters and properties of the different iron oxides. Adapted from reference [149]

Generally XRD allows to elucidate between iron oxides because of their different structural parameters, although high resolution XRD is required to differentiate between maghemite and hematite because of its similarity. However, the use of XRD requires the availability of crystalline samples. The use of complementary techniques as XPS and XAS provides a powerful method for the characterization of Fe_yO_x samples even if they present amorphous phases. Figure 3.6 shows the characteristics lineshapes for the Fe1s core level spectra as well for the Fe2p core level recorded at a photon energy of 13.5 keV and 12 keV respectively on FeO, Fe_3O_4 and γ-Fe_2O_3 standards. Each oxidation state for the iron cation is characterized by a different binding energy and by the presence of different satellites with well-defined positions

respect to the main peak, which are resumed in table 3.2. By the identification of these satellites the characterization of single phase iron oxide films by XPS and HAXPES is possible. In the case of heterogeneous samples, the identification of the different phases present and the quantification of the proportion in which each one is present can be carried out by curve fitting or factor analysis with the adequate references [157, 158].

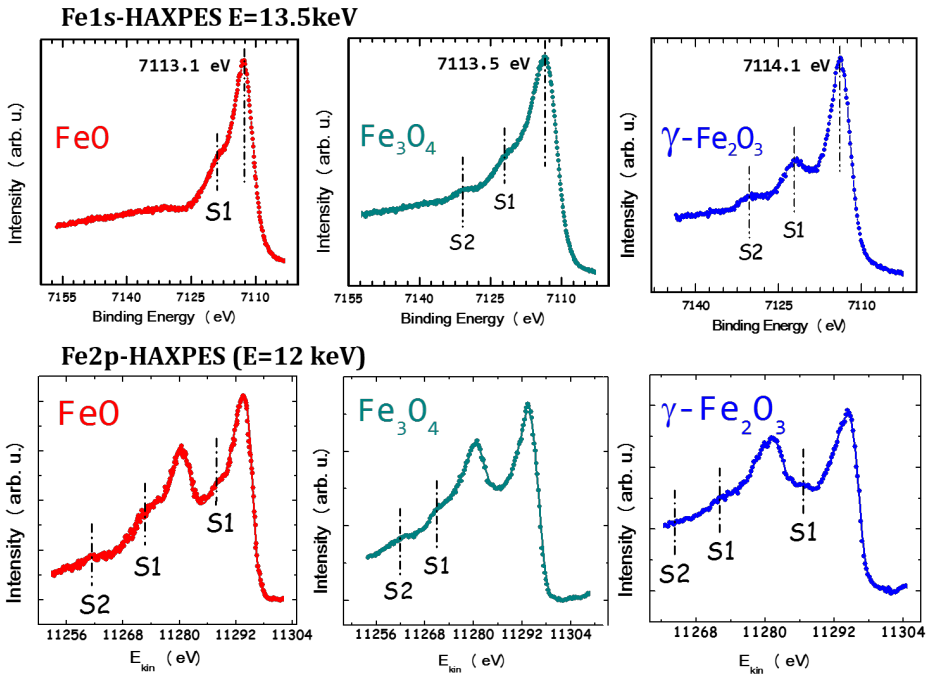

Figure 3.6: HAXPES spectra recorded on iron oxide references on the Fe1s and Fe2p core levels. The spectra show the presence of specific satellites for each iron cation

Phase	**FeO**			**Fe_3O_4**			**γ-Fe_2O_3**		
Core-level	E_B	ΔS1	ΔS2	E_B	ΔS1	ΔS2	E_B	ΔS1	ΔS2
Fe 1s	7113.1	5.9	-	7113.5	8.7	17.2	7114.1	7.6	15.7
Fe $2p_{3/2}$	710.0	5.8	-	710.6	-	-	710.5	7.6	-
Fe $2p_{1/2}$	723.6	7.2	-	724.2	9.6	19.9	724.1	8.9	17.0

Table 3.2: XPS peaks and satellite positions for FeO, Fe_3O_4 and γ-Fe_2O_3 bulk references

Standard photoelectron spectroscopy measurements provide useful information about elemental composition and oxidation state with high resolution, low acquisition times and high surface sensitivity. The complementary use of high energetic sources

as synchrotron radiation allows to perform this characterization with bulk sensitivity. Besides, the energy tunability allows to obtain information with depth resolution. Complementary XAS measurements make possible to distinguish between hematite and maghemite phases which is not possible by XPS. Figure 3.7 shows the x-ray absorption spectra measured on the Fe-K edge for different iron oxide references (fig.3.7.a) and the calibration line for the oxidation state of iron respect to the absorption edge energy (fig.3.7.b). The position of the edge is directly related with the oxidation state and through this calibration function, the oxidation state of iron on unknown samples can be identified from the position of the edge and be related with the presence of mixed phases.

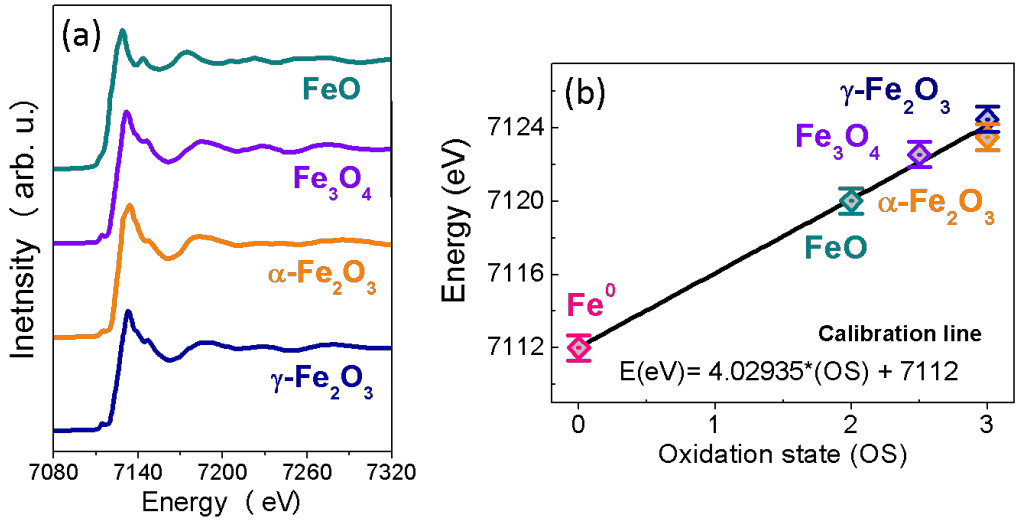

Figure 3.7: (a) XAS spectra measured on the Fe K-edge for different oxide standards. (b) Calibration line for the oxidation states of Fe as a function of the edge energy.

The characterization by XAS of Fe_yO_x samples can allow the identification of the oxidation state by analysis of the XANES region and of the phases present in heterogeneous samples by comparison with the available references. Once the phase or phases are identified, further analysis of the EXAFS region can provide deeper information about the structural properties of the sample.

3.4 Strontium titanate ($SrTiO_3$)

3.4.1 General overview

Crystalline $SrTiO_3$ has been widely used as substrate for epitaxial growth of complex oxides due to its interesting optical and insulator properties. Moreover, its

atomic structure and lattice parameters are compatible with a large number of functional materials as $LaAlO_3$ or $BaTiO_3$. The quality and characteristics of the grown films depends strongly on the initial quality of the $SrTiO_3$ surface. For instance, a two-dimensional electron gas (2DEG) with high carrier density on $LaAlO_3/SrTiO_3$ interface has been recently reported [159, 160]. Although the nature of this 2DEG is not completely understood, recent works attribute this effect to charge discontinuity at the $SrTiO_3$ surface produced by the presence of oxygen vacancies or to morphological and/or structural modifications [161, 162]. Some of these phenomena have also been used to explain the formation of a layer with metallic behavior on naked $SrTiO_3$ surface [163, 164].

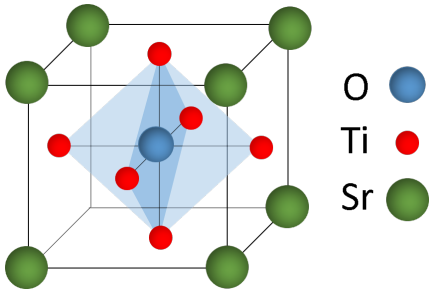

Figure 3.8: Strontium titanate crystallographic structure

Bulk $SrTiO_3$ presents a ABO_3 perovskite structure with a lattice parameter of 0.3905 nm which is represented in Figure 3.8. The Ti^{4+} ions are six-fold coordinated by O^{2-} ions, whereas each of the Sr^{2+} ions is surrounded by four TiO_6 octahedra so that it is coordinated by 12 O^{2-} ions. Within the TiO_6 octahedra the O^{2-}p states hybridate with the Ti^{3-}d states, generating a pronounced covalent bonding. On the contrary, Sr^{2+} and O^{2-} ions exhibit ionic bonding character and hence, $SrTiO_3$ has mixed ionic-covalent compound properties. This nature of chemical bonding leads to a unique structure, which makes it a model electronic material. In the (100) facet, the $SrTiO_3$ structure can present a TiO_2 or a SrO-terminated surface. In general, mechanically polished substrates show an alternation of SrO and TiO_2 planes. However, a TiO_2 termination is usually preferred in order to increase surface reactivity and consequently chemical procedures have been generally performed for the selective removal of the SrO layer [165–168]. Nevertheless, recent studies proved the strong impact of these treatments on the structural properties of the $SrTiO_3$ surface [169].

3.4.2 Oxygen defects in $SrTiO_3$

The presence of oxygen defects in the $SrTiO_3$ surface can induce a metallic behavior, completely modifying the good insulating properties of the material. Due to

the importance of preserving the insulator character of $SrTiO_3$ films for its use as a tunnel barrier, the conditions for the formation of oxygen vacancies were studied during this thesis. Bulk $SrTiO_3$ samples were characterized under different annealing conditions in order to analyze the effect of thermal treatment on them, especially regarding the formation of oxygen vacancies and the apparition of Ti or Sr-rich phases. The characterization performed here was intended to be used as a reference for the characterization of the tunnel barriers based on $SrTiO_3$ ultra-thin films. The experiment was carried out by annealing $SrTiO_3(100)$ substrates under UHV conditions at different temperatures in a range from 250 to 1150°C and performing XPS, XRD and LEED *in situ* characterization at each step.

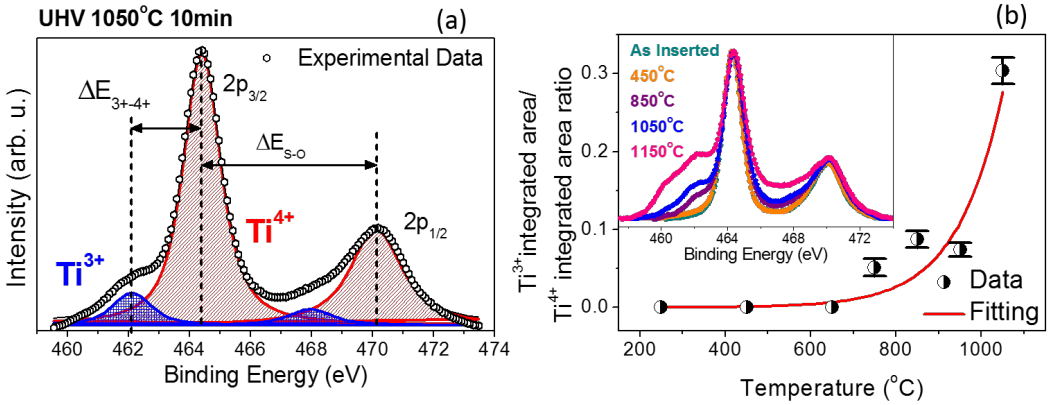

Figure 3.9: (a) XPS Ti2p core level spectra recorded in a $SrTiO_3$ samples annealed at 1050°C in UHV. The presence of oxygen defects is proved by the presence of a second doublet with an energy displacement $\Delta E_{3^+-4^+}$ of 2.14 eV. (b) Evolution of the Ti^{+3}/Ti_{+4} intensity ratio with annealing temperature in UHV conditions. These values are calculated by the deconvolution of the Ti2p spectra.

Figure 3.9(a) shows the XPS Ti2p core level spectrum recorded on a $SrTiO_3$ substrate after annealing at 1050°C under UHV conditions. Ti2p core level is characterized by an spin orbit splitting ΔE_{S-O} of 5.8 eV. The appearance of oxygen defects was characterized by the presence of a second doublet with an energy shift of $\Delta E_{3^+-4^+}$=2.14 eV due to the creation of Ti^{3+} centers. The amount of oxygen defects was calculated from the relative intensity between the doublets corresponding to Ti^{4+} and Ti^{3+} cations. Figure 3.9(b) shows the evolution of the ratio between the number of Ti^{3+} and Ti^{4+} centers with annealing temperature. Oxygen defects started to appear after annealing at 750°C showing a small percentage of 5 %. The increment of Ti^{3+} centers with annealing temperature was well described by an exponential trend reaching values up to 30 % at 1050°C. The formation of oxygen defects was avoided by introducing a partial oxygen pressure of 1×10^{-5} mbar during the annealing even at temperatures as high as 1150°C.

3.5 Iron Silicide (Fe_3Si)

3.5.1 General overview

Fe_3Si is an intermetallic compound with ferromagnetic properties and a high Curie temperature of 840 K. Besides, due to its Heusler alloy structure it is also predicted to be half metallic which increase its interest for the development of spin injection devices and semiconductor spintronics applications [72]. In its bulk form, Fe_3Si presents a DO_3 structure with a lattice parameter of 0.565 nm. The crystal lattice can be described as four interpenetrating fcc lattices with basis positions A(0, 0, 0), B(1/4, 1/4, 1/4), C(1/2, 1/2, 1/2) and D(3/3, 3/3, 3/3), where iron atoms occupy A, B and C positions while D positions are covered by Si atoms. This structure can also be considered as the simplest Heusler alloy Fe_2FeSi where there exist two crystallographic and magnetic iron sites [170].

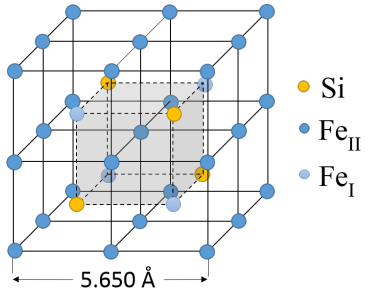

Figure 3.10: Crystallographic structure of Fe_3Si.

The interesting properties of this material have motivated great efforts on experiments focused on the growth of high quality Fe_3Si layers during this thesis, continuing the work carried out by other authors [171–174].

3.5.2 Identification of iron silicides phases

Figure 3.11 shows the accepted phase diagram for binary Fe-Si compounds. In this phase diagram there exist five equilibrium stoichiometric silicide phases: $FeSi_2$, Fe_5Si_3, ϵ-FeSi, β-$FeSi_2$ and α-$FeSi_2$. Fe_3Si is contained inside the phase α_1 which, based on Figure 3.11, occurs for a wide compositional range. Nevertheless, later works pointed to Fe_3Si as a stoichiometric compound, in disagreement with the previous results [175]. In any case, the complexity of the phase diagram can make the synthesis of single phase films a complex issue. The obtaining of single phase stoichiometric Fe_3Si fims is fundamental for the development of spin injection devices in order to preserve the desired half-metallic and ferromagnetic properties. Among the other stable phases, Fe_5Si_3 also shows ferromagnetic properties but its Curie temperature is much lower (T_C=380 K). On the contrary, β-$FeSi_2$ and ϵ-FeSi are

both semiconductors. Therefore, the controlled growth of single phase films and their correct characterization is fundamental for the successful application of Fe_3Si on semiconductor spintronics.

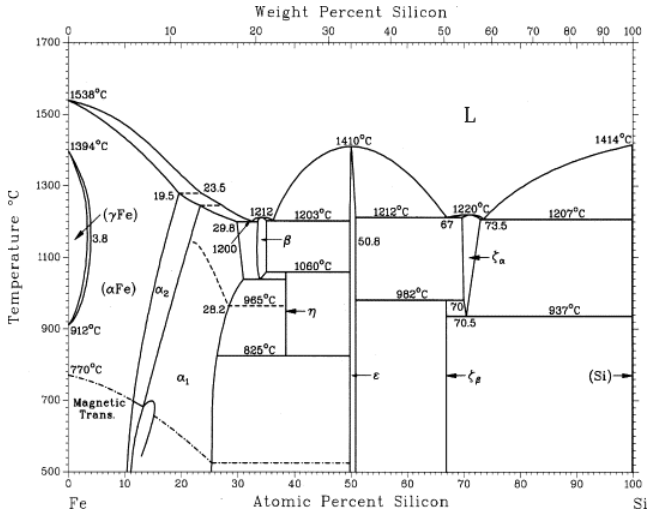

Figure 3.11: Binary Fe-Si phase diagram. Extracted from reference [176]

The crystallographic structure is one of the distinctive properties that can be used for the identification of Fe-Si compounds. Table 3.3 shows structural parameters for Fe, ϵ-FeSi, β-$FeSi_2$ and Fe_3Si. It can be seen that iron silicides present significantly different characteristics in terms of lattice parameter and symmetry of the lattice. Consequently, the structural parameters can be used to distinguish between different iron silicides phases on crystalline samples.

Formula	**Fe**	**ϵ-FeSi**	**β-$FeSi_2$**	**Fe_3Si**
Crystallographic system	Cubic	Cubic	Orthorhombic	Cubic
Space group	lm-3m	$P2_13$	Cmca	Fm3m
Lattice parameter (nm)	a=0.2866	a=0.4488	a=0.9865,b=0.7791,c=0.7833	a=0.565

Table 3.3: Structural parameters of the different iron silicides. Adapted from reference [149]

XRD is hence a powerful tool to determine the crystallographic growth of Fe_3Si films and also identify possible structural modifications respect to bulk parameters. Additionally, X-ray absorption spectroscopy measurements allow to disregard the presence of non-stoichiometric amorphous phases. By complementing the two techniques, the presence of unexpected silicides phases, which can have critical con-

sequences for transport properties, can be fully dismissed. XAS as well as XRD measurements were performed for ϵ-FeSi, β-$FeSi_2$ and Fe_3Si single crystal reference samples during this thesis. These spectra were recorded in order to have reliable standards for the characterization of the iron silicides films synthesized during this thesis. The study was especially motivated by the lack of references available on the consulted bibliography. XAS spectra recorded on the Fe K-edge is shown in Figure 3.12(a) with a close up of the XANES region in fig. 3.12(b).

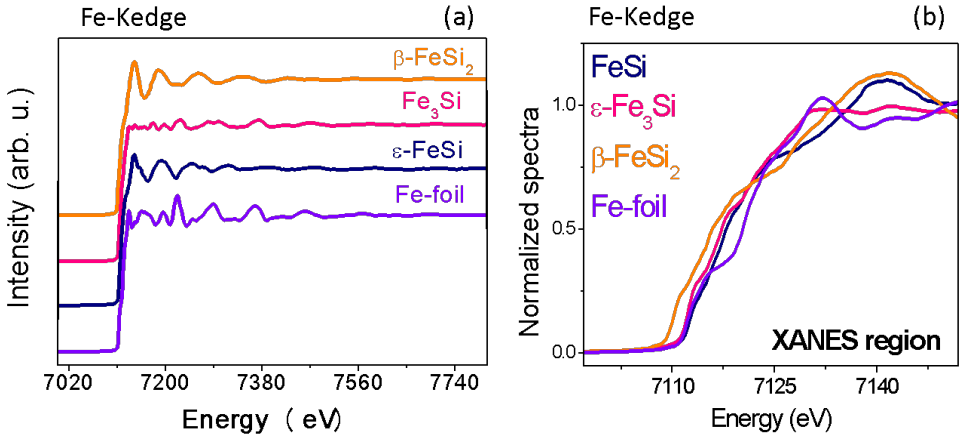

Figure 3.12: XAS spectra measured on the Fe K-edge for $FeSi_3$, ϵ-FeSi and $\beta FeSi_2$ single crystal references (a) and XANES region (b). Although the position of the edge does not vary for the different silicides, the XANES region shows clearly distinguishable aspects between the different phases.

XANES spectra showed considerably different lineshapes for each phase, proving to be an efficient tool for the identification of iron silicide phases. Despite this, the Fe K-edge has been used for the characterization of Fe-Si phase in a single study concerning the implantation of Fe ions on Si surface [177]. The Fe $L_{2,3}$ edge is more frequenty used as it provided information about the relation between the magnetic and structural properties of the films [178, 179].

Chapter 4

Fe_3O_4 based heterostructures

4.1 Introduction

The successful integration of magnetite in semiconductor spintronics requires the development of new strategies for the preparation of high quality magnetite films on the most commonly used semiconductors, as for example GaAs, Ge, or Si. It is especially attractive the implementation of this technology on silicon due to its optimal properties in terms of spin lifetimes and coherent transport. However, the preparation of magnetite epitaxial films on silicon can be hampered by the presence of an amorphous native oxide layer on the silicon surface formed due to exposition to air. Combined thermal and chemical procedures are systematically adopted in order to eliminate this oxide layer (see Section 3.2). However, cleaning methods include the use of aggressive acids as HF and exposure to high temperature. This might lead into poor silicon surfaces in terms of roughness and structural defects. As a consequence, the quality of the deposited films will also be restricted.

Some attempts have been made on the direct evaporation of magnetite on clean silicon surfaces with different results [180–183]. The formation of iron silicides due to the reaction of Fe with the Si surface has been observed even at room temperature, with the diffusion of silicon in the films at long distances from the interface [184]. The formation of uncertain silicides interfaces has also been observed during the evaporation of other metals as Co or Ni at room temperature, pointing out the high reactivity of clean silicon surfaces [185]. Studies involving the annealing of Fe films deposited on silicon substrates showed that the first nucleated phases are Fe_3Si and FeSi in a temperature range between 400°C-500°C and β-FeSi for temperatures above 600°C [186, 187]. Moreover, the catalytic action of metal atoms on the oxidation of silicon surface is well known [188–190]. Castro *et al.* observed, in agreement with other works, an enhanced oxygen uptake on Co-Si systems respect to clean Si surface. They concluded that the oxidation proceed via sticking of metal sites and bonding to Si. The formation of a 15 Å oxidized layer prevented the oxygen transfer

to the bulk, passivizing the system [188]. Soukiassian *et al.* arrived to a similar conclusion in alkali metal-silicon interfaces. The difference was that in this case the formation of silicides was not observed and the catalytic agent could be easily eliminated through further annealing [189]. In the particular case of Si/Fe interfaces, it has been observed how after annealing Si/Fe+Fe_yO_x systems in UHV conditions, oxygen was transferred from Fe to Si for T $\geq$ 330 ^{o}C resulting in the formation of SiO_2 clusters. Further annealing resulted on the migration of these clusters to areas near to the surface and formation $FeSi_2$ sicilide [191].

The formation of silicide/oxide interfaces can have critical consequences for the magnetic and transport properties of the films deposited on silicon. For instance, Boothman observed the formation of different Schottky barriers in magnetite films deposited directly on Si (111) and Si (100), with the consequent modification on the transport properties through the Fe_3O_4/Si interface depending on the substrate orientation [181]. In a different work, Jain *et al.* observed the presence of two different switching fields in magnetite films directly evaporated on Si. These results were in agreement with a previous work by Parker *et al.* [180, 192].These anomalies have been attributed to the formation of mixed layers at the Fe_3O_4/Si interface but no more details were given about them. This lack of knowledge about the properties of the interface hinders the understanding of the changes in the expected behavior of the magnetite films.

The non-reproducibility of the results on directly evaporated films brought to the general conclusion that a buffer layer was necessary in order to avoid the interaction between silicon and iron and passivize the silicon surface during the evaporation of magnetite. Different materials have been explored for this approach. Polycrystalline Fe_3O_4 films have been evaporated using Ti, Ta, SiO_2 or Fe_2O_3 buffer layers [193,194]. A strong influence of the buffer layer has been observed on the conductivity of magnetite films, especially below the Verwey temperature [193]. MgO has been suggested as an ideal candidate for the epitaxial growth of magnetite films due to their near perfect lattice match [195]. However, inter-diffusion effects have been observed in Fe_3O_4/MgO bi-layers for temperatures in a range between 250 ^{o}C - 300 ^{o}C [196]. Epitaxial films have also been reported using a TiN buffer layer [197, 198], but still the presence of an intermixing layer of around 2 nm was observed at the TiN/Fe_3O_4 interface due to the Ti diffusion into the Fe_3O_4 film [197].

Although the introduction of a buffer layer was intended to reduced the interaction between silicon and magnetite, the ideal system in terms of interface quality have not been achieved yet. During this thesis, two different approaches have been considered for the integration of magnetite films on silicon using an insulator buffer layer. On a first approach, which is presented in Section 4.2, magnetite films were directly evaporated on silicon keeping the SiO_2 native oxide layer to avoid the interaction of iron with the silicon surface. In a second attempt, described in Section 4.3, epitaxial $SrTiO_3$ ultra-thin films were grown on silicon as a seed for the epitaxial growth of magnetite films. The insulator buffer is intended to have a double function.

First, to passivize silicon surface during the evaporation, favoring the stabilization of magnetite and avoiding the formation of uncertain silicides interfaces. Second, the insulator layer is envisaged as a tunnel barrier in the design of spin injection devices based on the prepared heterostructures. The function of the tunnel barrier is to improve the efficiency of the spin polarized transport through the Fe_3O_4/Si interface. For this purpose, the insulator layer needs to fulfill certain requirements as the presence of flat interfaces, a high degree of homogeneity and the absence of mixed phases (silicides and/or silicates) at the interface. The characteristics of the synthesized heterostructures will be evaluated considering these criteria. General conclusions about the results will be presented in Section 4.4, discussing the advantage and disadvantage of each method regarding the quality of the magnetite films and the characteristics of the tunnel barrier.

4.2 $Fe_3O_4/SiO_2/Si$ heterostructures

4.2.1 Introduction

Silicon dioxide SiO_2 has been an appealing material for the semiconductor industry from an early time because of its good insulator properties. It presents high dielectric strength and a relatively wide band gap. Besides, its high thermal stability at temperatures up to 1600 ^oC avoids its degradation during manufacturing, which is highly desirable for industrial applications. Moreover, the SiO_2/Si interface presents a low degree of defects, approaching to the requirements of an ideal interface. The main inconvenience when using silicon native oxide is the impossibility of controlling its thickness below a certain value. Consequently, big efforts have been made in the development of new growing techniques for the preparation of ultra thin silicon oxide layers, trying to reproduce an equivalent or even better quality. Nowadays, technology allows to grow ultra-thin high quality SiO_2 films, either in a local way or covering wide surfaces, with similar properties to those of native oxide [199].

For the present thesis, silicon oxide was considered an optimal material for the integration of magnetite films on silicon through a tunnel contact. Its good insulator properties and the wide band offset between SiO_2 and silicon fulfill some of the indispensable requirements in order to achieve an efficient spin injection. Moreover, the presence of the silicon native oxide is expected to completely stabilize the silicon surface during magnetite evaporation, avoiding the formation of silicides at the interfaces. Although the thermal growth of silicon dioxide is well established in the industry for the fabrication of silicon-based devices, it requires the use of specific equipment which is not always present in a standard laboratory. On the other hand, silicon native oxide presents equivalently good properties in terms of morphology and homogeneity and hence was considered an equally suitable tunnel barrier. Besides, the stabilization of magnetite films using a silicon native oxide buffer would provide a non-expensive and reproducible method for the integration of this material

in silicon.

In the last 20 years, the interest of the system for the fabrication of spintronics devices have motivated several attempts in the preparation of $Fe_3O_4/SiO_2/Si$ heterostructures with diverse results. Balashev and Vikulov independently reported on the growth of polycrystalline Fe_3O_4 films with a strong texture in the 311-orientation, more remarked with increasing synthesis temperature [200,201]. However, the epitaxial growth of the films was impeded by the amorphous character of the SiO_2 layer regardless of the growth technique chosen. Considering the transport properties of the final $Fe_3O_4/SiO_2/Si$ heterostructures diverse behviors have been observed. In 2007, a work published by Qu *et al.* reported an enhanced GMR effect on $Fe_3O_4/SiO_2/Si$ heterostructures at 120 K, reaching values as high as 87 % under a bias voltage of 2 V and an applied field of 7 T [202]. The high MR value reported consolidated the interest of the system for its application in spintronics. Two years later, Wang *et al.* reported on a low field magnetoresistance in $Fe_3O_4/SiO_2/Si$ heterostructures, with a maximum value of 1.9 % at 230 K under an applied field of 0.05 T. In 2012, Zhang *et al.* [203] observed a tunnel magnetoresistance of 2% at 120 K under an applied field of 7 T and a small bias of 0.3 V, which was in accordance with previous observations in other p-n heterojunctions [204, 205] and in disagreement with the work published by Qu *et al.*. Zhang attributed the inconsistence between the results to the different prove methods used. Nevertheless, this incompatibility reinforces the necessity of further research on the system, including a deeper characterization of the structural and morphological properties of the system, paying special attention to interface properties.

During this thesis, the preparation of $Fe_3O_4/SiO_2/Si$ heterostructures was carried out by direct evaporation of magnetite films by PLD on untreated Si(100) substrates, keeping the silicon native oxide as a tunnel barrier. The details about the preparation and characterization of the heterostructures will be discussed during this section. In order to have an accurate characterization of the Fe_3O_4/SiO_2-Si interface and understand the evolution of the native oxide during magnetite evaporation, an *in situ* study of the first stages of evaporation was performed, which will be described in Section 4.2.2. The aspects related with the deposition of the Fe_3O_4 films by PLD will be addressed in Section 4.2.3. Section 4.2.4 will be focused on the characterization of the deposited magnetite films and the final $Fe_3O_4/SiO_2/Si$ heterostructures. The conclusions extracted from this part of the work will be resumed in Section 4.2.5.

4.2.2 *In situ* study of the first stages of evaporation

Considering the complex interaction between metal atoms and silicon, an *in situ* study was performed during the evaporation of magnetite on silicon in order to understand the effect of the Fe-Si interaction on the silicon dioxide properties. The experiment was carried out by performing angular-resolved XPS measurements at different iron oxide thickness in order to determine the phase of the deposited Fe_yO_x

film, the amount deposited and the composition of the Fe_yO_x/SiO_2-Si interface. The evaporation of metallic compounds on silicon can lead to a catalytic oxidation of silicon or even to the formation of iron silicates. The objective of monitoring the first stages of evaporation is to understand the interaction between the SiO_2 layer and the evaporated Fe_yO_x film, disclosing which factors can modify the characteristics of the native oxide layer or impede the formation of a stable Fe_3O_4 phase. Iron oxide deposition was carried out in the UHV chamber described in section 2.3.1. A MBE evaporator with an iron rod source was used and the substrate temperature was kept at 500ºC. An oxygen partial pressure of 4.7×10^{-6} mbar over a base pressure of 10^{-9} mbar was introduced on the chamber in order to oxidize iron. These conditions were chosen to be equivalent to those used for the preparation of the final Fe_3O_4 /SiO_2/ Si heterostructures by PLD.

4.2.2.1 Calculation of the Fe_yO_x evaporation rate

The evaporation rate for the Fe_yO_x films was calculated from the evolution of the XPS intensity. In order to do so, Fe2p and Si2p core level spectra were subsequently recorded after evaporating during different times. Assuming the formation of a flat Fe_yO_x layer, the increasing of the iron XPS intensity with increasing film thickness can be described using equation 2.6 (see section 2.3.3), which for this particular case can be rewritten as:

$$I_{Fe2p} = I^0_{Fe2p}(1 - \exp(-d_{FeO_x}/\cos(\theta)\lambda_{Fe}(E_{Fe2p}))) \tag{4.1}$$

Where I^0_{Fe2p} would be the XPS intensity corresponding to a bulk Fe_yO_x reference, d is the deposited layer thickness and λ is the ineslastic mean free path (IMFP) of the emitted photoelectrons. In a similar way, the attenuation of the silicon XPS intensity by the deposited iron oxide layer can be described applying equation 2.7 (see section 2.3.3), which given a thickness d can be written as:

$$I_{Si2s} = I^0_{Si2s}(\exp(-d_{FeO_x}/\cos(\theta)\lambda_{Fe}(E_{Si2s}))) \tag{4.2}$$

The layer thickness d, can be expressed as a function of the evaporation rate so d=Bt where B is the evaporation rate in nm/min. Substituting this expression on equations 4.1 and 4.2 and fitting the XPS intensity as a function of deposition time, the evaporation rate B can be calculated. Evolution of the XPS integrated intensity for the Fe2p and Si2s core levels are plotted as a function of the evaporation time in Figures 4.1(a) and 4.1(b) respectively. The integrated intensity for the Fe2p core level was calculated considering the sum of all Fe_yO_x contributions as well as the Si2p core level intensity comprehend elemental and oxidized silicon. I^0_{Fe2p} and I^0_{Si2s} values were kept as free parameters during the fitting. Three different fitting curves are represented for each set of data in Figure 4.1. In order to evaluate the congruence of the result obtained, the Fe2p and Si2s data was fitted independently (red line)

and then the evaporation rate obtained was used to fit the complementary data. In other words, the result obtained from the Si2s intensity was used to fit the Fe2p data and vice versa (blue line). Finally, an average value was calculated and used to fit both groups of data (green line), observing a good description of the experimental results. The growth rate and the fitting parameters obtained for each set of data are resumed in Table 4.1. The average value of 0.025 ± 0.003 nm/min was used subsequently to calculate the layer thickness of the deposited films.

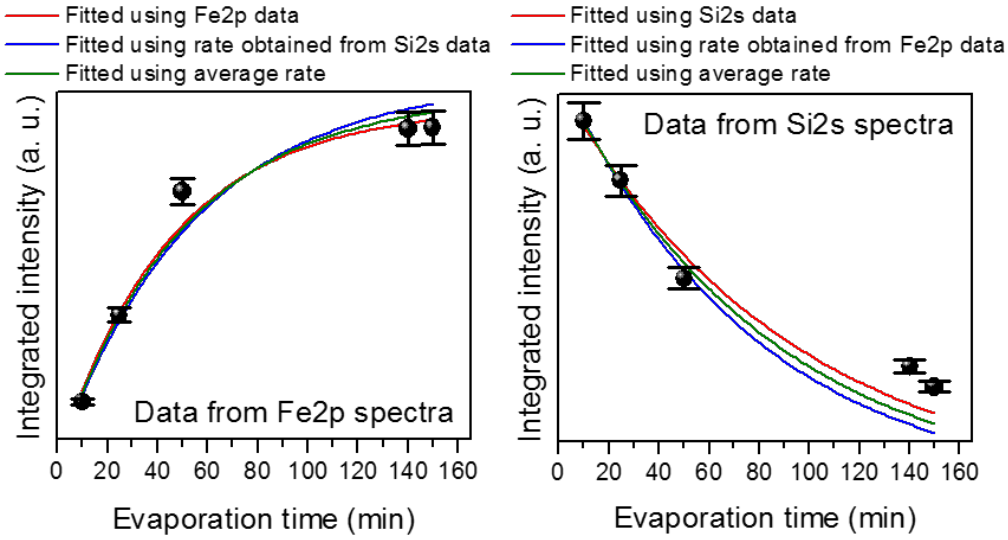

Figure 4.1: XPS integrated intensity as a function of evaporation time for Fe2p(a) and Si2s(b) core levels integrated intensity during the different stages of the evaporation. The values represented include the sum of all Fe_yO_x contributions inside the Fe2p spectra as well as Si and SiO_2 contributions are both considered to calculate the Si2s core level XPS intensity. Data was fitted using equations 4.1 and 4.2.

Core-level	Equation	I^0	B (nm/min)	λ(Å)	R-square
Si2s	$I_{Si2s}=I_{bulk}(\exp(-Bt/\lambda)$	61700±2400	0.023±0.003	21.37	0.96
Fe2p	$I_{Fe2p}=I_{bulk}(1\text{-}\exp(-Bt/\lambda)$	430000±30000	0.028±0.004	12.62	0.98

Table 4.1: Fitting parameters and results corresponding to the fitting curves showed in Figure 4.1. An average value of 0.025 ± 0.003 nm/min was finally considered for the calculation of the layer thickness.

4.2.2.2 Calculation of the SiO_x thickness

One of the aims of this experiment was to determine if the evaporation of magnetite induces modifications on the properties of the silicon native oxide layer. One of the expected changes was an increase of the SiO_2 thickness during the evaporation. The untreated Si(100) substrates were characterized before the deposition in order to determine the starting characteristics of the native oxide. Figure 4.2(a) shows XRR measurements performed on untreated Si(100) substrates using a photon energy of 12 keV. The presence of intensity modulations proved the smoothness the SiO_2/Si interface and the thickness of the SiO_2 layer was calculated by fitting the position of the minima using equation 2.11 (inset). The initial silicon native oxide thickness was determined to be 2.2 ± 0.2 nm for the studied substrate.

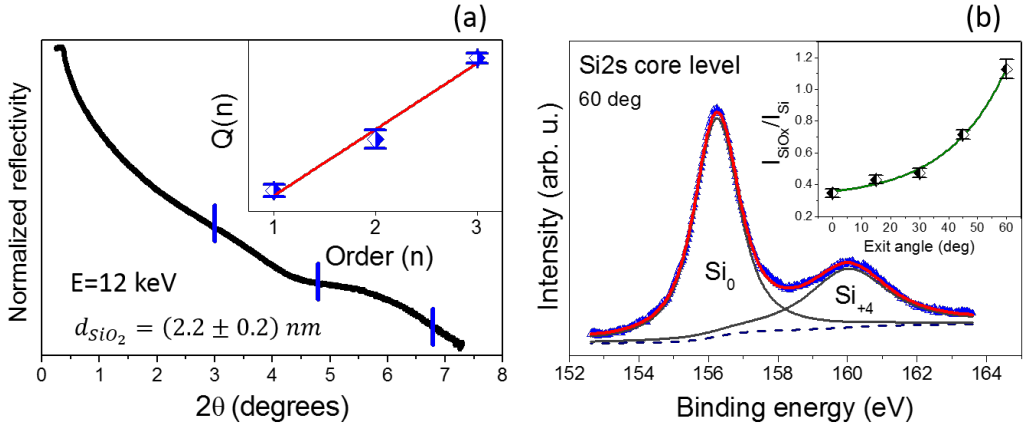

Figure 4.2: (a) XRR characterization of an untreated Si(100) substrate. The thickness of the native oxide was calculated from the periodicity of the intensity fringes. (b) Characterization of Si2s core level spectra on Si(100) substrates with an exit angle of 60°C and the evolution of the SiO_x/Si XPS intensity ratio with increasing exit angle. Increasing exit angle results in a higher surface sensitivity.

The thickness of the buried SiO_2 layer during the *in situ* experiment was calculated from the evolution of the relative intensity between silicon and silicon oxide XPS contributions. In order to simplify the calculations, the inelastic mean free path (IMFP) on SiO_2 of the photoelectrons arriving to the detector was considered to be equal for SiO_2 ($\lambda_{SiO_2}(E_{kin}$=1150.1 eV) = 32.43 $\AA$) and Si ($\lambda_{SiO_2}(E_{kin}$=1154.1 eV) = 32.51 $\AA$) energies. Under this approximation, the attenuation of the intensity due to the presence of the Fe_yO_x layer will be equal for both silicon and silicon oxide contributions so this term is canceled. After these considerations, equation 2.8 presented in section 2.3.3 can be simplified and written as:

$$\frac{I_{SiO_2}}{I_{Si}} = R_0(\exp\left(d_{SiO_x}/\lambda\cos\theta\right) - 1) \tag{4.3}$$

where θ is the exit angle, d_{SiO_2} is the SiO_2 thickness, λ is the photoelectrons IMFP and R_0 the ratio between $I^0_{SiO_2}/I^0_{Si}$ intensities. For the calculus on this thesis, the parameter R_0 was experimentally evaluated using the data obtained from untreated Si(100) substrates. Si2p and Si2s core level spectra were recorded at different exit angle on a Si(100) substrate for which the native oxide thickness was previously determined by XRR. Equation 4.3 was used to fit the evolution of the I_{SiO_2}/I_{Si} ratio with the cosine of the exit angle θ and obtain the value of R_0.

Source	**R_0 value**
Si2s core level data	0.41 ± 0.16
Si2p core level data	0.31 ± 0.13
Theoretical value for compact SiO_x [206]	0.53 ± 0.05
Theoretical value for porous SiO_x [206]	0.36 ± 0.04

Table 4.2: R_0 values calculated from the XPS measurements on silicon native oxide and theoretical calculations for porous and compact silicon reported on reference [206].

Figure 4.2(b) shows the fitted Si2s core level spectrum recorded for the untreated Si(100) substrate. Figure inset shows the exponential dependence of the I_{SiO_2}/I_{Si} ratio with the exit angle and the fitting curve obtained with equation 4.3 (green line). This procedure was repeated for the Si2p core level spectra (not-shown) and the results are shown in table 4.2. For the particular case of silicon native oxide the value of R_0 can also be theoretically evaluated using the following expression [207]:

$$R_0 \approx 0.2 \cdot \rho_{SiO_2} \cdot (\lambda_{SiO_2}/\lambda_{Si}) \tag{4.4}$$

Where, ρ_{SiO_2} is the silicon oxide density. A good consistence has been observed between the results obtained and the values reported by other authors using this semi-empirical evaluation (Table 4.2). For further calculations on this thesis, the value $R_0 = 0.41$ was adopted. Once the parameter R_0 is known, the thickness of the buried SiO_x layer can be calculated using equation 4.3.

4.2.2.3 Evolution of the $Fe_yO_x/SiO_x/Si$ system

XPS is a powerful technique for the identification of iron oxide phases due to the presence of characteristic satellites on the Fe2p core level spectra for each iron oxidation state (see Section 3.3). Figure 4.3(a) shows the evolution of the Fe2p (a) core level spectra as the Fe_yO_x thickness was increased. The thickness of the deposited layer was obtained from the evaporation rate calculated in Section 4.2.2.1 and the resulting values are shown in table 4.3. It is observed how at the first stages

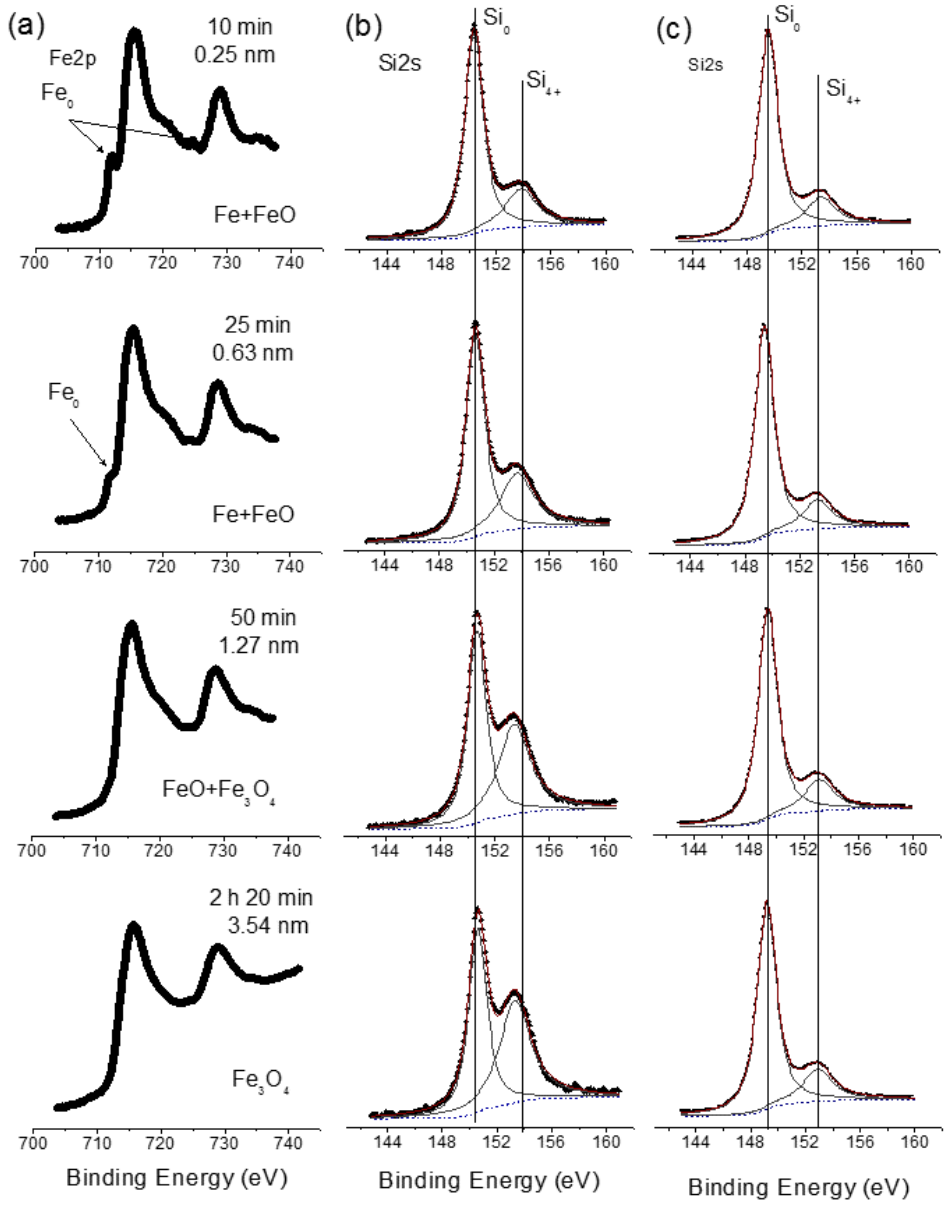

Figure 4.3: Fe2p (a) and Si2s (b) core-level spectra measured at different stages of the iron oxide evaporation. (c) Si2s core level spectra recorded on an untreated substrate yielded under equivalent conditions. Annealed substrates were stable under evaporation conditions but still, the silicon oxide signal increased during the evaporation of iron oxide, as is proved by the increase of the silicon oxide XPS intensity.

of evaporation a dominant FeO phase was formed with the presence of metallic iron traces. The proportion of metallic iron was progressively reduced until all iron was oxidized in a mixture of FeO and Fe_3O_4 after depositing 1 nm. After evaporating around 4 nm a single magnetite phase was obtained. Simultaneously to Fe2p, Si2s core level spectra was also recorded which is shown in Figure 4.3(b). The evolution of the Si2s spectra showed an increase of the SiO_2 signal together with a displacement of the peak to lower binding energies as the iron oxide thickness was increased. The thickness of the SiO_x layer was quantified using equation 4.3 and the values are also resumed in Table 4.3. Figure 4.3(c) shows Si2s core level spectra measured on a Si(100) substrate after annealing under equivalent conditions to those used for magnetite evaporation.

Evap.time(min)	$\mathbf{d}_{Fe_yO_x}$**(nm)**	$\mathbf{d}_{SiO_2}$**(nm)**	$\mathbf{Fe_yO_x}$ **phase**
10	0.25 ± 0.03	1.8 ± 0.1	Fe+FeO
25	0.63 ± 0.07	2.4 ± 0.2	Fe+FeO
50	1.3 ± 0.2	3.4 ± 0.4	FeO+Fe_3O_4
140	3.5 ± 0.4	3.7 ± 0.6	Fe_3O_4

Table 4.3: Evolution of the thickness on the first stages of evaporation for the deposited Fe_yO_x films and the buried SiO_2 layer. The iron oxide phases present at each stage are also indicated.

Measurements on the untreated substrates proved the stability of the native oxide layer under temperature and oxygen pressure conditions equivalents to those of the evaporation, which is in agreement with classical silicon oxidation models. These models foresee temperatures up to 700°C and oxygen pressures up to 1 bar to produce thermally grown silicon oxide [208, 209]. However, during the evaporation of magnetite a clear increase of the silicon oxide thickness was observed, increasing from an initial value of 2 nm up to almost 4 nm after the stabilization of a single magnetite phase on the deposited films. Besides the increase of intensity of the oxide contribution, a slight displacement of the Si^{+4} peak to lower binding energies is observed with increasing Fe_yO_x thickness. Lower binding energies are related with a lower oxygen saturation of silicon bonds. Previous works already reported on silicon oxidation under conditions of temperature and oxygen pressure far below those predicted by classical models. Ruhrnschopf *et al.* documented silicon oxidation on Fe_yO_x/Si (100) interfaces after annealing at 350 °C in UHV, which is quite consistent with the results presented here [191]. The enhanced oxidation in presence of metallic species is related with the catalyzed dissociation of oxygen molecules by metallic centers [188]. The enhanced uptake of oxygen by silicon in the presence of atomic and molecular oxygen has been studied experimentally showing an improve coverage and a higher adsorption probability at room temperature for atomic oxygen [210]. Taking into account the previous studies it was concluded that, during the evaporation

of iron the dissociation of the oxygen molecules is favored, enhancing the diffusion of oxygen through the SiO_2 layer and promoting oxygen adsorption on the SiO_2/Si interface. Consequently, the catalyzed dissociation of oxygen due to the presence of iron induces silicon oxidation even though temperature and pressure conditions are not enough to generate this effect under normal conditions. The uptake of oxygen by silicon impeded the oxidation of iron at early stages, hampering the stabilization of a single magnetite phase and inducing the formation of metallic iron clusters. As the SiO_2 layer thickness was increased, the arrival of oxygen to the SiO_2/Si interface was progressively slowed down until over a certain value (≈4 nm) the diffusion is low enough to allow the stabilization of magnetite. XPS measurements at different exit angles also proved a localized distribution of the silicon oxide at the interface between iron oxide and silicon, ruling out the segregation of SiO_x clusters through the iron oxide layer towards the surface. In contrast with other works, the appearance of iron silicides was not observed [184, 191].

4.2.3 Preparation of $Fe_3O_4/SiO_2/Si$ heterostructures by PLD

For the preparation of the $Fe_3O_4/SiO_2/Si$ heterostructures Fe_3O_4 films were evaporated by PLD directly on untreated Si(100) substrates by using a poly-crystalline Fe_3O_4 target. In order to obtain stoichiometric Fe_3O_4 films, the deposition was carried out under an oxygen partial pressure of $3x10^{-6}$ mbar over a base pressure of $4x10^{-8}$ mbar. Due to the amorphous character of the silicon native oxide it is mandatory to heat the substrates during the evaporation in order to favor the crystalline growth of the magnetite films. However, increasing evaporation temperature will have two consequences, an increase of the surface and interface roughness and an accelerated growth of the silicon native oxide thickness. Bearing this in mind, the substrate temperature was fixed at 500ºC as the best compromise between optimizing the crystallization of the deposited magnetite films and keeping the thickness of the native oxide layer in a few nanometers. *In situ* RHEED measurements were performed during the evaporation in order to monitor the crystalline growth of the films. A diffraction pattern consisted of rings, characteristic of poly-crystalline samples, appeared from the first pulses of evaporation proving the crystalline growth of the films. A total of five samples with different Fe_3O_4 thickness were prepared in order to analyze the influence of this variable on the properties of the deposited films and the final heterostructures.

4.2.3.1 Determination of the PLD growth rate

The deposition rate was calculated from the photoemission measurements, with a similar analysis to that performed in Section 4.2.2. Nevertheless, due to the increasing thickness of the films, standard XPS was no longer suitable for this purpose and a highly energetic source needed to be used. Si1s and Fe1s core level spectra

were recorded for the five prepared samples on the HAXPES station situated at the Spanish CRG BM25-SpLine beamline using a photon energy of 10 keV. Figure 4.4 represents the integrated intensity of the Si1s (left) and Fe1s (right) core level spectra as a function of the number of PLD cycles performed for each sample.

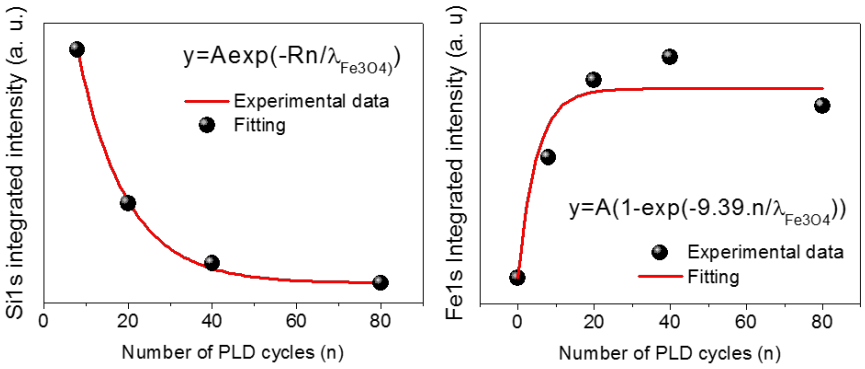

Figure 4.4: Evolution of the HAXPES integrated intensity for Si1s (left) and Fe1s (right) core level spectra as a function of the number of PLD cycles performed during the evaporation. Si1s data was fitted using equation 4.2 obtaining an evaporation rate of 0.94 nm/cycle. This value was used to fit the Fe1s intensity, obtaining a good description of the data and proving the soundness of the result.

Core-level	λ_{Fe3O4}(nm)	Growth rate (nm/cycle)	R-square
Si1s	10.83 (E_k=8169 eV)	0.94±0.06	0.997
Fe1s	4.56 (E_k=2879 eV)	0.94	0.921

Table 4.4: Fitting parameters for the evolution of the HAXPES intensity shown in Figure 4.4.

Considering a homogeneous growth of the magnetite films, the increase of the photoemission intensity can be described using the 4.1 equation presented in Section 4.2.2. Equally, the attenuation of the silicon signal due to the presence of a layer of thickness d of magnetite can be described through the equation 4.2, described in the same section. For convenience, the magnetite thickness was expressed as d=R.n, where R is the evaporation rate in nm/cycle and n the number of PLD cycles. The attenuation of the Si1s core level integrated intensity as a function of the number of PLD cycles performed was fitted by substituting this expression on equation 4.2 and an evaporation rate of R=0.94 nm/cycle was obtained. In order to evaluate the soundness of the result, this value was substituted in equation 4.1 and the Fe1s data was fitted using the resulting expression. It was verified that the results obtained in the first adjustment offered a good description of the second set of data, proving the consistency of the result. Fitting parameters are resumed in Table 4.4. The

magnetite thickness for the five $Fe_3O_4/SiO_2/Si$ samples are resumed in Table 4.5.

Sample 1	3.7 ± 0.3 nm
Sample 2	7.5 ± 0.6 nm
Sample 3	18.8 ± 1.3 nm
Sample 4	37.5 ± 2.6 nm
Sample 5	75.1 ± 5.2 nm

Table 4.5: Relation of magnetite thickness for the $Fe_3O_4/SiO_2/Si$ samples prepared by PLD

4.2.3.2 Characterization of the buried SiO_2 layer

It was already observed during this thesis how the deposition of magnetite induced modifications on the silicon native oxide layer. This effect was more pronounced on the first nm of evaporation and leaded progressively to an apparent equilibrium. The evolution of the SiO_2 layer after increasing magnetite thickness over a few nanometers is evaluated on this section. Given the characteristics of the system, synchrotron techniques were used for this purpose. The performance of photoemission measurements using a high energetic source allowed to obtain information at penetration depths of several tens of nanometers, reaching the buried silicon oxide. Moreover, XRR measurements enabled to evaluate the thickness of the SiO_2 layer and provided information about interface quality.

Si1s core level spectra were measured for the five prepared samples on the SXRD+HAXPES station at the Spanish CRG BM25-SpLine beamline using a photon energy of 10 keV. The collected spectra is presented in Figure 4.5(a). Two contributions are observed corresponding to the substrate (Si^0) and to the silicon native oxide (Si^{+4}). As the magnetite thickness is increased, an attenuation of the Si^0 contribution is observed, as well as an increase of the relative intensity of the oxide contribution. As observed by standard XPS in the first stages of evaporation, the silicon oxide contribution is displaced to lower binding energies with increasing magnetite thickness, which is related with a lower oxygen saturation on the silicon bounds. Simultaneously, reflectivity θ-2θ scans were recorded, which are presented in Figure 4.5(b) as a function of the out of plane momentum Q_z.

The thickness of the SiO_2 layer was evaluated from the analysis of the $I_{Si^0}/I_{Si^{+4}}$ ratio, obtained from the HAXPES spectra, using equation 4.3 and from the periodicity observed on the XRR curves using equation 2.12. In order to make the calculations for the high energy measurements, the parameter R_0 was reevaluated. In a process identical to that explained in section 4.2.2.2 for standard XPS measurements, an untreated Si(100) substrate with a known thickness of native oxide was characterized by HAXPES. The I_{SiO_2}/I_{Si} intensity ratio was calculated doing the deconvolution of the Si1s core level spectrum and the value of R_0 was then calculated.

The value obtained was 0.86 ± 0.06, which was used to evaluate the thickness of the SiO_2 buried layer in the $Fe_3O_4/SiO_2/Si$ samples. For the thickest films (37.5 and 75.1 nm), the photoemission intensity for the silicon contributions is almost completely attenuated hindering the analysis of the spectra. Thus, the I_{SiO_2}/I_{Si} ratio could not be procured. The evolution of the calculated SiO_2 thickness as a function of the magnetite thickness is represented in Figure 4.6.

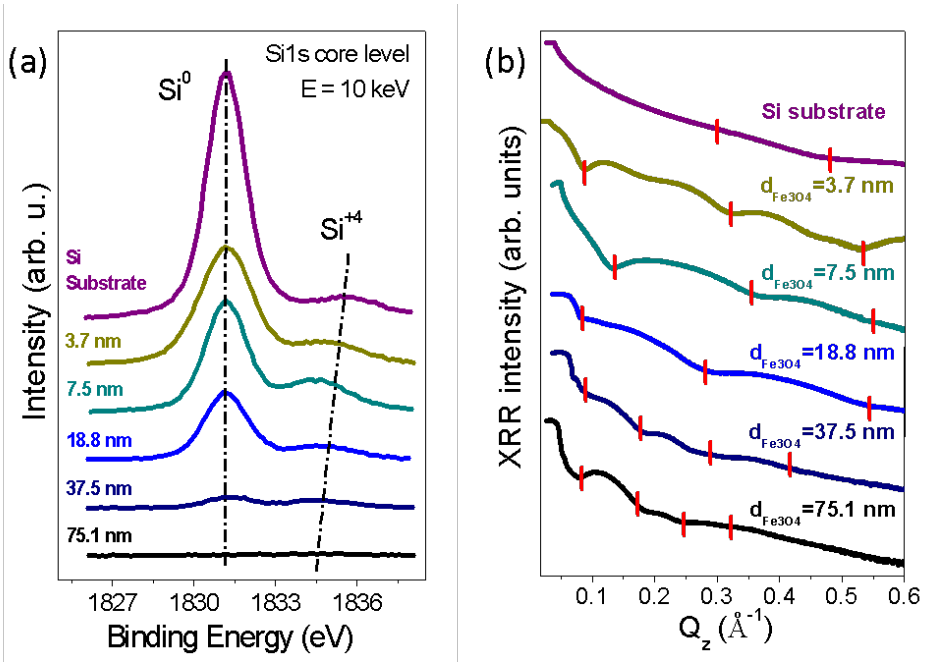

Figure 4.5: HAXPES (a) and XRR (b) characterization of the $Fe_3O_4/Si_2/Si$ heterostructures for different Fe_3O_4 thickness using a photon energy of 10 keV. HAXPES Si1s spectra show the presence of two contributions for silicon with a slight displacement of silicon oxide signal to lower binding energies with Fe_3O_4 thickness. XRR measurements showed the appearance of intensity oscillations for all samples probing the low roughness of the buried interfaces.

Complementary, the SiO_2 thickness was also calculated from the XRR measurements, which allowed the characterization of the whole set of samples. Despite its low contrast, the appearance of intensity oscillations proved the presence of flat Si/SiO_2 and SiO_2/Fe_3O_4 interfaces, due to the high susceptibility of x-ray interference to roughness. From the low periodicity of the oscillations appeared it was concluded that this interference was necessarily related with the buried SiO_2 layer and not with the deposited magnetite films. The absence of a second group of oscillations in most of the samples pointed to the formation of a rough magnetite surface. The position of the minima was used to calculate the layer thickness, indicated with red bars in Figure 4.5(b). The values obtained by XRR for the SiO_2 thickness are presented as

a function of the Fe_3O_4 thickness in Figure 4.6, together with the results obtained by HAXPES and by XPS in the first stages of evaporation (see section 4.2.2). A good correlation is observed between the data obtained from the *in situ* experiment and those calculated in this section. The variations on the thickness between the XRR and HAXPES calculations for the same sample can be explained by the fact that equations used for HAXPES analysis do not consider the effect of surface and interface roughness. Even so, the combination of the two techniques allowed to evaluate the problem in a reliable way.

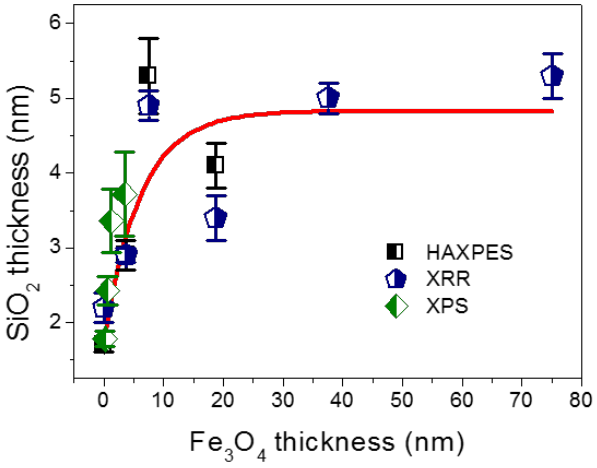

Figure 4.6: Evolution of the SiO_2 thickness calculated by HAXPES, XPS and XRR measurements as a function of magnetite thickness. The evolution of the silicon oxide layer with magnetite thickness is well described by an exponential function.

Figure 4.6 represents the evolution of the SiO_2 layer thickness as the evaporated magnetite thickness was increased. The progression of the system is well defined by an exponential function (red line), showing a fast growth for the first deposited nanometers and a gradual stabilization as the evaporation continues. This advance is consistent with the mechanism described in section 4.2.2.3 to explain the catalyzed oxidation of silicon by the presence of iron. When the magnetite film reached a thickness of around 25 nm, the SiO_2 thickness is almost completely stabilized. A value of around 5 nm was estimated for the final SiO_2 thickness after fitting the data with an exponential growth as a function of the magnetite thickness.

In order to have a direct observation of the SiO_2 layer and evaluate the interface quality in terms of homogeneity and smoothness, cross section TEM measurements were performed in Sample 4 ($d_{Fe_3O_4}$=37.5 nm). Figure 4.7(a) shows an overall image where the different regions of the sample can be distinguished. The overlapping dark grains in the top of the picture correspond with the polycrystalline Fe_3O_4 film. The

formation of these structures pointed to an island-like growth of the magnetite films. Significant fluctuations of the island height up to 10 nm were observed. The lightest area corresponds with the silicon oxide interlayer, which presents well-defined flat interfaces and a homogeneous distribution. Darker spots on the silicon substrate near to the SiO_2/Si interface are related to structural defects on the Si substrate.

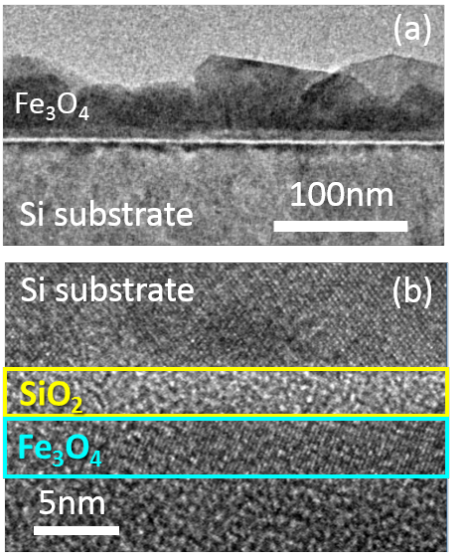

Figure 4.7: (a) Cross section TEM measurements performed in Sample 4 (37.5 nm) and (b) zoomed image of the interface area. The images showed the presence of a 4 nm SiO_2 layer at the interface (white area) with well-defined interfaces, in agreement with previous results. The amplification of the images also showed the presence of a single oriented magnetite phase near to the interface with the SiO_2 layer (blue square).

Figure 4.7(b) shows a zoomed TEM image of the SiO_2 layer. In the sample studied, the thickness of the silicon oxide layer was found to be 3.75 nm, which was slightly smaller than the previous estimations made by XRR (5±0.2 nm). After measuring different regions of the sample, no significant variations of this value were observed. When observing the system with a higher number of magnifications, the presence of an oriented region of the magnetite film in the area next to the interface was revealed, which is highlighted in the image with a blue square. This could indicate the formation of a single oriented film in the first stages of evaporation and a switch to a polycrystalline growth after the magnetite thickness was increased over a certain value. Nevertheless, after analyzing different areas of the sample it was observed that the orientation of the crystallographic planes respect to the substrate was different depending on the region proved, supporting the presence of different nucleation centers.

4.2.4 Characterization of the magnetite films

4.2.4.1 Identification of the iron oxide phase

Magnetite films were characterized by standard XPS and HAXPES in order to identify the iron oxide phases present on the sample. The combination of both techniques provided information about the composition of the sample with surface and bulk sensitivity respectively, enabling the detection of differences between the surface and the average depht of the film. Moreover, XPS Fe1s and Fe2p core level spectra present very recognizable lineshapes for each of iron oxidation state, constituting a truly valuable tool for the characterization of the system (see section 3.3).

Fe1s and Fe2p core level spectra are shown in Figure 4.8. The HAXPES spectra were recorded using a photon energy of 10 keV (Fig.4.8 (a) and (b) respectively). Fe2p core level was also characterized by standard XPS using a magnesium source (1253.6 eV) (Fig.4.8(c)). Sample 1 (3.7 nm) already showed a predominant magnetite phase as could be deduced from the presence of the characteristics satellites at a distance of 8.7 and 17.12 eV respect to the main peak in the Fe1s core level spectrum (red bars). However, there is a significant presence of metallic iron traces, evidenced by the appearance of a prominent shoulder to the left of the main peak (lower KE). This deformation was also evidenced in the HAXPES Fe2p spectrum, that showed a broad profile for the 3/2 and 1/2 spin-orbit split contributions. Measurements on the Fe2p core level with a standard x-ray source provided higher energy resolution and allow to identify also FeO traces on the surface area, evidenced by a characteristic satellite. Sample 2 (7.5 nm) still shows a slight deformation of the Fe1s spectrum, probably related with some remaining metallic traces, but the proportion was so low that they were not even noticeable on the Fe2p spectra, which presented a characteristic lineshape for magnetite. Fe1s and Fe2p HAXPES spectra recorded on Sample 3 (18.8 nm) pointed to the formation of a single magnetite phase, characterized by the position of the satellites on the Fe1s spectrum. In contrast, the measurements with standard XPS indicated the presence of a predominant Fe_2O_3 phase, which might indicate the over-oxidation of the sample surface after its exposition to air. For the following samples (increasing thickness) the spectra showed a characteristic lineshape for magnetite for the Fe1s as well for the Fe2p core levels for low and high incident photon energy. The presence of reduced iron oxide phases on the thinner films is related with the oxygen competition between silicon and iron during the evaporation. As the SiO_2 layer thickness increased, the uptake of oxygen by silicon was reduced and the stabilization of magnetite was favored. These results were consistent with the observations made in section 4.2.2 and supported the theory of a direct correlation between the stabilization of the silicon oxide layer and the stabilization of a single magnetite phase.

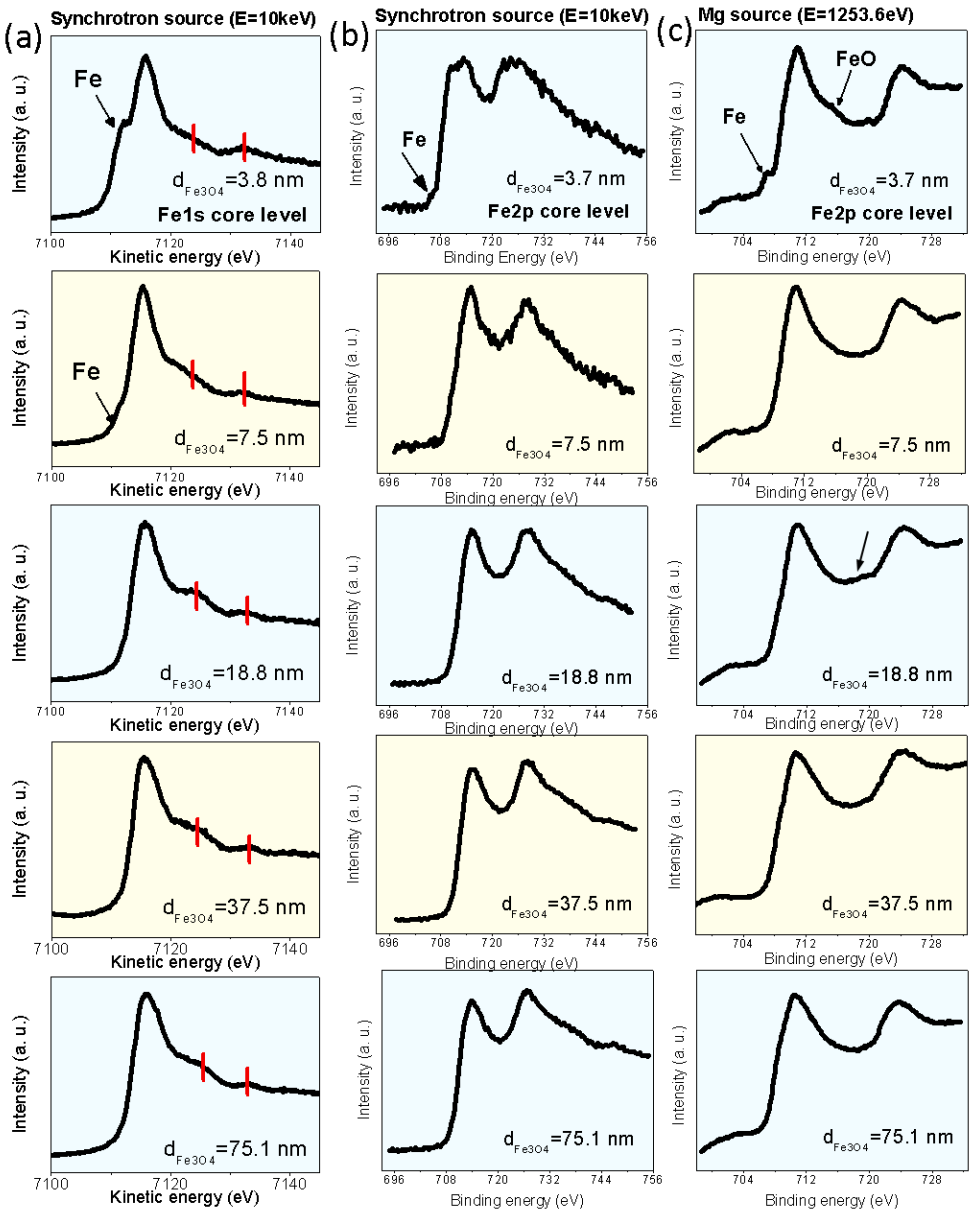

Figure 4.8: Characterization of the iron oxide phase by HAXPES and XPS of $Fe_3O_4/SiO_2/Si$ heterostructures with different Fe_3O_4 thickness. Fe1s (a) and Fe2p (b) core level spectra were recorded using a photon energy of 10 keV. Fe2p(c) core level spectra was also characterized using a standard K-alpha Mg source.

4.2.4.2 Structural characterization

$Fe_3O_4/SiO_2/Si$ samples were characterized by X-Ray Diffraction on the SXRD + HAXPES station at the Spanish CRG BM25-SpLine beamline. 2θ scans were performed with an incidence angle of 1^o using a photon energy of 10 keV. Figure 4.9(a) shows recorded 2θ scans after background subtraction. Five diffraction peaks were observed at 14.8º, 24.4º, 28.66º, 29.97º and 34.75º, which indexed on the basis of the fcc structure of magnetite correspond with the (111), (220), (311), (222) and (400) Bragg reflections. The appearance of this pattern confirmed the polycrystalline character of the films. The increasing intensity and narrowing of the diffraction peaks for thicker magnetite layers was a consequence of the larger quantity of material, the enhanced degree of crystallinity and the formation of bigger crystallographic domains.

After comparing these spectra with a reference pattern recorded from a Fe_3O_4 powder (inset in Fig.4.9(a)), a perfect match was observed in the position of the peaks but a different relation of intensities between the different Bragg reflections was evidenced. The most conspicuous difference was the larger intensity of the (111) and (222) reflections and the drop of intensity on the (400) reflection. θ - 2θ scans and rocking curves were performed on these particular reflections in order to identify the origin of this modification.

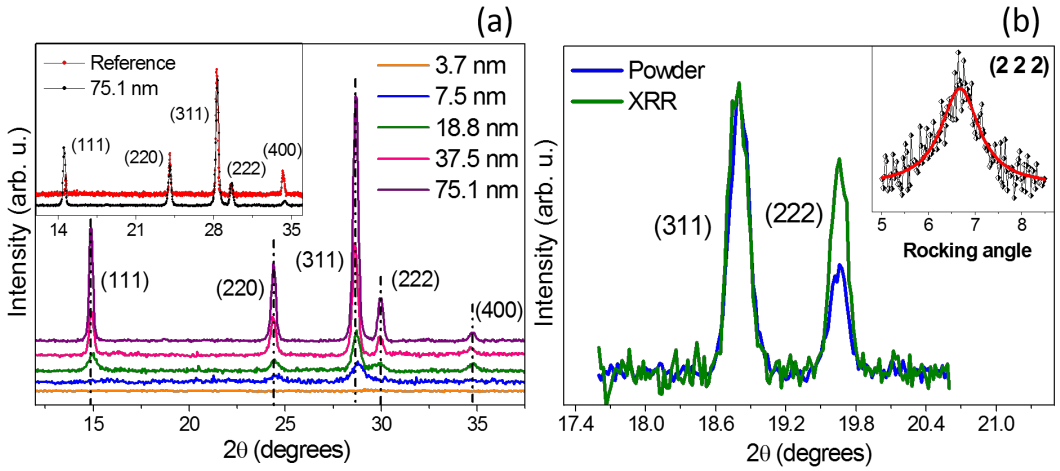

Figure 4.9: (a) 2θ scans recorded on $Fe_3O_4/SiO_2/Si$ heterostructures with different magnetite thickness after background subtraction. The spectra was vertically displaced for a better visualization. In the inset, diffraction pattern recorded in Sample 5 ($d_{Fe_3O_4}$=75.1 nm) together with a pattern corresponding with a powder magnetite reference. Both spectra were normalized with the intensity of the (311) reflection. (b) Comparison of the 2θ and θ-2θ scans for Sample 5 (75.1 nm). In the inset, rocking curve measured on the (222) Bragg reflection, and fitting of the profile with a Gaussian function (red line).

Figure 4.9(b) shows the comparison between 2θ and θ - 2θ scans recorded for Sample 5 (75.1 nm) including the Bragg reflections (311) and (222). It is observed how the relative intensity of the (222) reflection is increased when the θ and 2θ angles were coupled, pointing out the presence of single oriented domains on this particular direction. Rocking curves were recorded keeping the diffraction angle fixed at $2\theta_{hkl}$ and scanning the incident angle θ_{inc}. Inset in Fig.4.9(b) shows the rocking curve recorded at $2\theta_{222}$ in Sample 5 (75.1 nm). For a perfectly randomly oriented polycrystal a constant intensity should be observed meanwhile the recorded spectrum showed a Gaussian profile with a maximum of intensity when θ_{inc}=θ_{222}. Equivalent results were observed in thinner films.

The average size of the crystalline grains on the polycrystalline magnetite films was calculated from the FWHM of the diffraction peaks using Scherrer equation (eq. 2.24) presented in Section 2.6.3. Diffraction peaks observed in the 2θ scans were fitted using a pseudo-Voigt function. For the thinnest film (3.7 nm) the diffraction peaks were not intense enough to obtain a good fit, hence crystal domain sizes could not be evaluated. Obtained values are resumed in table 4.6. For samples from 2 to 4 (7.5 to 37.5 nm) average crystal grain size showed almost a linear correlation with magnetite thickness. Nevertheless, between samples 4 (37.5 nm) and 5 (75.1 nm) the grain size was almost unchanged although the thickness was doubled.

Fe_3O_4 thickness	**GS (nm)**
7.5 nm	5.9 ± 0.3 nm
18.8 nm	13.8 ± 1.9 nm
37.5 nm	22.5 ± 2.1 nm
75.1 nm	25 ± 4 nm

Table 4.6: Magnetite crystalline grain sizes.

Additional Raman spectroscopy measurements were performed especially focused on dismissing the presence of non-crystalline phases apart from magnetite with a high depth resolution. Raman spectra was recorded in the $Fe_3O_4/SiO_2/Si$ samples with a wavenumber range between 100-1500 cm^{-1}. Different areas of the sample were proved in order to corroborate the homogeneity of the sample and the recorded spectra were averaged. Normalized spectra are shown in Figure 4.10.

There exists five active modes in Raman for magnetite at room temperature. The theoretical values for these modes in bulk samples are T_{2G} (1) (ω = 241 cm^{-1}), T_{2G} (2) (ω = 296 cm^{-1}), E_{1G} (ω = 505 cm^{-1}), T_{2G} (3) (ω = 581 cm^{-1}) and A_{1G} (ω = 666 cm^{-1}) [211,212]. The recorded spectra evidenced the presence of the T_{2G} (1), T_{2G} (2) and A_{1G} modes in the characterized samples. Additional bands appeared related to the silicon substrate which are the F_{2G} (550 cm^{-1}) and the 2TO(L) (998 cm^{-1}) modes. The 2TO(L) band was used to normalize the intensity of the spectra in order to compare the magnetite Raman intensity between the different samples.

Magnetite modes E_{1G} and T_{2G} (3) could not be clearly identified as they overlapped with the more intense mode F_{2G} from silicon.

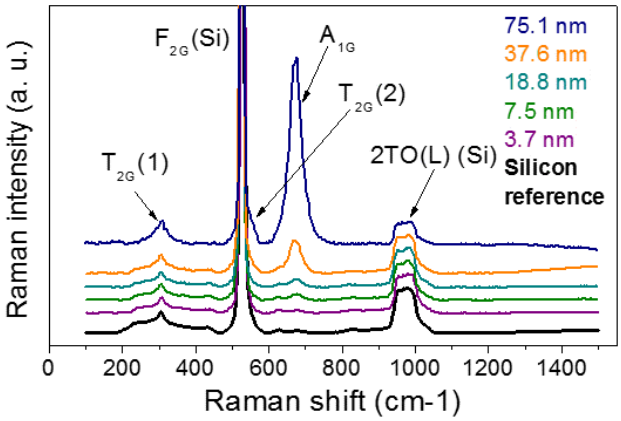

Figure 4.10: Raman spectra recorded on $Fe_3O_4/SiO_2/Si$ heterostructures with different magnetite thickness. Spectra was normalized respect to the substrate 2TO(L) band to study the evolution of the magnetite bands.

The most representative mode to study the evolution of the magnetite films is the A_{1G} mode, as it is the most intense and it did not overlap with any silicon modes. A progressive increment of the band intensity is observed with the increase of the magnetite thickness, which is directly related with the greater amount of material present on the system. Besides, a displacement of the band wavenumber to higher Raman shifts respect to bulk value was observed, which is a typical effect in nanoscaled systems. As the film thickness was increased, the band position approach to bulk values due to the increasing thickness and the higher degree of crystallinity [213, 214]. Although some ambiguity could be understood in the identification of magnetite, as modes A_{1G} and T_{2G} (2) are also active for maghemite and hematite, the absence of the characteristics overtones for these phases at 1320 cm^{-1} or at 1440 cm^{-1} respectively confirmed the single phase nature of the films [215].

4.2.4.3 Morphological characterization

Morphological characterization of the magnetite surface was carried out by AFM and SEM. Microscopy images obtained by both techniques are shown in Figure 4.11. AFM images were processed using the WSXM software [114] and roughness values were obtained from the height profile. Results are resumed in Table 4.7. The measurement was repeated in different regions in order to evaluate if the result was representative for the average of the sample.

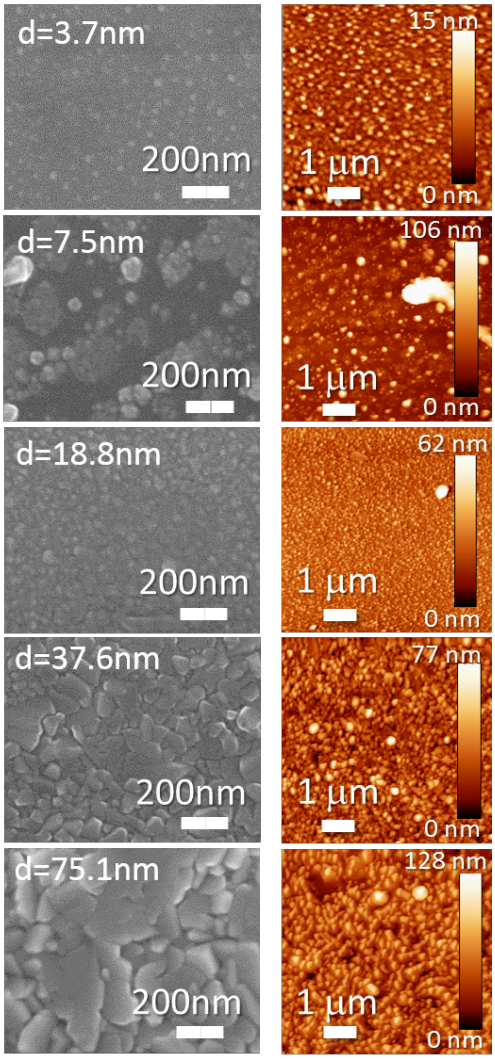

Figure 4.11: SEM (left) and AFM (right) images for the magnetite films with different thickness.

Magnetite films presented a strong granular aspect, as already observed by TEM (Fig. 4.7(a)). The continuity of the samples was already corroborated by XPS, with exception of Sample 1 (3.7 nm) where such a conclusion could not be reached due to the low thickness of the sample. Therefore, it can be assumed that all the surface observed is covered by magnetite, although the granular structures observed in the SEM micrographs, especially for samples 2 (7.5 nm) and 3 (18.8 nm), apparently do not overlap. This might be related with a homogeneous growth on the first layers and the subsequent formation of islands from a certain thickness (Stranski-Krastanov

growth). This growth mechanism would agree with the observation by TEM (Fig. 4.7(b)) of an oriented layer of magnetite in the first nanometers of the film. As the evaporation continued, the size of these islands increased, adopting more irregular shapes and presenting a greater size dispersion. Comparing the scale of the SEM micrographs with the average crystalline grain sizes calculated by XRD it could be concluded that both magnitudes are not directly related.

Fe_3O_4 thickness	Roughness (nm)
3.7 nm	2.01
7.5 nm	9.77
18.8 nm	2.50
37.5 nm	10.78
75.1 nm	18.74

Table 4.7: Roughness values obtained from the analysis of the height profiles in AFM images

In general, magnetite films presented significantly high roughness values, which progressively increased with layer thickness. Sample 2 (7.5 nm) showed a remarkably irregular surface and morphological features dissonant with the evolution observed in the other samples. The presence of isolated grains with a high height contrast was observed by SEM as well as in AFM images, which is also reflected in the roughness. The particularities on the morphology of this sample were not considered representative of the evolution of the system.

4.2.4.4 In-plane magnetic and transport properties

The electrical resistance of the magnetite films was measured as a function of temperature. Figure 4.12(a) shows the resistance (R) against the temperature (T). Resistance measurements for Sample 1 (3.7 nm) could not be performed as they were above the sensitivity of the experimental set-up. The samples showed high resistance values with an improvement of the conductivity with increasing film thickness. The Verwey transition, characterized by a critical drop on the conductivity of several orders of magnitude (see Section 3.3), was not observed in any of the samples. Due to the polycrystalline character of the films there are regions of the sample (grain boundaries) where the orientation of the crystallographic planes changes abruptly. During the transport, grain boundaries act as scattering centers increasing the resistance of the sample [216]. The thickening of the film resulted in the formation of bigger crystallographic domains, as confirmed by XRD, and consequently in a lower density of grain boundaries and a better conductivity. The high density of grain boundaries can also explain the rupture of the long range order required for the apparition of the Verwey transition.

In Figure 4.12(b) the resistance curves are represented as the neperian logarithm

of the resistance normalized by the resistance at room temperature as a function of the inverse of the square root of the temperature. This representation was chosen by comparison with previous works reported on polycrystalline magnetite films where a linear dependence was observed [217]. The experimental data was succesfully fit using a linear function (red line), observing this trend characteristic of highly particulate systems, which accords with the observations made by TEM and SEM. This behavior have been related with the conduction of electrons by tunneling through the grain boundaries. The physical meaning of this slope was analyzed by Sheng *et al.* [218] and they established a complex dependence with domain size, domain wall and electric field. Analyzing the evolution of the slope with crystalline grain size (Inset Fig. 4.12(b)) a linear dependence was observed, proving a direct correlation between the structural and the transport properties of the film.

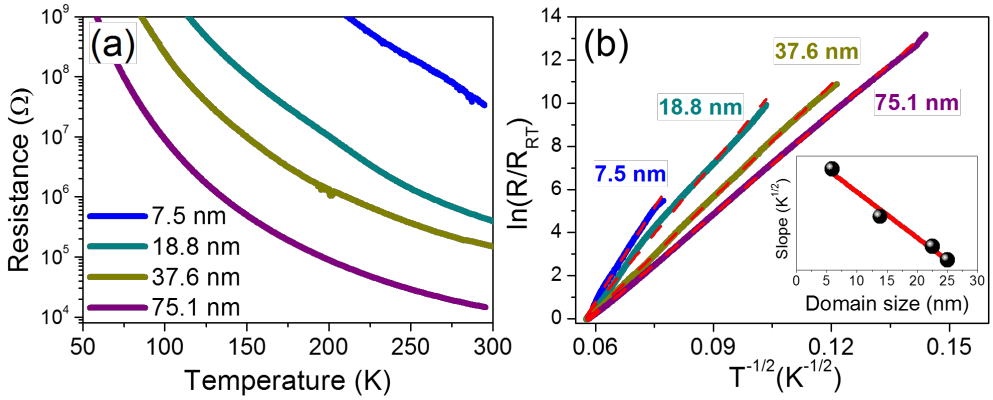

Figure 4.12: (a) Resistance as a function of the temperature curves measured on $Fe_3O_4/SiO_2/Si$ films with different thickness. (b) Representation of the curves as the $Ln(R/R_{RT})$ versus $T^{-1/2}$. The curves were linearly fitted and dependence of the slope with grain size is shown in the inset.

Magnetic response of the deposited magnetite films was characterized by MOKE. Hysteresis loops were recorded at room temperature and ambient pressure for Samples 2 (7.5 nm) to 5 (75.1 nm). The measurements were performed in a longitudinal configuration so the magnetic field was applied parallel to the sample surface and to the dispersion plane. Sample 1 (3.7 nm) was excluded as a non negligible presence of metallic iron was proved by HAXPES. All the samples characterized showed hysteresis and saturation for fields lower than 250 mT. Normalized hysteresis cycles are shown in Figure 4.13. The results showed an increase of the coercive field and also an increase of the remanence (M_R/M_S) with increasing magnetite thickness. For an ideal system, a fast response and a low energetic cost would be desired, which is related with low coercive fields and a sharp inversion of the magnetization, represented by $M_R/M_S \approx 1$. Increasing film thickness turned into a higher correlation between

the magnetite grains resulting in an increase of the remanence and thus the system presents a faster switch mechanism. The increase of grain size within the magnetite film also increases the coercive field due to the decrease on the surface/volume ratio [219]. Although this is translated in a higher energetic source the range of this variation is small.

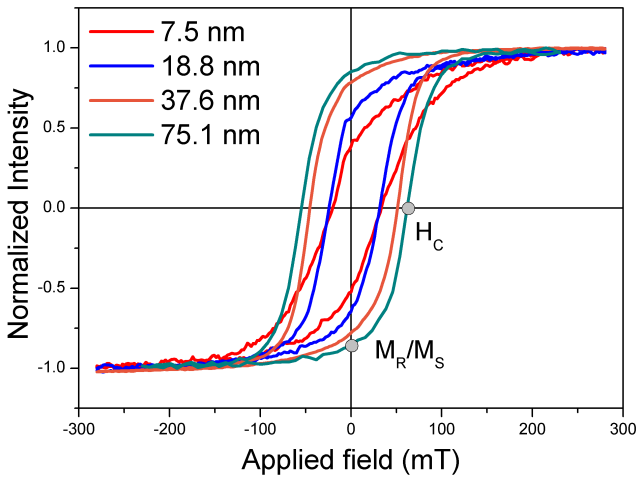

Figure 4.13: Normalized hysteresis cycles recoded by MOKE using a longitudinal configuration for different magnetite thickness on $Fe_3O_4/SiO_2/Si$ heterostructures

Additional cycles were recorded after rotating the sample around its surface normal at different angles without modifying the direction of the applied magnetic field (not shown). No changes were observed on the magnetic response dismissing the presence of in plane magnetic anisotropies on the samples, which was consistent with the non-textured character of the samples.

4.2.5 Conclusions

The direct evaporation of Fe_3O_4 films keeping the silicon native oxide was carried out with a two-fold objective, first the passivation of the silicon surface in order to avoid the formation of silicide phases during magnetite evaporation and second, evaluate the properties of the final SiO_2 layer and evaluate its suitability as a tunnel barrier for the fabrication of spin injection devices. After a complete characterization of the prepared $Fe_3O_4/SiO_2/Si$ heterostructures using a large number of techniques it can be concluded that the evaporation of single phase polycrystalline magnetite films on Si by PLD stabilizing the SiO_2 interlayer was successfully achieved.

Regarding the passivation of the silicon surface, the presence of the silicon native

oxide avoided the formation of silicides phases during the evaporation and favored the stabilization of Fe_3O_4 from early stages. However, it did not prevent from further silicon oxidation. On the first stages of the evaporation, a progressive increase of the silicon oxide thickness was observed, related with an enhance uptake of oxygen triggered by iron atoms. Either way, the SiO_2 layer was completely stabilized at certain thickness as it restricted itself the diffusion of oxygen to the SiO_2/Si interface. After a deep characterization by XPS, HAXPES, XRR and TEM, the final thickness for the SiO_2 layer was found to be around 4 nm after stabilization, being compatible with the engineering of a tunnel barrier. The final interlayer showed an homogeneous thickness and composition and presented abrupt Si/SiO_2 and SiO_2/Fe_3O_4 interfaces, which is an essential requirement regarding an efficient transport through the SiO_2 barrier.

The amorphous character of the silicon native oxide hampered the epitaxial growth of the magnetite films. Instead, the direct deposition by PLD led to the formation of non-textured polycrystalline films with a strong granular character. Nevertheless, a single oriented region was observed by TEM in the first nanometers close to the Fe_3O_4/SiO_2 layer. The single phase nature of the films after the stabilization of the SiO_2 layer was corroborated by combining XRD, RAMAN and HAXPES. The main limitation regarding the properties of the magnetite films was the large resistivity observed at low thickness. However, this can be overcome by increasing the thickness of the films, which results in a lower density of grain boundaries and a significant enhance of the transport properties. Larger thickness also provided a faster magnetic response, keeping low coercive fields in the range of tens of mT.

To summarize, it can be concluded that the direct evaporation of Fe_3O_4 films on SiO_2/Si substrates is an adequate fabrication method for the design of spin injection devices, fulfilling the preliminary requirements for an efficient spin injection.

4.3 Fe_3O_4/$SrTiO_3$/Si heterostructures

4.3.1 Introduction

$SrTiO_3$ is a complex oxide with a perovskite structure that presents an additional interest due to its tunable conductivity [220]. Because of its good insulator properties, the use of $SrTiO_3$ as tunnel barrier has been reported in magnetic tunnel junction heterostructures [221–223]. Vera *et al.* deeply analyzed the influence of the $SrTiO_3$ properties on $La_{0.67}Sr_{0.33}MnO_3$/ $SrTiO_3$/ Co junctions, proving a significant influence of the oxygen stoichiometry and the $SrTiO_3$/Co termination on the value of the measured TMR [224]. Regarding the integration of magnetite films on $SrTiO_3$, in a recent work Gilks *et al.* reported on high quality $Fe_3O_4(111)$/$SrTiO_3(111)$ heterostructures probing a sharp interface with a Fe_AFe_B/SrO nature. Density functional theory calculations demonstrated that under this particular atomic configu-

ration the negative spin polarization of magnetite is kept at the interface, which could be really resourceful for the design of spin injection devices [225]. Despite the large mismatch between magnetite and $SrTiO_3$ ($\approx 7\%$) the fabricated $Fe_3O_4/SrTiO_3$ heterostructures presented atomically abrupt interfaces with a preservation of the magnetite magnetic bulk properties on the deposited films, which has also been supported by other studies [226–228].

It has been emphasized during this thesis how the growth of epitaxial films on Si requires especial efforts due to the presence of a native oxide layer. The elimination of this oxide layer involves aggressive methods and lead into very reactive silicon surfaces. As a consequence, only a few oxides have been successfully grown epitaxially on silicon, being $SrTiO_3$ one of them [136, 229]. First attempts of integrating $SrTiO_3$ ultrathin films on Si were motivated by the search of alternative gate oxides for complementary metal-oxide-semiconductor devices (CMOS) [230]. Even though that idea has been dropped due to the smaller conduction band offset between Si and $SrTiO_3$ respect to SiO_2, the integration of $SrTiO_3$ films on Si is still of interest. Because of its good lattice match with several functional structures as manganites [231], the use of $SrTiO_3$ buffer layers can be a straightway strategy for the integration of these materials on Si [232, 233]. Moreover, because of its high dielectric constant, it is a perfect candidate for its use as a tunnel barrier on the design of silicon based spin injection devices [234].

In this second part of the chapter the preparation of magnetite films on silicon using a strontium titanate buffer layer is presented. Contrary to the preceding system, there are not previous references on $Fe_3O_4/SrTiO_3/Si$ heterostructures. $SrTiO_3$ was intended to play a double role, first as a spin dependent tunnel barrier and second as a seed for the epitaxial growth of magnetite films. The preparation of the heterostructures was performed in two steps. First, $SrTiO_3$ films were deposited on Si (100) substrates by MBE through a SrO buffer used to eliminate the silicon native oxide and passivate the substrate surface. All the details regarding the evaporation and characterization of the $SrTiO_3$ films will be described in Section 4.3.2. Subsequently, magnetite films were evaporated by PLD on top of the $SrTiO_3$ films, exploring different deposition conditions in order to successfully stabilize single phase magnetite films, which will be presented in Section 4.3.3. The final $Fe_3O_4/SrTiO_3$ heterostructures were deeply characterized considering the influence of two factors: i) The influence of the $SrTiO_3$ layer thickness on the final properties of the heterostructure (Section 4.3.4.2). ii) The influence of the deposition temperature for the magnetite films on the final properties of the heterostructures (Section 4.3.4.1). The conclusions extracted from this part of the chapter will be resumed in Section 4.3.5.

4.3.2 Preparation of epitaxial $SrTiO_3$ films on Si(001)

4.3.2.1 Evaporation of $SrTiO_3$ films on Si(001) by MBE

For the preparation of epitaxial $SrTiO_3$ films, the native oxide layer was previously eliminated from the Si(100) substrates. This was made using the SrO-deoxidation process described in Section 3.2.3. After silicon deoxidation, the evaporation of the $SrTiO_3$ films was performed in the following steps. First, three $SrTiO_3$ monolayers (ML) were deposited by co-evaporation of Sr and Ti at room temperature and low oxygen pressure (4x10^{-7} Torr). Then, the samples were heated up with a constant rate of 20°C/min under UHV conditions in order to recrystallize the deposited layer. The samples were annealed until the RHEED pattern was stable, which was normally in a range between 400-500°C. The exact temperature needed in each evaporation for the recrystallization will depend on the stoichiometry of oxygen on the deposited layer. The evaporation/annealing steps were repeated cyclically until the $SrTiO_3$ layer reached a thickness of around 5 nm. Afterwards, $SrTiO_3$ was evaporated directly by co-evaporation of Sr and Ti at 600°C increasing the oxygen pressure. The samples used on this thesis were prepared in collaboration with the Imec R&D center and the Catholic University of Leuven, in Belgium. For this work, four samples with different thickness from around 2 nm to 40 nm were prepared.

4.3.2.2 Characterization of the $SrTiO_3$ films

Characterization by XRR

$SrTiO_3$/Si films were characterized by XRR performing θ-2θ scans at low and at high θ angles. Low angle measurements allowed to confirm the thickness of the $SrTiO_3$ films for the different samples and to evaluate surface and interface roughness. Scans at high angle provided structural information about the crystallographic planes perpendicular to the surface normal. Recorded θ-2θ scans measured using a photon energy of 20 keV are shown in Figure 4.14. Low angle measurements (Fig. 4.14(a)) showed the appearance of well-defined intensity oscillations due to the interference between the reflected x-rays, proving an abrupt $SrTiO_3$/Si interface and low surface roughness for the $SrTiO_3$ films. The thickness of the films was calculated from the periodicity of the oscillations using equation 2.12 obtaining values of 1.80 $\pm$ 0.05 nm (Sample A), 4.8 $\pm$ 0.04 nm (Sample B), 10.9 $\pm$ 0.1 nm (Sample C) and 42.0 $\pm$ 0.5 nm (Sample D).

High angle measurements (Fig. 4.14(b)) proved the epitaxial growth of the $SrTiO_3$ films with its c axis co-lineal to that of silicon so (001)$SrTiO_3$ $\|$(001)Si relation. The most intense contribution corresponds to the 004 reflection of Si and the two broader peaks are related with the (001) and (002) reflections of the $SrTiO_3$ structure. Lower reflections on Si(001) were forbidden by selection rules, which determine that in order to have non-zero intensity h, k, l values must be all even or all

odd and fulfill h+k+l=4n, where n is an integer number. The diffraction peaks related with the $SrTiO_3$ (001) and (002) reflections became more intense and narrower as the thickness of the $SrTiO_3$ films was increased, showing also the appearance of intensity oscillations. The existence of a coherent interference at such high angles proved the high quality of the evaporated films in terms of low surface and interface roughness.

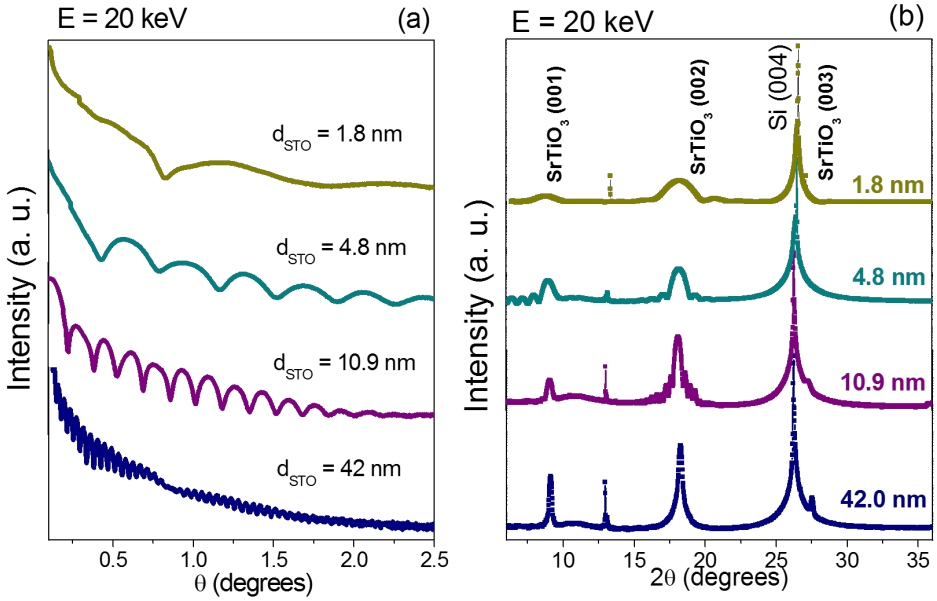

Figure 4.14: XRR measurements at low (a) and high (b) angle on $SrTiO_3$ films evaporated on Si by MBE. The appearance of x-ray interference at low and high angle proved the good quality of the films in terms of low roughness

Characterization by XRD

Silicon presents a face centered diamond cubic structure with α=β=γ=90 and lattice parameter a=b=c=0.543 nm. $SrTiO_3$ presents a simple perovskite structure with α=β=γ=90 and lattice parameters a=b=c=0.3905 nm. Considering the large lattice mismatch between both materials, a cube on cube growth was unlikely. A large number of reflections were measured in order to determine the in-plane atomic arrange of the $SrTiO_3$ films proving a (100)$SrTiO_3$‖(110)Si relation between both lattices. This rotation of 45 degrees of the (100)$SrTiO_3$ axis respect to the (100)Si axis reduced the lattice mismatch from -28% to 1.66% in the case of a relaxed growth, being a more favorable configuration.

The acquisition of two dimensional reciprocal space maps (RSM) provided complete information about the coupling between the $SrTiO_3$ and Si structures (shown in

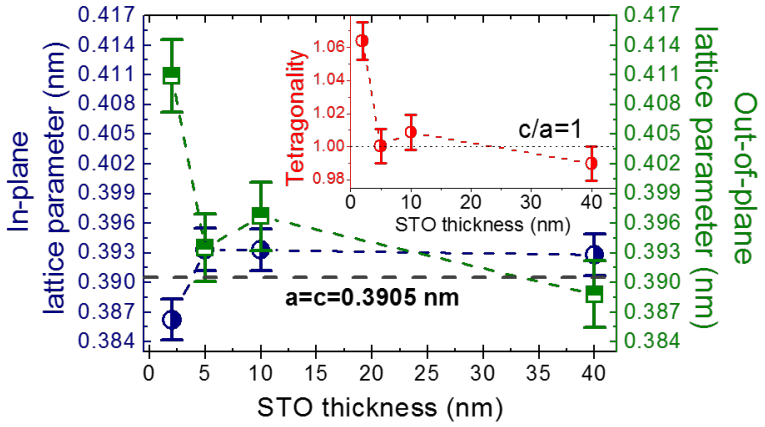

Figure 4.15: Evolution of the $SrTiO_3$ in-plane (a) and out-of-plane (c) lattice parameter values with film thickness on $SrTiO_3$/Si samples. In the inset, tetragonality values (c/a) for the four samples. The data showed a compression of the in-plane lattice parameter for Sample 1 (1.8 nm) and subsequent relaxation for thicker films, going from a tetragonal to a cubic structure.

d_{STO} (nm)	D (nm)
1.8	10.3 ± 0.2
4.8	11.1 ± 0.4
10.9	12.8 ± 0.7
42	16.3 ± 0.9

Table 4.8: Crystal domain size (DS) for $SrTiO_3$ films evaporated on Si

Figure fig:fe3o4-sto-si_rsm).*Fromthemeasurementsperformeditcouldbeconcludedthat the $SrTiO_3$* films grew incommensurate and relaxed on Si(100), showing lattice parameters close to that of $SrTiO_3$ bulk. Exceptionally, Sample 1 (1.8 nm) showed a commensurate growth indicating that, at the first stages of the evaporation, the $SrTiO_3$ structure compressed to adapt its lattice to the substrate. However, as the evaporation continued to a few tens of monolayers this strain was released and the film showed a bulk like structure.

Lattice parameters were calculated from XRD measurements and the evolution of the a (in-plane) and c (out-of-plane) parameters is resumed in Figure 4.15. Sample 1 (1.8 nm) showed a reduced lattice parameter, so a=0.386 nm, to adapt the diagonal of its cell to the Si lattice parameter so $\sqrt{2}$·0.386=0.546 nm when a_{Si}=0.543 nm. This contraction induced an expansion of the out of plane lattice parameter so that c=0.411 nm in order to conserve the volume of the cell (V=0.06 nm^3), going from a cubic to a tetragonal structure. This distortion was quantified by the tetragonality

of the lattice (c/a). This parameter allow to represent very well the relaxation of the lattice for $SrTiO_3$ films with increasing $SrTiO_3$ thickness. Thicker films showed bulk like lattice parameter values and presented a cubic structure. Fluctuations around the theoretical value were on the range of thousandth of nanometer and were related with the experimental error.

Rocking curves recorded on $SrTiO_3$ reflections showed a narrowing of the diffraction peaks with increasing film thickness, indicating the formation of larger crystallographic domains. Crystal domain sizes were calculated from the rocking curves recorded on $SrTiO_3$ reflections using equation 2.23. FWHM of the curves was obtained by fitting the measured peaks with a Pseudo-Voigt function. Average crystal domain sizes are shown in table 4.8.

4.3.2.3 Stability of the $SrTiO_3$ films

For the successful preparation of $Fe_3O_4/SrTiO_3/Si$ heterostructures it is mandatory to preserve the $SrTiO_3$ properties during and after the evaporation of the Fe_3O_4 films. Moreover, Hsu *et al.* reported on the presence of a remained amorphous silicate layer on the $SrTiO_3/Si$ interface, observed by cross-section HRTEM characterization on samples prepared under identical conditions to those used on this work [235]. TEM images reported by them are reproduced in Figure 4.16. The thickness of this amorphous interlayer increased slightly with $SrTiO_3$ thickness going from less than 1 nm for 5 nm thick $SrTiO_3$ films to almost 2 nm on 40 nm thick evaporated layers. The evolution of this interlayer needs to be considered when analyzing the stability of the system during the evaporation.

Anneal temperature (^oC)	350	550	650
Oxygen pressure (mbar)	8×10^{-7}	2×10^{-6}	1×10^{-5}
Annealing time (min)	30	30	30

Table 4.9: Annealed conditions used to study the stability of $SrTiO_3/Si$ films

In order to evaluate the stability of the $SrTiO_3/Si$ films under evaporation conditions, the films were yield under temperature and oxygen pressure equivalent to that chosen for magnetite evaporation and *in situ* characterized by XPS at each stage. Temperature and pressure conditions used during the annealing are resumed in 4.9. The base pressure of the chamber was 1×10^{-10} mbar. The process was repeated for the four $SrTiO_3$ thickness, carrying out the whole process in UHV and gradually increasing the annealing temperature. After annealing at the highest temperature, the samples were extracted from the UHV chamber and characterized by XRR and XRD.

This experiment was intended to evaluate the effect of the annealing temperature on the structural properties of the $SrTiO_3$ films, especially focusing on analyzing

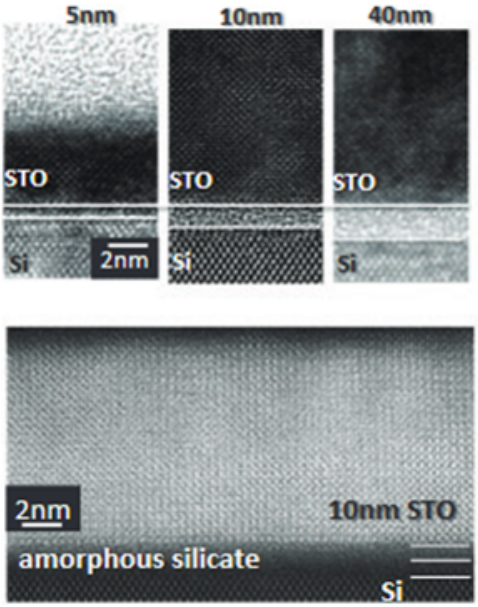

Figure 4.16: Cross section TEM characterization of the $SrTiO_3$/Si films. A remained silicate layer of around 1 nm thickness is observed on the $SrTiO_3$/Si interface. Figure reproduced from reference [235].

the formation of oxygen defects, which can completely modify the good insulator properties of the material. Additionally, it was aimed to evaluate the evolution of the $SrTiO_3$/Si interface, trying to identify the possible segregation of silicates species to the sample surface.

Structural parameters

After annealing successively at 350, 550 and 650°C the samples were extracted from the UHV chamber and characterized by XRR and XRD at ambient conditions using a photon energy of 20 keV. Figure 4.17 shows the low angle reflectivity for Samples from A to D (1.8, 4.8, 10.9 and 42 nm respectively) before and after the thermal treatment. In the as inserted samples, well defined intensity oscillations of the reflected beam appeared and the presence of a second frequency could be hinted in a slight modulation of the amplitude of the oscillations. After the annealing, the presence of this second frequency became more evident, which was especially remarkable in Sample D (42 nm). The appearance of a second group of oscillations was related with the formation of this amorphous silicate layer on the $SrTiO_3$/Si interface during $SrTiO_3$ evaporation, as already observed by Hsu *et al.* [235]. The modification on this frequency after annealing indicated the modification of this

interlayer, pointing to an increase of its thickness during annealing.

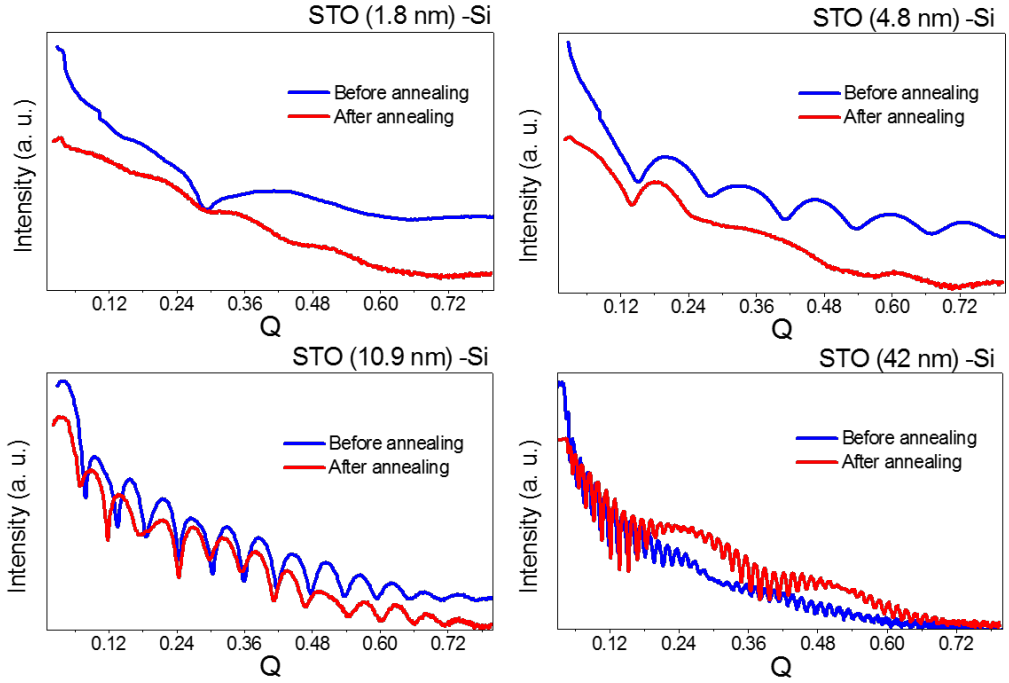

Figure 4.17: XRR measurements on $SrTiO_3$ films of 1.8, 4.8, 10.9 and 42 nm thickness before and after annealing at 650°C under oxygen atmosphere. The modification of the curve show the appearence of a second frequency related with the presence of a new layer with well-defined interfaces.

Lattice parameters and domain sizes were calculated and compared with those for as grown films. With exception of Sample A (1.8 nm), temperature had not an appreciable effect on the lattice parameter and values obtained for the in-plane (a) as well as for the out of plane (c) remained unaltered. In the particular case of Sample A, which showed a commensurate growth, exposition to temperature induced the relaxation of the initial strain resulting on a bulk-like lattice parameter after the treatment. Crystallographic domain size did not show any significant variations after annealing. It can therefore be inferred from the results that heating the samples had no effect on the structural properties of the $SrTiO_3$ films, so that they are expected to be preserved also during magnetite evaporation.

Formation of oxygen defects

$SrTiO_3$ is prompt to form oxygen vacancies during annealing at temperatures over 700°C under reductive conditions. Generally, the introduction of a partial oxy-

gen pressure during the annealing can prevent from the formation of these defects, and therefore evaporation conditions were not expected to modify the oxygen stoichiometry of the films. Moreover, the temperatures considered for the deposition are below the 700°C threshold. However, due to the important influence of this kind of defects on the insulator properties of the material, the possible formation of oxygen defects during the annealing was evaluated by XPS.

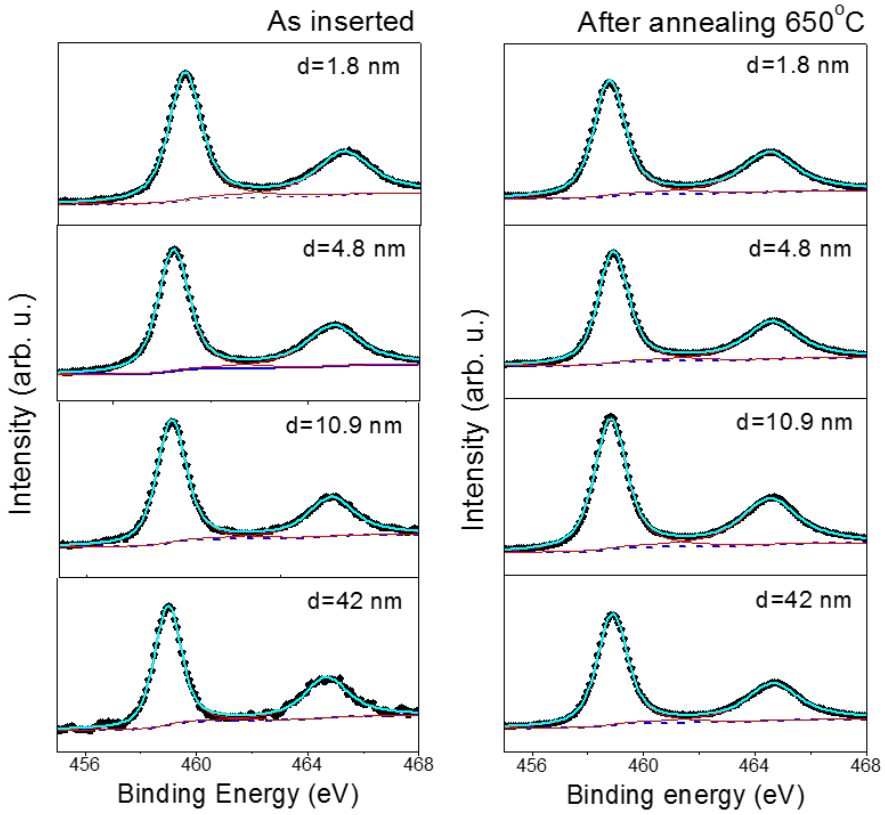

Figure 4.18: Ti2p core level XPS spectra measured on the as inserted $SrTiO_3$ films and after subsequently annealed them up to 650°C under O_2 atmosphere.

The appearance of oxygen vacancies on $SrTiO_3$ is expressed by a second doublet on the Ti2p core level spectra associated to the formation of Ti^{+3} centers (see Section 3.4). Figure 4.18 shows the recorded XPS Ti2p core level spectra for the four $SrTiO_3$ films before and after annealing up to 650°C. The spectra showed a single doublet, with the characteristic spin-orbit splitting of 5.8 eV. After annealing in a accumulative way at 350, 550 and 650°C, XPS measurements did not show any evidence of the presence of oxygen defects, in agreement with the previous studies performed in bulk $SrTiO_3$ (Section 3.4).

Evolution of the $SrTiO_3/Si$ interface

In order to have a better knowledge about the evolution of the amorphous silicate layer during the annealing, XPS measurements performed in Samples A (1.8 nm) and B (4.8 nm) were carefully analyzed. The low thickness of these films allowed the access to the interface, providing information about the progress of this silicate layer. Figure 4.19 shows the Si2p core level spectra for Sample A (1.8 nm) and Sample B (4.8 nm) before and after subsequently annealing. The charge correction was performed using the energy position of the C1s core level as reference (not shown).

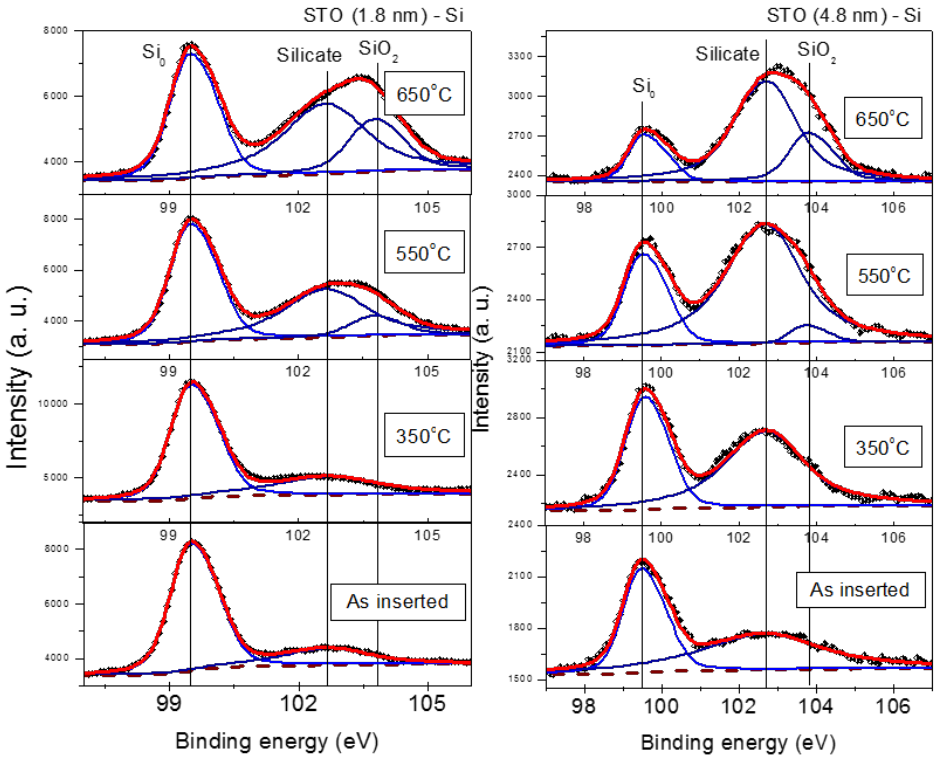

Figure 4.19: Evolution of the Si2p core level XPS spectra for $SrTiO_3$ films with thickness of 1.8 nm (left) and 4.8 nm (right) respectively upon subsequently annealing at 350, 550 and 650°C.

For the as inserted samples two intensity peaks were observed on the spectra. The Si2p core level presents a reduced spin orbit splitting of only 0.63 eV so that the two contributions overlap and appear like a single one. The most intense peak (E_B=99.5 eV) was related to the Si_0 signal from the substrate meanwhile the less intense signal was attributed to the buried silicate layer. This second signal presented an energy

displacement of 3.1 eV respect to the Si_0 signal and a much broader profile. The position of the peak was in agreement with previous reports on this silicate layer [235]. After annealing at 350°C, the relative intensity of this second contribution increased, which can indicate a larger amount of silicate or a segregation of this silicate to areas nearer to the surface. After annealing at 550°C the peak became significantly broader and showed a remarkable asymmetry. In order to fit the experimental data a third contribution needed to be considered, which presented an energy shift of 4.2 eV respect to the main peak. This chemical shift correspond with the expected position for SiO_2. This peak was associated with the formation of silicon dioxide on the Si interface due to oxygen diffusion through the $SrTiO_3$ layer. Upon annealing at 650°C both signals increased significantly. Based on these observations it was concluded that the exposition of the samples to high temperature resulted on an increase of the buried silicate layer thickness and, moreover, it also induced the formation of SiO_2 phases when the temperature was increased over 550°C. However, the distribution of these phases inside the sample could not be completely elucidated from the data collected. In any case, what was proved was the dependence of the $SrTiO_3$/Si interface with the temperature and the need of paying especial attention to this feature after magnetite evaporation. Moreover, as observed in the previous section for Fe_3O4/SiO_2/Si heterostructures, the presence of iron could even enhance oxygen uptake by Si and accelerate the oxidation process.

4.3.3 Preparation of the $Fe_3O_4/SrTiO_3$/Si heterostructures

4.3.3.1 Fe_3O_4 evaporation by PLD and phase identification by XAS

Magnetite films were evaporated on top of the $SrTiO_3$/Si films by PLD by hitting a polycrystalline Fe_3O_4 target. A set of nine samples in total was prepared with an equivalent expected thickness of around 15 nm of Fe_3O_4 but using different $SrTiO_3$ thicknesses (1.8, 4.8 and 10.9 nm) and different evaporation temperatures (350, 550 and 650°C). The oxygen pressures used during the growth for each temperature are resumed in table 4.9. The $SrTiO_3$ films were heated up during the evaporation in order to favor the crystalline growth of magnetite meanwhile the oxygen pressure is thought to preserve the stoichiometry of the Fe_3O_4 layer and avoid the formation of oxygen vacancies in the $SrTiO_3$ films. *In situ* RHEED characterization during the evaporation proved the crystalline growth of the magnetite layers, indicating the formation of single oriented films for temperatures up to 550°C. At 650°C a ring like pattern was observed by RHEED indicating the formation of polycrystalline phases.

In order to evaluate the oxidation state of iron on the evaporated films XAS measurements were performed in the 9 samples at ambient conditions. XAS is a powerful technique for the identification of iron oxide phases providing volumetric information (see section 3.3). XAS spectra recorded on the Fe K-edge for the whole set of samples are presented in Figure 4.20.

For $SrTiO_3$ thickness of 1.8 and 4.8 nm, a single magnetite phase was only stabilized when evaporating at 350°C. At 550°C metallic iron traces started to appear and at 650°C the XAS spectra proved the formation of iron silicides, showing a predominance of $FeSi_2$. The formation of metallic iron occurs at the same temperature for which XPS measurements proved the appearance of SiO_2 on annealed $SrTiO_3$ films. This behavior was already observed in $Fe_3O_4/SiO_2/Si$ systems, where the oxidation of silicon hampered the stabilization of the Fe_3O_4 films. When the $SrTiO_3$ thickness was increased to 10.9 nm, a single magnetite phase could also be stabilized at 550°C. Probably the increase on the $SrTiO_3$ thickness reduces the diffusion of oxygen to the interface with the silicon substrate and favors the stabilization of the Fe_3O_4 films at higher temperature. Still, at 650°C a similar spectra to that observed at 550°C for thinner $SrTiO_3$ films was observed, stating a significant presence of metallic iron. From this it can be deduced that increasing the $SrTiO_3$ thickness hampers the diffusion of oxygen towards the Si interface requiring higher temperature to produce silicon oxidation.

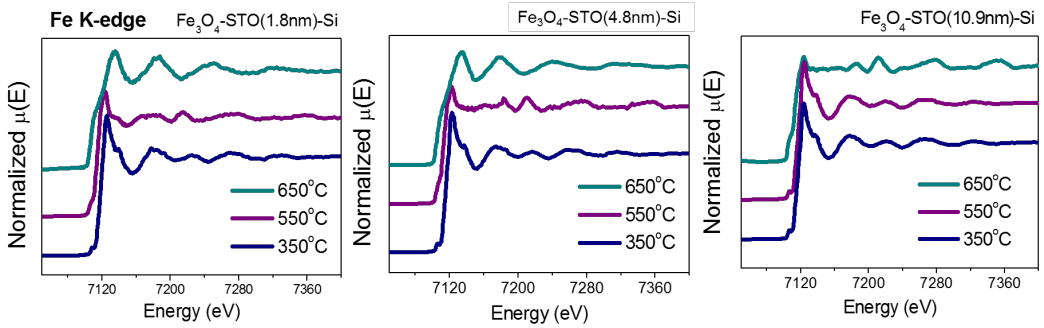

Figure 4.20: XAS spectra recorded on the Fe K-edge for the Fe_3O_4 heterostructures. Each graphic shows the spectra for the magnetite evaporated at different temperature on a $SrTiO_3$ film of different thicknesses (1.8, 4.8 and 10.9 nm).

T_{evap} (°C)	$SrTiO_3$ thickness		
	1.8 nm	**4.8 nm**	**10.9 nm**
350	Fe_3O_4	Fe_3O_4	Fe_3O_4
550	Fe_3O_4(68.5%) + Fe(31.5%)	Fe_3O_4(43.9%) + Fe(56.1%)	Fe_3O_4
650	β-$FeSi_2$(87.3%) + FeSi(12.7%)	Fe_3O_4(4.6%) + β-$FeSi_2$(78%) + FeSi(17.4%)	Fe_3O_4(35.2%) + Fe(64.8%)

Table 4.10: Iron phases identified by XAS on the $Fe_3O_4/SrTiO_3$(001)/Si(001) heterostructures. The proportion was calculated by linear combination fitting using different standards.

The identification of the different phases presented on each sample was made by linear combination fitting from different iron standards using the Demeter package [113]. Results obtained from the analysis are resumed in table 4.10, showing the different phases identified at each sample and the proportion in which they were found. Comparing the results obtained by XAS with the evolution observed for the $SrTiO_3$ films after annealing (Sec. 4.3.2.3),a the direct relation between the formation of SiO_2 on the Si interface and the formation of metallic iron phases was denoted. In order to avoid the oxidation of silicon and successfully prepared single phase magnetite films, evaporation temperature needed to be kept at 350°C. Increasing the $SrTiO_3$ thickness allowed the stabilization of Fe_3O_4 films at higher temperature. In the following sections, the properties of the $Fe_3O_4/SrTiO_3/Si$ heterostructures will be analyzed from two different perspectives. First, the characteristics of the system will be discussed considering static evaporation conditions and modifying the $SrTiO_3$ thickness (Section 4.3.4.1). Second, the characteristics of the system will be analyzed as a function of the evaporation temperature with a fixed $SrTiO_3$ thickness of 10.9 nm (Section 4.3.4.2).

4.3.4 Characterization of the Fe_3O_4/ $SrTiO_3$/Si heterostructures

4.3.4.1 Influence of the $SrTiO_3$ thickness

Magnetite films with an expected thickness of around 15 nm were evaporated at 350°C under an oxygen pressure of 8×10^{-7} mbar on top of $SrTiO_3$ films with thicknesses of 1.8, 4.8 and 10.9 nm, The samples were subsequently characterized by XRR, XRD, HRTEM, HAXPES, SEM and MOKE, trying to identify the possible influence of the $SrTiO_3$ thickness on the final properties of the heterostructure. Cross section HRTEM and HAXPES measurement were especially focused to the characterization of the buried $Si/SrTiO_3$ interface in order to evaluate the formation of silicates or silicon oxide phases during magnetite evaporation.

Structural characterization

Fe_3O_4/ $SrTiO_3$/Si samples were characterized by XRD using a photon energy of 20 keV. Two points were considered, the characteristics of the evaporated magnetite films and the modification of the $SrTiO_3$ films by influence of the iron oxide deposition. The characterization of the $SrTiO_3$ films previous to the evaporation of magnetite proved the epitaxial growth of the films on Si with an in plane rotation of 45 degrees (see section 4.3.2.2). Thinnest film (1.8 nm) showed a commensurate growth meanwhile for thicker films (4.8 and 10.9 nm) the structure was found to be completely relaxed revealing bulk like structural parameters.

Figure 4.21 shows two dimensional RSM representing H=K versus L on reciprocal space units refereed to the silicon substrate for the three $SrTiO_3$ thickness before

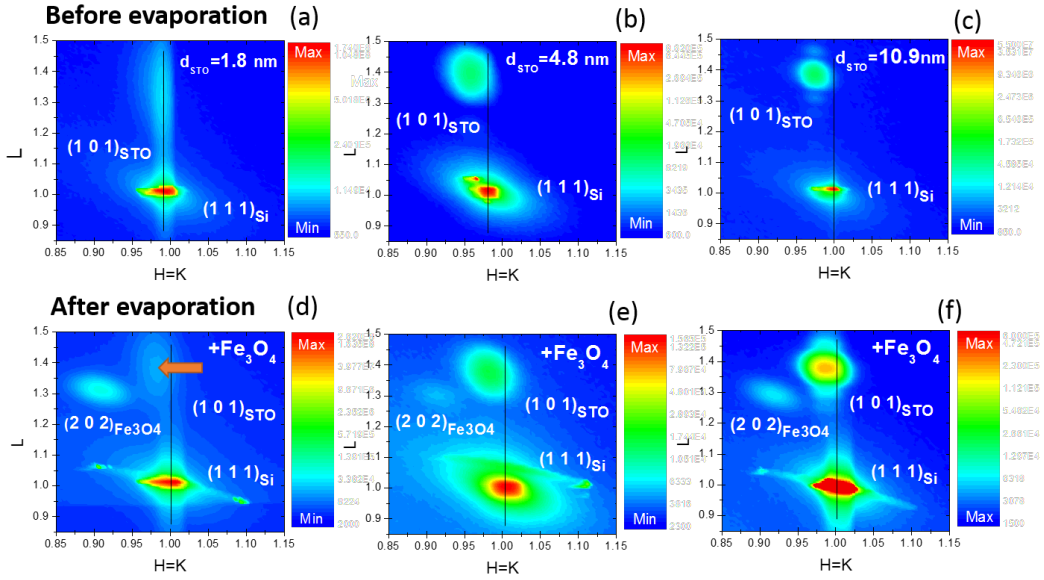

Figure 4.21: Reciprocal space maps showing the contribution of the silicon substrate, the Fe_3O_4 and $SrTiO_3$ films. The most significant feature is the displacement of the $SrTiO_3$ reflection after the evaporation of magnetite, indicating a relaxation of the structure.

(a-c) and after (d-f) magnetite evaporation. In the region of the reciprocal space probed three reflections were collected, (111)Si and (101)$SrTiO_3$ before the evaporation and (202)Fe_3O_4 after evaporation. In the thinnest $SrTiO_3$ film (1.8 nm), a displacement of the $SrTiO_3$(101) reflection was observed, which indicated the relaxation of the $SrTiO_3$ lattice after the deposition of the magnetite films. This behavior was already observed in $SrTiO_3$(1.8 nm)/Si films upon annealing. Consequently, in the final heterostructures $SrTiO_3$ films presented a relaxed structure regardless of its thickness.

Magnetite was found to grow incommensurate on $SrTiO_3$ axis, and consequently with a rotation of 45 degrees respect to the Si lattice so that (100)Fe_3O_4 $\|$ (100)$SrTiO_3$ $\|$ (110)Si. A commensurate growth was unlikely due to the high lattice mismatch between both structures ($0.839 >> 2\times0.390$). Calculated lattice parameters for the magnetite films, which are resumed in table 4.11, showed bulk-like values within the range of the experimental error regardless of the $SrTiO_3$ thickness. (202)Fe_3O_4 reflection presented a slightly elongated shape. This might be related with the formation of different crystallographic domains to favor the coupling between the lattices.

Crystal domain size for Fe_3O_4 films were calculated performing rocking scans on different diffraction peaks. In order to analyze the influence of the $SrTiO_3$ thickness on the structural properties of magnetite, scans measured on the same reflection were compared for the three samples in order to have a qualitative characterization

d_{STO}	Fe_3O_4 lattice parameter (nm)		
	In plane (a)	Out of plane (c)	Tetragonality (a/c)
1.8 nm	0.845±0.004	0.837±0.004	0.99±0.01
4.8 nm	0.845±0.004	0.842±0.005	0.99±0.01
10.9 nm	0.838±0.004	0.833±0.005	0.99±0.01

Table 4.11: Lattice parameter calculated for the Fe_3O_4 films evaporated on top of different $SrTiO_3$ thick films.

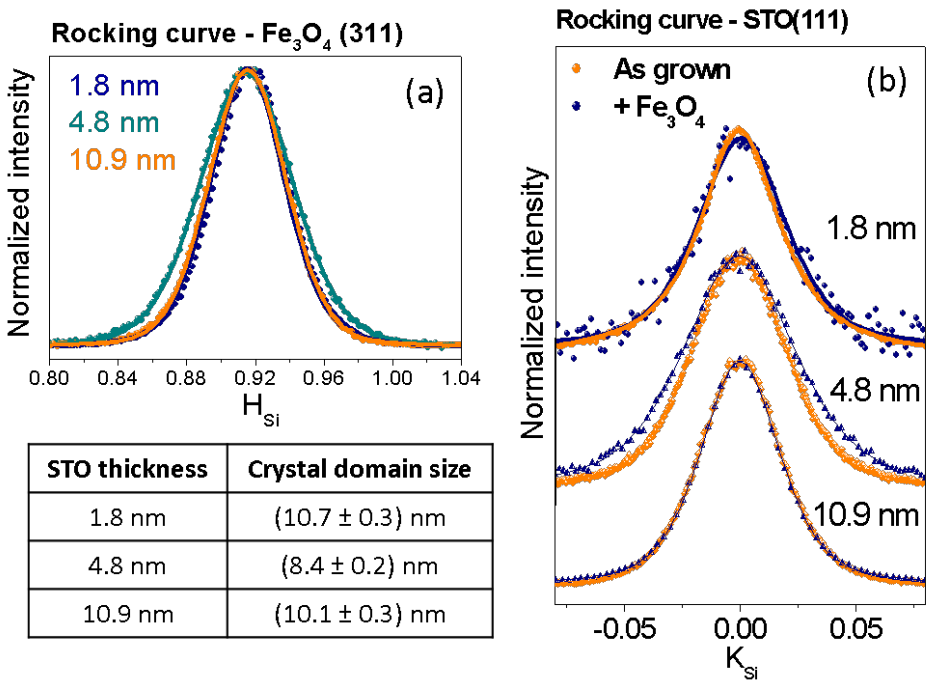

STO thickness	Crystal domain size
1.8 nm	(10.7 ± 0.3) nm
4.8 nm	(8.4 ± 0.2) nm
10.9 nm	(10.1 ± 0.3) nm

Figure 4.22: (a) Rocking curves on the (311) reflection of magnetite for different $SrTiO_3$ thickness. No influence of the $SrTiO_3$ thickness on Fe_3O_4 crystal domain sizes was observed. (b) Rocking curves for the $SrTiO_3$ films recorded on the (111) reflection before and after the evaporation. No significant differences were evidenced.

of the evolution of the system. Average crystal domain size values were calculated by fitting the rocking curves with a pseudo Voigt function and using equation 2.23. This information is resumed in Figure 4.22(a). The acquired spectra for Fe_3O_4 showed a very similar profile independently of the thickness of the $SrTiO_3$ layer. Crystal domain sizes for $SrTiO_3$ presented similar values before and after Fe_3O_4 evaporation. Most likely, the crystal domain sizes in the magnetite films are limited by domain boundaries in the buffer $SrTiO_3$ layer.

Crystal domain sizes on $SrTiO_3$ films were demonstrated to be unaltered after annealing at 350°C under a partial oxygen pressure (see section 4.3.2.3). The comparison of the rocking curves on the (111)$SrTiO_3$ reflection before and after the Fe_3O_4 evaporation confirmed the steadiness also during the evaporation of magnetite (Fig. 4.22(b)). Besides the release of the lattice in the thinnest film (1.8 nm), it can be concluded that the evaporation had not significant impact on the structural properties of the $SrTiO_3$ films. Therefore, for the final heterostructure $SrTiO_3$ as well as Fe_3O_4 films showed an incommensurate growth with a bulk-like lattice parameter and similar domain sizes of around 10 nm.

Morphological characterization

Morphological differences between the samples were hinted during the evaporation from the different features observed on the respective RHEED patterns. Figure 4.23 present the RHEED patterns and XRR measurements for the Fe_3O_4/ $SrTiO_3$/Si heterostructures before and after the evaporation of the magnetite layer.

The RHEED patterns for the $SrTiO_3$ films showed the presence of strikes for the three $SrTiO_3$ thickness, related in general with the formation of a flat surface. According to this, reflectivity measurements showed well defined oscillations proving a low surface and interface roughness. RHEED patterns for Fe_3O_4 showed a transition from a strike like pattern to a dot pattern as the $SrTiO_3$ thickness was increased, which is generally related with the formation of more particulate films. XRR curves presented a similar trend where a faster decay of the oscillations was observed after evaporating on top of thicker $SrTiO_3$ films. Moreover, after the evaporation of magnetite a new group of oscillations appeared. This second group of oscillations was supposed to be produced by the interference between the x-rays reflected in the magnetite surface and the $Fe_3O_4/SrTiO_3$ interface. Under this assumption, magnetite thickness was calculated from the minima of the fringes of the reflected intensity using equation 2.12. Resulting values were 18.2 ± 0.5, 16.7 ± 0.5 and 11.8 ± 0.4 nm for the layers evaporated on top of 1.8, 4.8 and 10.9 nm thick $SrTiO_3$ films respectively.

Magnetite surface was also characterized by SEM. Figure 4.24 show SEM images acquired at 70000X. The three images are represented on the same scale so they can be directly compared. Images were recorded for magnetite films evaporated on top of $SrTiO_3$ films with 1.8 (a), 4.8 (b) and 10.9 nm (c) thickness. Increasing $SrTiO_3$

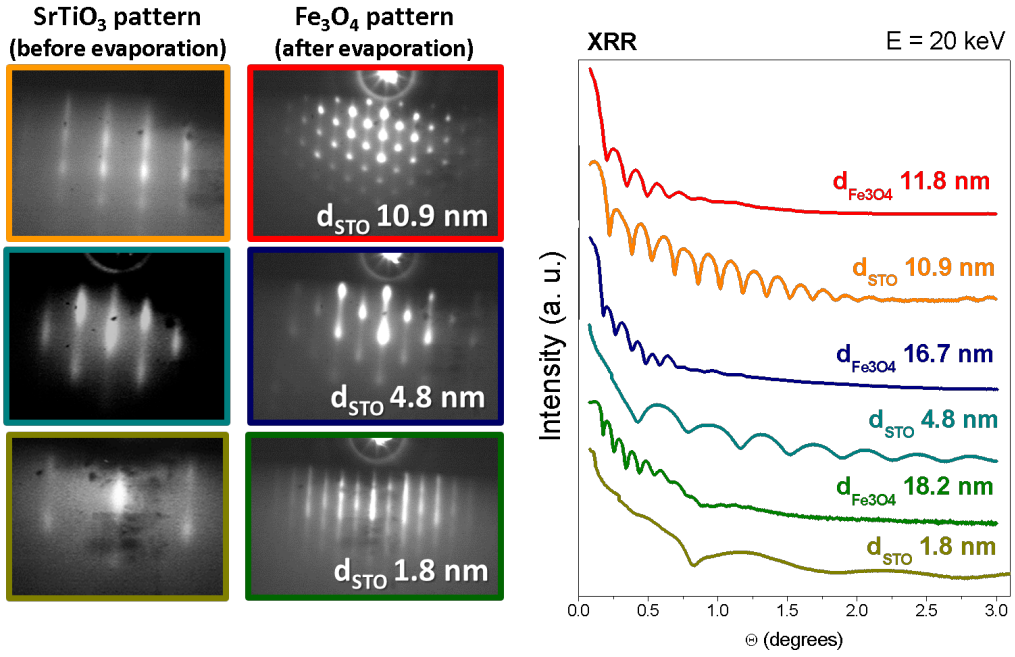

Figure 4.23: RHEED patterns (left) and XRR measurements (right) on Fe_3O_4/ $SrTiO_3$/Si systems with different $SrTiO_3$ thickness before and after evaporation of magnetite. RHEED patterns showed already different morphological features confirmed by XRR measurements. The appearance of spots on the RHEED patterns and a faster decay of the oscillations on the XRR curves proved an increase of surface roughness with $SrTiO_3$ thickness.

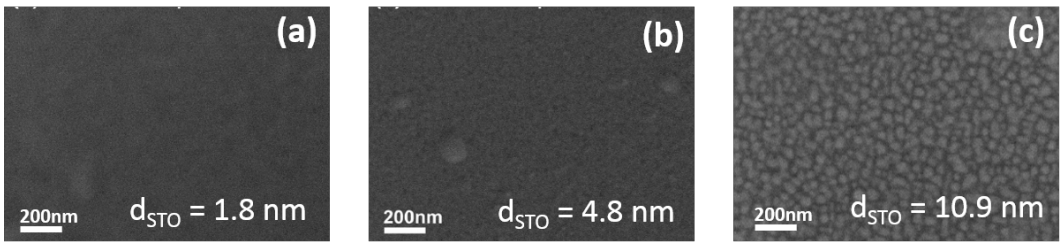

Figure 4.24: SEM images acquired at 70000X of the Fe_3O_4 surface for $SrTiO_3$ thickness of 1.8 (a), 4.8 (b) and 10.9 nm (c). (a) and (b) showed a highly homogeneous surface where only some perturbations with bubble shape appeared. These were due to contamination due to exposition to air. On the contrary, (c) showed the formation of a highly particulate film.

thickness induced a transition between an extremely smooth surface to the formation of granular structures. Fig. 4.24 (a) and (b) showed similar features, proving a smooth and highly homogeneous surface. Only small perturbations in the shape of a bubble were observed, which were related with surface contamination due to the exposition to air. On the contrary, fig. 4.24 (c) showed the formation of a highly particulate film. This explains also the appearance of a dot pattern in RHEED. The different islands formed presented similar height, regular distribution and a small size dispersion. The grains showed an average size of ≈70 nm. A low degree of overlapping between grains was observed, pointing to a transition from a continuous to a non-continuous film with increasing $SrTiO_3$ thickness. The conditions during the growth were identical for the three samples and could not justify this change in the morphology of the films. The most likely explanation was an increase on the surface roughness for $SrTiO_3$ films with increasing thickness. The higher roughness of the starting surface favored the formation of different nucleation centers and promoted an island like growth mechanism.

Characterization of the interface by HAXPES and HRTEM

Understanding the interface properties of the system was mandatory in order to evaluate its potential functionality. The formation of a silicate layer on the $SrTiO_3/Si$ interface during $SrTiO_3$ evaporation has been proved in previous works [235] as well as on the present thesis (see section 4.3.2.3). Moreover, in section 4.3.2.3 XPS measurements proved an increase of the amount of silicate on the system after annealing at 350^{o}C. HAXPES measurements were performed using a photon energy of 10 keV in order to obtain information about the buried $SrTiO_3/Si$ interface after magnetite evaporation.

Normalized Si1s core level spectra for the three samples are shown in Figure 4.25. Spectra prior to the evaporation (inset) showed similar features for the three samples, evidencing a main peak correspondent with Si with a small asymmetry at lower binding energies. The asymmetrical lineshape was related with the presence of a remained silicate layer on the $SrTiO_3/Si$ interface. After the evaporation of magnetite the three samples evolved in a similar way. The shoulder hinted at lower binding energy in the $SrTiO_3$ films became more evident. This pointed to the formation of more silicate/silicon oxide during magnetite evaporation. The deconvolution of the spectra showed that this second contribution had a energy shift of 4 ± 0.2 eV. Considering the results in section 4.3.2.3, this chemical shift was associated with the presence of silicates on the interface and not with the formation of silicon oxide.

Samples were also characterized by HRTEM. As a representative example, Figure 4.26 shows cross section TEM images for $Fe_3O_4/SrTiO_3$(4.8 nm)/Si sample. Fig.4.26(a) shows a general view of the multilayer heterostructure where the different compositions were indicated. Silicon substrate was followed by an amorphous

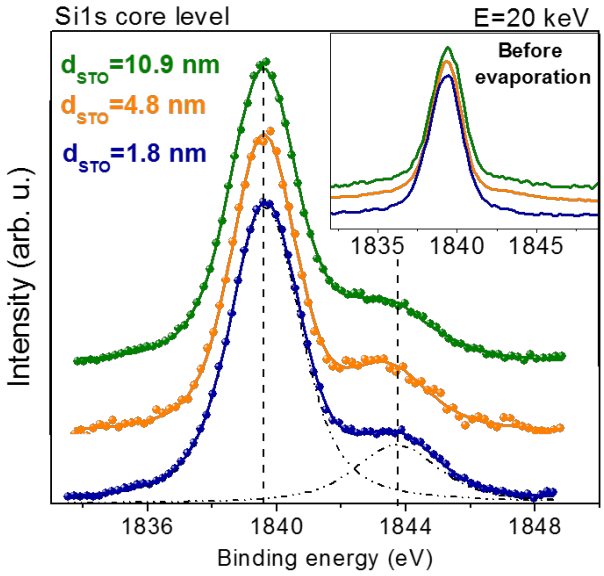

Figure 4.25: HAXPES measurements on the Si1s core level spectra on Fe_3O_4/ $SrTiO_3$/Si heterostructures with different $SrTiO_3$ thickness. The inset shows the spectra recorded before the evaporation. The three samples showed an identical evolution regardless of the $SrTiO_3$ thickness, proving the dependence of the interface with deposition temperature.

silicate layer of about 2 nm (brightest area). Although in the image this layer was identified as SiO_2, considering HAXPES measurements is more likely to be composed by a silicate. Then the epitaxial $SrTiO_3$ layer of 5 nm thickness and finally a flat Fe_3O_4 film with a thickness of around 10 nm. $SrTiO_3$ and Fe_3O_4 layers showed significantly low contrast due to the similar density between both materials (4.81 and 5.15 g/cm^3). In agreement with the observations made by SEM, Fe_3O_4 film showed a flat surface and a homogeneous thickness. Fig.4.26(b) shows a zoomed image of the interfaces, proving abrupt and significantly flat interfaces. No amorphous interface between $SrTiO_3$ and Fe_3O_4 was observable. The indexation of the fast Fourier transforms (FFT) (Fig. 4.26(c-e)) indicated that the zone axis for the silicon substrate was [110] meanwhile for the $SrTiO_3$ and Fe_3O_4 layers it was [100], in agreement with XRD.

The presence of an amorphous silicate layer characterized by HAXPES in the $SrTiO_3$/Si interface was confirmed by TEM for the three Fe_3O_4/$SrTiO_3$/Si characterized samples. Regardless of the $SrTiO_3$ thickness, this layer was estimated to be around 2 nm thick, proving the absence of correlation between the two parameters. In the same way, a well-defined $SrTiO_3$/Fe_3O_4 interface was observed in the three samples, without any proved presence of amorphous phases. Magnetite films evaporated on top of $SrTiO_3$ with a thickness of 1.8 and 4.8 nm showed a two dimensional

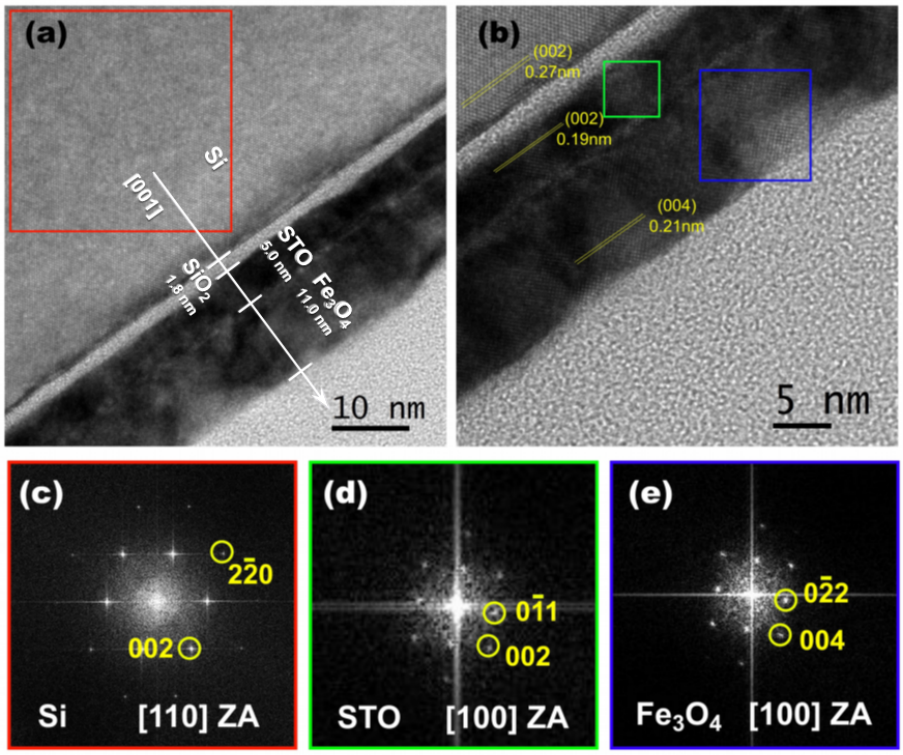

Figure 4.26: (a) Cross section TEM image on $Fe_3O_4/SrTiO_3$(4.8 nm)/Si sample and (b) zoomed HRTEM image. (c-e) FFT on the selected areas on colored boxes which proved the epitaxial growth of the films. Although in the image is labeled as SiO_2, the amorphous layer in the $SrTiO_3$/Si interface was identified as a silicate by HAXPES.

growth with thickness ranging between 10-15 nm and 10-11 nm respectively. Sample $Fe_3O_4/SrTiO_3$(10.9 nm)/Si showed an island like structure, as observed by SEM, with the island height ranging from 15 to 18 nm.

Magnetic characterization by MOKE

The magnetic response of the magnetite films was characterized by MOKE at room temperature and ambient pressure. Recorded hysteresis loops are shown in Figure 4.27. The three samples showed a ferromagnetic response at ambient conditions. As general trend, the magnetite films showed similar coercive field and smaller remanence with increasing $SrTiO_3$ thickness.

The samples showed a reduction of the magnetization, proportional to the normalized Kerr voltage, as the $SrTiO_3$ thickness was increased. The drop on the

magnetization for the sample evaporated using a $SrTiO_3$ thickness of 10.9 nm was explained by the transition from a 2D to a 3D growth in the shape of islands. Given the similar properties of the samples prepared with $SrTiO_3$ thickness of 1.8 and 4.8 nm, the magnetic properties could be expected to be similar. Nevertheless, the larger magnetization for the samples with a thinner $SrTiO_3$ layer (1.8 nm) could be explained by the higher thickness of the magnetite films (ranging between 11 and 15 nm respect to 10-11 nm for d_{SrTiO_3}=4.8 nm). Superimposed to the hysteresis cycles there was a paramagnetic contribution that impeded a complete saturation. This contribution was produced by the $SrTiO_3$ layer. The differences on the magnetic behavior of the films were related with the morphological features and the changes on the magnetite film thickness. The fluctuations on the coercive field can be related with different factors as the film thickness or the cohesion of the film.

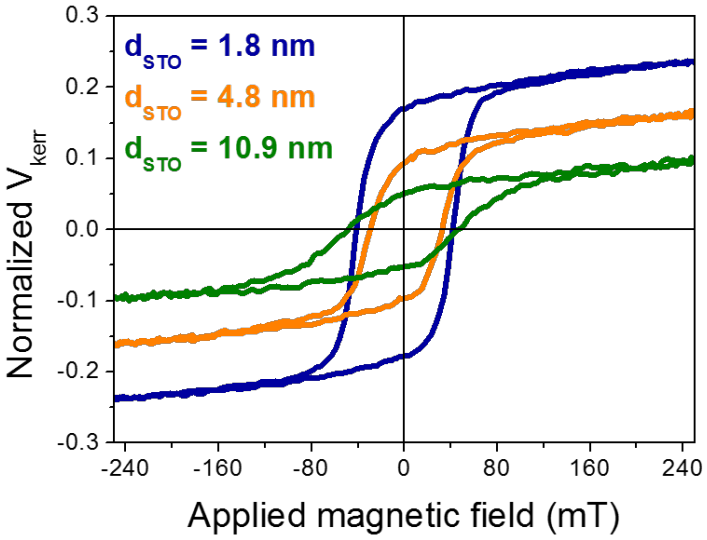

Figure 4.27: MOKE hysteresis loops recorded on $Fe_3O_4/SrTiO_3/Si$ heterostructures prepared under identical conditions with a variable $SrTiO_3$ thickness.

One of the interest on evaporating single oriented crystalline magnetite films is the possibility of tuning the magnetic properties of the system by varying its structural properties, as for example changing the strain of the lattice Previous works have discussed the influence of the strain and the crystallographic orientation on the magnetic properties of magnetite [236–238]. In the case of bulk magnetite, the magnetic anisotropy of the system is controlled by the crystal structure and can be defined by the anisotropy constant K_1 [239]. Nevertheless, in the case of nanoscale systems, there would exist a uniaxial anisotropy arisen from the shape of the magnetic particles or films and that might favor the magnetization in a particular

direction. This effect is driven by the constant of anisotropy K_u [239]. According to some predictions based on classical theory for the particular case of a thin film, where the length is much greater than the thickness (L>>d), this constant K_u will have a value of 1.4×10^5 meanwhile $|K_1|=1.3\times10^4$. In other words, in the case of a thin film the contribution of the unaxial anisotropy would be ten times that of the magnetocrystalline anisotropy, being a predominant effect.

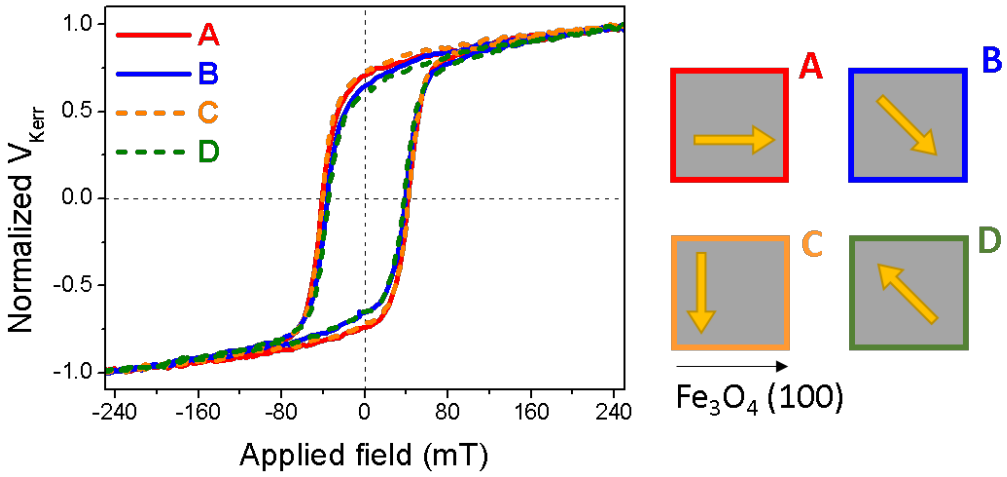

Figure 4.28: MOKE hysteresis loops recorded on $Fe_3O_4/SrTiO_3$(1.8 nm)/Si applying the magnetic field with a different angle respect to the crystallographic axis. Cycles recorded with the magnetic field parallel to the [100] and [010]Fe_3O_4 crystallographic axis showed a slightly higher remanence, indicating the presence of an easy axis on this direction with a symmetry of 90 degrees.

During this thesis, the presence of a preference direction for the magnetization was analyzed by changing the direction of the crystallographic axis of the magnetite structure respect to the applied magnetic field, always in a longitudinal configuration. Figure 4.28 shows normalized hysteresis loops for the Fe_3O_4 films evaporated at 350°C on $SrTiO_3$(1.8 nm)/Si recorded in different crystallographic directions. Results indicated the presence of an easy axis when the field was applied parallel to the [010] and [100] directions with a symmetry of 90 degrees. This easy axis was characterized by a slightly larger coercive field and higher remanent magnetization. The faint difference between the easy and hard axis was explained by the predominance of the unaxial anisotropy coefficient. Nevertheless, this effect could be significantly enlarged by increasing the thickness of the magnetite films so that the unaxial anisotropy coefficient is reduced. For instance, Zhang *et al.* observed clear difference on the magnetic properties of magnetite films with a thickness of 480 nm depending on the crystallographic texture of the films [240].

4.3.4.2 Influence of the evaporation temperature

Magnetite films were stabilized on $SrTiO_3$(10.9 nm)/Si at temperatures of 350 and 550°C. Studies on thinner films proved the accelerated formation of silicate species on the $SrTiO_3$/Si interface during annealing and the unlikely stabilization for $T_{evap} \leq 350$°C. Fe_3O_4/ $SrTiO_3$ (10.9 nm)/Si heterostructures prepared at 350 and 550°C were characterized by XRR, XRD, SEM and MOKE in order to establish the influence of the evaporation temperature on the structural, morphological and magnetic properties of the magnetite films. Moreover, HAXPES and HRTEM measurements were performed in order to study the evolution of the interface at higher deposition temperature.

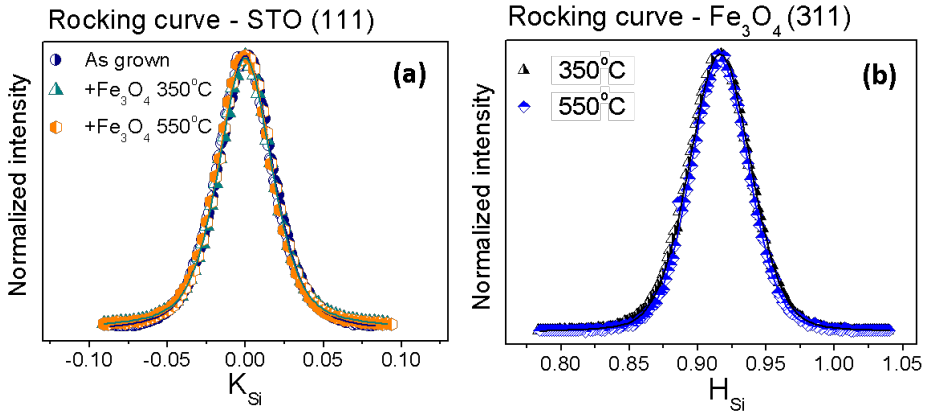

Figure 4.29: (a) Rocking curves on the (111)$SrTiO_3$ and (b) (311)Fe_3O_4 on Fe_3O_4/$SrTiO_3$(10.9 nm)/Si heterostructures prepared at 350°C and 550°C. The $SrTiO_3$ curves did not show any changes before and after the evaporation of magnetite. Equally, evaporation temperature did not significantly affect the crystallographic domains of the magnetite films.

Structural characterization

The Fe_3O_4/ $SrTiO_3$(10.9 nm)/Si heterostructures prepared at 350 and 550°C were characterized by XRD using a photon energy of 20 keV. In the previous section it was proved that Fe_3O_4 films evaporated at 350°C grew epitaxially and relaxed on $SrTiO_3$ films with Fe_3O_4[001]||$SrTiO_3$[001]||Si[001] and with an in-plane rotation of 45 degrees respect to the silicon axis so that Fe_3O_4[100]||$SrTiO_3$[100]||Si[110]. XRD measurements proved that increasing the evaporation temperature did not change significantly the structural properties of the Fe_3O_4 films. Magnetite layer evaporated at 550°C was proved to grow incommensurate axis on axis on $SrTiO_3$. An in plane lattice parameter of 0.842 ± 0.003 and an out of plane lattice parameter of 0.849 ± 0.007 nm was determined, approaching to bulk like values.

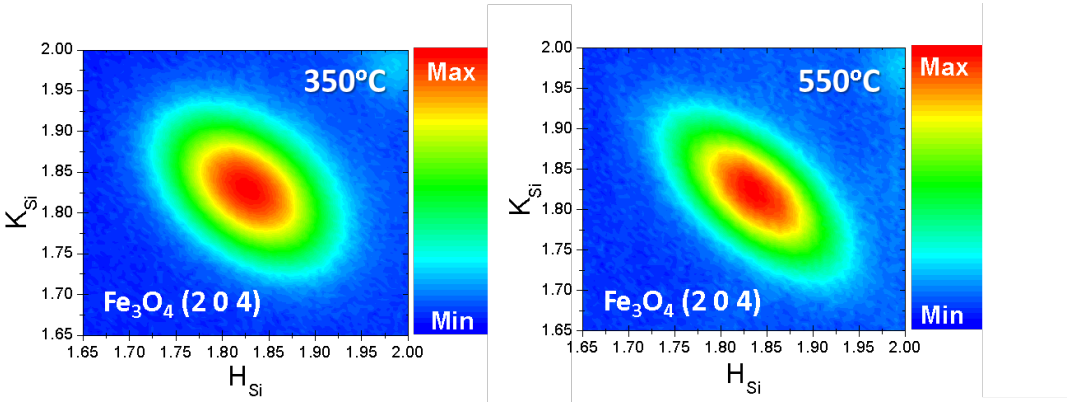

Figure 4.30: Reciprocal space maps of H_{Si} versus K_{Si} on the L_{Si} position corresponding to $L_{Fe_3O_4}$=4 on the reference system of the magnetite film. The images allow to obtain an in plane projection of the diffraction peaks showing a more elongated shape for the film evaporated at 550ºC

Crystal domain sizes were evaluated comparing several reflections and determining an average crystal domain size of 10.8 ± 0.2 nm for the magnetite films evaporated at 550ºC, respect to 11.1 ± 0.4 nm for films evaporated at 350ºC. Rocking curves were also recorded on $SrTiO_3$ reflections in order to evaluate the stability of the buried $SrTiO_3$ layer. Figure 4.29 shows rocking curves measured for the (311)Fe_3O_4(a) and (111)$SrTiO_3$(b) reflections. The results showed no modification of the peak profile for $SrTiO_3$ reflection and the unalterably of the average crystal domain size.

Figure 4.30 shows the in plane projection of the (204)Fe_3O_4 reflection. RSM were recorded scanning simultaneously on the H and K values relative to Si reference system with a fixed L value, corresponding to $L_{Fe_3O_4} = 4$. In both cases, the reflection showed an elongated shape, which is related with the formation of different crystallographic domains with slightly different lattice parameter in order to favor the coupling between the Fe_3O_4 and $SrTiO_3$ lattices. Nevertheless, at 550ºC this elongation became more evident, indicating a higher degree of mosaicity for magnetite films evaporated at higher temperature. To summarize, it could be concluded that evaporation temperature had no influence on the lattice parameter or crystal domain size. This can be said for the Fe3O4 as well as for the $SrTiO_3$ layer. The only difference in the structural properties of the sample was an increase of the mosaicity of the magnetite films when increasing the temperature during the deposition.

Morphological characterization

Figure 4.31(a) shows XRR measurements for the as grown $SrTiO_3$ (10.9 nm) film and after the evaporation of magnetite at 350 and 550ºC. As grown film showed the appearance of well-defined oscillations, proving a low interface and surface rough-

ness. After the evaporation of magnetite, the frequency of these oscillations was conserved but a faster decay at increasing incident angle was observed, related with an increased roughness of the $Fe_3O_4/SrTiO_3$ interface.

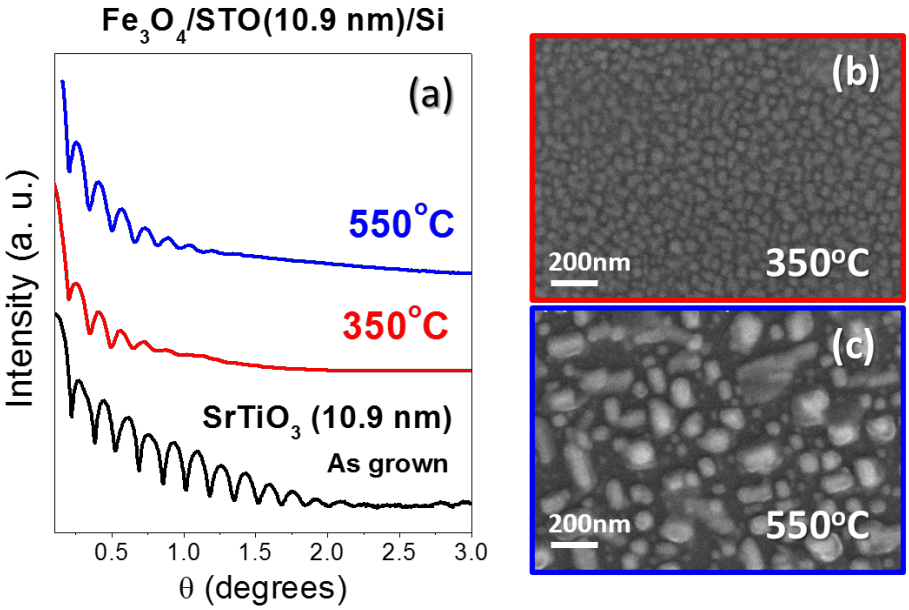

Figure 4.31: (a) XRR measurement at low angle and SEM images for $Fe_3O_4/SrTiO_3$(10.9 nm)/Si heterostructures prepared at (b) 350°C and (c) 550°C. XRR measurements showed the appearance of Kiessig fringes in both samples confirming the good quality of the buried interfaces. SEM images proved the granular character of the films, with the formation of larger grains and a greater size dispersion when increasing deposition temperature.

The absence of a coherent interference between the x-rays reflected on the interface and the magnetite surface was explained by the 3D growth of the magnetite films on top of the $SrTiO_3$ layer. XRR measurements did not show any significant effect of the temperature on the films morphology.

The surface morphology of the magnetite films was characterized by SEM. Images acquired at 70000 X are shown in Figure 4.31(b) and (c) for magnetite films evaporated at 350 and 550°C respectively. SEM images showed an island like growth in both samples. For magnetite films evaporated at 350°C, SEM images showed regular islands with a homogeneous distribution and a low size dispersion, with grains of around 70 nm width. Increasing the evaporation temperature resulted on the formation of bigger structures. Besides, the distance between the islands was increased together with the size dispersion. The scale of the structures ranged from a few tens of nanometers to values as high as 400 nm.

Characterization of the buried interfaces by HAXPES and HRTEM

Figure 4.32 shows HAXPES spectra of the Si1s core level for the $Fe_3O_4/SrTiO_3$(10.9 nm)/Si samples prepared at 350 and 550°C. A photon energy of 10 keV was used for the measurements and the binding energy was corrected using the silicon substrate signal as a reference. During the characterization of $SrTiO_3$/Si films a second contribution could be already hinted on the Si1s core level spectrum.

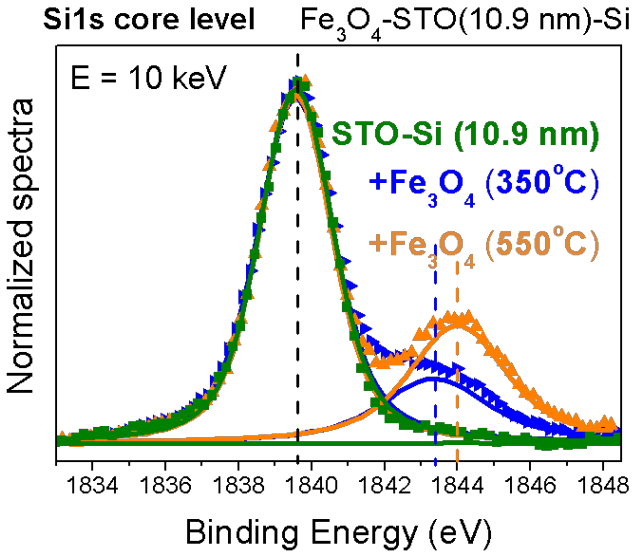

Figure 4.32: HAXPES measurements at 10 keV on the Si1s core level spectra performed on $Fe_3O_4/SrTiO_3$(10.9 nm)/Si heterostructures prepared at 350 and 550°C. The spectra showed two contributions, the most intense peak is related with the Si_0 and corresponds to the substrate. The second contribution observed at higher BE corresponds with the amorphous silicate interlayer. The energy shift of the silicate layer was increased from 3.8 to 4.4 eV when increasing the deposition temperature from 350 to 550°C.

After the evaporation of magnetite, the appearance of a second contribution was completely evidenced in the two samples, corresponding to the silicate layer observed by TEM on the $SrTiO_3$/Si interface. Nevertheless, the intensity and binding energy of this second peak showed a dependence with the evaporation temperature. For samples evaporated at 350°C this peak appeared with an energy shift of ΔE of 3.8 eV respect to Si_0 and was related to the formation of silicate species. After depositing at 550°C the peak was shifted to a final binding energy of ΔE=4.4 eV respect to the Si signal, corresponding with the energy shift observed in other samples for SiO_2. This result was consistent with the studies made on $SrTiO_3$/Si films, which indicated the formation of silicate species at annealing temperatures up to 350°C and the appearance of silicon oxide with increasing temperature (see section 4.3.2.3).

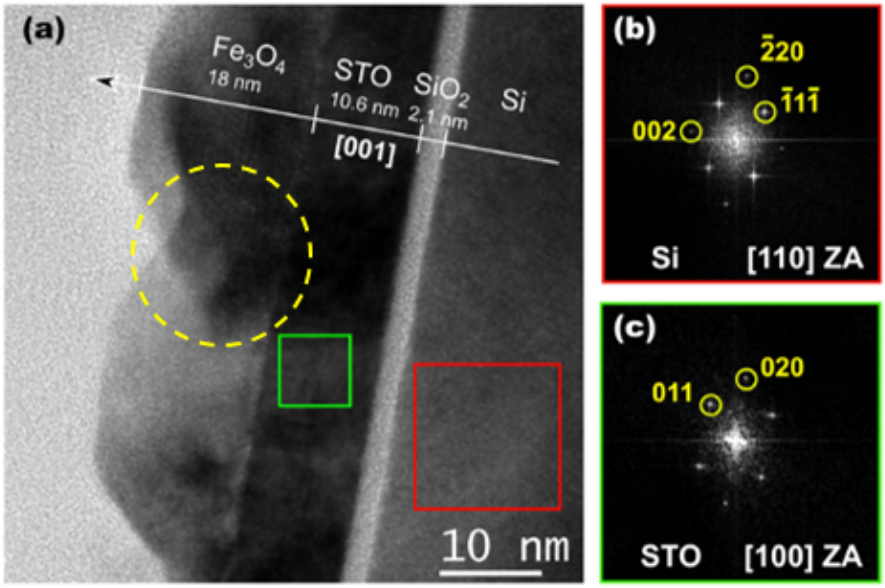

Figure 4.33: (a)TEM image of the $Fe_3O_4/SrTiO_3$(10.9 nm)/Si heterostructure prepared at 350°C. The lightest layer, identified in the image as SiO_2 corresponds with a 2 nm amorphous silicate layer on the $SrTiO_3$/Si interface as confirmed by HAXPES. The encircled areas pointed the overlapping of two magnetite grains. (b) FFT indexation of the Si substrate in the framed area (red box). (c) FFT indexation for the $SrTiO_3$ structure in the framed region (green box).

HRTEM measurements were also performed on these samples. Transmission microscopy provided insight information on the characteristics of the silicate/oxide interlayer presented on the $SrTiO_3$/Si interface. Figure 4.33(a) shows a TEM image of an area of the $Fe_3O_4/SrTiO_3$(10.9 nm)/Si sample prepared at 350°C. TEM measurements proved the formation of 3D islands as indicated by SEM with heights ranging between 15 and 18 nm. The encircled area (yellow circle) indicate the superposition of two magnetite islands, something observed with a relative frequency on different areas of the sample. Afterwards, the $SrTiO_3$ layer is present with a calculated thickness of 10.6 nm in that particular point. The lighter area corresponds to the amorphous silicate layer formed on the $SrTiO_3$/Si interface during the evaporation, which presents a thickness of 2 nm. Subfigures (b) and (c) show the indexation of the fast Fourier transforms (FFT) of the framed areas in Fig. 4.33(a). FFT indexation indicate that the zone axis (ZA) for the Si was [110] meanwhile for $SrTiO_3$ and magnetite was [100], confirming the in plane rotation of 45 degrees to reduce the mismatch between the two lattices.

Figure 4.34(a) shows a TEM image of an area of $Fe_3O_4/SrTiO_3$(10.9 nm)/Si heterostructure prepared at 550°C. In the image two of the formed structures are shown.

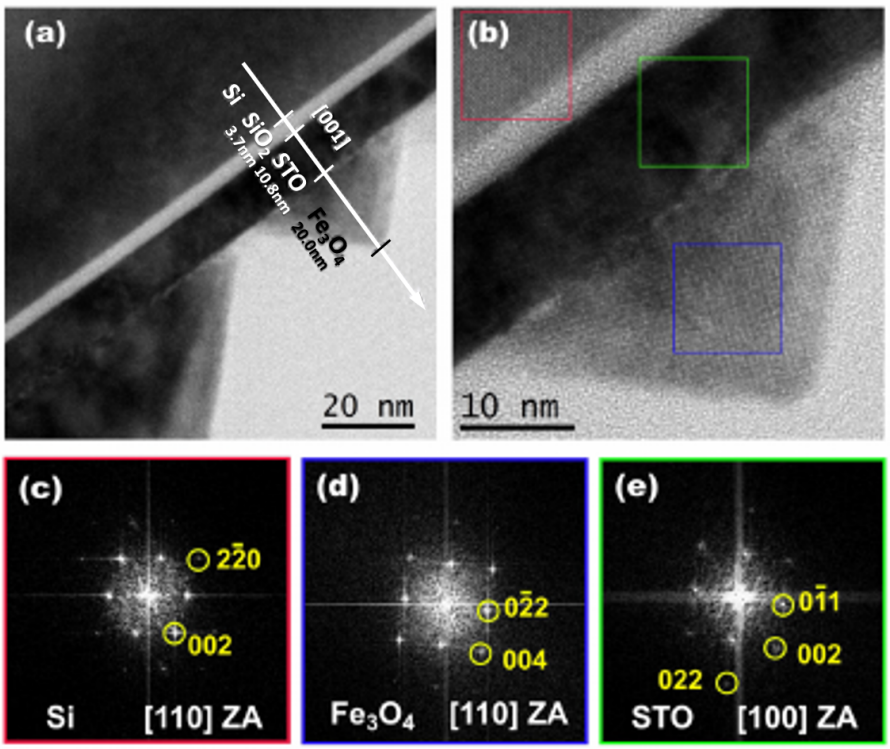

Figure 4.34: (a) TEM image of the $Fe_3O_4/SrTiO_3$(10.9 nm)/Si heterostructure prepared at 550°C showing two magnetite structures. The lightest area, labeled as SiO_2 in the image, corresponded with the amorphous siliicon oxide/silicate layer on the $SrTiO_3$/Si interface as corroborated by HAXPES. (b) Zoomed image of the smaller structure. (c), (b) and (c) show FFT indexation on the framed areas in the different regions of the sample.

As indicated by SEM, at 550°C bigger structures were formed with larger distances between them. This low degree of overlapping between the grains was confirmed on different areas of the sample. The islands presented pyramidal or trapezoidal shapes with heights ranging between 20 and 50 nm. Following the magnetite film the $SrTiO_3$ layer was observed without noticeable modifications. Afterwards a silicate/silicon oxide layer is observed with a thickness on this case of 3.7 nm. This higher thickness was in agreement with HAXPES measurements. Nevertheless, the modification on its composition could not be appreciated by this technique. Figure 4.34(b) shows a zoomed image of the smaller structure. Subfigures (c), (d) and (e) present FFT of the framed areas in the zoomed region, indicating a ZA[100] for silicon, ZA[110] for the $SrTiO_3$ and ZA[110] for the Fe_3O_4 layer, in agreement with the XRD data.

In both samples, a series of contrast effects were observed along the $Fe_3O_4/SrTiO_3$

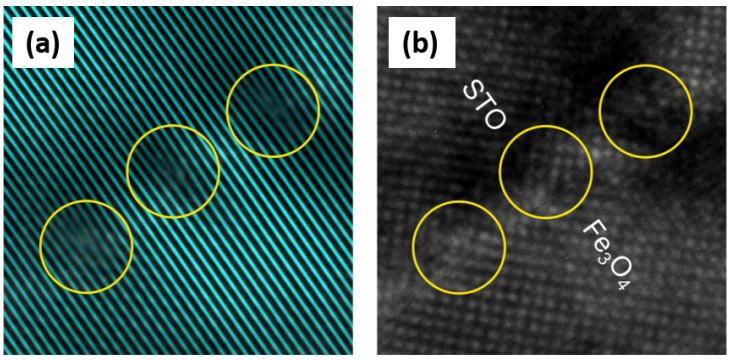

Figure 4.35: (a) Inverse FFT transformation performed on the close-up image of the $Fe_3O_4/SrTiO_3$ interface recorded on the sample prepared at 550°C (b). The presence of dark and bright zones indicated the presence of dislocations on the layer boundaries, represented more clearly after performing an inverse FFT after masking the original FFT in the selected area.

boundary. In other words, different dark and bright zones could be observed. This was related with dislocations on the layers boundary due to the lattice mismatch between Fe_3O_4 and $SrTiO_3$ structures. Figure 4.35 shows an amplification of the interface area on the sample prepared at 550°C. The encircled areas remark the mentioned contrast changes on the $Fe_3O_4/SrTiO_3$ interface. Figure 4.35(a) shows a representation of the crystallographic planes perpendicular to the interface on the area showed in Figure 4.35(b) where these dislocations are graphically represented. This image was obtained performing an inverse fast Fourier transformation after masking the original FFT and selecting only certain reflections of the diffraction pattern.

Although the majority of the islands showed an epitaxial growth of the magnetite films cube on cube on top of the $SrTiO_3$ lattice, during the study the rare appearance of magnetite islands grown in a different direction to that of $SrTiO_3$ and Si was observed. Hence, the growth was no longer epitaxial. This anomaly was observed in the two samples reported here. Still, the majority of the magnetite islands showed and epitaxial growth respect to the $SrTiO_3$ layer.

Magnetic characterization by MOKE

Figure 4.36 shows hysteresis loops for $Fe_3O_4/SrTiO_3$(10.9 nm)/Si samples prepared at 350 and 550°C. The cycles were recorded by MOKE at room temperature (RT) and ambient pressure varying the magnetic field in a range from -240 to 240 mT. Increasing the temperature during magnetite deposition resulted in an increase of the magnetization and an increase of the coercive field. Both effects could be explained by the formation of bigger magnetite structures as observed by SEM and

TEM for samples evaporated at higher temperature. Moreover, the two samples presented a paramagnetic contribution superimposed to the hysteresis loops that impede the complete saturation of the cycles. This was related with the paramagnetic character of the $SrTiO_3$ layer. Beyond this contribution, the sample evaporated at 550°C seemed not to be completely saturated under the highest achievable applied magnetic field (240 mT). The higher field required to saturate the sample could also be explained by the lower exchange coupling between the magnetite grains, as this sample showed a lower degree of overlapping.

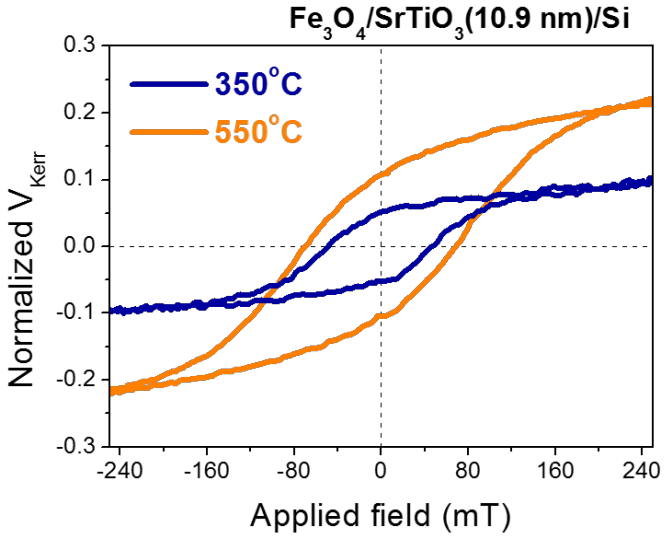

Figure 4.36: Comparative graphic of the hysteresis loops recorded by MOKE at RT and ambient pressure on $Fe_3O_4/SrTiO_3$(10.9 nm)/Si heterostructures prepared at 350 (blue) and 550°C (yellow). Increasing evaporation temperature resulted in an increase of the magnetization as well as of the coercive field.

The presence of magnetic anisotropies was also analyzed in these two samples, changing the orientation of the crystallographic axis of magnetite respect to the direction of the applied magnetic field, keeping a longitudinal configuration. Nevertheless, on these samples this effect could not be evidenced.

4.3.5 Conclusions

During this section the properties of $Fe_3O_4/SrTiO_3/Si$ heterostructures have been discussed. The objective of this part of the work was the preparation of magnetite films on silicon using a $SrTiO_3$ insulator buffer layer that could, on one hand, favor the epitaxial growth of magnetite on silicon and, on the other hand, serve as a tunnel barrier for the design of spin injection devices based on heterostructures fabricated with this method. The interest on evaporating epitaxial magnetite films

relied on the possibilities this would provide in terms of modifying the properties of the heterostructure by means of strain, for example. At the same time, this can play against the interest of the system, as the presence of distortions on the crystallographic structure can completely modify the desired magnetic and transport properties of the magnetite films.

After the study performed, the presence of an amorphous silicate layer on the $SrTiO_3$/Si interface formed during the $SrTiO_3$ evaporation was proved. The increase on the amount of silicate on the interface after magnetite evaporation was also corroborated by HRTEM and HAXPES. Different conditions were explored in order to achieve the stabilization of single phase magnetite films on $SrTiO_3$/Si, by means of modifying the $SrTiO_3$ thickness and the evaporation temperature of magnetite. The characterization of the films showed the formation of metallic iron and iron silicides phases for evaporation temperatures above 350°C. The formation of silicon oxide/silicate on the $SrTiO_3$/Si interface was also observed in $SrTiO_3$ films upon annealing at temperatures over this value. This pointed to a correlation between the evolution of the interface and the stabilization of single phase magnetite films.

Finally, it was concluded that in order to stabilize single phase magnetite films on top of the $SrTiO_3$ films regardless of the $SrTiO_3$ thickness the temperature during Fe_3O_4 deposition needed to be kept below 350°C. Magnetite films evaporated on top of $SrTiO_3$ layers with a thickness of 1.8 and 4.8 nm respectively resulted on a two dimensional growth. The obtained films showed a flat surface with an almost constant thickness and low roughness. These samples presented a ferromagnetic response at ambient pressure and room temperature with similar features. MOKE measurements in a longitudinal configuration changing the angle of the crystallographic axis respect to the magnetic field evidenced the presence of an easy axis on the [001] direction. Although the effect was minor, this property could be increased by, for example, modifying the thickness of the films being a potential source for tuning the characteristics of the system. Exceptionally, single phase Fe_3O_4 films were stabilized evaporating at 550°C when using a $SrTiO_3$ layer 10.9 nm thick. A 3D island-like growth was observed, in contrast with the Fe_3O_4 layers grown using thinner $SrTiO_3$ layers. Increasing the evaporation temperature favored the formation of bigger and more dispersed magnetite structures. Regarding the magnetic properties, this resulted in films with larger coercitivity and higher saturation fields, which is not favorable for the practical application of the system. Moreover, the discontinuity of the films can be detrimental for the electric transport properties of the films, resulting in an extremely high electric resistance of the films.

4.4 General conclusions from the study of Fe_3O_4 based heterostructures

During this chapter, the integration of single phase magnetite films on silicon was considered by two different strategies. On a first approach, the naturally present silicon native oxide was used to passivize the silicon surface and favor the stabilization of the magnetite films. In the second attempt, epitaxial $SrTiO_3$ films were evaporated on top of the silicon substrates after eliminating the native oxide in order to stabilize the substrate surface. Each method presented different advantage and disadvantage. For instance, the direct evaporation of magnetite on the untreated substrates provided an inexpensive and reproducible method for the integration of this material on Si. Nevertheless, the epitaxial growth of magnetite is hampered by the amorphous character of the native oxide and the thickness of the buffer layer could not be controlled. On the contrary, the use of a $SrTiO_3$ buffer allowed the deposition of epitaxial magnetite films on silicon controlling the thickness of the buffer layer. However, the preparation of the heterostructures required a complex procedure which involved several stages. Throughout this dissertation, the viability of the prepared samples was discussed from a point of view centered on the morphological and structural characteristics of the multilayer system. The magnetic response of the magnetite films and the good quality of the tunnel barrier interfaces are promising aspects for the introduction of these systems in spintronics. However, in order to determine the true applicability of the heterostructures as a basis for the development of spin injection devices additional work would be necessary. These additional studies should include the analysis of the transport and magnetotransport properties of the system.

Although the procedure for the preparation of the system was significantly different in each of the approaches, in both cases a direct correlation between the evolution of the buried insulator/silicon interface and the stabilization of the magnetite films was observed. If the thickness of the tunnel barrier is too thin or the evaporation temperature is too high, oxygen is transferred through the tunnel barrier inducing the oxidation of silicon and impeding the stabilization of stoichiometric Fe_3O_4 films. Moreover, Fe has a catalitic effect on the dissociation of O_2 molecules, favoring the ionic transport of oxygen through the tunnel barrier. This effect underlines the extreme difficulty involved in the evaporation of oxides in silicon, despite the interest that this type of systems may have for the development of new technologies. Comparing the two introduced systems, from the work presented here it can be concluded that the use of native oxide as a tunnel barrier would be the best option taking into account existing studies on spin dependent tunnel transport. The use of a $SrTiO_3$ barrier resulted on the formation of an additional silicate layer on the $SrTiO_3$/Si interface which thickness increased progressively with evaporation time. The presence of this layer will critically modify the insulator-semiconductor interface with

unpredictable consequences for the efficiency of the spin injection. Consequently, in order to apply $Fe_3O_4/SrTiO_3/Si$ heterostructures prepared through this method on spintronics it is mandatory to understand the effect of this silicate on spin dependent transport. In order to do so a deeper characterization of the interface would be necessaire to determine, for instance, the exact composition of this silicate layer and its electronic properties.

Contrary, $Fe_3O_4/SiO_2/Si$ heterostructures were proved to find an equilibrium when the SiO_2 layer reached a thickness of around 4 nm. Once this value was reached further oxidation of silicon was prevented even though the magnetite thickness was increased. The tunnel barrier presented a homogeneous thickness and composition with well-defined interfaces. The presence of mixed phases between the different layers of the system was completely dismissed. Although the thickness of the SiO_2 layer cannot be voluntary tuned, a thickness of 4 nm is low enough to allow tunnel transport between the silicon and the magnetite layer. The main limitation of the system would be the high resistance observed on the magnetite layer, related with the low thickness and the granular character of the films. Still, the conductivity could be improved directly by increasing the thickness of the films. Besides, post-evaporation treatments could be considered with the objective of improving the cohesion of the film and consequently favoring the electronic transport.

Chapter 5

Fe_3Si epitaxial thin films

5.1 Introduction

Fe_3Si have attracted great interest because of it Heusler alloy structure and its high Curie temperature up to 840 K (see section 3.5). From the beginning of the 2000s, numerous authors claim on the applicability of this material in spintronics [241–243]. A few studies have been reported on the use of Fe_3Si electrodes on MTJ structures [244,245]. These works have been supported by the high TMR values up to 5000 % predicted by theoretical studies [245]. However, Harada *et al.* reported TMR values of only 0.28 % in $Fe_3Si/CaF_2/Fe_3Si$ MTJs, well below this prediction, which has been related with diffusive scattering processes produced during the transport [245]. Concurrently, in 2009 Also *et al.* successfully induced and detected spin accumulation in a Si channel at low temperature in a lateral four-probe geometry using Fe_3Si/Si contacts, evidencing the usefulness for semiconductor spintronics [62]. More recently, Kawano *et al.* generated and detected spin accumulation on p-type doped Germanium through a Fe_3Si bottom electrode in a vertical configuration [246].

Although they are not numerous, the works published so far showed the potential of Fe_3Si for the design and manufacture of spintronic devices. Nevertheless, spin dependent phenomena is intimately related with the structural, chemical and morphological properties of the deposited materials, requiring the controlled growth of high quality heterostructures. Fe_3Si has been usually grown by co-evaporation of Fe and Si at evaporation temperatures below 200 ^{o}C. The most common substrate used for the preparation of Fe_3Si films has been GaAs, due to the similarity between their crystallographic structures, which favor the epitaxial growth of the films [241, 247, 248]. However, this resemblance can also favor atomic interdiffusion in regions close to the interface, modifying the properties of the system [249]. In addition, GaAs requires some preparation prior to evaporation in order to eliminate the native oxide layer. Cleaning procedures can result on the formation of carbonides, which require high temperature annealing (T>500^{o}C) for a complete elimination and

which might result in a As-rich stoichiometry at the surface [250].

Some attempts have been made to evaporate Fe_3Si in other important semiconductors as Ge or Si, with diverse results [242,243,251,252]. In general, resulting films were polycrystalline with different degrees of texturization. Exceptionally, Yoshitake *et al.* achieved the epitaxial growth of Fe_3Si on Si(111) with a high quality interface. The films presented a B_2 structure and magnetic measurements proved the presence of an easy axis on the [110] direction [251]. Although the large lattice mismatch, epitaxial Fe_3Si films have also been deposited on MgO [253]. This insulator has been widely used as a tunnel barrier in the design of MTJs and spin injection devices.

Extending the growth of high quality Fe_3Si films to new substrate materials would provide good opportunities for the design of highly functional heterostructures. Moreover, Tao *et al.* demonstrated theoretically the strong dependence of the half metallic behaviour of Fe_3Si on its structural properties. According to their results, in order to have only majority spin states at the Fermi level, the strain of the lattice must exceed the 1.3 % (c/a>1.04) [245]. Motivated by this result, during this thesis the evaporation of Fe_3Si films on $SrTiO_3$ (001) substrates was explored. $SrTiO_3$ (a_{SrTiO_3}=0.3905 nm) presents a large mismatch of around 31 % with Fe_3Si. Nevertheless, if the Fe_3Si lattice is placed on the diagonal of the $SrTiO_3$ (001) lattice so that $[110]Fe_3Si \| [100]SrTiO_3$, this mismatch is reduced to a 2.3 %. In the case of a commensurate growth, the degree of strain induced in the lattice would be c/a=1.07 revealing, as established by Tao *et al.*, the existence of a half-metallic behaviour. Moreover, $SrTiO_3$ presents excellent insulator properties and a perovskite structure that is compatible with a high number of functional materials.

During this chapter, the growth of epitaxial Fe_3Si films on $SrTiO_3$(001) substrates will be presented, analysing different evaporation conditions and discussing the properties of the deposited films, which will be treated in Section 5.2. The study considered two parameters, the temperature of the substrates during the deposition of the films (Section 5.2.1) and the thickness of the evaporated films (Section 5.2.2). Conclusions of the work will be presented in section 5.3.

5.2 Evaporation of epitaxial Fe_3Si films on $SrTiO_3$ by PLD

Different evaporation conditions and techniques have been considered in the past for the deposition of Fe_3Si films, being the most common the co-evaporation of Fe and Si by MBE. Substrate temperatures considered are commonly in a range between room-temperature and 300 ^oC in order to synthesize single phase Fe_3Si films. However, some reports demonstrated the formation of highly oriented Fe_3Si films after annealing at 800-900^oC [254].

The preparation of Fe_3Si films by PLD is less common. Some previous works explored this possibility through different strategies and with different results. Man-

tovan *et al.* studied the formation of a Fe_3Si phase by thermal treatment of Fe/Si bilayers prepared by PLD [242]. Yoshitake *et al.* reported the preparation of polycrystalline Fe_3Si films on Si and quartz by using a Fe_3Si stochiometric target [255]. They explored different evaporation temperatures in a range between RT and 500^{o}C obtaining the best results in terms of crystallinity at 300^{o}C degrees. Nevertheless, reports on the epitaxial growth of Fe_3Si films by PLD was not found. Yosikate *et al.* associated this fact with the high effective evaporation rate obtained by this technique [251].

In this thesis, epitaxial Fe_3Si films were successfully deposited by PLD on $SrTiO_3$(001) substrates by ablating an stoichiometric Fe_3Si target in a UHV chamber with a base pressure of 10^{-9} mbar. It is critical to perform the evaporation in a free contaminant environment due to the easiness of Si and Fe to oxidize in the presence of oxygen. Because of the lack of available literature concerning the deposition of Fe_3Si films on $SrTiO_3$ (001) substrates, a wide range of temperature between 200^{o}C and 800^{o}C was explored.

5.2.1 Influence of the substrate temperature

A total of five samples were prepared at substrate temperatures of 200, 300, 400, 600 and 800^{o}C respectively. In order to analyze the influence of the temperature on the structural properties of the deposited films they were characterized by XRR, XRD and XAS. The magnetic response of the films was studied by MOKE.

Characterization by XRR

XRR measurements were performed in the multipurpose diffractometer installed in the Branch B of the Spanish CRG BM25-SpLine at the ESRF (see section 2.6.1). The recorded curves for the five samples are shown in Figure 5.1. Reflected intensity was represented as a function of the momentum $Q_\perp$ in order to compare curves recorded at different photon energies. Samples evaporated at temperatures between 200 and 600^{o}C presented a flat interface and low surface roughness giving raise to the presence of Kiessig fringes. The faster decay of the fringes amplitude with increasing $Q_\perp$ as the evaporation temperature was increased indicated a progressive increase of the interface roughness. Sample deposited at 800^{o}C presented a significantly rougher surface and interface. Therefore, the coherence between the scattering from the surface and the interface was almost completely lost and Kiessig fringes became imperceptible.

The thickness of the deposited films was calculated from the position of the minima in the reflected intensity curves (blue bars) using equation 2.12 for the samples evaporated between 200 and 600^{o}C. In the case of the sample evaporated at 800 ^{o}C, the weak interference produced hampered the performance of this calculation. The fitting performed is presented in the insets of fig.5.1. The films presented thickness

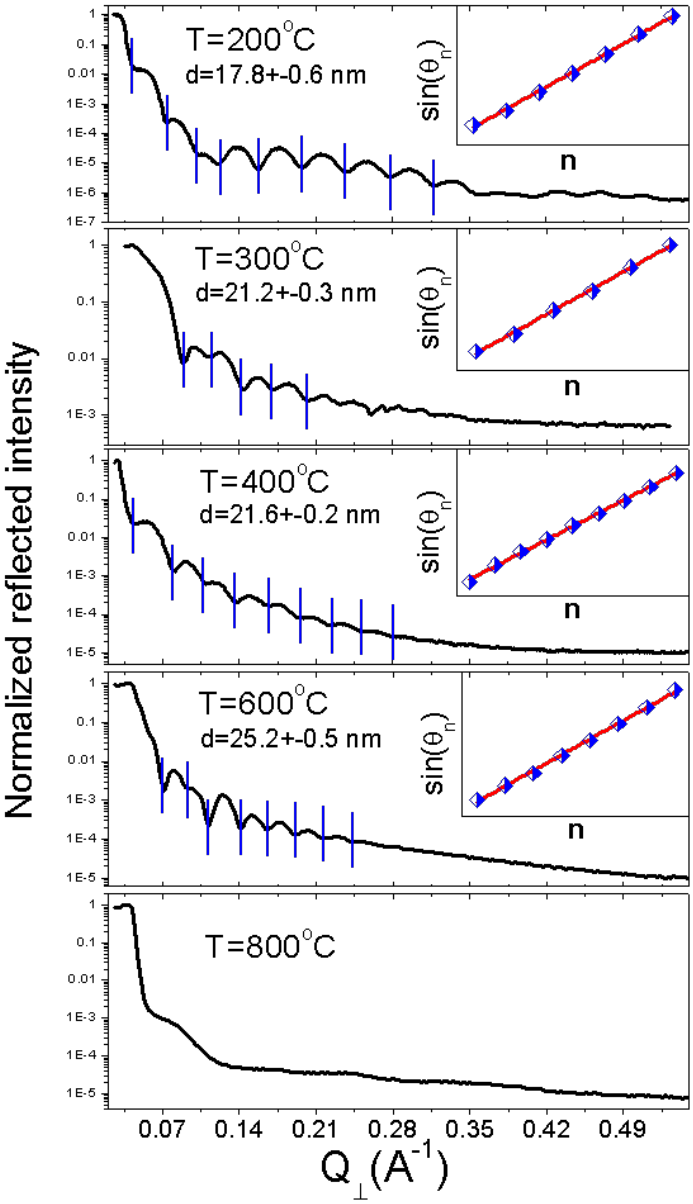

Figure 5.1: XRR measurements on the Fe_3Si films evaporated on $SrTiO_3$ with increasing evaporation temperature. The curves represent the normalized reflected intensity as a function of $Q_\perp$. The evolution with increasing temperature showed a faster decay of the amplitude of the oscillations, indicating an increase of interface roughness. In the inset, the fitting of $\sin(\theta_n)$ in the minima position as a function of the order n used are represented, which were used to calculate the thickness of the films.

of 17.8 (±0.6) nm, 21.2 (±0.3) nm, 21.6 (±0.2) nm and 25.2 (±0.5) nm respectively. In the recorded curves, a second frequency was intuited in the XRR profile, which was especially evident for the sample evaporated at 200^{o}C. The origin of this second periodicity could not be certainly identified but was most likely related with the oxidation of the Fe_3Si surface due to the exposition of the samples to air after the deposition, forming an oxide layer flat enough to produce a coherence interference.

Characterization by XRD

XRD measurements were performed in the five samples. A large number of reflections were recorded in order to determine the epitaxial growth of Fe_3Si on $SrTiO_3$(100). In order to adapt its lattice to that of the substrate, a 45 degrees in plane rotation occurs so that $Fe_3Si[001]\|SrTiO_3[001]$ and $Fe_3Si[100]\|SrTiO_3[110]$. This rotation reduces the large lattice mismatch from the 31% to a 2 %.

Figure 5.2 presents reciprocal space maps (RSM) for the five samples prepared. Two diffraction peaks could be seen, corresponding to the (203)$SrTiO_3$ and (224)Fe_3Si reflections. An incommensurate growth of the films was evidenced in the five samples based in the different $Q_{\|}$ values for the $SrTiO_3$ and Fe_3Si reflections. For samples evaporated at temperatures between 200^{o}C and 400^{o}C, RSM images showed faint and elongated diffraction peaks indicating a low degree of crystallization and a high grade of mosaicity. Mosaic crystal are characterized by the formation of multiple crystallites which are oriented almost, but not exactly, parallel to one another. Within this temperature range, the three samples showed similar characteristics with no remarkable differences.

After increasing the temperature up to 600^{o}C, the degree of crystallization of the Fe_3Si film increased significantly and diffraction peaks gained intensity. RSM showed the apparition of a third peak, which was identified as the (112)Fe reflection. This proved the formation of a crystalline iron phase with its axis co-linear to those of the Fe_3Si lattice. When evaporating at 800^{o}C this third contribution was still present, but the diffraction peaks became less intense. Some faint polycrystal intensity rings were also observed during the measurements.

Rocking curves recorded on the (202)Fe_3Si reflection are shown in Figure 5.3. Rocking scans for samples evaporated between 200^{o}C and 400^{o}C showed a highly irregular profile composed by the superposition of several narrower peaks. This was a consequence of the high degree of mosaicity presented by the films in this temperature range. Given this condition, representative crystal domain sizes could not be calculated for these samples. For higher substrate temperature (600^{o}C and 800^{o}C), the crystallization of Fe_3Si was favored and diffraction peaks were significantly more intense. Rocking scans showed a single peak with a narrower profile. Curves were fitted using a pseudo Voigt function and crystal domain sizes were calculated using equation 2.23. Average values of 31.7 (±0.6) and 24.1 (±0.4) nm were obtained for

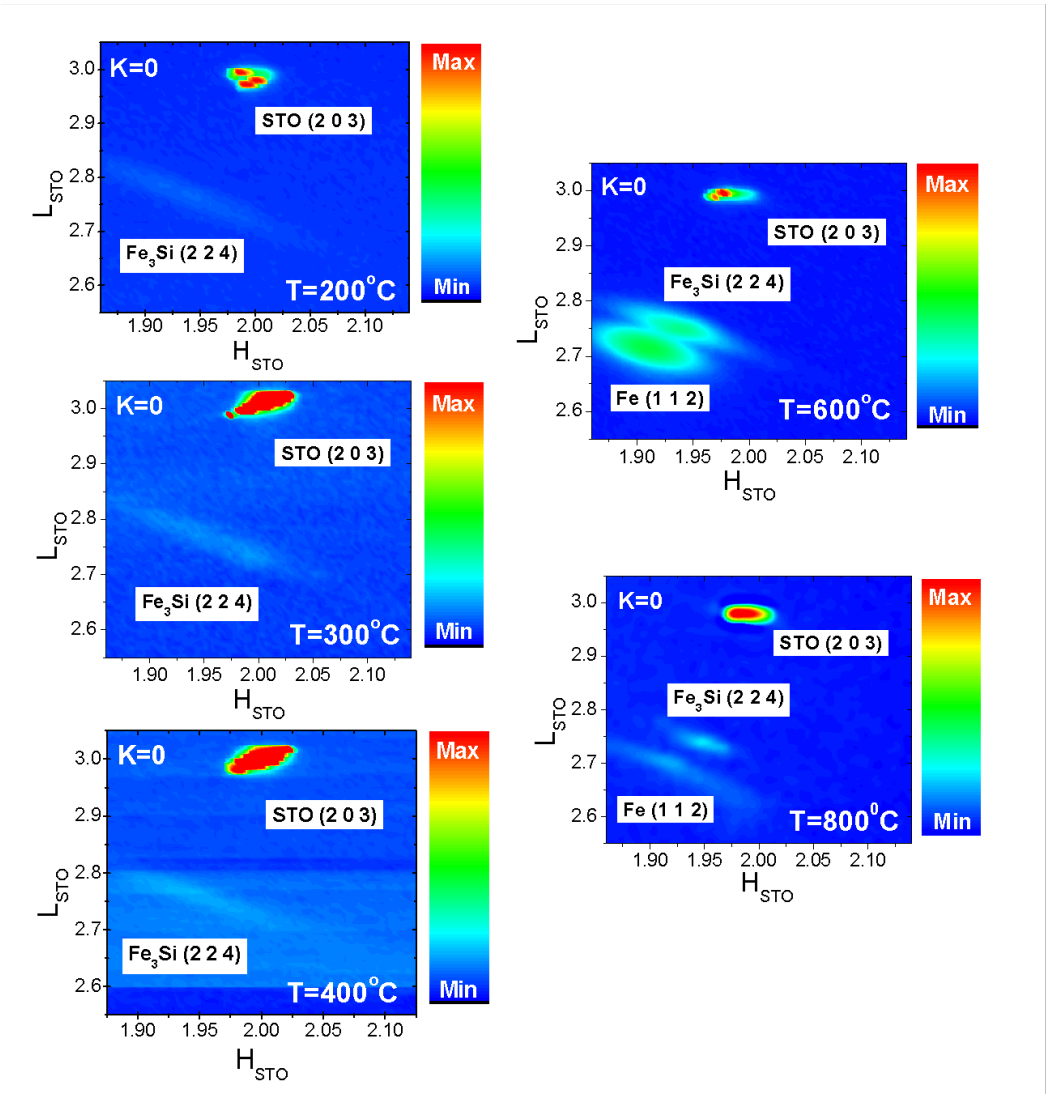

Figure 5.2: H_{STO} versus L_{STO} reciprocal space maps recorded at K_{STO}=0 for $Fe_3Si/SrTiO_3$ samples evaporated at 200, 300, 400, 600 and 800^{o}C respectively. The different H values observed for $SrTiO_3$ and Fe_3Si evidenced the incommensurate growth of the films. For evaporation temperatures of 600 and 800^{o}C, a third diffraction peak indicated the presence of iron.

the samples evaporated at 600^{o}C and 800^{o}C respectively.

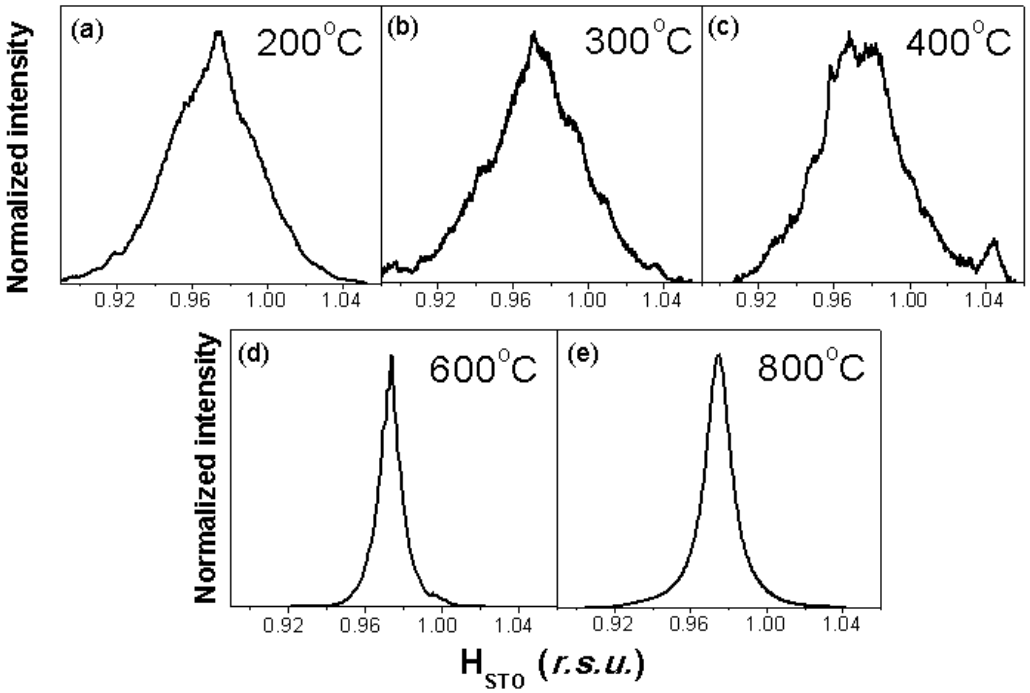

Figure 5.3: Rocking curves on the (202)Fe_3Si reflection for samples evaporated at 200 (a), 300 (b), 400 (c), 600(d) and 800^{o}C (e).The irregular lineshape observed in curves (a)-(c) evidenced the high degree of mosaicity of the samples in this temperature range. Curves (d) and (e) could be fitted using a pseudo voigt function giving crystal domains sizes of 31.7 ($\pm$0.6) and 24.1 ($\pm$0.4) nm respectively.

The properties of the crystalline iron phase formed in samples evaporated at 600^{o}C and 800^{o}C were also characterized. Iron presented an incommensurate growth respect to the $SrTiO_3$(001) substrates with a rotation of 45 degrees, equally to that observed for Fe_3Si, so that Fe[001]$\|$$SrTiO_3$[001] and Fe[100]$\|$$SrTiO_3$[110]. Rocking curves (not shown) demonstrated the single oriented character of this phase and provided average crystal domain sizes of 12.2($\pm$0.3) and 14.5($\pm$0.2) nm for 600^{o}C and 800^{o}C respectively, which indicated that increasing substrate temperature above 600^{o}C favored the crystallization of Fe in detrimental of Fe_3Si.

Based on XRD measurements it could be concluded that the crystallization of Fe_3Si films was optimized at 600^{o}C. Using higher evaporation temperatures resulted detrimental and even induced the formation of polycrystalline phases. However, the crystallization of the films with temperature was accompanied by the formation of iron. Therefore, in order to obtain single phase Fe_3Si films the temperature during the deposition must be kept below 600^{o}C.

Characterization by XAS

X-ray Absorption measurements on the Fe K-edge were performed in the Branch A of the Spanish CRG BM25-SpLine at room temperature (see section 2.6.1). Figure 5.4(a) shows the evolution of the X-ray absorption spectra for the samples evaporated at different temperature together with the spectra measured from a Fe standard and Fe_3Si single crystal reference sample. A clear evolution of the XANES spectra was observed, characterized by the apparition of features related to Fe scans as the deposition temperature was increased.

Given the high mosaicity of the films, confirmed by XRD measurements, samples prepared at 200 and 300^{o}C presented a flat spectra as a consequence of the absence of long range order on the films. The different degrees of crystallization of the films could explain the noticeable differences between the measurements performed in the single crystal reference and those measured in the samples, especially at the lowest temperatures, although they had the same composition. The thin film form could also be responsible of the absorption differences noted in the XANES response with respect to the Fe_3Si single crystal.

In the purpose of quantifying the weight of this phase in the total composition of the sample, the spectrum was simulated by linear combination fitting (LCF) using the Athena software included inside the Demeter package [113]. Samples evaporated at 200^{o}C and 300^{o}C presented identical features and XANES spectra was proved to be equivalent by LCF. However, providing new information regarding what had been concluded from XRD measurements, the XANES spectrum indicated the presence of iron in the sample evaporated at 400^{o}C. This step was also performed for the samples evaporated at 600 and 800^{o}C and the composition of each sample is resumed in table 5.1. After considering different combinations of standards for the fitting, the absence of iron silicides besides Fe_3Si or oxides in the samples was certainly confirmed. The XANES spectrum for the sample deposited at 200^{o}C was considered as standard to simulate the presence of Fe_3Si phases that only present short range order (SRO) meanwhile the single crystal reference was considered as standard for phases which present long range order (LRO). Given the strong dependence of the absorption spectra with the crystallographic properties, a spectrum recorded in a single crystal reference was not adequate to described the acquired data for samples in a temperature range between 200 and 400^{o}C. The best result in order to reproduce the data recorded for the sample evaporated at 400^{o}C is shown in figure 5.4(b).The results determined a composition of 71.2 ($\pm$ 2.1) % of Fe_3Si (SRO) and a 28.8 ($\pm$ 1.5) % of iron. Therefore, it could be concluded that in order to obtain single Fe_3Si films, temperature during the deposition must be kept below 400^{o}C.

XANES spectrum recorded for the sample evaporated at 600^{o}C showed clear similarities with the iron standard. The presence of crystalline iron was already determined by XRD and analysis of the XANES spectrum proved that iron was more than a 60 % of the composition of the sample. The best results for the simulation

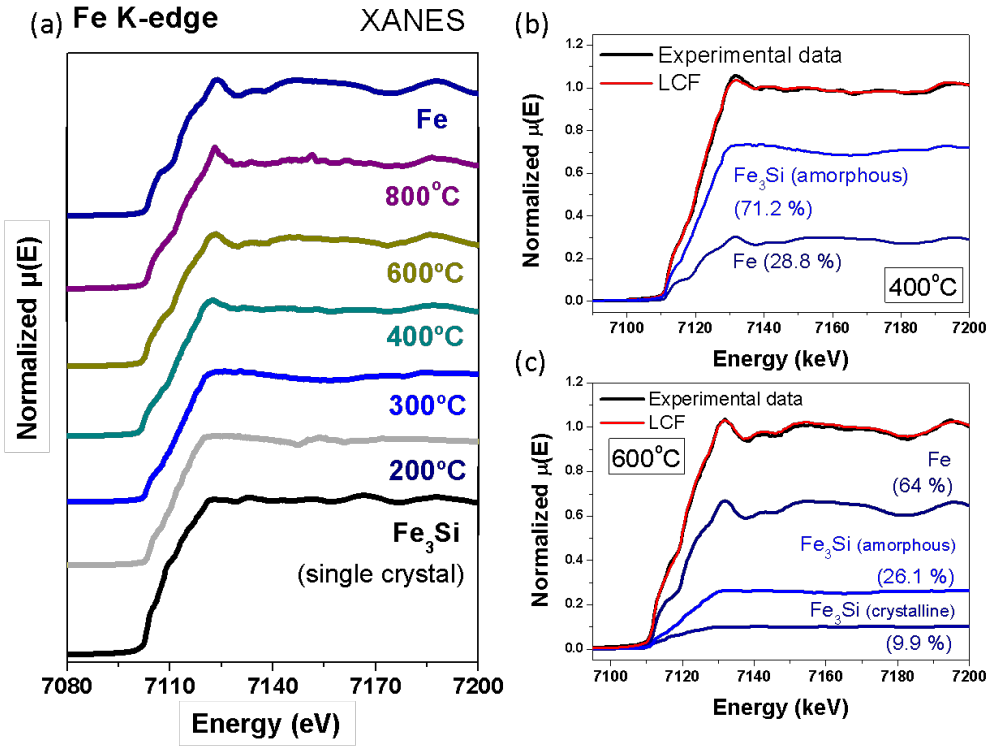

Figure 5.4: (a) XANES measurements at the Fe K-edge for Fe_3Si films evaporated on $SrTiO_3$ substrates at different temperature. The evolution of the spectra showed the progressive appearance of iron as temperature increases. (b) Linear combination fitting (LCF) for the spectrum measured for the samples evaporated at 400^{o}C and (c)600^{o}C. The results showed an increase of the proportion of iron at 600^{o}C and a higher crystallization of the Fe_3Si phase, in agreement with XRD measurements.

of the experimental data were achieved for a composition of 9.9 ($\pm$3.3) % of Fe_3Si (LRO), 26.1 ($\pm$ 2.6) % Fe_3Si (SRO) and a predominant 64 ($\pm$2) % of iron. The fitting is reproduced in figure 5.4(c). This evolution is consistent with XRD measurements, that proved a more single oriented character for Fe_3Si films evaporated at 600^{o}C.

Characterization of the sample evaporated at 800^{o}C proved the presence of a significant amount of iron and a deterioration of the crystallographic properties. Surprisingly, fitting of the XANES spectrum (not shown) lead to the conclusion that the proportion of iron was reduced respect to the sample evaporated at 600^{o}C. Still, a significant 48.4 ($\pm$2.4) % of the sample was composed of iron. The 51.6 ($\pm$2.4) % remaining was constituted of Fe_3Si, where only the 1.1 ($\pm$0.8) % was crystallized according to the simulation performed.

Magnetic response

T_S (^oC)	Fe_3Si (%) (SRO)	Fe_3Si (%) (LRO)	Fe (%)
300	100	-	-
400	71.2 ± 2.1	-	28.8 ± 1.5
600	26.1 ± 2.6	9.9 ± 3.3	64 ± 2
800	51.6 ± 2.4	1.1 ± 0.8	48.4 ± 2.4

Table 5.1: Composition in percentage of the samples evaporated on $SrTiO_3(001)$ substrates at different temperatures obtained from linear combination fitting from different standards of the XANES measurements.

Hysteresis loops were recorded by MOKE at ambient pressure and room temperature in the samples evaporated at 200, 300, 400 and 600^{o}C. The sample evaporated at 800^{o}C was excluded from this section. The reason to do this was that, given the unknown thickness of this sample, it behavior could not be directly compared with the other samples. The recorded cycles are shown in Figure 5.5. Presented curves were measured in a longitudinal configuration, so that the magnetic field was applied parallel to the sample surface. The direction of the crystallographic axis of the film was changed respect to the magnetic field, always keeping a longitudinal configuration, in order to elucidate the presence of magnetic anysotropies. The inalterability of the cycles proved the isotropic character of the samples.

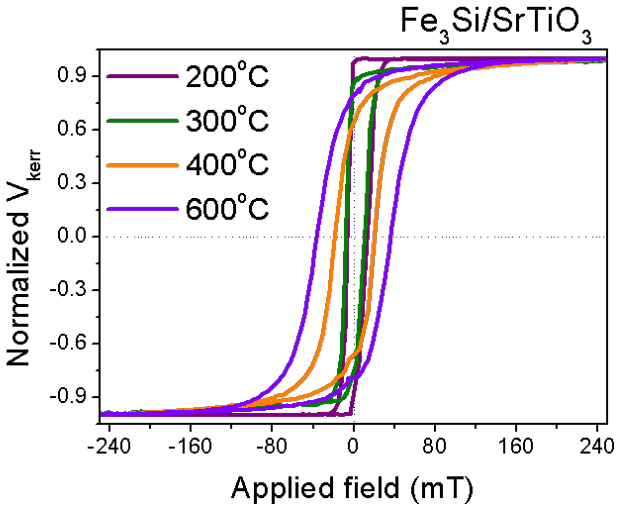

Figure 5.5: MOKE measurements in a longitudinal configuration at RT and ambient pressure in Fe_3Si films deposited on $SrTiO_3$ substrates at different temperature.

The coercive field (H_C) and the normalized remanence (M_S/M_R) were extracted from the hysteresis loops. Samples evaporated at 200^{o}C and 300^{o}C were both proved

to be single phase and single oriented, although with a poor crystallization and a high degree of mosaicity. As a consequence of their structural similarity, they presented a resembling magnetic response in terms of coercitivity and remanent magnetization. Increasing the evaporation temperature at 400^{o}C resulted in a noticeable increase of the coercive field and a significant drop of the remanence in comparison with samples evaporated at lower temperature. Nevertheless, XAS measurements indicated the presence of almost a 30 % of iron on the composition of the sample, which surely influenced the magnetic response of the film. Sample evaporated at 600^{o}C showed a more significant increase of the coercive field and a moderate drop of the normalized remanent magnetization (respect to the samples evaporated at 200 and 300^{o}C). Again, it needs to be remember that this samples showed a predominance of iron, being almost 65 % of its composition. Consequently, the response of the films deposited at 400 and 600^{o}C was in any case representative of an $Fe_3Si/SrTiO_3$ system. Because of the lack of information about the distribution of Fe and Fe_3Si phases on this sample as well as on the sample deposited at 400^{o}C, the contribution of each one to the magnetic response was difficult to analyze.

Given the presence of iron in samples evaporated at temperatures of 400^{o}C and 600^{o}C, it could be concluded that only the response of the samples evaporated at 200 and 300^{o}C are representative of the system. On this regard, considering that an ideal system needs to present a low energetic cost (low H_C) and a fast reversal mechanism (M_S/M_R=1), Fe_3Si films evaporated at 200 and 300^{o}C degrees presented promising magnetic properties, highlighting that sample grown at 200^{o}C almost showed an immediate response when inverting the sign of the magnetic field ($M_S/M_R \approx$1).

5.2.2 Influence of the layer thickness

In order to analyze the influence of the layer thickness on the structural properties of the Fe_3Si films. three samples were prepared under identical conditions, fixing the evaporation temperature at 400^{o}C and varying the film thickness. The samples were characterized by XRR, XRD and XAS.

Characterization by XRR

XRR measurements were performed at room temperature and ambient pressure on the multipurpose diffractometer installed in the Branch B of the Spanish CRG BM25-SpLine at the ESRF (see section 2.6.1). Recorded curves for the three samples are shown in Figure 5.6. The three samples presented a flat interface and smooth surface, originating the apparition of Kiessig fringes due to the coherent interference of the x-ray beam reflected on the Fe_3Si surface and the $Fe_3Si/SrTiO_3$ interface. The periodicity of this interference was dependence of the Fe_3Si thickness, and consequently could be used to calculate this parameter using equation 2.12. Thicknesses of 8.8 ($\pm$0.4), 21.6 ($\pm$0.2) and 70.2 ($\pm$1.5) nm were obtained respectively for each

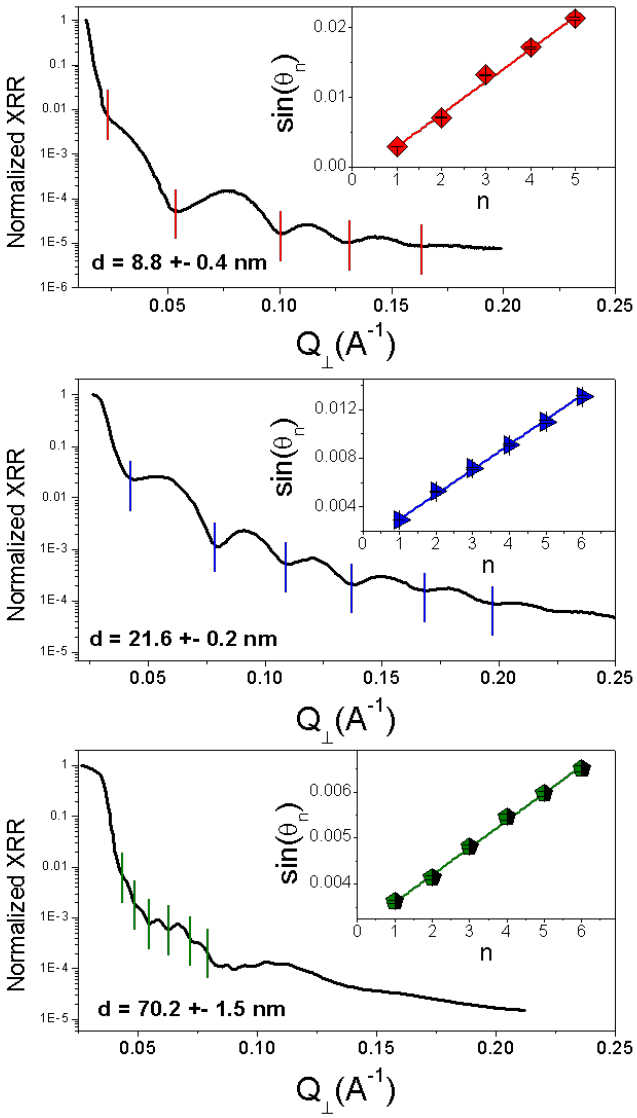

Figure 5.6: XRR measurements for $Fe_3Si/SrTiO_3$ films with different layer thickness. Low surface and interface roughness gave raise to the formation of Kiessig fringes. The periodicity of the oscillations was used to calculate the layer thickness giving values of 8.8 ($\pm$0.4), 21.6 ($\pm$0.2) and 70.2 ($\pm$1.5) nm.

sample. The three samples showed similar features in terms of surface and interface roughness. XRR measurements for the thicker film (70.2 nm) showed the appearance of a second frequency with a smaller periodicity. This effect was observed also in the previous section and its origin was not clearly identified. However, it was more likely to be produced by the oxidation of the Fe_3Si surface, forming a oxide layer flat enough to produce a coherent interference, although it was not identified by other techniques.

Characterization by XRD

A large number of reflections were recorded in order to elucidate the structural properties of the films. XRD measurements proved an epitaxial growth of the films with a 45 degrees in-plane rotation so that $Fe_3Si[100]\|SrTiO_3[110]$ and $Fe_3Si[001]\|SrTiO_3[001]$, independently of the thickness. The three films showed a relaxed growth, pointing to an incommensurate growth even for films only a few nanometer thick.

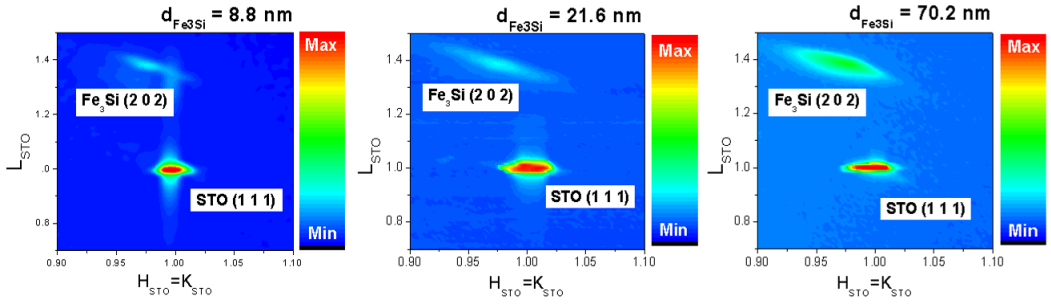

Figure 5.7: Reciprocal space maps on $Fe_3Si/SrTiO_3$ films with different thickness showing the (202)Fe_3S and (111)$SrTiO_3$ reflections. Diffraction peaks gained intensity progressively when increasing layer thickness. This is a consequence of the higher degree of crystallization of the films as well as of the larger amount of material present in thicker films.

Figure 5.7 shows reciprocal space maps for the three samples. RSM showed two diffraction peaks corresponding to the (202)Fe_3Si and (111)$SrTiO_3$ reflections. Films with thickness of 8.8 nm showed the formation of faint and elongated diffraction peaks. This peak profile was related with a low crystallization and a high degree of mosaicity. Sample with 21.6 nm thickness showed a similar profile. However, diffraction peaks gained intensity because of the larger amount of material present in the sample as a consequence of increasing the thickness. Because of this same reason, diffraction peaks for the thicker film (70.2 nm) are significantly more intense. Nevertheless, the RSM also showed a round shape of the diffraction peaks, which indicated a lower degree of mosaicity.

Rocking scans were measured around the (202)Fe_3Si reflection and are reproduced in figure 5.8. Samples with 8.8 and 21.6 nm thickness showed rocking curves with an

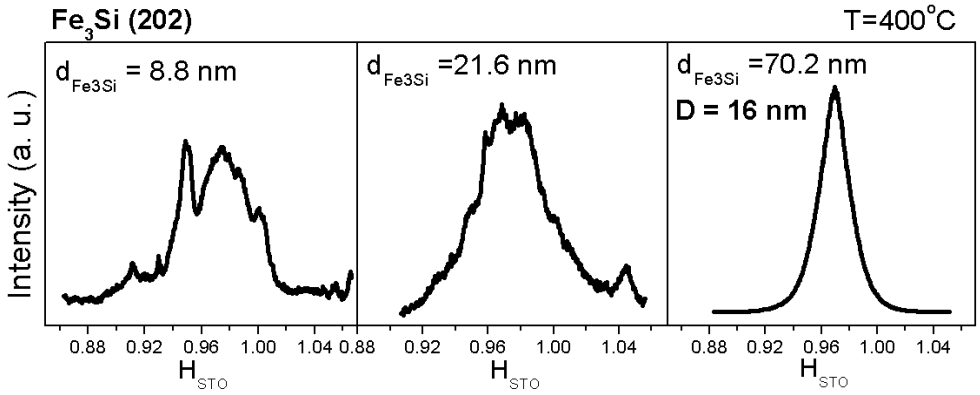

Figure 5.8: Rocking curves on the $Fe_3Si(202)$ reflection on $Fe_3Si/SrTiO_3$ films with different thickness.

irregular profile, originated by the superposition of multiple diffraction peaks. This confirmed the high degree of mosaicity present on the films, characterized by the formation of different domains not completely parallel to each other. Nevertheless, the film evaporated with a 70.2 nm thickness, showed a one and only contribution indicating the single oriented character of the film after increasing the thickness. This evolution clearly indicated a favor crystallization of the films with increasing layer thickness. The rocking curve for the 70.2 nm thickness layer was fitted using a pseudo Voigt function and crystal domain sizes were calculated using equation 2.23. An average value of 15.9 ($\pm$0.2) nm was obtained.

Characterization by XAS

The three samples evaporated with different thickness were characterized by XAS in the Branch A of the Spanish CRG BM25-SpLine at the ESRF (Section 2.6.1). Recorded XANES spectra at the Fe K-edge is shown in Figure 5.9(a). Spectrum for the thinnest film presented completely different features compared with the other two films. Given the low amount of material and the low degree of crystallization proved on this sample, a flat spectrum as that observed for samples evaporated at lower temperature could be expected. Nevertheless, the spectrum collected showed an intense whiteline that was not observed in any other of the films characterized. The particularity of this sample was probably explained by the oxidation of the sample surface due to exposition to air after the deposition, which is supported by a slight displacement of the edge to a higher energy. This effect was especially critical at low thickness and UHV should be considered for the characterization.

Sample evaporated with a 21.6 nm thickness presented a more defined spectra with the appearance of some oscillations characteristics of iron. The experimental data was simulated by linear combination fitting using the Athenas software [113] in order to determine the com-

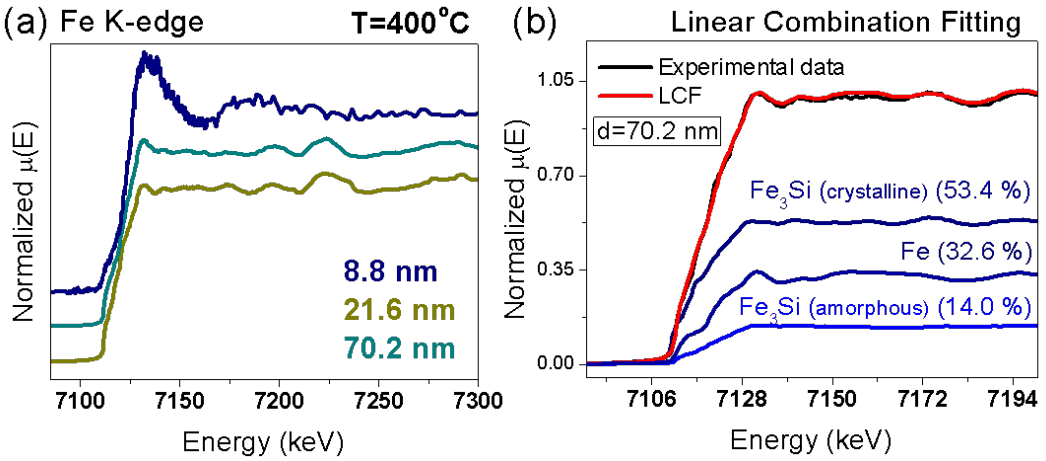

Figure 5.9: (a) Fe K-edge XANES spectra for samples evaporated at 400^o with different thickness. (b) Linear combination fitting of the spectrum recorded for the thicker film (70.2 nm) using Fe and Fe_3Si references. The simulation determined a predominance of 67.4 % of Fe_3Si in the composition of the sample.

d_{Fe_3Si} *(nm)*	Fe_3Si *(%) (SRO)*	Fe_3Si *(%) (LRO)*	*Fe (%)*
8.8	Oxidized		
21.6	71.2 ± 2.1	-	28.8 ± 1.5
70.2	14.0 ± 1.5	53.4 ± 2.4	32.6 ± 1.8

Table 5.2: Composition in percentage of the samples evaporated on $SrTiO_3(001)$ substrates with different thicknesses obtained by linear combination fitting from different standards of the XANES measurements.

position of the sample using the same references employed in the previous section. Results are resumed in table 5.2. It was demonstrated that Fe_3Si (SRO) was the predominant phase, constituting the 71.2 (±2.1) of the total weight, meanwhile iron represented the 28.8 (±1.5) % of the sample. After increasing the thickness to 70.2 nm, the spectrum showed a very similar lineshape to that observed in the spectrum recorded from a Fe_3Si single crystal. The better description of the data was achieved including iron, Fe_3Si (SRO) and Fe_3Si (LRO) standards. The fitting, showed in figure 5.9(b), indicated a predominance of Fe_3Si in the sample where a 53.4 (±2.4) % of the total weight presented long range structural order and only a 14.0 (±1.5) % presented short range order features. The proportion of iron observed, a 32.6 (±1.8) % of the total, was similar to that obtained for the 21.6 nm thick film. XANES, as well as XRD measurements, proved that increasing the thickness of the sample significantly favored the crystallization without increasing the percentage of iron present on the system. Consequently, as long as it is not conditioned by other factors, increasing the thickness of the films could be an effective method to improve the crystallization of the films keeping a single Fe_3Si phase.

5.3 Conclusions

One of the main motivations for the development of the present work was the theoretical study by Tao *et al.*, which established that pure half metallicity (100 % spin polarization) was only present in tetragonal Fe_3Si structures with a lattice strain over the 1.3 % [245]. This condition could be achieved through the commensurate growth of Fe_3Si on $SrTiO_3(001)$. With this idea, the deposition of Fe_3Si on $SrTiO_3(001)$ substrates by PLD was explored unless any successful attempt have been reported in the literature. The samples were characterized by XRR, XRD, XAS and MOKE to determine the structural and magnetic properties of the deposited films, studying the influence of the evaporation temperature and layer thickness. Low surface and interface roughness was determined by XRR. XRD proved the epitaxial and incommensurate growth of Fe_3Si on $SrTiO_3$ (001) with a 45 degrees rotation so that $Fe_3Si[100]\|SrTiO_3[110]$ and $Fe_3Si[001]\|SrTiO_3[001]$. Samples evaporated in a temperature range between 200 and 400^{o}C showed a low degree of crystallization and high mosaicity. For samples evaporated at 600^{o}C or higher, XRD determined the presence of a crystalline iron phase, which grew with its axis co-linear to those of Fe_3Si. XAS measurements demonstrated the presence of iron for samples evaporated at 400^{o}C and temperatures above, with an increasing proportion from a 30 % (400^{o}C) to a 60 % (600^{o}C). Given the short range structural order observed in the films evaporated at 200 and 300^{o}C, the XANES spectra showed a flat lineshape, that hampered the comparison of the data with those obtained from the single crystal Fe_3Si standard, although they presented the same composition. MOKE measurements showed that Fe_3Si films evaporated at 200^{o}C and 300^{o}C showed ferromagnetic behavior at ambient pressure and room temperature, presenting low coercive fields and a high remanent magnetization. Increasing the evaporation temperature resulted in a significant increase of the coercive field and a drop of the remanence. This change in the magnetic response was produced by the formation of iron in the system. However, in order to understand the mechanism that induced this response further information about the distribution of the Fe_3Si and Fe phases on the system should be acquired.

After the results obtained it could be concluded that in order to obtain single phase epitaxial Fe_3Si films, substrate temperature needed to be kept below 400^{o}C. Samples evaporated under this condition presented a low degree of crystallization and high mosaicity. Nevertheless, it was observed in samples evaporated at 400^{o}C that increasing the thickness of the film could increase the order and reduce the degree of mosaicity in the samples without increasing the proportion of iron in the films. According to the work presented by Tao *et al.*, the evaporated films would not present a pure half metallic behavior as a consequence of the incommensurate growth. However, high spin polarization have been also predicted for bulk (cubic) Fe_3Si [72]. Moreover, TMR values as high as 5000 % have been reported for $Fe_3Si/MgO/Fe_3Si$ heterostructures with a cubic symmetry [245]. Therefore, epitaxial Fe_3Si films with a cubic symmetry are a promising candidate for spintronics. Furthermore, the suc-

cessful deposition of epitaxial Fe_3Si films on $SrTiO_3$ (001) by PLD was an important result due to the absence of previous works with an equivalent output. It was demonstrated that PLD is a suitable technique for the preparation of Fe_3Si epitaxial films in $SrTiO_3$ (001), which has been the particular case of study during this chapter, and most likely in other substrates that are yet to be explored. However, in order to achieve a commensurate growth and modify the strain of the lattice, additional deposition parameters should be analyzed beyond the substrate temperature. An issue found during the characterization of the samples was the oxidation of the silicide surface due to the exposition to air. In future works, including an additional step to passivize the Fe_3Si surface through a capping layer or even by controlled oxidation of the surface, as proposed by Mantovan *et al.* [242], should be considered.

Chapter 6

General conclusions

The use of magnetic tunnel contacts has been proved as one of the most effective methods for the electrical injection of spin polarized carriers into semiconductors. The substitution of the conventional 3d-ferromagnet electrodes as $Ni_{80}Fe_{20}$ electrodes by half metal materials can significantly improve the spin polarization on the semiconductor after the injection. However, in order to obtain an efficient injection the ferromagnet/ insulator/ semiconductor heterostructures need to fulfil certain requirements. More concretely, the tunnel barrier needs to be thin enough and present flat and chemically abrupt interfaces so that the spin polarization of the ferromagnetic source is tranferred to the semiconductor. During this thesis, the integration of half metallic films, more concretely Fe_3Si and Fe_3O_4 films, on silicon using tunnel contacts has been studied. These materials were chosen because of high Curie temperature (T_C $>500^oC$), which is a key parameter for the design of spin injection devices able to operate at room temperature. The work has been especially focused to the integration of half metal based magnetic tunnel contacts on silicon. The main objective was to stablish new approaches for the fabrication of high quality magnetic tunnel contacts constituted by half metallic electrodes. The main results and conclusions obtained during the development of the work are summarized in this chapter.

Chapter 4 was devoted to the fabrication of Fe_3O_4/ insulator/ Si heterostructures. In a first approach, magnetite was directly evaporated on untreated Si(100) substrates by PLD, integrating the silicon native oxide as tunnel barrier in the system. In a second approach, the silicon native oxide was eliminated by Sr-induced deoxidation in order to evaporate epitaxial $SrTiO_3$ ultra thin films by MBE for the tunnel barrier and subsequently magenetite was evaporated. In the case of **Fe_3O_4/SiO_2/Si** heterostructures, the direct evaporation of magnetite on untreated Si(001) substrates resulted on the growth of polycrystalline films with a strong granular character. The amorphous character of the native oxide layer prevented from the epitaxial growth of the films. Nevertheless, HRTEM images showed the presence

of single oriented regions in the area near to the Fe_3O_4 interface. The combination of XRD, XPS, HAXPES and RAMAN confirmed the single phase character of the films once the SiO_2 layer was stabilized. The characterization of the buried SiO_2 was carried out by HAXPES, XRR and TEM. The native oxide was intended to prevent further oxidation of the silicon during the evaporation of magnetite. However, during the first stages of the deposition the thickness of the silicon oxide increased progressively. During this process, the magnetite films showed reduced phases and even iron clusters. At certain point, the native oxide was completely stabilized reaching a final thickness of $\sim$4 nm. Then, stochiometric Fe_3O_4 films could be successfully stabilished. The films showed a ferromagnetic response at ambient conditions with low coercive fields in the range of a tens of mT.

In the case of **Fe_3O_4/$SrTiO_3$/Si** heterostructures, native oxide was eliminated in order to evaporate epitaxial $SrTiO_3$ tunnel barriers. In a first approximation this method presents two clear advantages, the control over the thickness of the barrier tunnel and the possibility of growing epitaxial films of magnetite. Nonetheless, previous studies on $SrTiO_3$/Si films prepared by this method already evidenced the presence of an amorphous silicate/oxide layer in the $SrTiO_3$/Si interface after the evaporation of the films. Magnetite films were subsequently evaporated by PLD, exploring different deposition temperatures. It was concluded that in order to stabilized single Fe_3O_4 films for $SrTiO_3$ thicknesses below 10 nm the temperature during the evaporation needed to be kept at 350^{o}C. XAS measurements proved that evaporating at higher temperature resulted on the appearence of iron clusters and even the formation of iron silicides. At 350^{o}C, magnetite grew epitaxially and inconmensurate on top of the $SrTiO_3$ layer, as confirmed by XRD. The evolution of the silicate/oxide interlayer was studied by HAXPES and HRTEM. The results evidenced the increase of thickness of this layer during the evaporation from tenths of nm to 2 nm. The Fe_3O_4 films showed a layer by layer growth which switch to a granulate growth as the $SrTiO_3$ thickness increased. All the interfaces of the system were atomically and chemically flat, which was corroborated by HRTEM and XRR.

The influence of the temperature on Fe_3O_4/$SrTiO_3$/Si samples was analyzed using a $SrTiO_3$ thickness of 10 nm. Increasing the tunnel barrier thickness allowed the stabilization of a stochiometric magnetite films at temperatures up to 550^{o}C. Under these conditions the growth of the silicate/oxide interlayer was more evidenced going from 2 nm at 350^{o}C to almost 4 nm at 550^{o}C under equivalent deposited dosed. This result evidenced the relation between the evolution of this layer and the impossibility of stabilizing magnetite at higher temperature for lower $SrTiO_3$ thicknesses. On the contrary, interface quality and structural properties of the films were equivalent in both samples. From the morphological point of view, it was also observed that the films prepared using this $SrTiO_3$ thickness presented a granular structure. Increasing the temperature induced the formation of bigger structures and significantly increased size dispersion, which had a negative effect in the magnetic response of the samples.

It needs to be remarked that independently of the method used, a direct correlation was observed between the evolution of the insulator/silicon interface and the stabilization of stochiometric magnetite films. If the thickness of the oxide tunnel barrier is too thin or the deposition temperature too high oxygen is able to transferred through the tunnel barrier and induce the oxidation of silicon. This flux of oxygen towards the substrate resulted in the appearence of reduced Fe_yO_x phases and metallic iron. It was also observed that magnetite films in both cases presented a highly resistive character, which is a big drawback when thinking about the application of the system. Nevertheless, this problem could be overcome, by, for example, increasing the thickness of the films, without disminishing the performance of the system in terms of injection efficiency. After the study performed it was concluded that, taking into account the conditions necessary for an efficient spin injection, the use of $Fe_3O_4/SiO_2/Si$ heterostructures would be the best option for the development of spin injection devices. The applicability of the $Fe_3O_4/SrTiO_3/Si$ system is limited by the presence of a silicate layer on the $SrTiO_3/Si$ interface. This will critically modify the properties of the system with unpredictable consequences for the transport properties of the system.

In chapter 5 the evaporation and characterization of **Fe_3Si** thin films was studied. Epitaxial films were successfully stabilized by PLD on $SrTiO_3(001)$ substrates by using an stochiometric Fe_3Si target after exploring different deposition temperatures and thicknesses. The study performed showed that Fe_3Si films were stabilized in a temperature range between 200 and 300^oC under UHV atmosphere. Fe_3Si grew inconmensurate, so that the films presented bulk-like structural parameters. The samples evaporated in this temperature range presented a high degree of mosaicity and disorder but were proved to be single phase, as corroborated by XRD and XAS. Evaporating a higher temperatures slightly improved the crystallographic properties of the films but resulted on the formation of Fe clusters, becoming the predominant phase for temperatures of 600^oC. XRR measurements proved the formation of a flat $Fe_3Si/SrTiO_3$ interface, which is fundamental in the manufacture of magnetic tunnel contacts. As expected, Fe_3Si films presented a ferromagnetic response at ambient conditions as determined by MOKE. The samples presented extremely low coercive fields, in the range of a few mT, and a fast magnetic respones, especially at 200^oC where $M_R/M_S \approx 1$. Increasing the thickness of the films reduced the mosaic character of the films and increased their crystallinity keeping their single phase character. One problem found during the characterization of the samples was the fast surface oxidation after exposing the samples to air. This is an important fact to take into account in future works.

It is important to remark that the exhaustive characterization of the buried interfaces by non-destructive means was only possible because of the use of synchrotron based techniques. This is a fundamental aspect of the work as the properties of the interface play a key role in the development of efficient spin injection devices. The valuable information obtained from the silicon interface allowed to establish a direct

correlation between the stabilization of the half metal films and the passivation of the silicon surface during the growth independently of the tunnel barrier used or the crystallographic properties of the films. The formation of uncertain silicate/oxide phases at the silicon interface has been observed even after depositing a SrO buffer layer through a Sr-induced deoxidation process, which is known to be one of the most efficient methods for the passivation of silicon surfaces. The results obtained in this thesis emphasize the difficulty involved in the integration of half-metallic magnetic tunnel contacts in silicon and the imperative need to incorporate detailed studies of the structural and morphological properties of such systems in order to accelerate the progress in the development of silicon and semiconductor spintronics.

.

References

[1] Vinod Kumar Joshi. Spintronics: A contemporary review of emerging electronics devices. *Engineering Science and Technology, an International Journal*, 19(3):1503 – 1513, 2016.

[2] J. W. Lu, E. Chen, M. Kabir, M. R. Stan, and S. A. Wolf. Spintronics technology: past, present and future. *International Materials Reviews*, 61(7):456–472, 2016.

[3] I. Žutić, J. Fabian, and S. Das Sarma. Spintronics: Fundamentals and applications. *Rev. Mod. Phys.*, 76:323–410, Apr 2004.

[4] N. F. Mott. The Electrical Conductivity of Transition Metals. *Proceedings of the Royal Society of London Series A*, 153:699–717, February 1936.

[5] A. Fert and I. A. Campbell. Two-current conduction in nickel. *Phys. Rev. Lett.*, 21:1190–1192, Oct 1968.

[6] M. N. Baibich, J. M. Broto, A. Fert, F. Nguyen Van Dau, F. Petroff, P. Etienne, G. Creuzet, A. Friederich, and J. Chazelas. Giant magnetoresistance of (001)fe/(001)cr magnetic superlattices. *Phys. Rev. Lett.*, 61:2472–2475, Nov 1988.

[7] G. Binasch, P. Grünberg, F. Saurenbach, and W. Zinn. Enhanced magnetoresistance in layered magnetic structures with antiferromagnetic interlayer exchange. *Phys. Rev. B*, 39:4828–4830, Mar 1989.

[8] S. S. P. Parkin. Origin of enhanced magnetoresistance of magnetic multilayers: Spin-dependent scattering from magnetic interface states. *Phys. Rev. Lett.*, 71:1641–1644, Sep 1993.

[9] R Jansen. The spin-valve transistor: a review and outlook. *Journal of Physics D: Applied Physics*, 36(19):R289, 2003.

[10] R. Schad, C. D. Potter, P. Beliën, G. Verbanck, V. V. Moshchalkov, and Y. Bruynseraede. Giant magnetoresistance in fe/cr superlattices with very thin fe layers. *Applied Physics Letters*, 64(25):3500–3502, 1994.

[11] M. Jullière. Tunneling between ferromagnetic films. *Physics Letters A*, 54(3):225 – 226, 1975.

[12] Eiichi Hirota, Hirosi Sakakima, and Koichiro Inomata. *Tunnel-Type GMR (TMR) Devices*, pages 114–134. Springer Berlin Heidelberg, Berlin, Heidelberg, 2002.

[13] J. S. Moodera, Lisa R. Kinder, Terrilyn M. Wong, and R. Meservey. Large magnetoresistance at room temperature in ferromagnetic thin film tunnel junctions. *Phys. Rev. Lett.*, 74:3273–3276, Apr 1995.

[14] S. Ikeda, J. Hayakawa, Y. Ashizawa, Y. M. Lee, K. Miura, H. Hasegawa, M. Tsunoda, F. Matsukura, and H. Ohno. Tunnel magnetoresistance of 604% at 300k by suppression of ta diffusion in cofeb\mgo\cofeb pseudo-spin-valves annealed at high temperature. *Applied Physics Letters*, 93(8):082508, 2008.

[15] S. Tehrani, J. M. Slaughter, M. Deherrera, B. N. Engel, N. D. Rizzo, J. Salter, M. Durlam, R. W. Dave, J. Janesky, B. Butcher, K. Smith, and G. Grynkewich. Magnetoresistive random access memory using magnetic tunnel junctions. *Proceedings of the IEEE*, 91(5):703–714, 2003.

[16] S. Parkin, X. Jiang, C. Kaiser, A. Panchula, K. Roche, and M. Samant. Magnetically engineered spintronic sensors and memory. *Proceedings of the IEEE*, 91(5):661–680, 2003.

[17] J. Fabian, A. Matos-Abiague, C. Ertler, P. Stano, and $\check{Z}utić. Semiconductorsspintronics. Actaphysicaslovaca, (4-5), 2007.$

[18] D. D. Awschalom and M. E. Flatte. Challenges for semiconductor spintronics. *Nature Physics*, 3:153–159, 2007.

[19] T. Dietl, U. Hohenester, and J. Fabian. *Semiconductor Spintronics*, pages 1–46. Springer Berlin Heidelberg, Berlin, Heidelberg, 2007.

[20] S. Datta and B. Das. Electronic analog of the electroâoptic modulator. *Applied Physics Letters*, 56(7):665–667, 1990.

[21] G. Lampel. Nuclear dynamic polarization by optical electronic saturation and optical pumping in semiconductors. *Phys. Rev. Lett.*, 20:491–493, Mar 1968.

[22] D. Awschalom and N. Samarth. *Optical manipulation, transport and storage of spin coherence in semiconductors*, pages 147–194. Springer Berlin Heidelberg, Berlin, Heidelberg, 2002.

[23] I. Appelbaum, B. Huang, and D. J. Monsma. Electronic measurement and control of spin transport in silicon. *Nature*, 447:295, 2007.

[24] S. P. Dash, S. Sharma, R. S. Patel, M. P. de Jong, and R. Jansen. Electrical creation of spin polarization in silicon at room temperature. *Nature*, 462:491, 2009.

[25] S. A. Crooker, M. Furis, X. Lou, C. Adelmann, D. L. Smith, C. J. Palmstrøm, and P. A. Crowell. Imaging spin transport in lateral ferromagnet-semiconductor structures. *Science*, 309(5744):2191–2195, 2005.

[26] Xiaohua Lou, Christoph Adelmann, Scott A. Crooker, Eric S. Garlid, Jianjie Zhang, K. S. Madhukar Reddy, Soren D. Flexner, Chris J. Palmstrøm, and Paul A. Crowell. Electrical detection of spin transport in lateral ferromagnet-semiconductor devices. *Nature Physics*, 3:197–202, 2007.

[27] H. C. Koo, J. H. Kwon, J. Eom, J. Chang, S. H. Han, and M. Johnson. Control of spin precession in a spin-injected field effect transistor. *Science*, 325(5947):1515–1518, 2009.

[28] P. Chuang, S.-C. Ho, L. W. Smith, F. Sfigakis, M. Pepper, C.-H. Chen, J.-C. Fan, J. P. Griffiths, I. Farrer, H. E. Beere, G. A. C. Jones, D. A. Ritchie, and T.-M. Chen. All-electric all-semiconductor spin field-effect transistors. *Nature Nanotechnology*, 10:35–39, 2014.

[29] D. Hägele, M. Oestreich, W. W. Rühle, N. Nestle, and K. Eberl. Spin transport in gaas. *Applied Physics Letters*, 73(11):1580–1582, 1998.

[30] P. C. van Son, H. van Kempen, and P. Wyder. Boundary resistance of the ferromagnetic-nonferromagnetic metal interface. *Phys. Rev. Lett.*, 58:2271–2273, May 1987.

[31] I. Appelbaum. Introduction to spin polarized ballistic hot electron injection and detection in silicon, 2009.

[32] G. Schmidt, D. Ferrand, L. W. Molenkamp, A. T. Filip, and B. J. van Wees. Fundamental obstacle for electrical spin injection from a ferromagnetic metal into a diffusive semiconductor. *Phys. Rev. B*, 62:R4790–R4793, Aug 2000.

[33] L. Wang, T. Y. Chen, and C. Leighton. Spin-dependent band structure effects and measurement of the spin polarization in the candidate half-metal cos_2. *Phys. Rev. B*, 69:094412, Mar 2004.

[34] Roman Fetzer, Jan-Peter Wüstenberg, Tomoyuki Taira, Tetsuya Uemura, Masafumi Yamamoto, Martin Aeschlimann, and Mirko Cinchetti. Structural, chemical, and electronic properties of the co_2mnsi(001)/mgo interface. *Phys. Rev. B*, 87:184418, May 2013.

[35] A. Schmehl, V. Vaithyanathan, A. Herrnberger, S. Thiel, C. Richter, M. Liberati, T. Heeg, M. Röckerath, L. Fitting Kourkoutis, S. Mrüshlbauer, P. Böni, D. A. Muller,

Y. Barash, J. Schubert, Y. Idzerda, J. Mannhart, and D. G. Schlom. Epitaxial integration of the highly spin-polarized ferromagnetic semiconductor euo with silicon and gan. *Nature Materials*, 6:882–887, 2007.

[36] Tomasz Dietl. Ferromagnetic semiconductors. *Semiconductor Science and Technology*, 17(4):377, 2002.

[37] T. Dietl, H. Ohno, F. Matsukura, J. Cibert, and D. Ferrand. Zener model description of ferromagnetism in zinc-blende magnetic semiconductors. *Science*, 287(5455):1019–1022, 2000.

[38] Lin Chen, Xiang Yang, Fuhua Yang, Jianhua Zhao, Jennifer Misuraca, Peng Xiong, and Stephan von MolnÃ¡r. Enhancing the curie temperature of ferromagnetic semiconductor (ga,mn)as to 200 k via nanostructure engineering. *Nano Letters*, 11(7):2584–2589, 2011. PMID: 21696165.

[39] E. I. Rashba. Theory of electrical spin injection: Tunnel contacts as a solution of the conductivity mismatch problem. *Phys. Rev. B*, 62:R16267–R16270, Dec 2000.

[40] A. Fert and H. Jaffrès. Conditions for efficient spin injection from a ferromagnetic metal into a semiconductor. *Phys. Rev. B*, 64:184420, Oct 2001.

[41] B. T Jonker, G. Kioseoglou, A. T. Hanbicki, C. H. Li, and P. E. Thompson. Electrical spin-injection into silicon from a ferromagnetic metal/tunnel barrier contact. *Nature Physics*, 3:542–546, 2007.

[42] O. M. J. van ât Erve, A. T. Hanbicki, M. Holub, C. H. Li, C. Awo-Affouda, P. E. Thompson, and B. T. Jonker. Electrical injection and detection of spin-polarized carriers in silicon in a lateral transport geometry. *Applied Physics Letters*, 91(21):212109, 2007.

[43] Toshio Suzuki, Tomoyuki Sasaki, Tohru Oikawa, Masashi Shiraishi, Yoshishige Suzuki, and Kiyoshi Noguchi. Room-temperature electron spin transport in a highly doped si channel. *Applied Physics Express*, 4(2):023003, 2011.

[44] A. B. Balantekin and N. Takigawa. Quantum tunneling in nuclear fusion. *Rev. Mod. Phys.*, 70:77–100, Jan 1998.

[45] Yuriy Makhlin, Gerd Schön, and Alexander Shnirman. Quantum-state engineering with josephson-junction devices. *Rev. Mod. Phys.*, 73:357–400, May 2001.

[46] Yuriy Makhlin, Gerd Schön, and Alexander Shnirman. The quantum theory of nuclear disintegration. *Nature*, 122:805–806, 1928.

[47] Edward U. Condon. Nuclear motions associated with electron transitions in diatomic molecules. *Phys. Rev.*, 32:858–872, Dec 1928.

[48] E. Merzbacher. *Quantum mechanics*. Wiley&Sons, 3^{rd} edition edition, 1998.

[49] P. M. Tedrow and R. Meservey. Spin-dependent tunneling into ferromagnetic nickel. *Phys. Rev. Lett.*, 26:192–195, Jan 1971.

[50] P. M. Tedrow and R. Meservey. Spin polarization of electrons tunneling from films of fe, co, ni, and gd. *Phys. Rev. B*, 7:318–326, Jan 1973.

[51] Mary Beth Stearns. Simple explanation of tunneling spin-polarization of fe, co, ni and its alloys. *Journal of Magnetism and Magnetic Materials*, 5(2):167 – 171, 1977.

[52] J. C. Slonczewski. Conductance and exchange coupling of two ferromagnets separated by a tunneling barrier. *Phys. Rev. B*, 39:6995–7002, Apr 1989.

[53] W. H. Butler, X.-G. Zhang, T. C. Schulthess, and J. M. MacLaren. Spin-dependent tunneling conductance of Fe|MgO|Fe sandwiches. *Phys. Rev. B*, 63:054416, Jan 2001.

[54] J. Mathon and A. Umerski. Theory of tunneling magnetoresistance of an epitaxial fe/mgo/fe(001) junction. *Phys. Rev. B*, 63:220403, May 2001.

[55] P. LeClair, H. J. M. Swagten, J. T. Kohlhepp, R. J. M. van de Veerdonk, and W. J. M. de Jonge. Apparent spin polarization decay in cu-dusted Co/al$_2O_3$/Co tunnel junctions. *Phys. Rev. Lett.*, 84:2933–2936, Mar 2000.

[56] P. LeClair, J. T. Kohlhepp, H. J. M. Swagten, and W. J. M. de Jonge. Interfacial density of states in magnetic tunnel junctions. *Phys. Rev. Lett.*, 86:1066–1069, Feb 2001.

[57] P. LeClair, B. Hoex, H. Wieldraaijer, J. T. Kohlhepp, H. J. M. Swagten, and W. J. M. de Jonge. Sign reversal of spin polarization in co/ru/al$_2$o$_3$/Co magnetic tunnel junctions. *Phys. Rev. B*, 64:100406, Aug 2001.

[58] S. Yuasa, T. Nagahama, and Y. Suzuki. Spin-polarized resonant tunneling in magnetic tunnel junctions. *Science*, 297(5579):234–237, 2002.

[59] J. P. Velev, K. D. Belashchenko, D. A. Stewart, M. van Schilfgaarde, S. S. Jaswal, and E. Y. Tsymbal. Negative spin polarization and large tunneling magnetoresistance in epitaxial Co|srtio$_3$|Co magnetic tunnel junctions. *Phys. Rev. Lett.*, 95:216601, Nov 2005.

[60] K. D. Belashchenko, E. Y. Tsymbal, I. I. Oleynik, and M. van Schilfgaarde. Positive spin polarization in Co$\hat{a}$al$_2$o$_3\hat{a}$Co tunnel junctions driven by oxygen adsorption. *Phys. Rev. B*, 71:224422, Jun 2005.

[61] J. M. De Teresa, A. Barthélémy, A. Fert, J. P. Contour, R. Lyonnet, F. Montaigne, P. Seneor, and A. Vaurès. Inverse tunnel magnetoresistance in

Co/srtio$_3$/la$_{0.7}$sr$_{0.3}$mno$_3$: New ideas on spin-polarized tunneling. *Phys. Rev. Lett.*, 82:4288–4291, May 1999.

[62] Y. Ando, K. Hamaya, K. Kasahara, Y. Kishi, K. Ueda, K. Sawano, T. Sadoh, and M. Miyao. Electrical injection and detection of spin-polarized electrons in silicon through an fe$_3$si/si schottky tunnel barrier. *Applied Physics Letters*, 94(18):182105, 2009.

[63] K. Hamaya, Y. Baba, G. Takemoto, K. Kasahara, S. Yamada, K. Sawano, and M. Miyao. Qualitative study of temperature-dependent spin signals in n-ge-based lateral devices with fe3si/n+-ge schottky-tunnel contacts. *Journal of Applied Physics*, 113(18):183713, 2013.

[64] Y. Ando, K. Kasahara, K. Yamane, Y. Baba, Y. Maeda, Y. Hoshi, K. Sawano, M. Miyao, and K. Hamaya. Bias current dependence of spin accumulation signals in a silicon channel detected by a schottky tunnel contact. *Applied Physics Letters*, 99(1):012113, 2011.

[65] R. Jansen and B. C. Min. Detection of a spin accumulation in nondegenerate semiconductors. *Phys. Rev. Lett.*, 99:246604, Dec 2007.

[66] R Jansen, S P Dash, S Sharma, and B C Min. Silicon spintronics with ferromagnetic tunnel devices. *Semiconductor Science and Technology*, 27(8):083001, 2012.

[67] Kun-Rok Jeon, Byoung-Chul Min, Il-Jae Shin, Chang-Yup Park, Hun-Sung Lee, Young-Hun Jo, and Sung-Chul Shin. Electrical spin accumulation with improved bias voltage dependence in a crystalline cofe/mgo/si system. *Applied Physics Letters*, 98(26):262102, 2011.

[68] C. H. Li, O. M. J. van Érve, and B. T. Jonker. Electrical injection and detection of spin accumulation in silicon at 500 k with magnetic metal/silicon dioxide contacts. *Nature Communications*, 2:245, 2011.

[69] R. Jansen, B. C. Min, S. P. Dash, S. Sharma, G. Kioseoglou, A. T. Hanbicki, O. M. J. van 't Erve, P. E. Thompson, and B. T. Jonker. Electrical spin injection into moderately doped silicon enabled by tailored interfaces. *Phys. Rev. B*, 82:241305, Dec 2010.

[70] B.-C. Min, K. Motohashi, C. Lodder, and R. Jansen. Tunable spin-tunnel contacts to silicon using low-work-function ferromagnets. *Nature Materials*, 5:817–822, 2006.

[71] S. P. Dash, S. Sharma, J. C. Le Breton, J. Peiro, H. Jaffrès, J.-M. George, A. Lemaître, and R. Jansen. Spin precession and inverted hanle effect in a semiconductor near a finite-roughness ferromagnetic interface. *Phys. Rev. B*, 84:054410, Aug 2011.

[72] R. A. de Groot, F. M. Mueller, P. G. van Engen, and K. H. J. Buschow. New class of materials: Half-metallic ferromagnets. *Phys. Rev. Lett.*, 50:2024–2027, Jun 1983.

[73] K. E. H. M. Hanssen, P. E. Mijnarends, L. P. L. M. Rabou, and K. H. J. Buschow. Positron-annihilation study of the half-metallic ferromagnet nimnsb: Experiment. *Phys. Rev. B*, 42:1533–1540, Jul 1990.

[74] J. M. D. Coey and M. Venkatesan. Half-metallic ferromagnetism: Example of cro2 (invited). *Journal of Applied Physics*, 91(10):8345–8350, 2002.

[75] Myron B. Salamon and Marcelo Jaime. The physics of manganites: Structure and transport. *Rev. Mod. Phys.*, 73:583–628, Aug 2001.

[76] R. Arras, L. Calmels, and B. Warot-Fonrose. Half-metallicity, magnetic moments, and gap states in oxygen-deficient magnetite for spintronic applications. *Applied Physics Letters*, 100(3):032403, 2012.

[77] C. B. Eom, R. J. Cava, R. M. Fleming, Julia M. Phillips, R. B. vanDover, J. H. Marshall, J. W. P. Hsu, J. J. Krajewski, and W. F. Peck. Single-crystal epitaxial thin films of the isotropic metallic oxides sr1–xcaxruo3 ($0 \leq x \leq 1$). *Science*, 258(5089):1766–1769, 1992.

[78] Yu Lu, X. W. Li, G. Q. Gong, Gang Xiao, A. Gupta, P. Lecoeur, J. Z. Sun, Y. Y. Wang, and V. P. Dravid. Large magnetotunneling effect at low magnetic fields in micrometer-scale epitaxial $la_{0.67}sr_{0.33}mno_3$ tunnel junctions. *Phys. Rev. B*, 54:R8357–R8360, Sep 1996.

[79] K. D. Belashchenko, J. K. Glasbrenner, and A. L. Wysocki. Spin injection from a half-metal at finite temperatures. *Phys. Rev. B*, 86:224402, Dec 2012.

[80] P. Alagarsamy and A. Srinivasan. Physics of magnetic recording and recording media, 2013.

[81] D.D. Sarma, E.V. Sampathkumaran, Sugata Ray, R. Nagarajan, Subham Majumdar, Ashwani Kumar, G. Nalini, and T.N. Guru Row. Magnetoresistance in ordered and disordered double perovskite oxide, sr2femoo6. *Solid State Communications*, 114(9):465 – 468, 2000.

[82] I Galanakis and Ph Mavropoulos. Spin-polarization and electronic properties of half-metallic heusler alloys calculated from first principles. *Journal of Physics: Condensed Matter*, 19(31):315213, 2007.

[83] J. Navarro, C. Frontera, D. Rubi, N. Mestres, and J. Fontcuberta. Aging of sr2femoo6 and related oxides. *Materials Research Bulletin*, 38(9):1477 – 1486, 2003.

[84] P. A. Dowben and R. Skomski. Finite-temperature spin polarization in half-metallic ferromagnets. *Journal of Applied Physics*, 93(10):7948–7950, 2003.

[85] M. Ležaić, Ph. Mavropoulos, J. Enkovaara, G. Bihlmayer, and S. Blügel. Thermal collapse of spin polarization in half-metallic ferromagnets. *Phys. Rev. Lett.*, 97:026404, Jul 2006.

[86] Qiang Zhang, A. V. Nurmikko, G. X. Miao, G. Xiao, and A. Gupta. Ultrafast spin-dynamics in half-metallic Cro_2 thin films. *Phys. Rev. B*, 74:064414, Aug 2006.

[87] Z Nedelkoski, B. Kuerbanjiang, S. E. Glover, A. M. Sanchez, A. Kepaptsoglou, D. Ghasemi, C. W. Burrows, S. Yamada, K. Hamaya, Q. M. Ramasse, P. J. Hasnip, T. Hase, G. R. Bell, A. Hirohata, and V. K. Lazarov. Realisation of magnetically and atomically abrupt half-metal/semiconductor interface: Co2fesi0.5al0.5/ge(111). *Scientific Reports*, 6:37282, 2016.

[88] R. Jansen. Silicon spintronics. *Nature Materials*, 11:400–408, 2012.

[89] A. Jain, C. Vergnaud, J. Peiro, J. C. Le Breton, E. Prestat, L. Louahadj, C. Portemont, C. Ducruet, V. Baltz, A. Marty, A. Barski, P. Bayle-Guillemaud, L. Vila, J.-P. Attané, E. Augendre, H. Jaffrés, J.-M. George, and M. Jamet. Electrical and thermal spin accumulation in germanium. *Applied Physics Letters*, 101(2):022402, 2012.

[90] M. Tran, H. Jaffrès, C. Deranlot, J.-M. George, A. Fert, A. Miard, and A. Lemaître. Enhancement of the spin accumulation at the interface between a spin-polarized tunnel junction and a semiconductor. *Phys. Rev. Lett.*, 102:036601, Jan 2009.

[91] F. J. Jedema, A. T. Filip, and B. J. van Weels. Electrical spin injection and accumulation at room temperature in an all-metal mesoscopic spin valve. *Nature*, 410:345, 2001.

[92] Kun-Rok Jeon, Byoung-Chul Min, Young-Hun Jo, Hun-Sung Lee, Il-Jae Shin, Chang-Yup Park, Seung-Young Park, and Sung-Chul Shin. Electrical spin injection and accumulation in cofe/mgo/ge contacts at room temperature. *Phys. Rev. B*, 84:165315, Oct 2011.

[93] Tetsuya Uemura, Kenji Kondo, Jun Fujisawa, Ken-ichi Matsuda, and Masafumi Yamamoto. Critical effect of spin-dependent transport in a tunnel barrier on enhanced hanle-type signals observed in three-terminal geometry. *Applied Physics Letters*, 101(13):132411, 2012.

[94] S. Sharma, A. Spiesser, S. P. Dash, S. Iba, S. Watanabe, B. J. van Wees, H. Saito, S. Yuasa, and R. Jansen. Anomalous scaling of spin accumulation in ferromagnetic tunnel devices with silicon and germanium. *Phys. Rev. B*, 89:075301, Feb 2014.

[95] P. A. Savale. Physical Vapor Deposition (PVD) Methods for Synthesis of Thin Films: A Comparative Study. *Archives of Applied Science Research*, 8:1–8, 2016.

[96] Ian W. Boyd. Thin film growth by pulsed laser deposition. *Ceramics International*, 22(5):429 – 434, 1996.

[97] Peter K. Schenck, Mark D. Vaudin, David W. Bonnell, John W. Hastie, and Albert J. Paul. Particulate reduction in the pulsed laser deposition of barium titanate thin films. *Applied Surface Science*, 127-129:655 – 661, 1998.

[98] John R. Arthur. Molecular beam epitaxy. *Surface Science*, 500(1):189 – 217, 2002.

[99] D. R. Penn S. Tanuma, C. J. Powell. Calculations of electron inelastic mean free paths. v. data for 14 organic compounds over the 50–2000 ev range. *Surface and Interface Analysis*, 21(3):165 – 176, 1994.

[100] Kuppers G. Ertl, J. *Low energy electrons and surface chemistry*. VCH, 1985.

[101] J.R. Rubio-Zuazo and G.R. Castro. Hard x-ray photoelectron spectroscopy (haxpes) ($\leq$15kev) at spline, the spanish crg beamline at the esrf. *Nuclear Instruments and Methods in Physics Research Section A: Accelerators, Spectrometers, Detectors and Associated Equipment*, 547(1):64 – 72, 2005. Proceedings of the Workshop on Hard X-ray Photoelectron Spectroscopy.

[102] Proceedings of Recent Trends in Charged Particle Optics and Surface Physics instrumentation. *An energy analyser for Hard X-ray Photoelectron Spectroscopy*, Brno, Czech Republic, 2006.

[103] J. Rubio-Zuazo and G. R. Castro. Hard x-ray photoelectron spectroscopy (haxpes) and x-ray surface diffraction station. *Pico*, 10(2), 2006.

[104] M. Yasaka. X-ray thin film measurement techniques (v). x-ray reflectivity. *The Rikago Journal*, 26(2):1–9, 2010.

[105] C. Kittel. *Introduction to solid state physics*. John Wiley and Sons, 1996.

[106] N. W. Ashcroft and N. D. Mermin. *Introduction to solid state physics*. Brooks/Cole, 1976.

[107] R. Feidenhans'l. Surface structure determination by x-ray diffraction. *Surface Science Reports*, 10(3):105 – 188, 1989.

[108] I K Robinson and D J Tweet. Surface x-ray diffraction. *Reports on Progress in Physics*, 55(5):599, 1992.

[109] J. I. Langford and A. J. C. Wilson. Scherrer after sixty years: A survey and some new results in the determination of crystallite size. *Journal of Applied Crystallography*, 11(2):102–113, Apr 1978.

[110] J. Rubio Zuazo and G. Castro. Information depth determination for hard xâray photoelectron spectroscopy up to 15 kev photoelectron kinetic energy. *Surface and Interface Analysis*, 40:1438 – 1443, 11 2008.

[111] J. Als-Nielsen and D. McMorrow. *Elements of modern X-ray physics*. John Wiley and Sons, 2001.

[112] J. Lubeck, B. Beckhoff, R. Fliegauf, I. Holfelder, P. H́onicke, M. Ḿuller, B. Pollakowski, F. Reinhardt, and J. Weser. A novel instrument for quantitative nanoanalytics involving complementary x-ray methodologies. *Review of Scientific Instruments*, 84(4):045106, 2013.

[113] B. Ravel and M. Newville. *ATHENA*, *ARTEMIS*, *HEPHAESTUS*: data analysis for X-ray absorption spectroscopy using *IFEFFIT*. *Journal of Synchrotron Radiation*, 12(4):537–541, Jul 2005.

[114] I. Horcas, R. Fernández, J. M. Gómez-Rodríguez, J. Colchero, J. Gómez-Herrero, and A. M. Baro. Wsxm: A software for scanning probe microscopy and a tool for nanotechnology. *Review of Scientific Instruments*, 78(1):013705, 2007.

[115] C. V. Raman. A new radiation [reproduced from indian j. phys., 1928, 2, 387â398]. *Current Science*, 74(4):382–386, 1998.

[116] T. Jawhari. Micro-raman spectroscopy of the solid state: applications to semiconductors and thin films. *Analusis*, 28(1):15–21, 2000.

[117] A. Achiq, R. Rizk, F. Gourbilleau, R. Madelon, B. Garrido, A. Pérez-Rodríguez, and J. R. Morante. Effects of prior hydrogenation on the structure and properties of thermally nanocrystallized silicon layers. *Journal of Applied Physics*, 83(11):5797–5803, 1998.

[118] J. Macía, E. Martín, A. Pérez-Rodríguez, J. Jiménez, J. R. Morante, B. Aspar, and J. Margail. Raman microstructural analysis of silicon-on-insulator formed by high dose oxygen ion implantation: As-implanted structures. *Journal of Applied Physics*, 82(8):3730–3735, 1997.

[119] B. Huang, D. J. Monsma, and I. Appelbaum. Coherent spin transport through a 350 micron thick silicon wafer. *Phys. Rev. Lett.*, 99:177209, Oct 2007.

[120] V. Sverdlov and S. Selberherr. Silicon spintronics: Progress and challenges. *Physics Reports*, 585:1 – 40, 2015. Silicon spintronics: Progress and challenges.

[121] M. I. Dýakanov and V. I. Perel. The effect of strain on the spin relaxation of conduction electrons in iii-v semiconductors. *Sov. Phys. Solid State*, 13:3023, 1972.

[122] M. Morita, T. Ohmi, E. Hasegawa, M. Kawakami, and K. Suma. Control factor of native oxide growth on silicon in air or in ultrapure water. *Applied Physics Letters*, 55(6):562–564, 1989.

[123] R. J. Archer. Optical measurement of film growth on silicon and germanium surfaces in room air. *Journal of The Electrochemical Society*, 104(10):619–622, 1957.

[124] F. Lukeš. Oxidation of si and gaas in air at room temperature. *Surface Science*, 30(1):91 – 100, 1972.

[125] T. Hattori, K. Takase, H. Yamagishi, R. Sugino, Y. Nara, and T. Ito. Chemical structures of native oxides formed during wet chemical treatments. *Japanese Journal of Applied Physics*, 28(2A):L296, 1989.

[126] M. Morita, T. Ohmi, E. Hasegawa, M. Kawakami, and M. Ohwada. Growth of native oxide on a silicon surface. *Journal of Applied Physics*, 68(3):1272–1281, 1990.

[127] R. C. Henderson, R. B. Marcus, and W. J. Polito. Carbide contamination of silicon surfaces. *Journal of Applied Physics*, 42(3):1208–1215, 1971.

[128] K. Arima, K. Endo, T. Kataoka, Y. Oshikane, H. Inoue, and Y. Mori. Atomically resolved scanning tunneling microscopy of hydrogen-terminated si(001) surfaces after hf cleaning. *Applied Physics Letters*, 76(4):463–465, 2000.

[129] J. H. Comfort, L. M. Garverick, and R. Reif. Silicon surface cleaning by low dose argonâion bombardment for lowâtemperature (750âÂ°c) epitaxial silicon deposition. i. process considerations. *Journal of Applied Physics*, 62(8):3388–3397, 1987.

[130] M.C. Moore, N. Kalyanasundaram, J.B. Freund, and H.T. Johnson. Structural and sputtering effects of medium energy ion bombardment of silicon. *Nuclear Instruments and Methods in Physics Research Section B: Beam Interactions with Materials and Atoms*, 225(3):241 – 255, 2004.

[131] K. C. Pandey. Reconstruction of the si(100)-2x1 surface. In *Proceedings of the 17th International Conference on the Physics of Semiconductors.* Springer, 1985.

[132] F. Dominguez, A. Tempel, and A. Zehe. Rheed studies during surface cleaning of silicon for mbe substrates. *Crystal Research and Technology*, 26(2):207–210, 1991.

[133] K. Hubbard and D. Schlom. Thermodynamic stability of binary oxides in contact with silicon. *Journal of Materials Research*, 11(11):2757–2776, 1996.

[134] Yi Wei, Xiaoming Hu, Yong Liang, D. C. Jordan, Brad Craigo, Ravi Droopad, Z. Yu, Alex Demkov, John L. Edwards, and William J. Ooms. Mechanism of cleaning si(100) surface using sr or sro for the growth of crystalline $srtio_3$ films. *Journal of Vacuum Science & Technology B: Microelectronics and Nanometer Structures Processing, Measurement, and Phenomena*, 20(4):1402–1405, 2002.

[135] D. Klement, M. Spreitzer, and D. Suvorov. Formation of a strontium buffer layer on si(001) by pulsed-laser deposition through the sr/si(001) (2×3) surface reconstruction. *Applied Physics Letters*, 106(7):071602, 2015.

[136] G. Delhaye, C. Merckling, M. El-Kazzi, G. Saint-Girons, M. Gendry, Y. Robach, G. Hollinger, L. Largeau, and G. Patriarche. Structural properties of epitaxial srtio$_3$ thin films grown by molecular beam epitaxy on si(001). *Journal of Applied Physics*, 100(12):124109, 2006.

[137] J. Ramdani, R. Droopad, Z. Yu, J. A. Curless, C. D. Overgaard, J. Finder, K. Eisenbeiser, J. A. Hallmark, W. J. Ooms, V. Kaushik, P. Alluri, and S. Pietambaram. Interface characterization of high-quality srtio$_3$ thin films on si(100) substrates grown by molecular beam epitaxy. *Applied Surface Science*, 159-160:127 – 133, 2000.

[138] Z. Jovanović, M. Spreitzer, J. Kovač, D. Klement, and D. Suvorov. Silicon surface deoxidation using strontium oxide deposited with the pulsed laser deposition technique. *ACS Appl. Mater. Interfaces*, 6:18205–18214, 2000.

[139] Ze Zhang and Sashi Satpathy. Electron states, magnetism, and the verwey transition in magnetite. *Phys. Rev. B*, 44:13319–13331, Dec 1991.

[140] Akira Yanase and Kiiti Siratori. Band structure in the high temperature phase of fe3o4. *Journal of the Physical Society of Japan*, 53(1):312–317, 1984.

[141] K. Jordan, A. Cazacu, G. Manai, S. F. Ceballos, S. Murphy, and I. V. Shvets. Scanning tunneling spectroscopy study of the electronic structure of fe$_3$o$_4$ surfaces. *Phys. Rev. B*, 74:085416, Aug 2006.

[142] D.J. Huang, C.F. Chang, J. Chen, L.H. Tjeng, A.D. Rata, W.P. Wu, S.C. Chung, H.J. Lin, T. Hibma, and C.T. Chen. Spin-resolved photoemission studies of epitaxial fe3o4(100) thin films. *Journal of Magnetism and Magnetic Materials*, 239(1):261 – 265, 2002. International Symposium on Physics of Magnetic Materials/Internat ional Symposium on Advanced Magnetic Technologies.

[143] J G Tobin, S A Morton, S W Yu, G D Waddill, I K Schuller, and S A Chambers. Spin resolved photoelectron spectroscopy of fe 3 o 4 : the case against half-metallicity. *Journal of Physics: Condensed Matter*, 19(31):315218, 2007.

[144] Yu. S. Dedkov, U. Rüdiger, and G. Güntherodt. Evidence for the half-metallic ferromagnetic state of fe$_3$o$_4$ by spin-resolved photoelectron spectroscopy. *Phys. Rev. B*, 65:064417, Jan 2002.

[145] M Fonin, Yu S Dedkov, R Pentcheva, U Rüdiger, and G Güntherodt. Spin-resolved photoelectron spectroscopy of fe 3 o 4 ârevisited. *Journal of Physics: Condensed Matter*, 20(14):142201, 2008.

[146] W. Wang, J.-M. Mariot, M. C. Richter, O. Heckmann, W. Ndiaye, P. De Padova, A. Taleb-Ibrahimi, P. Le Fèvre, F. Bertran, F. Bondino, E. Magnano, J. Krempaský, P. Blaha, C. Cacho, F. Parmigiani, and K. Hricovini. Fe t_{2g} band dispersion and spin polarization in thin films of fe$_3$o$_4$(0 0 1)/mgo(0 0 1): Half-metallicity of magnetite revisited. *Phys. Rev. B*, 87:085118, Feb 2013.

[147] Wei Wu, Zhaohui Wu, Taekyung Yu, Changzhong Jiang, and Woo-Sik Kim. Recent progress on magnetic iron oxide nanoparticles: synthesis, surface functional strategies and biomedical applications. *Science and Technology of Advanced Materials*, 16(2):023501, 2015. PMID: 27877761.

[148] Sinhué López, A. H. Romero, J. Mejía-López, J. Mazo-Zuluaga, and J. Restrepo. Structure and electronic properties of iron oxide clusters: A first-principles study. *Phys. Rev. B*, 80:085107, Aug 2009.

[149] R. M. Cornell and U. Schwertmann. *The iron oxides: Structure, properties, reactions, ocurrences and uses*. Wiley-VCH, 2006.

[150] E. J. W. Verwey. Electronic conduction of magnetite (fe3o4) and its transition point at low temperatures. *Nature*, 144:327–328, August 1939.

[151] Friedrich Walz. The verwey transition - a topical review. *Journal of Physics: Condensed Matter*, 14(12):R285, 2002.

[152] Przemysław Piekarz, Krzysztof Parlinski, and Andrzej M. Oleś. Mechanism of the verwey transition in magnetite. *Phys. Rev. Lett.*, 97:156402, Oct 2006.

[153] Przemysław Piekarz, Krzysztof Parlinski, and Andrzej M. Oleś. Origin of the verwey transition in magnetite: Group theory, electronic structure, and lattice dynamics study. *Phys. Rev. B*, 76:165124, Oct 2007.

[154] A. J. M. Kuipers and V. A. M. Brabers. Electrical transport in magnetite near the verwey transition. *Phys. Rev. B*, 20:594–600, Jul 1979.

[155] M. Ziese and H. J. Blythe. Magnetoresistance of magnetite. *Journal of Physics: Condensed Matter*, 12(1):13, 2000.

[156] I. Bernal-Villamil and S. Gallego. Electronic phase transitions in ultrathin magnetite films. *Journal of Physics: Condensed Matter*, 27(29):293202, 2015.

[157] M.F. Koenig and J.T. Grant. Comparison of factor analysis and curve-fitting for data analysis in xps. *Journal of Electron Spectroscopy and Related Phenomena*, 41(1):145 – 156, 1986.

[158] M. Aronniemi, J. Sainio, and J. Lahtinen. Aspects of using the factor analysis for xps data interpretation. *Surface Science*, 601(2):479 – 489, 2007.

[159] A. Ohtomo and H. Y. Hwang. A high-mobility electron gas at the laalo3/srtio3 heterointerface. *Nature*, 427:423, January 2004.

[160] S. Thiel, G. Hammerl, A. Schmehl, C. W. Schneider, and J. Mannhart. Tunable quasi-two-dimensional electron gases in oxide heterostructures. *Science*, 313(5795):1942–1945, 2006.

[161] Juan Shen, Hunpyo Lee, Roser Valentí, and Harald O. Jeschke. Ab initio study of the two-dimensional metallic state at the surface of $srtio_3$: Importance of oxygen vacancies. *Phys. Rev. B*, 86:195119, Nov 2012.

[162] N. Pavlenko, T. Kopp, E. Y. Tsymbal, J. Mannhart, and G. A. Sawatzky. Oxygen vacancies at titanate interfaces: Two-dimensional magnetism and orbital reconstruction. *Phys. Rev. B*, 86:064431, Aug 2012.

[163] Y. Aiura, I. Hase, H. Bando, T. Yasue, T. Saitoh, and D. S. Dessau. Photoemission study of the metallic state of lightly electron-doped srtio3. *Surface Science*, 515(1):61 – 74, 2002.

[164] D. Kan, T. Terashima, R. Kanda, A. Masuno, K. Tanaka, S. Chu, H. Kan, A. Ishizumi, Y. Kanemitsu, Y. Shimakawa, and M. Takano. Blue-light emission at room temperature from ar+-irradiated srtio3. *Nature Materials*, 4:816, 2005.

[165] Masashi Kawasaki, Kazuhiro Takahashi, Tatsuro Maeda, Ryuta Tsuchiya, Makoto Shinohara, Osamu Ishiyama, Takuzo Yonezawa, Mamoru Yoshimoto, and Hideomi Koinuma. Atomic control of the srtio3 crystal surface. *Science*, 266(5190):1540–1542, 1994.

[166] G. Koster, B. L. Kropman, G. J. H. M. Rijnders, D. H. A. Blank, and H. Rogalla. Quasi-ideal strontium titanate crystal surfaces through formation of strontium hydroxide. *Applied Physics Letters*, 73(20):2920–2922, 1998.

[167] V. Leca, G. Rijnders, G. Koster, D. Blank, and H. Rogalla. Wet etching methods for perovskite substrates. *Appl*, 587, 01 2000.

[168] M. Kareev, S. Prosandeev, J. Liu, C. Gan, A. Kareev, J. W. Freeland, Min Xiao, and J. Chakhalian. Atomic control and characterization of surface defect states of tio2 terminated srtio3 single crystals. *Applied Physics Letters*, 93(6):061909, 2008.

[169] I. Arnay, J. Rubio-Zuazo, and G. R. Castro. Impact of cleaning methods on the structural properties and morphology of $srtio_3$ surface. *Applied Surface Science*, 427:561 – 565, 2018.

[170] W. A. Hines, A. H. Menotti, J. I. Budnick, T. J. Burch, T. Litrenta, V. Niculescu, and K. Raj. Magnetization studies of binary and ternary alloys based on fe_3si. *Phys. Rev. B*, 13:4060–4068, May 1976.

[171] Y. Nishino, S. Inoue, S. Asano, and N. Kawamiya. Anomalous temperature dependence of the electrical resistivity in binary and pseudobinary alloys based on fe$_3$si. *Phys. Rev. B*, 48:13607–13613, Nov 1993.

[172] E.A. Kümmerle, K. Badura, B. Sepiol, H. Mehrer, and H.-E. Schaefer. Thermal formation of vacancies in fe$_3$si. *Phys. Rev. B*, 52:R6947–R6950, Sep 1995.

[173] G. Rixecker, P. Schaaf, and U. Gonser. Ordered iron-silicon alloys: Antiphase boundaries seen by mössbauer spectroscopy. *physica status solidi (a)*, 151(2):291–298, 1995.

[174] U. Starke, W. Meier, C. Rath, J. Schardt, W. Weib, and K. Heinz. Phase transition and atomic structure of an fe$_3$si(100) single crystal surface. *Surface Science*, 377-379:539 – 543, 1997. European Conference on Surface Science.

[175] N. R. Baldwin and D. G. Ivey. Iron slicide formation in bulk iron-silicon diffusion couples. *Journal of Phase Equilibria*, 16(4):300–307, Aug 1995.

[176] O. Kubaschewski. *Iron-binary phase diagrams*. Springer, 1982.

[177] B. Khanbabaee, D. Lützenkirchen-Hecht, R. Hübner, J. Grenzer, S. Facsko, and U. Pietsch. Near surface silicide formation after off-normal fe-implantation of si(001) surfaces. *Journal of Applied Physics*, 116(2):024301, 2014.

[178] B. Krumme, C. Weis, H. C. Herper, F. Stromberg, C. Antoniak, A. Warland, E. Schuster, P. Srivastava, M. Walterfang, K. Fauth, J. Minár, H. Ebert, P. Entel, W. Keune, and H. Wende. Local atomic order and element-specific magnetic moments of fe$_3$Si thin films on mgo(001) and gaas(001) substrates. *Phys. Rev. B*, 80:144403, Oct 2009.

[179] C Weis, B Krumme, H C Herper, F Stromberg, C Antoniak, A Warland, P Entel, W Keune, and H Wende. Magnetic properties of ultrathin fe 3 si films on gaas(001). *Journal of Physics: Conference Series*, 200(7):072105, 2010.

[180] S. Jain, A. O. Adeyeye, and D. Y. Dai. Magnetic properties of half-metallic fe$_3$o$_4$ films. *Journal of Applied Physics*, 95(11):7237–7239, 2004.

[181] C. Boothman, A. M. Sánchez, and S. van Dijken. Structural, magnetic, and transport properties of fe$_3$o$_4$/si(111) and fe$_3$o$_4$/si(001). *Journal of Applied Physics*, 101(12):123903, 2007.

[182] H. Aireddy, S. Bhaumik, and A. K. Das. Electric field dependence of junction magnetoresistance in magnetite/semiconductor heterostructure at room temperature. *Applied Physics Letters*, 107(23):232406, 2015.

[183] W. B. Mi, E. Y. Jiang, and H. L. Bai. Electrical transport properties and magnetoresistance of polycrystalline Fe_3O_4/p-Si heterostructures. *Journal of Applied Physics*, 107(10):103922–103922–5, May 2010.

[184] J. M. Gallego, J. M. García, J. Alvarez, and R. Miranda. Metallization-induced spontaneous silicide formation at room temperature: The fe/si case. *Phys. Rev. B*, 46:13339–13344, Nov 1992.

[185] H. von Känel. Growth and characterization of epitaxial ni and co silicides. *Materials Science Reports*, 8(5):193 – 269, 1992.

[186] J. Alvarez, J. J. Hinarejos, E. G. Michel, J. M. Gallego, A. L. Vazquez de Parga, J. de la Figuera, C. Ocal, and R. Miranda. Surface characterization of epitaxial, semiconducting, fesi2 grown on si(100). *Applied Physics Letters*, 59(1):99–101, 1991.

[187] J. Alvarez, J. J. Hinarejos, E. G. Michel, G. R. Castro, and R. Miranda. Electronic structure of iron silicides grown on si(100) determined by photoelectron spectroscopies. *Phys. Rev. B*, 45:14042–14051, Jun 1992.

[188] G.R. Castro, J.E. Hulse, and J. Küppers. Metal atom catalyzed oxidation of silicon. *Applied Surface Science*, 27(3):262 – 274, 1986.

[189] P. Soukiassian, T. M. Gentle, M. H. Bakshi, and Z. Hurych. Sio2âsi interface formation by catalytic oxidation using alkali metals and removal of the catalyst species. *Journal of Applied Physics*, 60(12):4339–4341, 1986.

[190] E.G. Michel, E.M. Oellig, M.C. Asensio, and R. Miranda. Alkali-induced oxidation of silicon. *Surface Science*, 189-190:245 – 251, 1987.

[191] K. R$\acute{}$uhrnschopf, D. Borgmann, and G. Wedler. Interaction of oxygen with the system si(100)fe(film). *Surface Science*, 374(1):269 – 276, 1997.

[192] C. Park, Y. Shi, Y. Peng, K. Barmak, J.-G. Zhu, D. E. Laughlin, and R. M. White. Interfacial composition and microstructure of fe_3o_4 magnetic tunnel junctions. *IEEE Transactions on Magnetics*, 39(5):2806–2808, 2003.

[193] S. Jain, A. O. Adeyeye, and C. B. Boothroyd. Electronic properties of half metallic fe3o4 films. *Journal of Applied Physics*, 97(9):093713, 2005.

[194] D. Tripathy, A. O. Adeyeye, and C. B. Boothroyd. Effect of fe2o3 on the transport and magnetic properties of half metallic fe3o4. *Journal of Applied Physics*, 99(8):08J105, 2006.

[195] S. S. A. Hassan, Y. Xu, and S. M. Wu, J. Thompson. Epitaxial growth and magnetic properties of half-metallic fe3 o4 on si(100) using mgo buffer layer. *IEEE Transactions on Magnetics*, 45(10):4357–4359, 2009.

[196] K. A. Shaw, E. Lochner, and D. M. Lind. Interdiffusion study of magnesium in magnetite thin films grown on magnesium oxide (001) substrates. *Journal of Applied Physics*, 87(4):1727–1733, 2000.

[197] H. Xiang, F. Shi, M. S. Rzchowski, P. M. Voyles, and Y. A. Chang. Epitaxial growth and magnetic properties of fe3o4 films on tin buffered si(001), si(110), and si(111) substrates. *Applied Physics Letters*, 97(9):092508, 2010.

[198] P. Prieto, J. de la Figuera, L. Martín-García, J. E. Prieto, and J. F. Marco. Fourfold in-plane magnetic anisotropy of magnetite thin films grown on tin buffered si(001) by ion-assisted sputtering. *J. Mater. Chem. C*, 4:7632–7639, 2016.

[199] W. Braun, M. Bader, E. Holub-Krappe, J. Haase, and P. Eichinger. Structural properties of native and ultra thin thermal oxides of silicon as studied by sexafs. *Surface and Interface Analysis*, 10(5):250–252, 1987.

[200] V. V. Balashev, V. A. Vikulov, A. A. Dimitriev, T. A. Pisarenko, E. V. Pustovalov, and V. V. Korobtsov. Evolution of the structural and magnetotransport properties of magnetite films depending on the temperature of their synthesis on the sio2/si(001) surface. *Physics of Metals and Metallography*, 118(7):644–651, 2017.

[201] V. A. Vikulov, V. V. Balashev, T. A. Pisarenko, A. A. Dimitriev, and V. V. Korobtsov. The effect of synthesis temperature on structural and magnetic properties of fe3o4 films grown on the sio2/si(001) surface. *Technical Physics Letters*, 38(4):336–339, 2012.

[202] T. L. Qu, Y. G. Zhao, H. F. Tian, C. M. Xiong, S. M. Guo, and J. Q. Li. Rectifying property and giant positive magnetoresistance of fe3o4âsio2âsi heterojunction. *Applied Physics Letters*, 90(22):223514, 2007.

[203] L.T. Zhang, P. Li, W.B. Mi, E.Y. Jiang, and H.L. Bai. Positive and negative magnetoresistance in fe3o4-based heterostructures. *Journal of Magnetism and Magnetic Materials*, 324(22):3731 – 3736, 2012.

[204] K. Jin, H. Lu, Q. Zhou, K. Zhao, B. Cheng, Z. Chen, Y. Zhou, and G.-Z. Yang. Positive colossal magnetoresistance from interface effect in $p-n$ junction of $la_{0.9}sr_{0.1}mno_3$ and $srnb_{0.01}ti_{0.99}o_3$. *Phys. Rev. B*, 71:184428, May 2005.

[205] W. B. Mi, E. Y. Jiang, and H. L. Bai. Current-perpendicular-to-plane transport properties of polycrystalline fe_3o_4/α-fe_2o_3 heterostructures. *Applied Physics Letters*, 93(13):132504, 2008.

[206] F.J. Ferrer, J. Gil-Rostra, L. González-García, J. Rubio-Zuazo, P. Romero-Gómez, M.C. López-Santos, and F. Yubero. Attenuation lengths of high energy photoelectrons in compact and mesoporous sio2 films. *Surface Science*, 606(9):820 – 824, 2012.

[207] M. P. Seah and R. White. Ultrathin sio2 on si: Iii mapping the layer thickness efficiently by xps. *Surface and Interface Analysis*, 33(12):960–963, 2002.

[208] B. E. Deal and A. S. Grove. General relationship for the thermal oxidation of silicon. *Journal of Applied Physics*, 36(12):3770–3778, 1965.

[209] H. Z. Massoud, J. D. Plummer, and E. A. Irene. Thermal oxidation of silicon in dry oxygen growthârate enhancement in the thin regime: I . experimental results. *Journal of The Electrochemical Society*, 132(11):2685–2693, 1985.

[210] J.R. Engstrom, D.J. Bonser, and T. Engel. The reaction of atomic oxygen with si(100) and si(111): Ii. adsorption, passive oxidation and the effect of coincident ion bombardment. *Surface Science*, 268(1):238 – 264, 1992.

[211] I. Chamritski and G. Burns. Infrared- and raman-active phonons of magnetite, maghemite, and hematite:â a computer simulation and spectroscopic study. *The Journal of Physical Chemistry B*, 109(11):4965–4968, 2005.

[212] R. Gupta, A. K. Sood, P. Metcalf, and J. M. Honig. Raman study of stoichiometric and zn-doped fe_3o_4. *Phys. Rev. B*, 65:104430, Feb 2002.

[213] P. M. Fauchet and I. H. Campbell. Raman spectroscopy of low-dimensional semiconductors. *Critical Reviews in Solid State and Materials Sciences*, 14(sup1):s79–s101, 1988.

[214] P. Colomban. How raman spectra of nanomaterials are related to disorder and particle/domain size? an overview. 3:361–380, 08 2014.

[215] L. Bellot-Gurlet, D. Neff, S. Reguer, J. Monnier, M. Saheb, and P. Dillmann. Raman studies of corrosion layers formed on archaeological irons in various media. *Journal of Nano Research*, 8:147–156, 2009.

[216] S. I. Rybchenko, Y. Fujishiro, H. Takagi, and M. Awano. Effect of grain boundaries on the magnetoresistance of magnetite. *Phys. Rev. B*, 72:054424, Aug 2005.

[217] C. Park, Y. Peng, J.-G. Zhu, D. E. Laughlin, and R. M. White. Magnetoresistance of polycrystalline fe3o4 films prepared by reactive sputtering at room temperature. *Journal of Applied Physics*, 97(10):10C303, 2005.

[218] P. Sheng, B. Abeles, and Y. Arie. Hopping conductivity in granular metals. *Phys. Rev. Lett.*, 31:44–47, Jul 1973.

[219] Q. Li, C. W. Kartikowati, S. Horie, T. Ogi, T. Iwaki, and K. Okuyama. Correlation between particle size/domain structure and magnetic properties of highly crystalline fe3o4 nanoparticles. *Scientific Reports*, 7:9894, 2017.

[220] K. K. Adepalli, J. Yang, J. Maier, H. L. Tuller, and B. Yildiz. Tunable oxygen diffusion and electronic conduction in $srtio_3$ by dislocation-induced space charge fields. *Advanced Functional Materials*, 27(22):1700243, 2017.

[221] K. Ghosh, S. B. Ogale, S. P. Pai, M. Robson, E. Li, I. Jin, Z. Dong, R. L. Greene, R. Ramesh, T. Venkatesan, and M. Johnson. Positive giant magnetoresistance in a $fe_3o_4/srtio_3/la_{0.7}sr_{0.3}mno_3$ heterostructure. *Applied Physics Letters*, 73(5):689–691, 1998.

[222] E. M. J. Hassen, B. Viala, M. C. Cyrille, M. Cartier, O. Redon, P. Lima, B. Belhadji, H. X. Yang, J. Velev, and M. Chshiev. Room temperature magnetoresistance in cofeb/srtio3/cofeb magnetic tunnel junctions deposited by ion beam sputtering. *Journal of Applied Physics*, 111(7):07C727, 2012.

[223] N. Kumar, P. Misra, R. K. Kotnala, A. Gaur, and R. S. Katiyar. Room temperature magnetoresistance in $sr_2femoo_6/srtio_3/sr_2femoo_6$ trilayer devices. *Journal of Physics D: Applied Physics*, 47(6):065006, 2014.

[224] I. J. V. Marún, F. M. Postma, J. C. Lodder, and R. Jansen. Tunneling magnetoresistance with positive and negative sign in $la_{0.67}sr_{0.33}mno_3$âsrtio$_3$âCo junctions. *Phys. Rev. B*, 76:064426, Aug 2007.

[225] D. Gilks, K. P. McKenna, Z. Nedelkoski, B. Kuerbanjiang, K. Matsuzaki, T. Susaki, L. Lari, D. Kepaptsoglou, Q. Ramasse, S. Tear, and V. K. Lazarov. Polar spinel-perovskite interfaces: an atomistic study of $fe_3o_4(111)/srtio_3(111)$ structure and functionality. *Scientific Reports*, 6:29724, 2016.

[226] A. Hamie, Y. Dumont, E. Popova, A. Fouchet, B. Warot-Fonrose, C. Gatel, E. Chikoidze, J. Scola, B. Berini, and N. Keller. Investigation of high quality magnetite thin films grown on $srtio_3(001)$ substrates by pulsed laser deposition. *Thin Solid Films*, 525:115 – 120, 2012.

[227] Y. Z. Chen, J. R. Sun, Y. N. Han, X. Y. Xie, J. Shen, C. B. Rong, S. L. He, and B. G. Shen. Microstructure and magnetic properties of strained fe_3o_4 films. *Journal of Applied Physics*, 103(7):07D703, 2008.

[228] J. G. Zheng, G. E. Sterbinsky, J. Cheng, and B. W. Wessels. Epitaxial fe_3o_4 on $srtio_3$characterized by transmission electron microscopy. *Journal of Vacuum Science & Technology B: Microelectronics and Nanometer Structures Processing, Measurement, and Phenomena*, 25(4):1520–1523, 2007.

[229] G. Niu, G. Saint-Girons, B. Vilquin, G. Delhaye, J.-L. Maurice, C. Botella, Y. Robach, and G. Hollinger. Molecular beam epitaxy of $srtio_3$ on si (001): Early stages of the growth and strain relaxation. *Applied Physics Letters*, 95(6):062902, 2009.

[230] S. A. Chambers, Y. Liang, Z. Yu, R. Droopad, J. Ramdani, and K. Eisenbeiser. Band discontinuities at epitaxial $srtio_3$/si(001) heterojunctions. *Applied Physics Letters*, 77(11):1662–1664, 2000.

[231] A. K. Pradhan, D. Hunter, T. Williams, B. Lasley-Hunter, R. Bah, H. Mustafa, R. Rakhimov, J. Zhang, D. J. Sellmyer, E. E. Carpenter, D. R. Sahu, and J.-L. Huang. Magnetic properties of $la_{0.6}sr_{0.4}mno_3$ thin films on $srtio_3$ and buffered si substrates with varying thickness. *Journal of Applied Physics*, 103(2):023914, 2008.

[232] F. X. Hu, J. R. Sun, B. G. Shen, C. B. Rong, and J. Gao. Epitaxial growth of colossal magnetoresistive films onto si(100). *Journal of Applied Physics*, 103(7):07F706, 2008.

[233] F. Niu and B. W. Wessels. Epitaxial growth and strain relaxation of $batio_3$ thin films on $srtio_3$ buffered (001) si by molecular beam epitaxy. *Journal of Vacuum Science & Technology B: Microelectronics and Nanometer Structures Processing, Measurement, and Phenomena*, 25(3):1053–1057, 2007.

[234] T. Fix, V. Da Costa, C. Ulhaq-Bouillet, S. Colis, A. Dinia, K. Bouzehouane, and A. Barthélémy. High quality $srtio_3$ tunnel barrier obtained by pulsed laser deposition. *Applied Physics Letters*, 91(8):083104, 2007.

[235] M.-H. Mark Hsu, D. Van Thourhout, M. Pantouvaki, J. Meersschaut, T. Conard, O. Richard, H. Bender, P. Favia, M. Vila, R. Cid, J. Rubio-Zuazo, G. R. Castro, J. Van Campenhout, P. Absil, and C. Merckling. Controlled orientation of molecular-beam-epitaxial $batio_3$ on si(001) using thickness engineering of $batio_3$ and $srtio_3$ buffer layers. *Applied Physics Express*, 10(6):065501, 2017.

[236] O. Kuschel, N. Pathé, T. Schemme, K. Ruwisch, J. Rodewald, R. Buss, F. Bertram, T. Kuschel, K. Kuepper, and J. Wollschläger. Impact of strain and morphology on magnetic properties of fe3o4/nio bilayers grown on nb:srtio3(001) and mgo(001). *Materials*, 11(7), 2018.

[237] H. F. Tian, T. L. Qu, L. B. Luo, J. J. Yang, S. M. Guo, H. Y. Zhang, Y. G. Zhao, and J. Q. Li. Strain induced magnetoelectric coupling between magnetite and batio3. *Applied Physics Letters*, 92(6):063507, 2008.

[238] X. W. Li, A. Gupta, Gang Xiao, and G. Q. Gong. Transport and magnetic properties of epitaxial and polycrystalline magnetite thin films. *Journal of Applied Physics*, 83(11):7049–7051, 1998.

[239] L. Tauxe, H. N. Bertram, and C. Seberino. Physical interpretation of hysteresis loops: Micromagnetic modeling of fine particle magnetite. *Geochemistry, Geophysics, Geosystems*, 3(10):1–22, 2002.

[240] G. Zhang, C. Fan, L. Pan, F. Wang, P. Wu, H. Qiu, Y. Gu, and Y. Zhang. Magnetic and transport properties of magnetite thin films. *Journal of Magnetism and Magnetic Materials*, 293(2):737 – 745, 2005.

[241] J. Herfort, H.-P. Schönherr, A. Kawaharazuka, M. Ramsteiner, and K.H. Ploog. Epitaxial growth of fe_3si/gaas(001) hybrid structures for spintronic application. *Journal of Crystal Growth*, 278(1):666 – 670, 2005. 13th International Conference on Molecular Beam Epitaxy.

[242] R. Mantovan, M. Georgieva, M. Fanciulli, A. Goikhman, N. Barantcev, Yu. Lebedinskii, and A. Zenkevich. Synthesis and characterization of fe_3si/sio_2 structures for spintronics. *physica status solidi (a)*, 205(8):1753–1757, 2008.

[243] Masanobu Miyao, Koji Ueda, Yu ichiro Ando, Mamoru Kumano, Taizoh Sadoh, Kazumasa Narumi, and Yoshihito Maeda. Atomically controlled hetero-epitaxy of fe_3si/sige for spintronics application. *Thin Solid Films*, 517(1):181 – 183, 2008. Fifth International Conference on Silicon Epitaxy and Heterostructures (ICSI-5).

[244] K Harada, K S Makabe, H Akinaga, and T Suemasu. Room temperature magnetoresistance in $fe_3si/caf_2/fe_3si$ mtj epitaxially grown on si(111). *Journal of Physics: Conference Series*, 266(1):012088, 2011.

[245] L. L. Tao, S. H. Liang, D. P. Liu, H. X. Wei, J. Wang, and X. F. Han. Tunneling magnetoresistance in fe_3si/mgo/fe_3si(001) magnetic tunnel junctions. *Applied Physics Letters*, 104(17):172406, 2014.

[246] M. Kawano, M. Ikawa, K. Santo, S. Sakai, H. Sato, S. Yamada, and K. Hamaya. Electrical detection of spin accumulation and relaxation in p-type germanium. *Phys. Rev. Materials*, 1:034604, Aug 2017.

[247] B. Jenichen, J. Herfort, U. Jahn, A. Trampert, and H. Riechert. Epitaxial $fe_3si/ge/fe_3si$ thin film multilayers grown on gaas(001). *Thin Solid Films*, 556:120 – 124, 2014.

[248] S. Gaucher, B. Jenichen, J. Kalt, U. Jahn, A. Trampert, and J. Herfort. Growth of $fe_3si/ge/fe_3si$ trilayers on gaas(001) using solid-phase epitaxy. *Applied Physics Letters*, 110(10):102103, 2017.

[249] C. Gusenbauer, T. Ashraf, J. Stangl, G. Hesser, T. Plach, A. Meingast, G. Kothleitner, and R. Koch. Interdiffusion in heusler film epitaxy on gaas(001). *Phys. Rev. B*, 83, 01 2011.

[250] V.L. Alperovich, O.E. Tereshchenko, N.S. Rudaya, D.V. Sheglov, A.V. Latyshev, and A.S. Terekhov. Surface passivation and morphology of gaas(100) treated in hcl-isopropanol solution. *Applied Surface Science*, 235(3):249 – 259, 2004. Proceedings of the 3rd International Workshop on Semiconductor Surface Passivation.

[251] T. Yoshitake, D. Nakagauchi, T. Ogawa, M. Itakura, N. Kuwano, Y. Tomokiyo, T. Kajiwara, and K. Nagayama. Room-temperature epitaxial growth of ferromag-

netic fe$_3$si films on si(111) by facing target direct-current sputtering. *Applied Physics Letters*, 86(26):262505, 2005.

[252] K. Hamaya, K. Ueda, Y. Kishi, Y. Ando, T. Sadoh, and M. Miyao. Epitaxial ferromagnetic fe$_3$siâsi(111) structures with high-quality heterointerfaces. *Applied Physics Letters*, 93(13):132117, 2008.

[253] K. Zakeri, I. Barsukov, N. K. Utochkina, F. M. Römer, J. Lindner, R. Meckenstock, U. von Hörsten, H. Wende, W. Keune, M. Farle, S. Kalarickal, K. Lenz, and Z Frait. Magnetic properties of epitaxial fe$_3$si/mgo(001) thin films. *Physical Review B*, 76:214421, 12 2007.

[254] Jing Xie, Quan Xie, Rui Ma, Jin Huang, Chong Zhang, and Dong Liu. Annealing temperature dependent structures and properties of ferromagnetic fe$_3$si films fabricated by resistive thermal evaporation. *Journal of Materials Science: Materials in Electronics*, 29(2):1369–1376, Jan 2018.

[255] T. Yoshitake, D. Nakagauchi, and K. Nagayama. Ferromagnetic iron silicide thin films prepared by pulsed-laser deposition. *Japanese Journal of Applied Physics*, 42(7B):L849, 2003.